Jet Substructure at the LHC with SCET

Pedro Cal

Jet Substructure at the LHC with Soft Collinear Effective Theory

Pedro Cal

Jet Substructure at the LHC with Soft Collinear Effective Theory

Pedro Cal

Title: Jet Substructure at the LHC with Soft Collinear Effective Theory
Printed by: Gildeprint

UNIVERSITEIT VAN AMSTERDAM

Nikhef

European Research Council
Established by the European Commission

This work is supported by the ERC grant ERC-STG-2015-677323.

Jet Substructure at the LHC with Soft Collinear Effective Theory

ACADEMISCH PROEFSCHRIFT

ter verkrijging van de graad van doctor
aan de Universiteit van Amsterdam
op gezag van de Rector Magnificus
prof. dr. ir. K.I.J. Maex
ten overstaan van een door het College voor Promoties ingestelde
commissie, in het openbaar te verdedigen in de Aula der Universiteit
op woensdag 29 september 2021, te 14.00 uur

door

Pedro Miguel Rocio Rodrigues Cal

geboren te Lisboa

Promotiecommissie:

Promotor:	dr. W.J. Waalewijn	Universiteit van Amsterdam
Co-promotor:	prof. dr. E.L.M.P. Laenen	Universiteit van Amsterdam
Overige leden:	dr. A. Castro Anich	Universiteit van Amsterdam
	prof. dr. P.J.G. Mulders	Vrije Universiteit Amsterdam
	dr. J. M. Sonneveld	Universiteit van Amsterdam
	dr. J. Thaler	Massachusetts Institute of Technology
	prof. dr. E.P. Verlinde	Universiteit van Amsterdam
	prof. dr. M. Vreeswijk	Universiteit van Amsterdam

Faculteit der Natuurwetenschappen, Wiskunde en Informatica

The material presented in this thesis is based on the following publications:

[1] P. Cal, F. Ringer and W. J. Waalewijn, *The jet shape at NLL′*, *JHEP* **05** (2019) 143 [1901.06389]

[2] P. Cal, D. Neill, F. Ringer and W. J. Waalewijn, *Calculating the angle between jet axes*, *JHEP* **04** (2020) 211 [1911.06840]

[3] P. Cal, K. Lee, F. Ringer and W. J. Waalewijn, *Jet energy drop*, *JHEP* **11** (2020) 012 [2007.12187]

[4] P. Cal, K. Lee, F. Ringer and W. J. Waalewijn, *The soft drop momentum sharing fraction z_g beyond leading-logarithmic accuracy*, 2106.04589

Author contributions:

In Ref. [1], I determined the collinear function, including the effect of recoil, implemented the jet shape at NLL′ numerically and produced the figures and plots, under the supervision of FR and WW.

In Ref. [2], I computed the fixed-order expressions, the ingredients in the factorization theorem, obtained the numerical results for the angles between the three different axes and produced the publication figures, with input of DN, FR, and WW. Together with my co-authors, I obtained the factorization formula for the angle between the standard and groomed jet axes in collaboration.

In Ref. [3], I proposed and carried out the study of the energy drop for iterated soft drop. I performed the analytical calculations of the fixed-order and SCET ingredients for all grooming techniques, and together with KL obtained the numerical results and produced the figures and plots, with input from WW and FR.

In Ref. [4], I worked on the framework and numerical implementation of z_g beyond LL together with KL, with input from WW and FR. I produced the figures and plots.

I have contributed to the writing of the manuscripts of all these works.

Contents

Introduction

The goal of particle physics is to understand the laws of nature at their most fundamental level. Theorists do so by resorting to a mathematical framework known as quantum field theory (QFT), which has led to the most spectacular agreement between theory and experiment in the history of science.

Our modern understanding of particle physics is embodied by the Standard Model (SM), which contains all known elementary particles and describes the strong, weak and electromagnetic interactions. With the discovery of the Higgs boson by the ATLAS [5] and CMS [6] experiments during the 7 and 8 TeV LHC runs, the last missing piece was finally found. Since then the SM has been hailed as a great triumph of modern physics since it successfully describes all current accelerator data (with possible exceptions like the 4.2σ discrepancy of the muon $g-2$ or the 3.1σ significance of lepton flavor universality violation [7]).

Despite its phenomenal effectiveness, we know the Standard Model does not correspond to the ultimate theory of reality. Besides the non-inclusion of gravity, there are questions regarding neutrino masses, matter-antimatter asymmetry in the universe, or the nature of dark energy and dark matter that have no explanation under the current formulation of the theory.

Interestingly, the LHC has covered a wide region of phase-space and no new physics has emerged. Under these circumstances it becomes paramount to resort to *precision physics*. Rather than hoping to directly produce a new resonance which might never show up at LHC energies, the clues for new physics lie in small but statistically significant deviations from SM predictions. In order to detect such indirect effects, theorists must match the astonishing precision of current collider experiments by pushing their calculations to higher accuracy, both logarithmic and fixed-order. Precision assumes an even more prominent role in the advent of the high-luminosity LHC, scheduled to start in 2027. The upgrade will increase the integrated luminosity of the four main experiments by a factor of 10, thereby drastically increasing the machine's discovery potential.

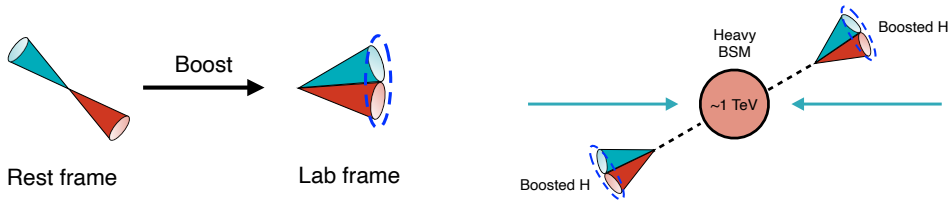

(a) Hadronic decay of a boosted Higgs in rest and lab frames

(b) Heavy BSM resonance decaying to two boosted Higgs

Figure 0.1 Boosted Higgs hadronic decay, and its importance for new physics searches.

Quantum Chromodynamics and jet substructure

The Standard Model is invariant under the $\mathrm{SU(3)_c} \times \mathrm{SU(2)_L} \times \mathrm{U(1)_Y}$ gauge symmetry group. The focus of this thesis is the $\mathrm{SU(3)_c}$ sector corresponding to the theory of the strong interaction, Quantum Chromodynamics (QCD). One of the most fascinating aspects of QCD is the emergence of *jets*: sprays of collimated particles that occur whenever energetic quarks or gluons are produced in high energy collisions.

Jets are the most frequently detected objects at the LHC multipurpose experiments ATLAS and CMS, and are present in the vast majority of interesting collisions. The typical energy of a hard process at the LHC ranges from ∼100 GeV to several TeV, leaving a large phase-space between this scale and $\Lambda_{\mathrm{QCD}} \sim 200$ MeV, the scale at which colored particles (quarks and gluons) become confined into colorless hadrons. The way an energetic parton evolves from high to low energies is by undergoing multiple *soft* (low-energy) and *collinear* (collimated) emissions known as a parton shower. The resulting particles ultimately hadronize and become the collection of hadrons we call a jet.

The complex radiation pattern inside jets contains valuable information we want to exploit. This is studied through the set of tools known as *jet substructure*, which is the topic of this thesis. Even though the first jet substructure developments date back to Mike Seymour in the 90s [8, 9] it wasn't until the LHC era that the field began its staggering growth. The large center-of-mass energies, the exceptional granularity of LHC detectors as well as the introduction of fast jet finding algorithms like anti-k_t [10] generated a renewed interest in jet substructure techniques. In particular, one of its early applications was the identification of hadronically decaying boosted heavy objects, i.e. the W/Z and Higgs bosons and the top quark.

To illustrate this, consider a hadronic decay of the Higgs, for example $H \to b\bar{b}$

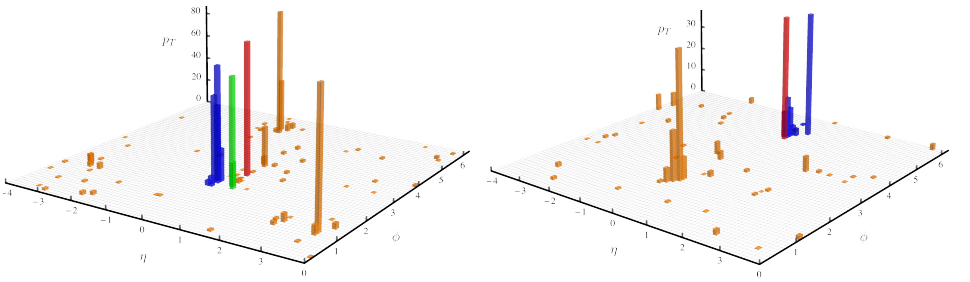

(a) $pp \to$ boosted top $+ X$ **(b)** $pp \to$ boosted Higgs $+ X$

Figure 0.2 Fat jets originating from $t \to W\, b \to q\, \bar{q}'\, b$ (left), and from $H \to q\, \bar{q}$ (right). QCD jets are shown in orange.

displayed in figure 0.1a. In the rest-frame of the Higgs, the b and $\bar{b}$ quarks produce two jets which must be back-to-back due to momentum conservation. When the Higgs is produced at high energies, the boost to the lab-frame makes the decay products collimated into a single direction. What corresponds to two jets in the rest-frame will be reconstructed as one large jet in our detector, often called a *fat-jet*. Under close inspection one should be able to distinguish a fat-jet with its 2-prong structure from a regular QCD jet displaying a single-prong structure, as can be seen in figure 0.2. Such a task can be done statistically and falls within the purview of jet substructure.

The identification of boosted heavy objects also plays a vital role in improving the sensitivity to new physics signals at the LHC. Consider a beyond the Standard Model (BSM) resonance with mass $M \sim 1$ TeV, which decays into two heavy electroweak particles. Given the difference in mass between the BSM particle and its decay products, the electroweak particles will be highly boosted and reconstructed into a fat-jet, as displayed in figure 0.1b.

Since the start of the LHC, jet substructure has become a lively field whose applications now extend well beyond the identification of boosted heavy objects. These recent developments include precision tests of the SM, quark/gluon jet discrimination, the use of jet grooming techniques, the improvement of parton showering modelling and the study of the quark-gluon plasma. For an excellent review on the topic of jet substructure, including the wide scope of applications and impact on the broader QCD community, we refer the reader to [11] . Finally the use of machine learning techniques has also led to a surge of innovative ideas in jet physics, which are also covered in this review.

In this thesis our focus lies in obtaining precision QCD predictions for jet substructure observables using the framework of soft-collinear effective theory (SCET) [12–16]. Since these observables are dominated by soft and collinear

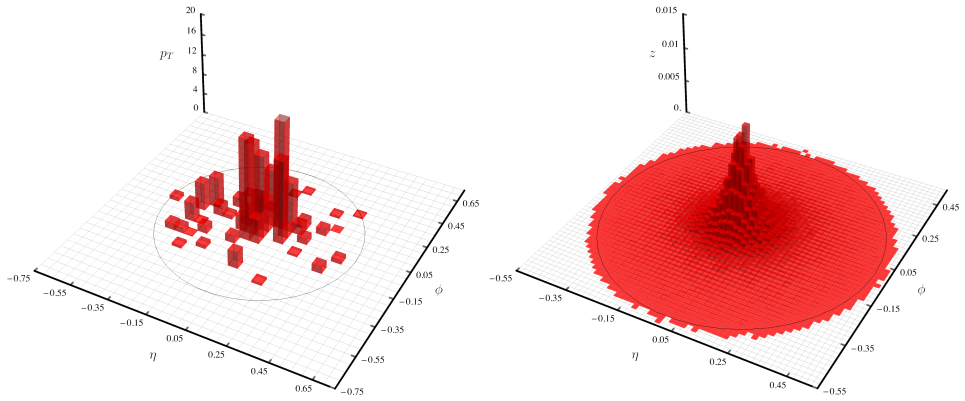

(a) Typical QCD jet at low p_T **(b)** Average over 10000 jets

Figure 0.3 QCD jet at $p_T \sim 30$ GeV (left), and average energy distribution for jets with $p_T = 30 - 50$ GeV (right).

radiation, it is imperative to perform resummation at high logarithmic accuracy in order to achieve precision, which we accomplish through factorization and resummation methods in SCET. These concepts will be introduced in chapters 1 and 2.

One example of an observable tackled in this thesis is the *jet shape*, displayed in figure 0.4. The jet shape constitutes one of the most basic questions one can ask about the anatomy of a jet: what is the average energy distribution *within* a jet? This classic observable has been measured extensively at a variety of colliders since the days of LEP, but from the theory side it was not clear how to obtain more precise predictions for many decades. This was our goal with [1] and will be the topic of chapter 3.

We should also highlight that jet substructure provides an ideal playground for pushing SCET techniques, which is one of the main goals of this thesis. This is because we essentially work with an effective theory *within* an effective theory. In our case the "full theory" corresponds simply to the jet function (itself an object in the effective theory), which is already factorized from the hard scattering process and does not require cumbersome convolutions over parton distribution functions (PDFs). In other words, it is a rare occasion to have such complete control over the full theory. This allows us to perform precision calculations of exceedingly complex and multi-differential observables, which might follow exotic factorization theorems and require joint resummation, as we will see later in the thesis.

Outline of the thesis

The structure of this thesis is such that the first two chapters present introductory material while the remaining ones lay out original research.

Chapter 1 reviews basic concepts of QCD and jet physics at hadron colliders. In the first three sections we discuss the QCD Lagrangian and renormalization, the structure of perturbative calculations, and the infrared of QCD. In the last section we direct our attention to the topic of jets. We cover the reason for jet formation as well as practical aspects of studying jets at the LHC. For example, the particles that compose a jet at the LHC are more than just those arising from the final state quark or gluon. Radiation emitted from other sources (initial state radiation, underlying event and pile-up) ends up inside the jet as well. This contaminating radiation is unwelcome and procedures have been developed to remove it from jets known as *grooming techniques*, as we discuss in section 1.4.3.

Finally, we perform all-order resummation for the simplest substructure observable: the jet mass. This chapter is based on the jet substructure reviews [11, 17] and well as the outstanding lectures [18].

The theme of chapter 2 is effective field theories (EFT), and in particular soft-collinear effective theory (SCET). We start by discussing the philosophy behind the EFT approach, as well as the use of the renormalization group to resum large logarithms. Next, we provide a brief introduction to the topic of SCET and some of its most basic features. This EFT portion of the chapter is based on the lecture notes [19, 20] and the SCET part on the lecture notes and series [21, 22].

Regarding the research chapters, we begin with chapter 3 whose topic is the precision calculation of the jet shape, as we already mentioned.

Different definitions of jet axes exist and are suitable for different situations. In chapter 4 we carefully examine the angles between three different axes: the standard, the winner-take-all (WTA) and the groomed jet axis. Each of these angles has a different degree of sensitivity to soft and nonperturbative radiation. For example, the WTA axis is insensitive to soft radiation at leading power, and the groomed axis is obtained with the particles that remain after the grooming procedure. As such, this angle has a low dependence on soft physics. On the other hand, the angle between the standard and groomed axes is exclusively determined by soft wide-angle radiation, with a very high dependance on nonperturbative physics. The latter is directly connected to nonperturbative contributions to the rapidity anomalous dimension (Collins-Soper kernel) for transverse momentum distributions. This opens the door for exciting new predictions, such as the dependence of nonperturbative physics on the grooming parameters and jet transverse momentum.

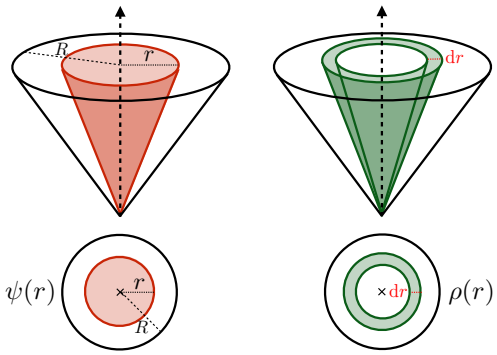

Figure 0.4 The integrated (differential) jet shape, shown in the left (right) panel, is the fraction of the jet transverse momentum contained in a circle (annulus) in (η, ϕ) coordinates, centered on the jet axis.

In chapter 5 we performed a detailed study of how much energy is removed from the jet as it undergoes the grooming procedure for three different types of grooming techniques: Soft Drop [23], Trimming [24] and Iterated Soft Drop [25]. These observables stand out because they only probe soft radiation, making them ideal candidates for the tuning of parton shower Monte Carlo event generators and for probing medium effects in heavy-ion collisions.

Finally, in chapter 6 we study the momentum sharing fraction z_g [26] of the two branches in a jet that pass the soft drop condition. This observable has received a lot of attention by both the theoretical and experimental particle and nuclear physics communities in the past years. The main reason for this is that it allows for the most direct measurement of the QCD splitting functions, providing a glimpse into fundamental splittings at the parton level. We make the first precision calculation for this observable.

1

Jet physics at hadron colliders

1.1 Quantum Chromodynamics essentials

1.1.1 Lagrangian

Quantum Chromodynamics (QCD) is the fundamental theory of the strong interaction describing the dynamics of quarks and gluons. An essential aspect of the theory is its gauge symmetry: the invariance under the special unitary group of 3×3 matrices $SU(3)$. Quarks transform under the fundamental representation of $SU(3)$

$$\psi(x) \to U(x)\psi(x), \tag{1.1}$$

where $U(x)$ is a $SU(3)$ matrix and $\psi(x)$ is the Dirac spin-$\frac{1}{2}$ field describing the quark. The gluons follow the adjoint representation of $SU(3)$ and are described by the spin-1 field $A_\mu(x)$. This field transforms as

$$A_\mu(x) \to U(x)A_\mu U^\dagger(x) + \frac{i}{g_s}U(x)[\partial_\mu U^\dagger(x)]. \tag{1.2}$$

It is useful to decompose the matrix $A_\mu(x)$ into a linear combination the generators of SU(3), denoted by t_a,

$$A_\mu(x) \equiv A^a_\mu(x)\, t_a, \qquad a = 1, .., 8. \tag{1.3}$$

The non-abelian nature of the group is reflected in the commutation relation for the generators

$$[t_a, t_b] = i f^{abc} t_c, \tag{1.4}$$

with f^{abc} known as the structure constants. The generators are conventionally normalized to

$$\mathrm{Tr}[t_a t_b] = T_F \delta_{ab}, \qquad T_F = \frac{1}{2}. \tag{1.5}$$

For a group SU(N_c) the Casimir operators of the fundamental and adjoint representation (C_F and C_A respectively) are given by

$$C_F = \frac{N_c^2 - 1}{2N_c}, \qquad C_A = N_c, \tag{1.6}$$

yielding $C_F = \frac{4}{3}$ and $C_A = 3$ for $N_c = 3$. These can be related to the generators through

$$(t^a t_a)_{ij} = C_F\, \delta_{ij}, \qquad f_{acd} f^{bcd} = C_A \delta^a_b \tag{1.7}$$

We are now ready to discuss the QCD Lagrangian:

$$\mathcal{L}_{\text{QCD}} = -\frac{1}{4} G^{\mu\nu}_a G^a_{\mu\nu} + \sum_f \bar{\psi}_f (i \not{D} - m_f) \psi_f + \mathcal{L}_{\text{gf}} + \mathcal{L}_{\text{ghost}}, \tag{1.8}$$

with the subscript f denoting the flavour of the quark. The gluon field A^a_μ appears in the covariant derivative D_μ and field-strength tensor $G^a_{\mu\nu}$

$$\begin{aligned} D_\mu &= \partial_\mu + i g_s t_a A^a_\mu \\ G^{\mu\nu}_a &= \partial^\mu A^\nu_a - \partial^\nu A^\mu_a - g_s f_a{}^{bc} A^\mu_b A^\nu_c. \end{aligned} \tag{1.9}$$

In order to obtain the gluon propagator one needs to add a gauge-fixing term $\mathcal{L}_{\text{gf}}$ that makes its equations of motion invertible. In this thesis we work with the covariant R_ξ gauge

$$\mathcal{L}_{\text{gf}} = -\frac{1}{2\xi} (\partial_\mu A^\mu_a)(\partial^\nu A^a_\nu). \tag{1.10}$$

With this choice of gauge-fixing come unphysical degrees of freedom called Fadeev-Popov ghosts, encoded in the Lagrangian:

$$\mathcal{L}_{\text{gh}} = (\partial^\mu \bar{c}_a)(\delta^{ab} \partial_\mu + g_s f^{abc} A^\mu_c) c_b. \tag{1.11}$$

The c_a and $\bar{c}_a$ are anti-commuting scalar fields in the adjoint representation, which makes them unphysical since they violate the spin-statistics theorem. Ghosts cannot therefore appear as external states for S-matrix elements, but nothing prevents them from appearing in the path-integral and hence as virtual states. Their role is to cancel unphysical degrees of freedom found in gluon loops, e.g. the longitudinal polarization. While some non-covariant gauges (such as axial gauges) are free of ghosts, calculations are much simpler in covariant gauges. Unless otherwise specified in this thesis we set $\xi = 1$, corresponding to the Feynman-'t Hooft gauge.

1.1.2 Renormalization and Renormalization Group

Quantum field theory is plagued with infinities: radiative corrections often contain integrals over momenta of virtual particles that are divergent. Infinities that arise from the large momentum limit of the integrand are called *ultraviolet* (UV) divergences. The other type of divergences are *infrared divergences*, which we cover in detail in section 1.3.

The mechanism that provides a systematic way of removing ultraviolet divergences is called *renormalization*, whereby a finite number of redefinitions of the parameters in the Lagrangian render S-matrix elements UV-finite. When performing renormalization, two elements need to be specified: the *regularization method* and the *renormalization scheme*.

The regularization method is the manner in which the divergences of the integral are tamed and made explicit. A naive way to achieve this is by introducing a sharp cutoff Λ_c ,

$$\begin{aligned} g^2 \int \frac{\mathrm{d}^4 k}{(2\pi)^4} \frac{1}{(k^2 - m^2)^2} &\to \frac{ig^2}{8\pi^2} \int_0^{\Lambda_c} \mathrm{d}k \, \frac{k^3}{(k^2 - m^2)^2} \\ &= \frac{ig^2}{16\pi^2} \left[\frac{\Lambda_c^2}{m^2 - \Lambda_c^2} + \ln \frac{m^2 - \Lambda_c^2}{m^2} \right] \to \text{Log divergent} \end{aligned} \tag{1.12}$$

In practice this choice of regulator is poor for a number of reasons. It explicitly breaks translation invariance $k \to k + p$, which is often needed when using Feynman parameters to combine denominators. Another equally important drawback is that it breaks gauge invariance: By putting a cutoff on momentum we are restricting the partial derivative $i\partial_\mu \sim p_\mu$, and not the covariant derivative $D_\mu = i\partial_\mu + g_s A_\mu$.

The usual regulator of choice is instead *dimensional regularization* [27, 28], or dim. reg. for short. Dim. reg. works by taking a divergent integral in $d = 4$ dimensions and introducing a small deviation to the spacetime dimension such that $d = 4 - 2\epsilon$ with $\epsilon \to 0$. Consider once again the integral

$$I = \mu^{2\epsilon} g^2 \int \frac{\mathrm{d}^{4-2\epsilon} k}{(2\pi)^{4-2\epsilon}} \frac{1}{(k^2 - m^2)^2} = \frac{ig^2}{16\pi^2} \left[\frac{1}{\epsilon} - \gamma_E + \ln 4\pi + \ln \frac{\mu^2}{m^2} \right] + \mathcal{O}(\epsilon). \tag{1.13}$$

The divergence manifests itself as a pole in ϵ related to the infinitesimal deviation from four dimensions. Note also that we introduced a dimensionful scale μ to make the argument of the log dimensionless. We call μ the *renormalization scale*. This scale will play an important role in our discussion of the renormalization group later in this section.

The list of merits of dim. reg. is long, including the preservation of Lorentz and gauge symmetries, which explains its popularity as a choice of regulator. It is additionally convenient in the context of effective field theories for reasons we will discuss in section 2.1.1.

Now that the divergence is regularized, the course of action is to cancel the $1/\epsilon$ pole by adding a so-called *counterterm* δ, which we manually choose such that $I + \delta$ becomes finite. The choice of which finite terms to include in the counterterm defines the renormalization scheme. In this thesis we will exclusively use the modified minimal subtraction ($\overline{\text{MS}}$) scheme [29, 30], which besides the $1/\epsilon$ term also removes $\gamma_E + \ln 4\pi$. In practice this is often done by defining the $\overline{\text{MS}}$ scale $\bar{\mu}$

$$\bar{\mu}^2 = 4\pi e^{-\gamma_E}\mu^2. \tag{1.14}$$

The counterterms then simply remove the ϵ pole and we relabel $\bar{\mu} \to \mu$ after the renormalization procedure. By choosing the appropriate counterterm δ, in $\overline{\text{MS}}$ we obtain

$$\delta = -\frac{ig^2}{16\pi^2}\frac{1}{\epsilon} \implies I + \delta = \frac{ig^2}{16\pi^2}\ln\frac{\bar{\mu}^2}{m^2}, \tag{1.15}$$

which is finite.

The way to include these counterterms in the Lagrangian is through multiplicative redefinitions of the fields and parameters, hence the name renormalization. Consider the bare QCD Lagrangian for a single quark flavor,

$$\mathcal{L} = -\frac{1}{4}G^{\mu\nu}_{0\,a}G^{a}_{0\,\mu\nu} + \bar{\psi}_0[i(\not{\partial} + ig_{s\,0}\not{A}_0)]\psi_0 + (\partial^\mu \bar{c}_{a\,0})(\delta^{ab}\partial_\mu + g_{s\,0}f^{abc}A^{\mu}_{0\,c})c_{0\,b}, \tag{1.16}$$

where we omitted the gauge-fixing term and neglected quark masses for simplicity. The bare fields and parameters are related to the renormalized quantities via the introduction of renormalization factors Z

$$\psi_0 = Z_\psi^{\frac{1}{2}}\,\psi, \qquad A^a_{0\,\mu} = Z_A^{\frac{1}{2}}A^a_\mu, \qquad c^a_0 = Z_c^{\frac{1}{2}}c^a, \qquad g_{s0} = \mu^\epsilon Z_g\, g_s. \tag{1.17}$$

Note the purpose of the μ^ϵ factor (which already appeared in equation (1.13)) is to keep the renormalized coupling g_s dimensionless in $d = 4 - 2\epsilon$. The renormalization factors are then carefully picked such that they give rise to the necessary counterterms order by order in the strong coupling $\alpha_s \equiv g_s^2/(4\pi)$.

$$Z_a = 1 + \sum_{n=0}^{\infty}\left(\frac{\alpha_s}{4\pi}\right)^n Z_a^n, \qquad \text{with} \quad a = \psi, A, c, g_s. \tag{1.18}$$

For example, the one-loop quark self-energy and gluon vacuum polarization have their divergences canceled by setting Z_ψ and Z_A to

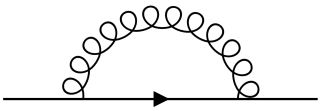

$$\implies Z_\psi = 1 - \frac{\alpha_s C_F}{4\pi\epsilon} + \mathcal{O}(\alpha_s^2)$$

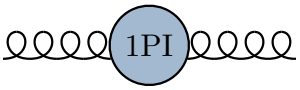

$$\implies Z_A = 1 + \frac{\alpha_s}{4\pi\epsilon}\left[\left(\frac{13}{6} - \frac{\xi}{2}\right)C_A - \frac{4}{3}n_f T_F\right] + \mathcal{O}(\alpha_s^2) \tag{1.19}$$

where the one particle irreducible (1PI) bubble in the vacuum polarization contains diagrams with quark, gluon and ghost loops. Let us take a closer look at the quark-gluon vertex in eq. (1.16)

$$\begin{aligned}\bar{\psi}_0\, i g_{s\,0}\, \not{A}_0\, \psi_0 =& Z_{g_s} Z_\psi Z_A^{\frac{1}{2}}\, (\bar{\psi}\, i\mu^\epsilon g_s\, \not{A}\, \psi) \\ =& (1 + \delta_{q\bar{q}g})(\bar{\psi}\, i\mu^\epsilon g_s\, \not{A}\, \psi).\end{aligned} \tag{1.20}$$

Here $\delta_{q\bar{q}g}$ denotes the counterterm that effectively cancels the divergence in the quark-gluon vertex. This tells us the choice of Z_{gs} must cancel not only the divergences from the correction to the $q\bar{q}g$ vertex but also the ones introduced by the renormalization factors Z_A and Z_ψ, yielding the relation

$$Z_{g_s} = Z_{q\bar{q}g} Z_\psi^{-1} Z_A^{-\frac{1}{2}}, \tag{1.21}$$

where we defined $Z_{q\bar{q}g} \equiv (1 + \delta_{q\bar{q}g})$. By getting $Z_{q\bar{q}g}$ from the diagrams

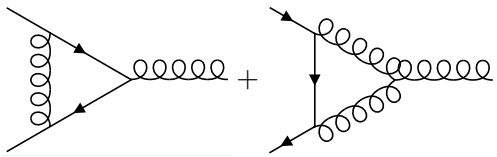

$$\implies Z_{q\bar{q}g} = 1 - \frac{\alpha_s}{4\pi\epsilon}\left(C_F + \frac{3+\xi}{4}C_A\right), \tag{1.22}$$

we obtain Z_{g_s}

$$Z_{g_s} = 1 - \frac{\alpha_s}{4\pi}\frac{1}{2\epsilon}\left(\frac{11}{3}C_A - \frac{4}{3}n_f T_F\right), \tag{1.23}$$

where n_f is the number of light-quarks.

Having gone through the basics of renormalization we can now discuss the *renormalization group*. Recall we introduced the renormalization scale μ in

order to keep the coupling g_s dimensionless

$$g_{s0} = \mu^{\epsilon} g_s(\mu) Z_{g_s}(g_s(\mu)). \tag{1.24}$$

The crucial aspect here is that the bare g_{s0} does not depend on μ - the scale was introduced by the renormalization procedure. There are two implications to this observation: 1) the renormalized coupling g_s must be a function of μ and 2) the μ dependence has to cancel between factors since the RHS must be μ independent. First let us switch to the more common variable $\alpha_s = g_s^2/(4\pi)$ and define $Z_{\alpha_s} \equiv Z_{g_s}^2$

$$\alpha_{s,0} = \mu^{2\epsilon} Z_{\alpha_s}(\mu) \alpha_s(\mu) \tag{1.25}$$

Taking the $\mu \frac{\mathrm{d}}{\mathrm{d}\mu}$ yields

$$\mu \frac{\mathrm{d}\alpha_{s,0}}{\mathrm{d}\mu} = 0 = \mu^{2\epsilon} Z_{\alpha_s}(\mu) \alpha_s(\mu) \left[2\epsilon + Z_{\alpha_s}^{-1}(\mu) \frac{\mathrm{d}Z_{\alpha_s}(\mu)}{\mathrm{d}\ln\mu} + \frac{1}{\alpha_s(\mu)} \frac{\mathrm{d}\alpha_s(\mu)}{\mathrm{d}\ln\mu} \right], \tag{1.26}$$

leading to

$$\frac{\mathrm{d}\alpha_s(\mu)}{\mathrm{d}\ln\mu} = \alpha_s(\mu) \left[-2\epsilon - Z_{\alpha_s}^{-1}(\mu) \frac{\mathrm{d}Z_{\alpha_s}(\mu)}{\mathrm{d}\ln\mu} \right] \equiv \beta(\alpha_s, \epsilon) \alpha_s(\mu), \tag{1.27}$$

where $\beta(\alpha_s, \epsilon)$ is the so-called β-function. This equation defines the scale dependence of the strong coupling, which will be the subject of the next section. The same reasoning applies to all Lagrangian parameters. Take the quark mass m, whose renormalization we previously ignored but is completely analogous. We define the renormalization factor $m_0 \equiv Z_m(\mu)\, m(\mu)$, and follow the same logic to obtain

$$\mu \frac{\mathrm{d}m(\mu)}{\mathrm{d}\ln\mu} = \left[-Z_m^{-1}(\mu) \frac{\mathrm{d}Z_m(\mu)}{\mathrm{d}\ln\mu} \right] m(\mu) \equiv \gamma_m(\mu)\, m(\mu). \tag{1.28}$$

Here $\gamma_m(\mu)$ is known as the *anomalous dimension*, and just like the β-function it governs the μ dependence of the parameter.

Finally, if we consider a physical observable $\mathcal{O}$ in the $\overline{\mathrm{MS}}$ that depends on $\alpha_s(\mu)$ and $m(\mu)$, the scale dependence must once again drop out:

$$\mu \frac{\mathrm{d}}{\mathrm{d}\mu} \mathcal{O}(\alpha_s(\mu), m(\mu), \mu) = \mu \frac{\mathrm{d}\alpha_s(\mu)}{\mathrm{d}\mu} \frac{\partial \mathcal{O}}{\partial \alpha_s} + \mu \frac{\mathrm{d}m(\mu)}{\mathrm{d}\mu} \frac{\partial \mathcal{O}}{\partial m} + \mu \frac{\partial \mathcal{O}}{\partial \mu} = 0. \tag{1.29}$$

Equations that exploit the μ-independence of bare parameters or physical observables are known as *renormalization group equations* (RGE). The renormalization group will play a central role in this thesis because it allows us to resum large logarithms, thereby restoring the convergence of perturbation theory. We will discuss this in detail in sections 1.2 and 2.1.2.

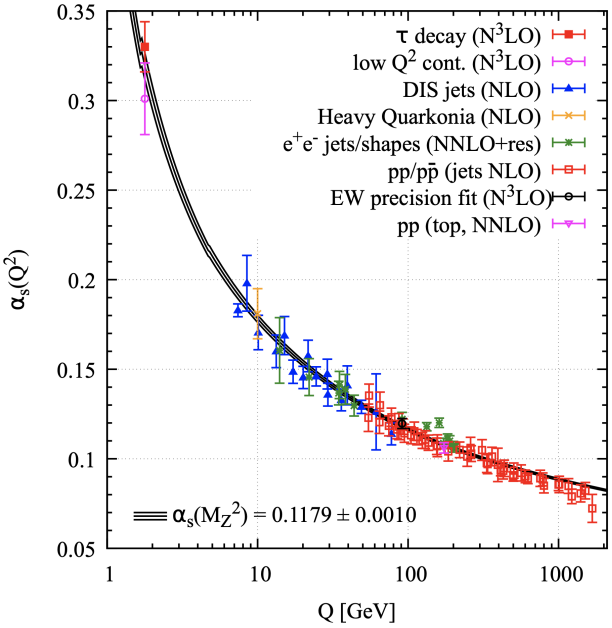

Figure 1.1 Summary of measurements of α_s as a function of the energy scale Q. The coupling becomes small at high energies and large at low energies. Figure taken from PDG's Review of Particle Physics [31].

1.1.3 Asymptotic Freedom

Due to the enormous difficulty of solving the path-integral exactly, theoretical predictions are usually approximated by an expansion in the coupling of the theory. In QCD the perturbative series is done in powers of the strong coupling α_s. This begs the question: if strong interactions are strong, how can α_s be treated as a small parameter? The answer comes from a feature unique to non-abelian gauge theories: they can be *asymptotically free*.

As we saw, equation (1.27) governs the scale dependence of the strong coupling. Let us take the limit $\epsilon \to 0$ such that

$$\frac{\mathrm{d}\alpha_s(\mu)}{\mathrm{d}\ln\mu} = \beta(\alpha_s), \tag{1.30}$$

where $\beta(\alpha_s)$ has an expansion in powers of $\alpha_s(\mu)$.

$$\beta(\alpha_s) = -2\alpha_s \sum_{n=0}^{\infty} \left(\frac{\alpha_s}{4\pi}\right)^n \beta_n \tag{1.31}$$

The β-function is currently known up to five-loop order [32]. In what follows we will solve this equation at 1-loop, which is enough to study the qualitative

features of the running of the coupling. We get

$$\frac{\mathrm{d}\alpha_s(\mu)}{\mathrm{d}\ln\mu} = -\beta_0\frac{\alpha_s^2(\mu)}{2\pi} \implies \alpha_s(\mu) = \frac{\alpha_s(\mu_0)}{1+\alpha_s(\mu_0)\frac{\beta_0}{2\pi}\ln\left(\frac{\mu}{\mu_0}\right)}. \tag{1.32}$$

Here μ_0 is a reference scale at which the value $\alpha_s(\mu_0)$ is measured with high precision. Usually μ_0 taken to be the mass of the Z-boson $m_Z = 91.188$ GeV, at which $\alpha_s(m_Z) = 0.1179 \pm 0.0010$ [31]. In the last section we obtained $Z_{\alpha_s} = Z_{g_s}^2$, which determines β_0

$$\beta_0 = \frac{11}{3}C_A - \frac{4}{3}n_f T_F. \tag{1.33}$$

The crucial point here is that $\beta_0 > 0$ (for not too large n_f), making the overall β-function *negative*. As a consequence the strong coupling gets weaker at higher energies, a phenomenon known as *asymptotic freedom* [33, 34]. This feature is responsible for our ability to do perturbative calculations in QCD - at short-distances α_s becomes small and therefore a valid expansion parameter. The running of the coupling can be seen in figure 1.1

Conversely, at low-energies the coupling grows large and diverges at a scale

$$\Lambda_{\mathrm{QCD}} = \mu_0 \exp\left[-\frac{2\pi}{\beta_0\alpha_s(\mu_0)}\right], \tag{1.34}$$

known as the *Landau pole*, which experimentally is at $\Lambda_{\mathrm{QCD}} \sim 0.2$ GeV. At this low scale QCD is strongly coupled and quarks and gluons become confined into hadrons. Perturbative calculations cease to be applicable and one must instead resort to nonperturbative techniques such as lattice QCD in order to understand this regime.

1.2 Structure of perturbative calculations

We discussed last section how theoretical predictions in QCD are expressed as a perturbative series in powers of the strong coupling α_s. For example, for a cross section σ,

$$\begin{aligned}\sigma(\tau) &= \sum_{n=0}^{\infty}\sigma^{(n)}\left(\frac{\alpha_s}{4\pi}\right)^n \\ &= \sigma^{(0)} + \frac{\alpha_s}{4\pi}\sigma^{(1)}(\tau) + \left(\frac{\alpha_s}{4\pi}\right)^2\sigma^{(2)}(\tau) + ...,\end{aligned} \tag{1.35}$$

where $\sigma^{(0)}$ is the Born-level cross-section for the process in question. This is known as a fixed-order (FO) expansion. The first term is called leading-order (LO), the second next-to-leading-order (NLO) and the k-th term (next-to)^k-leading-order (N^{k}LO). However, there is more structure to the FO expansion than what is apparent in equation (1.35). The energetic collisions we intend to study usually connect multiple scales, inducing the $\sigma^{(n)}(\tau)$ to depend on the ratio of these scales. In particular, the soft and collinear limits of QCD lead to the appearance of logarithms of this ratio, e.g. measuring the jet mass m_J leads to logs of $\tau = m_J^2/p_T^2$, where p_T is the transverse momentum of the jet.

To illustrate the relevance of these logarithms let us define the normalized spectrum $\tilde{\sigma}(\tau)$ and the cumulant $R(\tau)$ (also called the radiator) for a generic dimensionless observable τ:

$$\tilde{\sigma}(\tau) \equiv \frac{1}{\sigma^{(0)}} \frac{\mathrm{d}\sigma}{\mathrm{d}\tau}, \qquad R(\tau) \equiv \int_0^\tau \mathrm{d}\tau' \tilde{\sigma}(\tau') \tag{1.36}$$

A more detailed depiction of the perturbative series is then

$$\begin{aligned}\tilde{\sigma}(\tau) = \delta(\tau) &+ \frac{\alpha_s}{4\pi}\Big[a_{12}\mathcal{L}_1(\tau) + a_{11}\mathcal{L}_0(\tau) + a_{10}\delta(\tau)\Big] \\ &+ \Big(\frac{\alpha_s}{4\pi}\Big)^2\Big[a_{24}\mathcal{L}_3(\tau) + a_{23}\mathcal{L}_2(\tau) + a_{22}\mathcal{L}_1(\tau) + a_{21}\mathcal{L}_0 + a_{20}\delta(\tau)\Big] \\ &+ \Big(\frac{\alpha_s}{4\pi}\Big)^3\Big[a_{36}\mathcal{L}_5(\tau) + a_{35}\mathcal{L}_4(\tau) + a_{34}\mathcal{L}_3(\tau) + a_{33}\mathcal{L}_2(\tau) + ... + a_{30}\delta(\tau)\Big] \\ &+ ... + d(\tau)\end{aligned} \tag{1.37}$$

where the plus distribution $\mathcal{L}_n(\tau) = \big[\theta(\tau)\frac{\ln^n \tau}{\tau}\big]_+$ is defined in appendix A. The function $d(\tau)$ contains higher powers in τ (e.g. polynomials in τ or $\tau\,\mathcal{L}_n(\tau) = \ln^n \tau$ terms) and is therefore referred to as the *power corrections*. Integrating this expression we obtain the cumulant

$$\begin{aligned}R(\tau) = 1 &+ \frac{\alpha_s}{4\pi}\Big[b_{12}\ln^2\tau + b_{11}\ln\tau + b_{10}\Big] \\ &+ \Big(\frac{\alpha_s}{4\pi}\Big)^2\Big[b_{24}\ln^4\tau + b_{23}\ln^3\tau + b_{22}\ln^2\tau + b_{21}\ln\tau + b_{20}\Big] \\ &+ \Big(\frac{\alpha_s}{4\pi}\Big)^3\Big[b_{36}\ln^6\tau + b_{35}\ln^5\tau + b_{34}\ln^4\tau + b_{33}\ln^3\tau + b_{32}\ln^2\tau + b_{31}\ln\tau + b_{30}\Big] \\ &+ ... + D(\tau).\end{aligned} \tag{1.38}$$

The first thing to notice is that $R(\tau)$ diverges as $\tau \to 0$ at each order in perturbation theory. In fact, as τ becomes smaller, the logarithms become enhanced and perturbation theory *breaks down*. In this regime it is no longer true that higher orders are progressively suppressed, therefore disallowing the truncation of the series at any given order in α_s.

For the purpose of obtaining valid theory predictions we must therefore *resum* all terms with the same scaling, since they have comparable contributions to the cross-section. This can be done by employing our knowledge of the all-order structure of QCD. Notice that for $\ln\tau \sim \frac{1}{\alpha_s^2}$ all terms in each vertical column of (1.38) have the same scaling:

$$\alpha_s^n \ln^{2n}\tau \sim 1, \qquad \alpha_s^n \ln^{2n-1}\tau \sim \alpha_s, \qquad \alpha_s^n \ln^{2n-2}\tau \sim \alpha_s^2, \qquad \ldots \quad (1.39)$$

and that the contribution from the first column is dominant compared to the second, and so forth. In the context of resummation this is referred to as *logarithmic accuracy*. In order to distinguish this from the FO expansion we call the first column leading-logarithimic (LL) accuracy, the second next-to-leading-logarithmic (NLL), and the k-th as (next-to)^k-leading-logarithmic (N^k LL). Unlike for the FO expansion, there is some ambiguity in how to define logarithimic-accuracy [35]. By doing the counting in (1.38) this is referred to as doing the counting in the *expansion*. This is however not the best of way of organizing our resummation. Systematic methods of resummation prefer to resum the logarithm of the cumulant. We write $R(\tau)$

$$R(\tau) = C(\alpha_s)\Sigma(\alpha_s,\tau) + D(\tau,\alpha_s) \quad (1.40)$$

where,

$$C(\alpha_s) = 1 + \sum_{n=1}^{\infty}\left(\frac{\alpha_s}{4\pi}\right)^n C_n, \qquad \ln\Sigma(\alpha_s,\tau) = \sum_{n=1}^{\infty}\sum_{m=1}^{n+1}\left(\frac{\alpha_s}{4\pi}\right)^n G_{nm}\ln^m\tau, \quad (1.41)$$

with C_n and G_{nm} real coefficients. Writing $\ln\Sigma(\alpha_s,\tau)$ explicitly the structure emerges

$$\begin{aligned}\ln\Sigma(\alpha_s,\tau) =& \left(\frac{\alpha_s}{4\pi}\right)\Big[G_{12}\ln^2\tau + G_{11}\ln\tau\Big] \\ &+\left(\frac{\alpha_s}{4\pi}\right)^2\Big[G_{23}\ln^3\tau + G_{22}\ln^2\frac{1}{\tau} + G_{21}\ln\tau\Big] \\ &+\left(\frac{\alpha_s}{4\pi}\right)^3\Big[G_{34}\ln^4\tau + G_{33}\ln^3\tau + G_{32}\ln^2\tau + G_{31}\ln\tau + G_{32}\ln\tau\Big] + \ldots\end{aligned} \quad (1.42)$$

With $\ln\tau \sim \frac{1}{\alpha_s}$ we see that each column has uniform scaling, with first column being defined as LL and so on. In modern calculations N^{k}LL invariably refers to this definition, called the CTTW convention [36] or resumming the *exponent*. This counting is also much more natural and consistent with renormalization

group methods like soft-collinear effective theory (SCET), since increasing logarithmic accuracy corresponds to computing certain perturbative ingredients (e.g. β-function, anomalous dimensions) to higher order in α_s.

As a final comment, note the fixed-order and resummation expansions are complementary, each appropriate in a certain region of phase-space. When the logarithms are not enhanced, i.e. for $\ln \tau \sim 1$, keeping only the logarithms and not the power-corrections leads to unreliable results, so one should instead use the fixed-order result.

1.3 The infrared of QCD

1.3.1 Infrared divergences

Besides the UV divergences we discussed in section 1.1.2, in QFT one encounters another type of infinities: Infrared (IR) divergences. We saw UV divergences can be handled through the renormalization procedure which renders S-matrix elements UV-finite. Unlike UV divergences, infrared divergences cannot be handled at the S-matrix level, however they do cancel at the cross-section level as we will show in this section.

Consider the probability of a final-state quark emitting a low-energy gluon at a small angle

$$\mathrm{P}(q \to qg) \sim \frac{\alpha_s C_F}{\pi} \int \frac{\mathrm{d}\theta}{\theta} \int \frac{\mathrm{d}z}{z}, \tag{1.43}$$

where z denotes the momentum fraction of the gluon and θ the angle between the two particles. We see there are two divergences: the *soft* singularity at $z \to 0$, and the *collinear* singularity at $\theta \to 0$. Collectively these are known as the IR divergences. Unlike what happens with UV-divergences, S-matrix elements cannot be made IR-finite. Instead, IR divergences only cancel after combining cross sections for processes involving different initial or final states. The reason for this is that ultimately only observable quantities are guaranteed to be finite, and it is physically impossible to distinguish a final-state quark from its cloud of zero-momentum gluons. It is similarly impossible to distinguish a particle that undergoes an exactly collinear splitting from one that does not.

To illustrate how this cancellation happens, let us consider the process $e^+e^- \to$ hadrons. [1] The cross-section of the Born process $e^+e^- \to \gamma^* \to q\bar{q}$ is

$$\sigma^{(0)} = \frac{4\pi}{3s} \alpha_s N_c \sum_q e_q^2. \tag{1.44}$$

[1] We consider e^+e^- instead of pp collisions because we are only interested in the final state, and this allows us to avoid discussing initial state divergences and their absorption into parton-distribution-functions (PDFs).

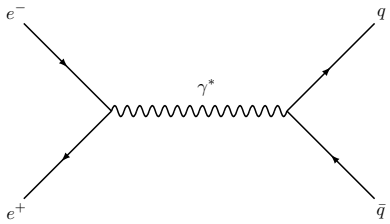

(a) Born-level diagram

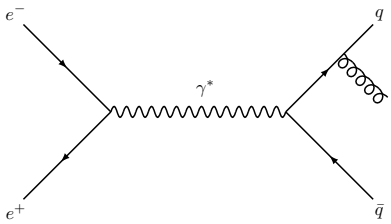

(b) Real emission diagram

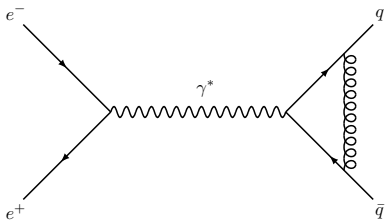

(c) Virtual emission diagram

Figure 1.2 Matrix-elements that contribute to $\sigma^{(1)}$.

In order to compute the NLO cross-section we need to include all terms that contribute to order α_s (here we do not consider NLO electroweak corrections). These terms will be a combination of the Born-level, real-emission and virtual-emission diagrams seen in figure 1.2. One contribution, which we denote $\sigma^{(1)}_{\text{real}}$, comes from squaring the matrix-element of the real emission, since each diagram comes with a power of the coupling g_s, with $\alpha_s \propto g_s^2$. The second contribution comes from from the interference of the tree-level with the virtual exchange diagram, since the former goes as α_s^0 and the latter as α_s. We denote this contribution by $\sigma^{(1)}_{\text{virtual}}$. The results for $\sigma^{(1)}_{\text{real}}$ and $\sigma^{(1)}_{\text{virtual}}$ are given by

$$\begin{aligned}
\sigma^{(1)}_{\text{real}} &= \sigma^{(0)} \frac{2C_F}{\Gamma(1-\epsilon)} \left(\frac{4\pi\mu^2}{s}\right)^{\epsilon} \left(\frac{2}{\epsilon^2} + \frac{3}{\epsilon} - \pi^2 + \frac{19}{2} + \mathcal{O}(\epsilon)\right) \\
\sigma^{(1)}_{\text{virtual}} &= \sigma^{(0)} \frac{2C_F}{\Gamma(1-\epsilon)} \left(\frac{4\pi\mu^2}{s}\right)^{\epsilon} \left(-\frac{2}{\epsilon^2} - \frac{3}{\epsilon} + \pi^2 - 8 + \mathcal{O}(\epsilon)\right).
\end{aligned} \tag{1.45}$$

We see that individually both $\sigma^{(1)}_{\text{real}}$ and $\sigma^{(1)}_{\text{virtual}}$ have double and single poles in ϵ. The ϵ^2 poles come from emissions that are simultaneously soft and collinear, while the ϵ poles originate from emissions that are either soft or collinear but not both. When we add these two contributions we get

$$\sigma(e^+e^- \to \gamma^* \to \text{hadrons}) = \sigma^{(0)} + \frac{\alpha_s}{4\pi}\left(\sigma^{(1)}_{\text{real}} + \sigma^{(1)}_{\text{virtual}}\right) + \mathcal{O}(\alpha_s^2)$$

$$= \sigma^{(0)}\left(1 + \frac{\alpha_s}{\pi}\right) + \mathcal{O}(\alpha_s^2). \tag{1.46}$$

We notice that the divergences cancel and the NLO prediction is rendered finite. Fortunately this is true not only at NLO but to all orders, as ensured by the Kinoshita–Lee–Nauenberg (KLN) theorem [37–39]. The KLN theorem states that IR-divergences cancel to all orders in perturbation theory when summing over sufficiently inclusive initial and final states.

What does it mean for a process to be sufficiently inclusive? In this section we have shown that the cancellation works for an inclusive process (one in which we do not measure anything on the final state). Ultimately we do want to perform measurements in the final state, but this cannot come at the expense of spoiling the cancellation of IR-divergences, otherwise the theory prediction will be infinite. This leads us to the introduction of a crucial concept in jet physics, the notion of *infrared-and-collinear safety.*

1.3.2 Infrared-and-collinear safety

When performing a measurement on final state particles, we must design our observable in such a way as to not interfere with the cancellation of IR-divergences. In other words, the coefficients of the poles in the real-emission must not be altered by the measurement, meaning the observable must be inclusive when dealing with an arbitrarily soft or collinear splitting.

This concept is known as **infrared-and-collinear** (IRC) safety : an observable is IRC-safe if its value remains unchanged under an exactly soft or exactly collinear splitting,

$$\begin{aligned} \text{Collinear safety:} \quad & \text{Obs}(\{p_i\}, k_1, k_2) = \text{Obs}(\{p_i\}, k_1 + k_2) \quad \text{if} \quad \vec{k}_1 \parallel \vec{k}_2 \\ \text{Soft safety:} \quad & \text{Obs}(\{p_i\}, k) = \text{Obs}(\{p_i\}) \quad \text{if} \quad k \to 0. \end{aligned} \tag{1.47}$$

Another way to think about this is that nothing is ever measured on the virtual emission, so we must rely on observables that, in the soft and/or collinear limit, are not sensitive to the real emission either. Under these conditions a perturbative expansion in α_s gives finite results order by order in perturbation theory, making IRC-safety a sufficient condition for calculability.

Although IRC-safety is usually desirable, there are many observables of interest that are not IRC-safe. In fact, even though it is a *sufficient* condition for calculability, it is not a *necessary* one, as we will see in our discussion of Sudakov-safety in the next section. One example of an IRC-unsafe observable is charged particle multiplicity. This observable is extremely useful for quark/gluon jet discrimination and has a long history in QCD, having been measured at many collider experiments. Its being unsafe can be easily seen by

the fact that a gluon splitting into two collinear quarks changes the number of charged particles. Even though it is unsafe and therefore does not have a finite prediction at fixed-order in α_s, the running of the multiplicity with the jet energy can be perturbatively calculated. That is, the mean charged particle multiplicity at any jet energy can be computed from its value at a specific jet energy, the latter being a non-perturbative input obtained from experiment.

Finally, let us note that even though the soft and collinear poles cancel when we consider an IRC-safe observable, we leave behind logarithms. These are the logarithms that can become large if the emission is soft and/or collinear and therefore spoiling the convergence of perturbation theory, as we saw in section 1.2.

1.3.3 Sudakov safety

In this section we discuss Sudakov-safety [23, 26, 40] and how it extends calculability beyond the constraints of IRC-safety by using exclusively perturbative techniques. Consider an IRC-*unsafe* observable u, which has therefore an ill-defined probability $\mathrm{P}(u)$ at any fixed-order in α_s,

$$\mathrm{P}(u) = \frac{1}{\sigma}\frac{\mathrm{d}\sigma}{\mathrm{d}u}(u). \tag{1.48}$$

Now consider an auxiliary observable s that is IRC-*safe*. Even though $\mathrm{P}(u)$ is ill-defined, the conditional probability $\mathrm{P}(u|s)$ is finite at any order in perturbation theory, except at isolated values of s like $s = 0$. We can rewrite $\mathrm{P}(u)$ as

$$\mathrm{P}(u) = \int \mathrm{d}s\ \mathrm{P}(u, s) = \int \mathrm{d}s\ \mathrm{P}(u|s)\mathrm{P}(s) \tag{1.49}$$

If we simply compute $\mathrm{P}(u|s)$ and $\mathrm{P}(s)$ at fixed order then we get back the ill-defined expansion of $\mathrm{P}(u)$ and nothing was accomplished. It becomes therefore clear that all-order resummation is required on $\mathrm{P}(s)$ and/or $\mathrm{P}(u|s)$ in order to have a finite prediction for $\mathrm{P}(u)$. If $\mathrm{P}(u)$ can be made finite through this procedure we deem u **Sudakov-safe**. For all known Sudakov-safe observables of interest it suffices to have a finite $\mathrm{P}(u|s)$ and resummed $\mathrm{P}(s)$ in order to get a finite $\mathrm{P}(u)$. In this thesis we will compute two Sudakov-safe observables: the jet energy drop (specifically for soft drop with $\beta = 0$) and the soft drop groomed momentum fraction z_g. Both of these observables are made finite by the resummation of the auxiliary variable R_g, the groomed jet radius. A discussion on jet grooming will follow in chapter 2.

In case only one auxiliary observable is insufficient to regulate u, the definition of Sudakov-safety can be generalized to accommodate n IRC-safe observ-

ables $s_1, ..., s_n$

$$\mathrm{P}(u) = \int \mathrm{d}s_1 ... \mathrm{d}s_n \mathrm{P}(u|s_1, ..., s_n)\mathrm{P}(s_1, ..., s_n). \tag{1.50}$$

Let us stress that Sudakov-safety does not rescue all IRC-unsafe observables, and therefore its definition is not empty. Consider the case of particle multiplicity. In order to be made safe this observable would require the introduction of an infinite number of IRC-safe observables s_i, since perturbation theory allows for an arbitrary number of soft and collinear emissions. This makes it impossible to obtain a finite prediction through Sudakov-safety.

1.4 Jets

1.4.1 Why do jets form?

Jets are sprays of collimated particles occurring whenever energetic quarks or gluons are produced. By now we have emphasized the importance of understanding these objets, but we have not yet addressed what causes jet formation. This is the goal of this section.

The first reason is the enhancement of soft and collinear emissions. Recall from equation (1.43) that the probability of a quark or gluon emitting a gluon with momentum fraction z at an angle θ goes as $(z\theta)^{-1}$ in the soft-collinear limit. Even though we saw infrared divergences must cancel between real and virtual contributions when using an IRC-safe observable, the cuts on phase-space induced by the measurement leave behind logarithms that become large in this region of phase-space. This was the reason for performing all-order resummation: there was no suppression for having extra soft and collinear emissions. This means there is a large probability of having a collection of many such splittings, which is ultimately what we call a jet.

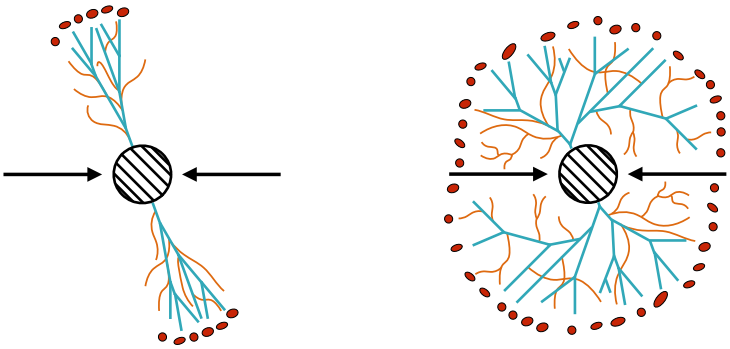

Figure 1.3 Collimated jets obtained in QCD (left) and spherical events obtained in a quasi-conformal, strongly-coupled theory (right).

The enhancement of soft and collinear emissions is not unique to QCD, in fact the same structure can be found for a photon emission off an electron in QED. The reason one forms jets and the other does not is related to value of the coupling. The QCD coupling at the Z-boson mass is $\alpha_s(M_Z) \sim 0.118$, whereas the QED coupling is $\alpha_{\text{QED}}(M_Z) \sim 0.008$, so the suppression of each emission is much larger in QED.

On the other hand, in order to obtain collimated jets it is also important that the theory not be too strongly coupled over a large range of energies. For a sufficiently high coupling, quarks and gluons would simply radiate too much which would nullify the enhancement of soft and collinear emissions, leading to the existence of the spherical events depicted in figure 1.3 . In this sense, asymptotic freedom is also an important reason we have jets - final state partons radiate less at short distances and increasingly more as the energy runs down, as shown in figure 1.4.

One final reason is the existence of light quarks. The fact that the masses of u- and d-quarks are much smaller than Λ_{QCD} means it is fairly energetically inexpensive to produce a $q\bar{q}$ pair out of the vacuum. This allows the color strings connecting two final state partons to break easily without having much of an effect on their individual directions. This is also why we can think of jets as proxies for the underlying parton, as well as expect hadronization effects to not invalidate theoretical predictions altogether.

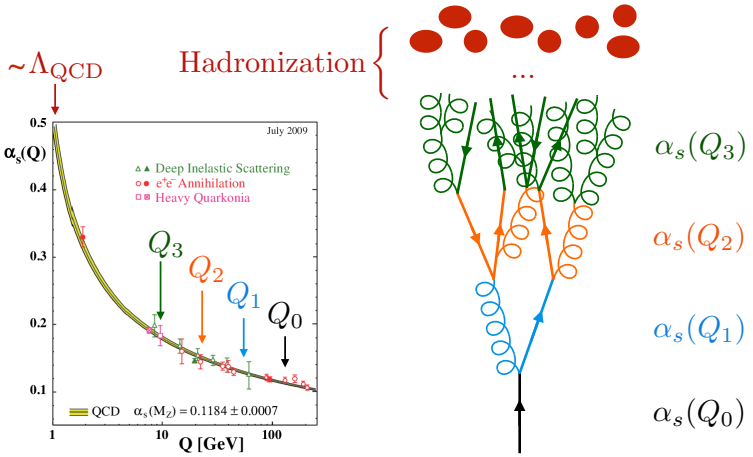

Figure 1.4 Running of the strong coupling as the parton shower evolves. As the scale gets lower more radiation is emitted, until the scale becomes non-perturbative and hadronization takes place.

1.4.2 Jet algorithms

Consider the high-energy event in figure 1.5a. Is it clear how many jets there are? What about which particles belong to which jet? These questions have a certain degree of ambiguity - it is up to us to define which emissions are "hard enough" to warrant their own jet. In order to practically identify jets in an event it is not sufficient to rely on the intuitive notion of what a jet is supposed to represent. Instead one must have a precise definition of a jet.

An adequate jet definition must satisfy specific properties. These were described in 1990 by a group of prominent theorists and experimentalists in what became known as the *Snowmass accord* [41]. According to the Snowmass accord, a jet definition must be:

1. Simple to implement in an experimental analysis
2. Simple to implement in a theory calculation
3. Defined at any order of perturbation theory
4. Yields finite cross sections at any order of perturbation theory
5. Yields a cross section that is relatively insensitive to hadronization

We see conditions 3 and 4 are essentially the requirement that the jet definition be IRC-safe. Condition 5 comes from our desire to have jets act as proxies for the underlying hard partons, and hence to minimize their sensitivity to hadronization effects.

A jet definition is comprised of two components: the *jet algorithm* and the *recombination scheme*. The jet algorithm is simply a recipe for grouping particles into jets. Once the algorithm determines two particles must be clustered together, one must then decide how to assign momentum to the newly formed object. This is done through the recombination scheme.

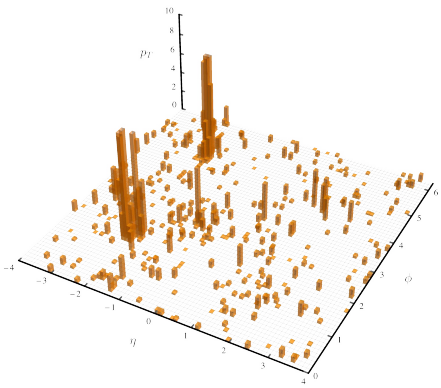

(a) Unclustered event

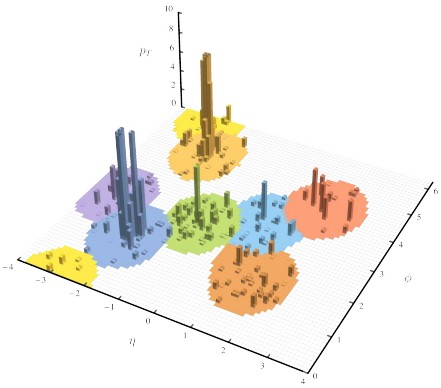

(b) Anti-k_t with $R = 1$

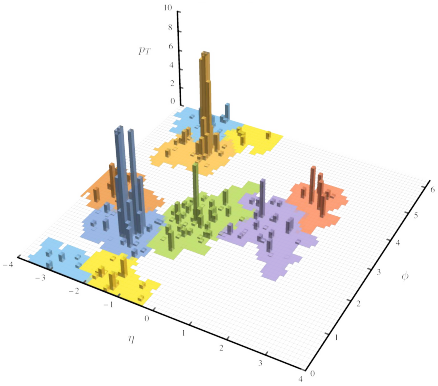

(c) Cambridge-Achen with $R = 1$

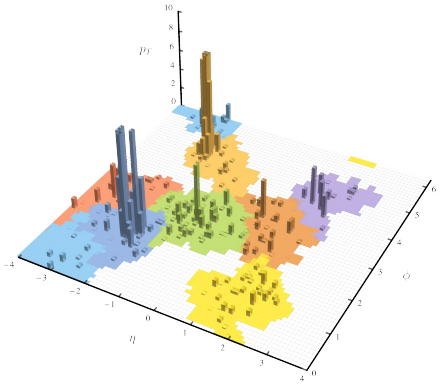

(d) k_t with $R = 1$

Figure 1.5 High-energy event: Unclustered and clustered with different algorithms (keeping only the jets).

The jet algorithm usually involves free parameters that one needs to specify, for example the jet radius R or the cut on the transverse-momentum p_T^{cut}. The

jet radius determines how broad the typical jet will be, while p_T^{cut} corresponds to the minimum p_T an object must have in order to be deemed a jet.

At the LHC almost all jets are reconstructed using *sequential recombination algorithms*. The spirit of this class of algorithms is to mimic the dynamics of the parton shower by noting that jets are the result of consecutive one-to-two splittings. They aim to invert this process by iteratively combining pairs of particles into one object, using a distance metric that is small (and therefore likely to cluster) when the QCD splitting is kinematically enhanced, i.e. soft and/or collinear. The most widely used algorithm is *anti-k_t* [10] . In this thesis we will also make reference to two others: *Cambridge-Aachen* (C/A) [42, 43] and the k_t-algorithm [44, 45]. Together these three can be grouped into the *generalized-k_t algorithm*, each corresponding to a different value of the exponent p. The generealized-k_t algorithm is defined as follows:

1. Construct the initial list of objects by taking all the particles in the event.
2. For each pair of objects construct the *inter-particle distance* d_{ij}

$$d_{ij} = \min(p_{T,i}^{2p}, p_{T,j}^{2p})\Delta R_{i,j}^2, \tag{1.51}$$

   with p being a free parameter and ΔR_{ij} the geometric distance in the η-ϕ plane, $\Delta R_{ij}^2 = (\eta_i - \eta_j)^2 + (\phi_i - \phi_j)^2$
3. For each object obtain the *beam-distance* d_{iB}

$$d_{iB} = p_{T,i}^{2p} R^2, \tag{1.52}$$

   with R being a free parameter referred to as the jet radius.
4. Find the smallest distance of all the d_{ij} and d_{iB}. If the smallest distance is a $d_{i,j}$, i and j are combined into a new object k through a recombination scheme. If the smallest distance is a d_{iB} then i is classified as a jet and removed from the list.
5. Go back to step 2 and repeat the procedure until the list is empty.

The choice $p = 1$ corresponds to the k_t-algorithm. We see soft emissions are the first to be clustered together, so k_t-jets are very sensitive to this type of radiation. Even though this is desirable from the point of view of perturbative QCD (soft emissions are enhanced) it has the drawback of being highly sensitive to contamination, i.e. soft radiation coming from sources other than the hard parton in question. A more detailed discussion on contamination and what can be done to mitigate it will be presented in the next section.

For $p = 0$ we have the Cambridge-Aachen algorithm. In this case the distance is purely geometric, meaning we begin by clustering the pairs that are closest together in the $\eta - \phi$ plane. Besides finding jets, this algorithm is also particularly useful for organizing the particles into an angular-ordered tree. We will see the relevance of having such a structure in our discussion of soft drop in section 1.4.3.

Finally, for $p = -1$ we recover the anti-k_t algorithm. In this algorithm the clustering grows outwards around "hard seeds", aggregating the soft radiation around a hard parton until it has reached a geometric distance R. We can see in figure 1.5 that unlike k_t or C/A, anti-k_t produces fairly circular jets. This has the advantage of facilitating experimental calibration, and is why it has been adopted as the default algorithm at the LHC.

1.4.3 Jet grooming and LHC environment

The environment at a hadron collider is rather messy compared to its e^+e^- counterpart. As a result the particles that compose a jet at the LHC are more than just those arising from the final state quark or gluon. Radiation from other sources ends up inside the jet as well, and their contribution cannot be computed from the theory side [2]. The main sources of contamination are *initial-state radiation* (ISR), *underlying event* (UE) and *pile-up* (PU), which can be seen in figure 1.6. Initial-state radiation refers to soft radiation emitted by incoming partons that ends up inside the jet, while underlying event concerns the secondary collisions in the proton (collisions other than the one we are studying) whose products contaminate the jet. Finally, the LHC does not collide two protons at a time but rather bunches of $\mathcal{O}(10^{11})$ protons, which is what we mean by pile up. Contrary to ISR and UE, pile up is truly uncorrelated with the event. Charged pile up leaves tracks that can be traced back to the collision it originated from and subtracted from the event prior to jet reconstruction, using techniques like charged-hadron subtraction (CHS). Neutral pile up however is just as inconvenient as ISR and UE.

[2] Initial state radiation is in principle calculable, but for the narrow jets we consider its contribution is R^2 suppressed.

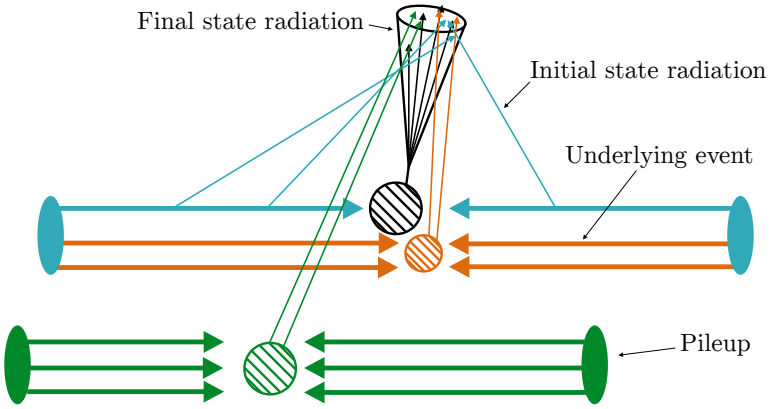

Figure 1.6 Environment at a hadron collider

In order to remove this unwelcome radiation, procedures known as *grooming techniques* have been developed. The goal is to remove most if not all of the radiation infecting our jet, at the expense of losing some of the radiation we are interested in. This is not a problem because the effects of grooming on final state radiation can be predicted by theory, and we therefore expect a significantly better agreement with data for groomed observables compared to their ungroomed equivalents.

In this thesis we will work with three different grooming techniques: *soft drop* (SD) [23], its variant *iterated soft drop* (ISD) [25], and *trimming* [24] . Soft drop is the most widely used and goes as follows:

1. Recluster the jet constituents using the Cambridge-Achen (C/A) algorithm to obtain a pairwise clustering tree.

2. Undo the last stage of the C/A clustering to break the jet - call it j - into two subjets j_1 and j_2.

3. If the subjets pass the soft drop condition

$$\frac{\min(p_{T,1}, p_{T,2})}{p_{T,1} + p_{T,2}} > z_{\text{cut}} \left(\frac{\Delta R_{12}}{R}\right)^{\beta}, \tag{1.53}$$

   then j is the final soft-drop jet and the procedure stops.

4. If the subjets fail the soft drop condition then remove the softest subjet from the definition of j, go back to step 2 and repeat until either the soft drop condition is satisfied or there is only one particle left in the jet.

For iterated soft drop instead of stopping once we find a splitting that satisfies the SD condition, we keep running the algorithm following the leading branch until it is only composed of one particle. This can be visualized in figure 1.7.

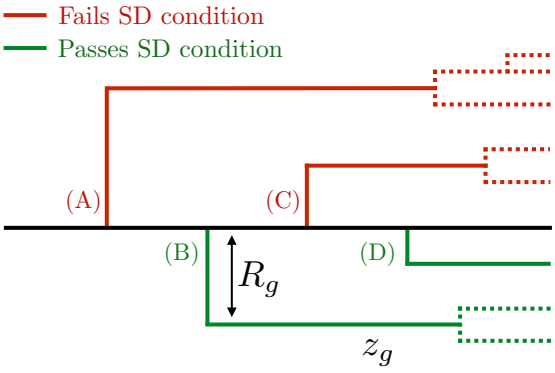

Figure 1.7 Illustration of (iterated) soft drop for a jet with a hard parton. Soft drop grooms away emission A while keeping emissions B, C and D. Iterated soft drop continues to evaluate the soft drop condition in the leading branch, therefore also grooming away emission C.

Trimming is the default grooming technique used by ATLAS and the algorithm is the following:

1. Cluster all particles into jets using any algorithm (usually anti-k_t). The resulting jets are called the seed jets.

2. Within each seed jet, recluster the constituents using a (possibly different) jet algorithm into subjets with a characteristic radius R_{sub} smaller than that of the seed jet.

3. Consider each subjet, and discard the contributions of subjet i to the associated seed jet if $z_i < f_{\text{cut}}$, where $z_i = p_T^i / p_T^J$ and f_{cut} is a fixed dimensionless parameter

4. Assemble the remaining subjets into the trimmed jet.

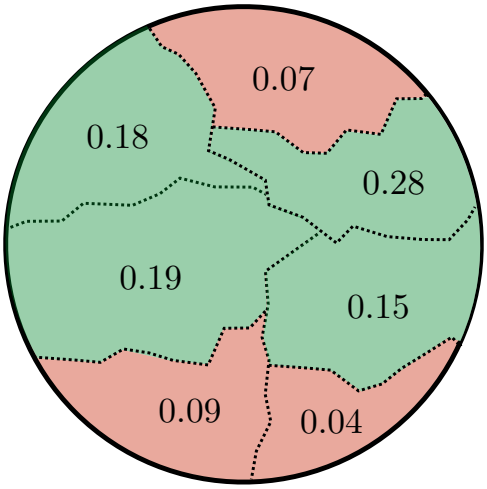

Figure 1.8 Illustration of trimming with $f_{\text{cut}} = 0.1$. Subjets in red are groomed away while those in green are kept. The numbers represent the fraction of the jet p_T carried by each subjet.

1.4.4 A simple case: Jet mass resummation

In order to highlight some features of a typical jet substructure calculation, in this section we consider one of the simplest observables, the *jet mass*, and show how to perform all-order resummation (here at LL accuracy in the cross-section) in two different ways.

Even though the partons intervening in the shower are considered massless, jets have a mass corresponding to the virtuality of the originating parton. Exactly soft and/or collinear splittings do not contribute to the jet mass, making it IRC safe, but any deviation from this limit does. The jet mass is then defined as

$$m_J^2 \equiv \left(\sum_{i \in J} p_i^\mu \right)^2 \tag{1.54}$$

In hadronic collisions, this is

$$m_J^2 = 2p_T^2 \sum_{i<j \in J} z_i z_j (\cosh \Delta\eta_{ij} - \cos \Delta\phi_{ij}), \tag{1.55}$$

and when the jet radius is small this simplifies to

$$\rho \equiv \frac{m_J^2}{p_T^2 R^2} = \sum_{i<j \in J} z_i z_j \left(\frac{\theta_{ij}}{R} \right)^2 + \mathcal{O}(\Delta\eta_{ij}^4, \Delta\phi_{ij}^4), \tag{1.56}$$

where $\theta_{ij}^2 = \Delta\eta_{ij}^2 + \Delta\phi_{ij}^2$ and we introduced ρ for later convenience. Alternatively, one can also write the jet mass as a function of the distances between each particle and the jet axis

$$\rho = \sum_{i\in J} z_i \Big(\frac{\theta_i}{R}\Big)^2, \tag{1.57}$$

where $\theta_i^2 = \Delta\eta_{iJ}^2 + \Delta\phi_{iJ}^2$ and the jet axis is located at $\eta_J = \sum_{i\in J} z_i\eta_i$ and $\phi_J = \sum_{i\in J} z_i\phi_i$. An NLO computation of the cumulant $\Sigma = \frac{1}{\sigma^{(0)}}\int \mathrm{d}\rho \frac{\mathrm{d}\sigma}{\mathrm{d}\rho}$ yields [3]

$$\Sigma_q(\rho) = 1 - \frac{\alpha_s C_F}{\pi}\Big(\frac{1}{2}\ln^2\rho + \frac{3}{4}\ln\rho\Big) + \mathcal{O}(R^2,\rho). \tag{1.58}$$

This is the structure we expected from our discussion in section 1.2. At NLO there is only a single emission, which gives rise to the double-log in the region of phase-space where it is soft *and* collinear, and to the single-log when it becomes soft *or* collinear.

Our intention now is to recover the leading logarithmic terms at all orders, thus we must account for an arbitrary number of emissions. At LL accuracy each emission comes with the maximal number of logarithms, meaning all of them need to be both soft and collinear. This allows us to consider n independent emissions that yield a measurement of the jet mass smaller than ρ:

$$\begin{aligned}\Sigma_q(\rho) \overset{\text{LL}}{=} &\sum_0^\infty \frac{1}{n!}\prod_{i=1}^n \frac{2\alpha_s C_F}{\pi}\int\frac{\mathrm{d}\theta_i}{\theta_i}\int\frac{\mathrm{d}z_i}{z_i}\,\Theta_{i\in\text{jet}}\,\Theta\Big(\sum_{j=0}^n \rho_j < \rho\Big)\\ &+\sum_0^\infty \frac{1}{n!}\prod_{i=1}^n \frac{2\alpha_s C_F}{\pi}\int\frac{\mathrm{d}\theta_i}{\theta_i}\int\frac{\mathrm{d}z_i}{z_i}(\Theta_{i\notin\text{jet}} - 1)\end{aligned} \tag{1.59}$$

where $\rho_j = z_j\frac{\theta_j^2}{R^2}$ from eq. 1.57. The first line refers to the emissions that contribute to the jet mass measurement, while the second line to those that do not: particles outside the jet and virtual emissions. At this accuracy we can further assume that these emissions are *strongly ordered*. In other words, for n emissions we impose the hierarchies $z_1 \gg z_2 \gg ... \gg z_n$ and $\theta_1 \gg \theta_2 \gg ... \gg \theta_n$ simultaneously, such that the measurement will be dominated by only one emission: the least soft-collinear. This allows us to write

$$\Theta\Big(\sum_{j=1}^n \rho_j < \rho\Big) \simeq \Theta(\max_j \rho_j < \rho) = \prod_{j=1}^n \Theta(\rho_j < \rho). \tag{1.60}$$

[3] Here Σ denotes the cumulant cross-section, and not its exponent. This convention is common in the literature.

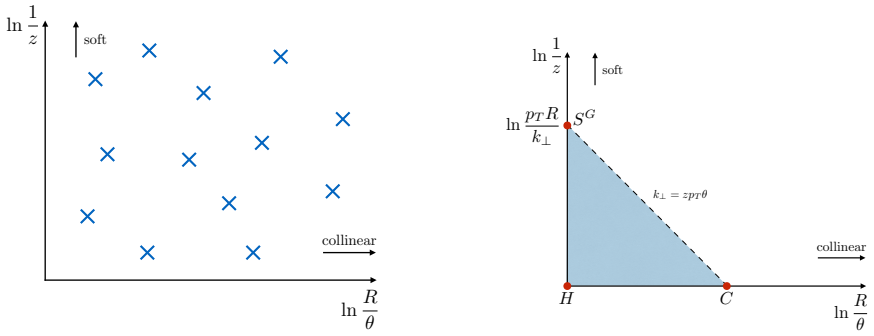

Figure 1.9 Left: Several emissions uniformly distributed on the Lund plane, with the vertical axis corresponding to the jet boundary.

By writing $\Theta(\rho_j < \rho) = 1 - \Theta(\rho_j > \rho)$ and $\Theta_{\in\text{jet}} + \Theta_{\notin\text{jet}} = 1$ we get

$$\begin{aligned}\Sigma_q(\rho) &\overset{\text{LL}}{=} -\sum_0^\infty \frac{1}{n!}\prod_{i=1}^n \frac{2\alpha_s C_F}{\pi}\int\frac{\mathrm{d}\theta_i}{\theta_i}\int\frac{\mathrm{d}z_i}{z_i}\,\Theta\Big(z_i\frac{\theta_i^2}{R^2}>\rho\Big)\Theta_{\in\text{jet}}\\ &=\exp\Big[-\frac{2\alpha_s}{\pi}\int_0^R\frac{\mathrm{d}\theta}{\theta}\int_0^1\frac{\mathrm{d}z}{z}\Theta\Big(z_i\frac{\theta_i^2}{R^2}>\rho\Big)\Big]\\ &=\exp\Big[-\frac{\alpha_s}{2\pi}\ln^2\rho\Big].\end{aligned} \tag{1.61}$$

This remarkable result constitutes a case of LL resummation and is known as the Sudakov factor, with the exponent representing the no-emission probability. This exponential contains the leading-logarithmic term at all orders. In fact, if we expand (1.61) to order α_s we recover the double-log term in the NLO expression (1.58). Expanding (1.61) to order α_s^2 would recover the $\alpha_s^2\ln^4\rho$ term from NNLO, and so forth.

Let us obtain the LL expression again in a simpler way by resorting to a powerful tool in jet physics - the *Lund plane*. Consider once more the probability of a parton emitting a gluon with momentum fraction z and at an angle θ in the soft-collinear limit

$$\mathrm{d}P(z,\theta) = \frac{2\alpha_s C_i}{\pi}\frac{\mathrm{d}z}{z}\frac{\mathrm{d}\theta}{\theta} = \frac{2\alpha_s C_i}{\pi}\mathrm{d}\Big[\ln\frac{1}{z}\Big]\mathrm{d}\Big[\ln\frac{R}{\theta}\Big], \tag{1.62}$$

where $C_i = C_F$ or C_A depending on whether the emission originates from a quark or a gluon respectively. On the second equality we switched variables to $\ln\frac{1}{z}$ and $\ln\frac{R}{\theta}$. Phase-space is flat under these new variables, meaning that an emission has a uniform probability of falling anywhere on the $\big(\ln\frac{R}{\theta}, \ln\frac{1}{z}\big)$ plane. This is the definition of the Lund plane, which can be seen in figure 1.9.

One of the main advantages of the Lund plane is that it allows us to get the leading-logarithmic (LL) expression for any substructure observable in a straightforward manner. To illustrate this, let us consider the jet mass once more, given the the simple nature of this observable.

As before the LL expression is determined by the dominant emission, hence we compute the cumulative distribution by requiring

$$\alpha_s \Sigma^{(1)}(\rho) = \frac{2\alpha_s C_i}{\pi} \int \mathrm{d}\Big[\ln \frac{1}{z}\Big] \int \mathrm{d}\Big[\ln \frac{R}{\theta}\Big] \Theta(z\theta^2 \leq \rho), \tag{1.63}$$

where $\Sigma^{(1)}(\rho)$ is the NLO term in the expansion $\Sigma(\rho) = 1 + \alpha_s \Sigma^{(1)}(\rho) + \mathcal{O}(\alpha_s^2)$. In the Lund plane this corresponds to tracing a line at $\rho = z\theta$ and only allowing emissions that contribute to the jet mass with $\rho_{\text{emission}} < \rho$. In fact, the integral in equation (1.63) corresponds to the area of Lund plane where emissions are allowed:

$$\alpha_s \Sigma^{(1)}(\rho) = \frac{2\alpha_s C_i}{\pi}$$  $$= -\frac{2\alpha_s C_i}{\pi}$$  . $$\tag{1.64}$$

On the second equality we used the fact that the area of the entire Lund plane vanishes, which can be understood multiple ways. One way is by noticing the real-emission diagrams entirely cancel the virtual diagrams in the soft-collinear limit. Alternatively, one can interpret this in terms of unitarity: if we are completely inclusive then the cumulative distribution must be $\Sigma(\text{inclusive}) = 1$, which sets $\Sigma^{(1)}(\text{inclusive}) = 0$ and therefore the area of the Lund plane must vanish. By exponentiating the RHS of equation (1.64) we get the LL result:

$$\begin{aligned} \Sigma(\rho^{\mathrm{c}}) &= \exp\left[-\frac{2\alpha_s C_i}{\pi} \right. \\ &= \exp\left[-\frac{\alpha_s C_i}{2\pi} \ln^2 \rho^{\mathrm{c}} \right]. \end{aligned} \tag{1.65}$$

The Lund plane allows us to perform LL resummation no matter how complex or multi-differential the observable. To go beyond LL however, the Lund plane is not sufficient and we instead turn to Soft-Collinear Effective Theory (SCET). In SCET we are able to go to higher logarithmic accuracy by obtaining a factorization theorem whose ingredients - also known as *modes* - describe physics occurring at different scales. In this context the Lund plane still proves to be a useful tool since it allows us to quickly discern which modes are necessary to construct the desired factorization theorem, as we will discuss in the following chapter.

2

Soft-Collinear Effective Theory

2.1 Effective field theories

2.1.1 The EFT approach

It is often the case that the most general theory is not suitable for obtaining theoretical predictions. One should instead exploit the simplest framework that captures the essential physics: an *effective theory*. Newton's theory of gravitation is sufficient when designing a bridge - there is no need to consider quantum gravity. Likewise, quantum mechanics successfully describes the spectrum of the Hydrogen atom despite not taking into account top quark effects. Accounting for these effects would not only result in insignificant changes to the final result, it would likely make the computation so cumbersome that it becomes impossible to obtain any prediction at all.

The same attitude is true in quantum field theory. A solution is to introduce an *effective field theory* (EFT) that keeps only the relevant degrees of freedom and interactions, and is usually a low-energy approximation of the full theory. Formally an EFT has a small expansion parameter λ defined as the ratio of two well separated scales, known as the *power counting* parameter. In the effective theory we expand in λ up to some order n, which (in principle) can be made arbitrarily high, making the theoretical error of order λ^{n+1} as small as desired.

EFTs are used in two distinct ways: the top-down and the bottom-up approaches. In the top-down approach we know what the high-energy theory is, but we find useful to have a simpler theory for studying low energy physics. The idea is that when constructing the EFT Lagrangian we write down all possible operators consistent with the symmetries of the full theory (gauge symmetry, Lorentz invariance, etc.), but the coefficients of these operators still need to be determined. This is done through a *matching* procedure. We calculate simple observables in the full theory and remove unwanted degrees of freedom, then we choose the coefficients in $\mathcal{L}_{\text{EFT}}$ such that a direct calcula-

tion in the EFT gives the same result. After the matching is performed up to some order in λ, we can use the EFT as a stand-alone theory to compute any observable of interest up to that same order in the power counting. Examples of top-down effective theories include heavy quark effective theory (HQET), which describes a B-meson or C-meson by integrating out the mass of the b-quark or c-quark respectively, and non-relativistic QED and QCD (NRQED and NRQCD) where the expansion is done in the velocity of the particle over the speed of light. The focus of this thesis will be on soft-collinear effective theory (SCET), a top-down theory for energetic QCD processes.

In bottom-up EFTs we want to use the effective field theory logic but the high energy theory is either unknown or doing the matching is too difficult. In this case all the couplings are unknown and need to be fit to experiment. The theory is still powerful when you can make more predictions than the number of fit parameters. Bottom-up theories are an efficient method to characterize new physics in terms of coefficients of higher dimension operators, as in the case of Standard Model effective field theory (SMEFT).

Let us consider the EFT functional integral

$$\int \mathcal{D}\phi\, e^{iS_{\rm EFT}[\phi]}, \qquad \text{where} \qquad S_{\rm EFT}[\phi] = \int \mathrm{d}^d x\, \mathcal{L}_{\rm EFT}(x). \tag{2.1}$$

The mass dimension of the Lagrangian must equal the space-time dimension d, $[\mathcal{L}_{\rm EFT}] = d$, since the action $S_{\rm EFT}$ is dimensionless. Now suppose we are interested in physics at a scale much smaller than a new-physics scale Λ, and therefore wish to only keep degrees of freedom below Λ. The EFT Lagrangian is then written as an expansion

$$\mathcal{L}_{\rm EFT} = \sum_{D\geq 0} \frac{1}{\Lambda^{D-d}} \mathcal{L}^{(D)}_{\rm EFT} = \sum_{D\geq 0} \frac{1}{\Lambda^{D-d}} c_i^{(D)} O_i^{(D)}. \tag{2.2}$$

The O_i are operators constructed with the light degrees of freedom, those below Λ. The c_i are referred to as the *Wilson coefficients*, here made dimensionless by extracting the necessary factors of Λ.

The recipe for setting up an EFT is the following:

1. Identify the relevant low-energy degrees of freedom ϕ_i.

2. Write down all possible operators consistent with the symmetries of the full theory, up to the desired order in the power counting. One can subsequently relate some of these operators by using their equations of motion and integration by parts, arriving at an irreducible operator basis.

3. Obtain the Wilson coefficients C_i in $\mathcal{L}_{\rm EFT} = \sum_i C_i\, O_i$. In a top-down theory this means performing the matching, while in a bottom-up theory this amounts to fitting the coefficients to experiment.

4. Compute the desired observables in the effective theory.

To illustrate the matching procedure explicitly, consider the following Lagrangian for the full theory:

$$\mathcal{L}_{\text{full}} = \frac{1}{2}[(\partial_\mu\phi)^2 - m^2\phi^2] + \frac{1}{2}[(\partial_\mu\xi)^2 - M^2\xi^2] - \frac{1}{2}g\phi^2\xi, \tag{2.3}$$

where ϕ is a light-scalar of mass m and ξ a heavy scalar of mass M, with $m \ll M$. Say we are interested in processes that only have ϕ as external particles because we cannot get to high enough energies to produce ξ particles. Let us write down the EFT Lagrangian by considering all Lorentz invariant operators involving only ϕ fields with $\phi \to -\phi$ symmetry

$$\mathcal{L}_{\text{EFT}} = \frac{1}{2}[(\partial_\mu\phi)^2 - m^2\phi^2] - \frac{C_4}{4!}\,\phi^4 - \frac{1}{6!}\frac{C_6}{M^2}\phi^6 + ... \tag{2.4}$$

where C_n are dimensionless Wilson coefficients of operators of dimension n. Note that all other dimension-6 operators (e.g. $\phi^2\Box\phi^2$, $\phi\Box\phi^3$, ...) can be traded for ϕ^6 using the equations of motion up to $\mathcal{O}(M^{-4})$. We can determine C_4 at lowest order in λ by computing 4-point ϕ Green's function in the full-theory and performing an expansion in $\lambda = m^2/M^2$.

$i\mathcal{M}_{\text{full}} =$

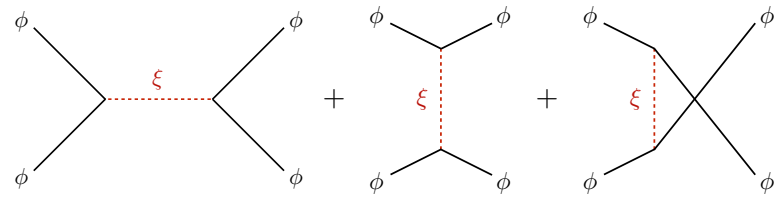

$$\begin{aligned} &= -ig^2\left(\frac{1}{s-M^2} + \frac{1}{t-M^2} + \frac{1}{u-M^2}\right) \\ &= i\frac{g^2}{M^2}\left(3 + \frac{s+t+u}{M^2} + \frac{s^2+t^2+u^2}{M^4} + ...\right) = i\frac{3g^2}{M^2} + \mathcal{O}(\lambda), \end{aligned} \tag{2.5}$$

with $s, t, u \sim m^2 \ll M^2$. The same process in the effective field theory gives

$i\mathcal{M}_{\text{EFT}} =$

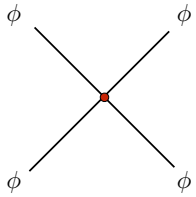

$$= -iC_4 \tag{2.6}$$

At tree-level the matching simply consists of equating $\mathcal{M}_{\text{full}} = \mathcal{M}_{\text{EFT}}$ which sets $C_4 = -3g^2/M^2$. In the case of this particular theory C_4 turns out to be the only coefficient we need. If we wanted to perform a matching calculation for C_6 we would start by computing the 6-ϕ correlator, but this process is already included in the EFT through C_4:

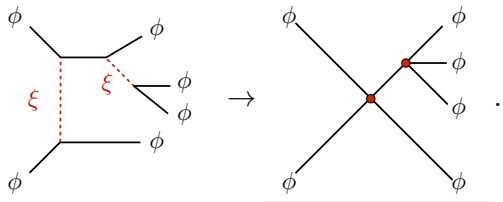

(2.7)

Thus, when matching one should only include contributions that are one-ϕ-particle irreducible. In this example we have all $C_n = 0$ for $n > 4$, since the only interaction in the full theory is $\phi^2\xi$.

2.1.2 Renormalization Group improved perturbation theory

One of the most powerful aspects of using an EFT is that we get to use the renormalization group (RG) to resum large logarithms that would otherwise spoil the convergence of perturbation theory, as we discussed in section 1.2. This technique is known as *RG improved perturbation theory*.

Consider an EFT with a light scalar ϕ and just the ϕ^4 interaction

$$\mathcal{L}_{\text{EFT}} = \frac{1}{2}\left[(\partial_\mu\phi)^2 - m^2\right] + \frac{1}{4!}C_4\phi^4 \tag{2.8}$$

Our goal now is to compute the one-loop correction to the 4-point Green's function, meaning we must specify a regularization and renormalization scheme. The most common choice is dimensional regularization (dim. reg.) paired with the $\overline{\text{MS}}$ renormalization scheme, which we discussed in section 1.1.2. There we also mentioned that the combination of dim. reg. and $\overline{\text{MS}}$ is particularly helpful in the EFT context for several reasons. First, the renormalization scale $\bar{\mu}$ only appears as logs of $\bar{\mu}$ and never in powers of $\bar{\mu}$. The only source of $\bar{\mu}$ in the calculation comes from powers of μ^ϵ in the coupling constants, such that an expansion in ϵ only gives rise to $\ln\bar{\mu}$ terms. Another convenient property of dim. reg. is that scaleless integrals vanish, e.g.

$$\int \frac{\mathrm{d}^d k}{(2\pi)^d}(k^2)^a = 0. \tag{2.9}$$

A proof of this statement for any a (integer or not) can be found in [46]. Here we simply illustrate what happens to a logarithmicly divergent integral when

it is scaleless. Consider the following integral in $d = 4 - 2\epsilon$ dimensions

$$\mu^{2\epsilon} \int \frac{\mathrm{d}^d k}{(2\pi)^d} \frac{1}{k^4} = \mu^{2\epsilon} \int \frac{\mathrm{d}^d k}{(2\pi)^d} \left[\frac{1}{k^2(k^2 - m^2)} - \frac{m^2}{k^4(k^2 - m^2)} \right], \tag{2.10}$$

where split the scaleless integral by introducing an arbitrary mass scale m^2. With this separation the first integral is divergent only in the UV and the second exclusively in the IR. Let us call these integrals I_{UV} and I_{IR}, respectively.

$$\begin{aligned} I_{\mathrm{UV}} =& \frac{i}{16\pi^2} \left[\frac{1}{\epsilon_{\mathrm{UV}}} + \ln \frac{\mu^2}{m^2} + 1 \right] + \mathcal{O}(\epsilon_{\mathrm{UV}}) \\ I_{\mathrm{IR}} =& - \frac{i}{16\pi^2} \left[\frac{1}{\epsilon_{\mathrm{IR}}} + \ln \frac{\mu^2}{m^2} + 1 \right] + \mathcal{O}(\epsilon_{\mathrm{IR}}), \end{aligned} \tag{2.11}$$

which gives

$$\mu^{2\epsilon} \int \frac{\mathrm{d}^d k}{(2\pi)^d} \frac{1}{k^4} = I_{\mathrm{UV}} + I_{\mathrm{IR}} = \frac{i}{16\pi^2} \left[\frac{1}{\epsilon_{\mathrm{UV}}} - \frac{1}{\epsilon_{\mathrm{IR}}} \right] = 0, \tag{2.12}$$

where $\epsilon_{\mathrm{UV}} = \epsilon_{\mathrm{IR}} \equiv \epsilon$ since they both represent the deviation from 4-dimensions.

Finally, dim. reg. leaves the symmetries of the theory untouched. Just as important in the EFT context is the fact that dim. reg. does not break the power counting, which means we can do the power counting for regulated graphs prior to renormalizing them.

After this discussion we are now ready to compute the one-loop correction to the ϕ^4 operator in the (2.8) Lagrangian. At threshold this is

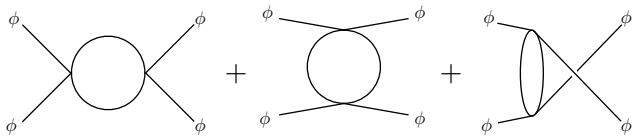

$$= \frac{3}{32\pi^2} C_4^2 \left(\frac{1}{\epsilon} + \ln \frac{\bar{\mu}^2}{m^2} + \frac{2}{3} \right) \tag{2.13}$$

with $\bar{\mu}^2 = \mu^2 4\pi e^{-\gamma_E}$. At this point we need to renormalize the coupling $C_4^{(0)}$ in order to obtain the couterterm that cancels the UV divergences. In the $\overline{\mathrm{MS}}$ scheme we have

$$C_4^{(0)} = Z_4(\mu)\, \mu^{2\epsilon}\, C_4(\mu), \qquad \text{with} \qquad Z_4(\mu) = 1 - \frac{3}{32\pi^2} \frac{C_4(\mu)}{\epsilon}, \tag{2.14}$$

where the $\mu^{2\epsilon}$ factor keeps C_4 dimensionless in $d = 4 - 2\epsilon$ dimensions. Adding the counterterm $Z_4 - 1$ as well as the tree-level piece yields the renormalized amplitude at NLO:

$$i\mathcal{M}_{\mathrm{EFT}}(\phi\phi \to \phi\phi) = -iC_4(\mu) \left[1 - \frac{3}{32\pi^2} C_4(\mu) \left(\ln \frac{\mu^2}{m^2} + \frac{2}{3} \right) \right], \tag{2.15}$$

where in the final result we substituted $\bar{\mu} \to \mu$, in accordance with $\overline{\text{MS}}$.

As we discussed in 1.1.2, the point of the renormalization group is that the bare Lagrangian and couplings do not depend on μ, since this is an unphysical scale introduced by the renormalization procedure. The renormalization group equation (RGE) is simply

$$0 = \mu \frac{\mathrm{d}}{\mathrm{d}\mu} C_4^{(0)} = \mu \frac{\mathrm{d}}{\mathrm{d}\mu} \big[Z_4(\mu) \mu^{2\epsilon} C_4(\mu) \big], \tag{2.16}$$

which can be rewritten as

$$\mu \frac{\mathrm{d}C_4(\mu)}{\mathrm{d}\mu} = \gamma_4(\mu)\, C_4(\mu), \qquad \text{with} \qquad \gamma_4(\mu) = -2\epsilon \bigg(1 - C_4(\mu) \frac{\partial Z_4}{\partial C_4} \bigg). \tag{2.17}$$

Solving this equation allows us to resum logs of the type $C_4^n \ln^n \frac{\mu^2}{m^2}$ to all orders in the coupling C_4. By plugging in Z_4 at one-loop from (2.14) we obtain the RGE

$$\mu \frac{\mathrm{d}C_4(\mu)}{\mathrm{d}\mu} = \frac{3}{16\pi^2} C_4^2(\mu), \tag{2.18}$$

whose solution is

$$\int_{C_4(\mu_0)}^{C_4(\mu)} \frac{\mathrm{d}C_4'}{{C_4'}^2} = \frac{3}{16\pi^2} \int_{\mu_0}^{\mu} \mathrm{d} \ln \mu' \implies C_4(\mu_0) = \frac{C_4(\mu)}{1 + \frac{3}{16\pi^2} C_4(\mu) \ln \frac{\mu}{\mu_0}}. \tag{2.19}$$

This expression gives us the running of C_4 with the scale μ, and represents the resummation at LL accuracy of the proccess $\phi\phi \to \phi\phi$. Indeed, one can quickly see that by choosing $\mu_0 = m$ and expanding (2.19) to order C_4^2 recovers the logarithmic term in equation (2.15).

It is worth noting that the logs we resummed in this example are single logs coming from the UV and not the IR double logs we saw in section 1.2. In order to resum Sudakov logarithms we turn instead to *soft-collinear effective theory* (SCET), whose degrees of freedom encode the IR divergent structure of the full theory. In the following section we introduce SCET and discuss its degrees of freedom and symmetries, as well as obtain its Lagrangian from the QCD Lagrangian. How we employ SCET to resum IR logs will be the topic of section 2.2.5.

2.2 SCET: an effective theory for the infrared of QCD

2.2.1 Degrees of freedom

The work in this thesis is carried out using Soft-Collinear Effective Theory (SCET) [12–16], an effective theory for the infrared of QCD in the presence of

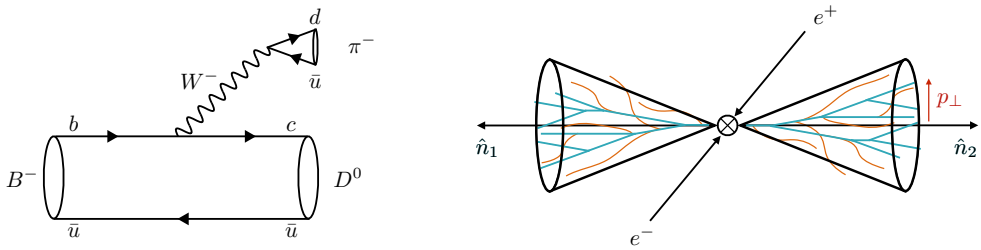

(a) $B^- \to D^0\pi^-$ **(b)** $e^+e^- \to$ dijets

Figure 2.1 Examples of processes that can be described using SCET.

a large separation of scales. Most of what we discuss in this chapter follows the SCET review and lectures [21]. Other resources for SCET include [20, 47].

SCET is a top-down EFT describing the interactions of soft and collinear degrees of freedom in the presence of a hard interaction, the full theory being QCD. In some ways SCET follows the same general principles described in section 2.1.1, but it is also distinct in many ways from the traditional effective theories we have come across so far.

In SCET the the most convenient coordinates are *light-cone coordinates*. Let us motivate this choice of coordinates by looking at $B^- \to D^0\pi^-$, seen in figure 2.1a. Solving for energy and momentum conservation allows us to obtain the 4-momentum of the resulting pion p_π^μ. By aligning the momentum of the π along the $\hat{z}$ axis we get

$$p_\pi = (2.310\text{ GeV}, 0, 0, 2.306\text{ GeV}) \simeq Q(1, 0, 0, 1) \tag{2.20}$$

Since the masses of the B^- and D^0 mesons are much larger than the pion mass it is not surprising to see p_π^μ is very close to the light-cone, i.e. $p_\pi^2 \simeq 0$. Light-cone coordinates are therefore appropriate when dealing with particles whose energy is much greater than their mass. We start by defining two light-cone basis vectors n and $\bar{n}$

$$n^\mu = (1, 0, 0, 1), \qquad \bar{n}^\mu = (1, 0, 0, -1) \tag{2.21}$$

which satisfy $n^2 = \bar{n}^2 = 0$ and $n \cdot \bar{n} = 2$. Any 4-vector p^μ can be represented in the light-cone basis

$$p^\mu = \frac{\bar{n}^\mu}{2} p^+ + \frac{n^\mu}{2} p^- + p_\perp^\mu, \tag{2.22}$$

where

$$p^+ \equiv n \cdot p = p^0 - p^3, \qquad p^- \equiv \bar{n} \cdot p = p^0 + p^3 \qquad \text{and} \qquad p_\perp^\mu \equiv (0, p^1, p^2, 0). \tag{2.23}$$

It is also useful to introduce the notation

$$p^\mu = (p^+, p^-, \vec{p}_\perp), \tag{2.24}$$

which will be used whenever studying the scaling of degrees of freedom. Finally let us note that in these coordinates the inner product of two vectors is

$$p \cdot q = \frac{1}{2}(p^+ q^- + p^- q^+) - \vec{p}_\perp \cdot \vec{q}_\perp, \tag{2.25}$$

such that $p^2 = p^+ p^- - \vec{p}_\perp^{\,2}$.

To illustrate how to choose the relevant degrees of freedom in the EFT let us now return to the example of $B^- \to D^0 \pi^-$. The B and D mesons can both be described by heavy quark effective theory (HQET), one of the top-down EFTs we mentioned in section 2.1.1. This is because both mesons are composed of a heavy quark, which is nearly static, surrounded by soft quarks and gluons. This is not true for the pion which is composed of two light-quarks. In the rest-frame of the pion we know the 4-momenta components of its constituents are of the order of the confinement scale $\Lambda_{\rm QCD}$

$$\pi \text{ rest-frame:} \qquad p^\mu \sim (\Lambda_{\rm QCD}, \Lambda_{\rm QCD}, \Lambda_{\rm QCD}), \tag{2.26}$$

in the $p^\mu \sim (p^+, p^-, p_\perp)$ notation. Now we want to boost along the z axis into the CM frame of the decay. In light-cone coordinates, a boost by an amount β is simply

$$(p^+, p^-, p_\perp) \xrightarrow{\text{boost}} (\beta^{-1} p^+, \beta\, p^-, p_\perp). \tag{2.27}$$

By choosing $\beta = Q/\Lambda_{\rm QCD}$ we obtain the scaling of the pion momentum in the lab frame

$$p_c^\mu \sim Q\,(\lambda^2, 1, \lambda), \tag{2.28}$$

with $\lambda = \Lambda_{\rm QCD}/Q$. We see here that this scaling follows the hierarchy $p^- \gg p_\perp \gg p^+$. Physically this means almost all of the momentum is along the n^μ direction: $p^\mu \simeq (0, Q, 0)$ with fluctuations $\mathcal{O}(\lambda)$ in the perpendicular direction, and smaller fluctuations $\mathcal{O}(\lambda^2)$ in the $\bar{n}^\mu$ direction (which coincides with the direction opposite to n^μ). Therefore, whenever momenta have the scaling from eq. (2.28) we say they have *collinear scaling*.

One can also ask what the scaling is for the soft constituents of the B and D mesons in these coordinates. Once again the momentum of the soft particles is of the order of the confinement scale $\Lambda_{\rm QCD}$: $p^\mu \sim (\Lambda_{\rm QCD}, \Lambda_{\rm QCD}, \Lambda_{\rm QCD})$. However this time there is no need to boost to the CM frame - we are already

in it. This way we see there is no preferred direction and all components are uniformly suppressed:

$$p_s^\mu \sim Q\,(\lambda, \lambda, \lambda), \tag{2.29}$$

which defines the *soft scaling*.

While the $B^- \to D^0\pi^-$ example nicely motivates the use of light-cone coordinates and the emergence of the soft and collinear scalings, in this thesis we are interested in processes involving jets. Let us then focus on a second process: dijet production, which at lowest order is just $e^+e^- \to \gamma^* \to q\bar{q}$, shown in figure 2.1b. We write the momentum of the off-shell photon in the CM frame $q^\mu = (Q, 0, 0, 0)$ and we deem Q the hard scale of the process.

By momentum conservation the jets will be approximately back to back, and we make that direction our z-axis. We expect the momentum of the constituents of jets 1 and 2 to follow collinear scaling along n and $\bar{n}$ respectively

$$\begin{aligned} p_n^\mu &\sim Q(\lambda^2, 1, \lambda) \\ p_{\bar{n}}^\mu &\sim Q(1, \lambda^2, \lambda), \end{aligned} \tag{2.30}$$

where we write $\lambda = \Delta/Q$, the ratio of a scale Δ yet to be identified, and the hard scale Q. The natural question now is: what should Δ be? To answer this, let's start with what it cannot be. The scale Δ cannot be so small as to be $\Delta \sim \Lambda_{\mathrm{QCD}}$. In that case, instead of being part of an energetic jet the constituents would be bound into a hadron, just like the $B^- \to D^0\pi^-$ case. It cannot be so large as to be $\Delta \sim Q$ either, which would spoil the collinear scaling. We have then restricted Δ to be $\Lambda_{\mathrm{QCD}} \ll \Delta \ll Q$.

Notice also that Δ characterizes the perpendicular spread of the jet, since $p_\perp \sim Q\lambda = \Delta$. A good choice for Δ could therefore be the jet mass m_J, since we saw in section 1.4.4 the jet mass is a way of characterizing how wide the jet is: the smaller the mass, the more collimated the jet.

In jet processes there is also need for a mode to describe soft radiation between jets,

$$p_{\mathrm{us}} \sim Q(\lambda^2, \lambda^2, \lambda^2). \tag{2.31}$$

Modes with this scaling are usually called *ultrasoft* to distinguish them from the ones seen in equation 2.29. To derive the ultrasoft scaling consider the restrictions that requiring $\Delta \sim m_J$ imposes on a hemisphere jet composed of one collinear and one ultrasoft particle,

$$m_J^2 = (p_n + p_{\mathrm{us}})^2 = p_n^2 + p_{\mathrm{us}}^2 + 2p_{\mathrm{us}} \cdot p_n \sim \Delta^2. \tag{2.32}$$

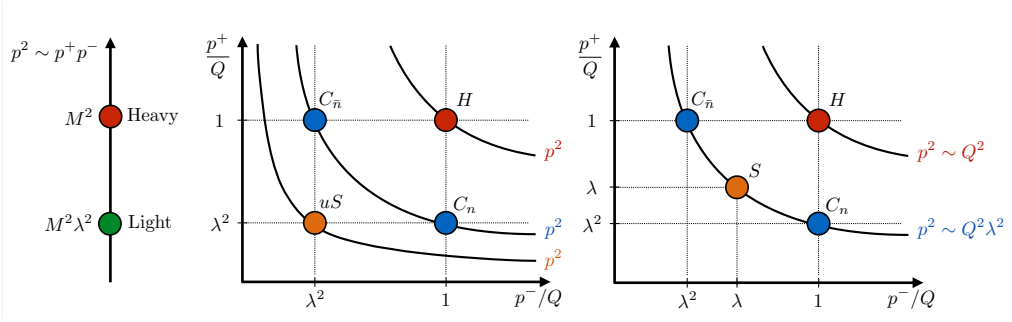

(a) Invariant mass EFT **(b)** SCET I **(c)** SCET II

Figure 2.2 Degrees of freedom for an invariant mass EFT, SCET_I and SCET_II.

Each of these terms is individually restricted to be of order Δ^2 or higher. The term $2p_{\text{us}} \cdot p_n = p_{\text{us}}^+ \cdot p_n^- + p_{\text{us}}^- \cdot p_n^+ + 2p_n^\perp \cdot p_{\text{us}}^\perp$ determines (2.31) to be the only allowed scaling, otherwise either the contribution of the ultrasoft or collinear radiation is suppressed.

Theories with ultrasoft modes (2.31) are called SCET_I theories, while those with soft modes (2.29) are known as SCET_II theories. Unlike traditional EFTs in which the degrees of freedom can be characterized by one variable, i.e. their invariant mass p^2, in SCET they are defined in the p^+-p^- plane ($p_\perp$ is redundant due to the on-shell condition), as shown in figure 2.2.

For both SCET_I and SCET_II the collinear modes C_n and the anti-collinear modes $C_{\bar{n}}$ live in the same mass hyperbola $p^2 \sim \Delta^2$, and the hard modes with scaling $p^2 \sim Q^2$ are integrated out when designing the EFT. In SCET_II the collinear and soft modes live in the same mass hyperbola, which means they can be related to each other under a boost (this is how we derived the collinear scaling). On the other hand, in SCET_I the ultrasoft modes live on a mass hyperbola $p^2 \sim \Delta^4/Q^2$ but can still interact in the Lagrangian with the collinear sector since ultrasoft and collinear momenta have the same scaling for p^+ (or p^- for the anti-collinear mode).

2.2.2 SCET Lagrangian

While a detailed derivation of the SCET Lagrangian is beyond the scope of this introduction, it is perhaps still useful to schematically describe how to obtain it. The full derivation can be found in [12–15], or the SCET lecture

notes [21]. The leading-power SCET Lagrangian is composed of three terms

$$\mathcal{L}^{(0)}_{\text{SCET}} = \mathcal{L}^{(0)}_{n\xi} + \mathcal{L}^{(0)}_{ng} + \mathcal{L}^{(0)}_{us}. \tag{2.33}$$

The term $\mathcal{L}^{(0)}_{n\xi}$ describes the propagation of collinear quark fields and their interactions with ultrasoft or collinear gluons. The second term $\mathcal{L}^{(0)}_{ng}$ encodes the propagation of collinear gluons and their interactions, and finally $\mathcal{L}^{(0)}_{us}$ is the Lagrangian for the ultrasoft degrees of freedom for both quarks and gluons. In what follows, we will obtain $\mathcal{L}^{(0)}_{n\xi}$ starting from the massless QCD Lagrangian

$$\mathcal{L}^{\psi}_{\text{QCD}} = \bar{\psi} i \not{D} \psi. \tag{2.34}$$

There are four stages to this derivation

1. Removing spinor components that are subleading in the collinear limit
2. Separating collinear and ultrasoft gauge fields
3. Performing a multipole expansion to separate momenta
4. Expanding the Lagrangian

The first step is to introduce projector operators that allow us to separate the quark field into larger and smaller spin components, represented by the fields $\hat{\xi}_n$ and $\varphi_{\bar{n}}$ respectively

$$\psi = \hat{\xi}_n + \varphi_{\bar{n}}, \qquad \text{where} \qquad \hat{\xi}_n \equiv \frac{\not{\bar{n}}\not{n}}{4}\psi, \quad \varphi_{\bar{n}} \equiv \frac{\not{n}\not{\bar{n}}}{4}\psi. \tag{2.35}$$

By writing the covariant derivative in the light-cone basis the QCD Lagrangian can be rewritten as

$$\mathcal{L}^{\psi}_{\text{QCD}} = \left(\bar{\varphi}_{\bar{n}} + \bar{\hat{\xi}}_n\right)\left[\frac{\not{\bar{n}}}{2} in\cdot D + \frac{\not{n}}{2} i\bar{n}\cdot D + i\not{D}_\perp\right]\left(\varphi_n + \hat{\xi}_n\right) \tag{2.36}$$

This result can be simplified since the fields $\hat{\xi}_n$ and $\varphi_{\bar{n}}$ contain factors of $\not{n}$ and $\not{\bar{n}}$ in their definition, leading to terms proportional to $\not{n}^2 = \not{\bar{n}}^2 = 0$ (recall that n^μ and $\bar{n}^\mu$ are light-like). After this simplification we are left with only four terms,

$$\mathcal{L}^{\psi}_{\text{QCD}} = \bar{\hat{\xi}}_n \frac{\not{\bar{n}}}{2} in\cdot D\, \hat{\xi}_n + \bar{\varphi}_{\bar{n}} i\not{D}_\perp \hat{\xi}_n + \bar{\hat{\xi}}_n i\not{D}_\perp \varphi_{\bar{n}} + \bar{\varphi}_{\bar{n}} \frac{\not{n}}{2} i\bar{n}\cdot D\, \varphi_{\bar{n}}. \tag{2.37}$$

Although written in an unusual way, the above Lagrangian is still just QCD since no expansion has been done at this point. We can now eliminate $\varphi_{\bar{n}}$

using equations of motion. The assumption here is that since $\varphi_{\bar{n}}$ corresponds to spinor components that are subleading in the collinear limit, one does not need to consider a source term for $\varphi_{\bar{n}}$ in the path integral. This leads to the equation of motion

$$\frac{\delta\mathcal{L}}{\delta\varphi_{\bar{n}}} = 0 \implies \varphi_{\bar{n}} = \frac{1}{i\bar{n}\cdot D} i\not{D}_\perp \frac{\not{\bar{n}}}{2}\hat{\xi}_n, \tag{2.38}$$

which plugging into expression (2.37) yields

$$\mathcal{L} = \bar{\hat{\xi}}_n \left(in\cdot D + i\not{D}_\perp \frac{1}{i\bar{n}\cdot D} i\not{D}_\perp \right) \frac{\not{\bar{n}}}{2}\hat{\xi}_n. \tag{2.39}$$

At this stage we need to proceed to the second step of the derivation: separating collinear and ultrasoft gauge fields. In order to do so we need to derive the scalings for the gauge fields, and therefore introduce the notation A_n^μ and A_{us}^μ to denote collinear and ultrasoft gluons respectively. Ultimately our collinear gluons A_n^μ must behave as propagating spin-one degrees of freedom, so their kinetic term takes the usual $F_{\mu\nu}^2$ form. The propagator in the R_ξ-gauge is then

$$\begin{aligned}\int \mathrm{d}^4x\, e^{ip_n\cdot x} \langle 0|T\{A_n^\mu(x)A_n^\nu(x)\}|0\rangle =& \frac{-i}{p_n^2}\left(g^{\mu\nu} - (1-\xi)\frac{p_n^\mu p_n^\nu}{p_n^2}\right) \\ =& \frac{-i}{p_n^4}\left(p_n^2\, g^{\mu\nu} - (1-\xi)\, p_n^\mu\, p_n^\nu\right)\end{aligned} \tag{2.40}$$

The first thing to note is that $\mathrm{d}^4x = \mathrm{d}x^+\mathrm{d}x^-\mathrm{d}\vec{x}_\perp \sim \lambda^{-4}$ since the exponent $p_n\cdot x \sim 1$. We know collinear momenta have virtuality $p_n^2 \sim Q^2\lambda^2$, so the scaling coming from d^4x on the LHS matches up with the one coming from p_n^4 on the RHS. If we pick $\mu = \nu = \perp$ the term in parenthesis scales as λ^2, which tells us $A_{n\perp}^\mu \sim \lambda$. Picking other combinations for μ and ν, and matching the power counting on the LHS and RHS leads us to conclude that the collinear gluon fields scale the same way as the components of their momentum. Performing the same exercise for ultrasoft fields A_{us}^μ yields the same conclusion. We therefore have:

$$A_n^\mu \sim (\lambda^2, 1, \lambda), \qquad A_{us}^\mu \sim (\lambda^2, \lambda^2, \lambda^2). \tag{2.41}$$

Another way to derive this result is by noting that we want to construct a collinear covariant derivative $D^\mu = \partial^\mu + igA^\mu$, and therefore the components of the collinear momenta ∂^μ and of the gauge field must have the same scaling. We can now safely expand our gauge field A^μ into collinear and ultrasoft modes

$$A^\mu(x) = A_n^\mu(x) + A_{us}^\mu(x). \tag{2.42}$$

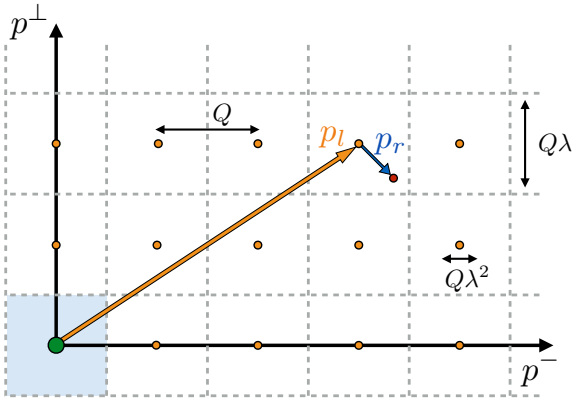

Figure 2.3 Label momenta carries us to a specific box in the grid, while residual momenta takes us to a specific point within that box

This tells us that $A_{us\perp}$ and A^-_{us} can be dropped from the leading order analysis since in $A^\mu_n + A^\mu_{us}$ they are dominated by the collinear gluon. On the other hand A^+_{us} is of the same order as A^+_n and therefore must be kept.

We now proceed to the third stage of the derivation of the SCET_I Lagrangian: disentangling momenta by performing a multipole expansion (analogous to the one in electromagnetism). In order to do this we introduce the so-called *label formalism*. This formalism allows us to derive the Feynman rules directly in momentum space and it simplifies the formulation of gauge transformations in the effective theory, as we will see in the next section. Consider the Fourier transform $\tilde{\xi}_n(p)$ of the collinear quark field $\hat{\xi}_n(x)$

$$\tilde{\xi}_n(p) = \int \mathrm{d}^4x\, e^{ip\cdot x}\hat{\xi}_n(x). \tag{2.43}$$

The idea of the label formalism is to separate the momentum of our modes p^μ into the sum of a *label momentum* p^μ_l which carries the large momentum components, and a *residual momentum* p^μ_r that carries the small momentum components:

$$p^\mu = p^\mu_l + p^\mu_r. \tag{2.44}$$

Given the scaling of collinear and ultrasoft momenta, this separation works as follows

$$\begin{aligned} &\text{collinear:}\ p^\mu_l \sim Q(0,1,\lambda),\quad p^\mu_r \sim Q(\lambda^2,\lambda^2,\lambda^2) \\ &\text{ultrasoft:}\ p^\mu_l \sim Q(0,0,0),\quad p^\mu_r \sim Q(\lambda^2,\lambda^2,\lambda^2), \end{aligned} \tag{2.45}$$

where we see that ultrasoft momenta have no label momenta since they have no large components. Figure 2.3 is a fitting way to think about label and residual momenta. For any momentum $p^\mu = p_l^\mu + p_r^\mu$ we can interpret the label momentum p_l as defining a grid of points separated by $Q\lambda$ in the $\perp$-direction and Q in the p^- direction. Adding the residual momenta can take us to any point within the cell surrounding the label momentum.

This picture, though convenient, can be slightly misleading since it suggests there are hard cuttoffs at the cell boundaries. This is however not the case since the cells in figure 2.3 should actually be of infinite size. Moreover, although all momenta will ultimately be continuous it is convenient to work with discrete label momenta and continuous residual momenta, taking the continuum limit afterwards. Depending on the scaling the integration over momenta then changes to

$$\begin{aligned} \text{collinear:} \quad & \int \mathrm{d}^4 p \to \sum_{p_l \neq 0} \int \mathrm{d}^4 p_r \\ \text{ultrasoft:} \quad & \int \mathrm{d}^4 p \to \int \mathrm{d}^4 p_r, \end{aligned} \tag{2.46}$$

where for the collinear mode we have excluded the bin where the label momentum goes to zero [48], since this corresponds to the ultrasoft region and would introduce double counting. We also update the notation of our fields to incorporate both components:

$$\begin{aligned} &\text{collinear:} \ \tilde{\xi}_n(p) \to \tilde{\xi}_{n,p_l}(p_r) \\ &\text{ultrasoft:} \ \tilde{\xi}_{us}(p) \to \tilde{\xi}_{us}(p_r), \end{aligned} \tag{2.47}$$

with separate conservation laws for label and residual momenta,

$$\int \mathrm{d}^4 x \, e^{(k_l - q_l)\cdot x} e^{(k_r - q_r)\cdot x} = (2\pi)^4 \delta_{k_l, q_l} \delta^4(k_r - q_r). \tag{2.48}$$

Finally we transform the residual momenta back to position space, thereby obtaining our final collinear quark field

$$\xi_{n,p_l}(x) = \int \frac{d^4 p_r}{(2\pi)^4} e^{-ip_r \cdot x} \tilde{\xi}_{n,p_l}(p_r). \tag{2.49}$$

The relation between the hatted collinear quark field appearing in (2.39) and the final field is therefore:

$$\hat{\xi}_n(x) = \sum_{p_l \neq 0} \int \mathrm{d}^4 p_r e^{-ip_l \cdot x} e^{-ip_r \cdot x} \tilde{\xi}_{n,p_l}(p_r) = \sum_{p_l \neq 0} e^{-ip_l \cdot x} \xi_{n,p_l}(x) \tag{2.50}$$

With the introduction of the decomposition into label-residual momenta, we can see that:

- Interactions from collinear fields with ultrasoft fields do not change their label momenta
- Interactions from collinear fields with collinear fields change label momenta
- The collinear label n (corresponding to the collinear direction) is preserved by both ultrasoft and collinear interactions

Our next goal is to introduce derivatives that act on these fields. To do so we start by defining the label momentum operator $\mathcal{P}^\mu$,

$$\mathcal{P}^\mu \xi_{n,p_l} \equiv p_l^\mu \xi_{n,p_l}(x), \tag{2.51}$$

and introduce the notation $\mathcal{P}^\mu = (0, \overline{\mathcal{P}}, \mathcal{P}_\perp)$, where $\overline{\mathcal{P}} \equiv \bar{n}\cdot\mathcal{P} \sim p_l^-$ and $\mathcal{P}_\perp^\mu \sim p_{l\perp}^\mu$. The (partial) derivative acting on ξ_{n,p_l} is only sensitive to residual momenta

$$i\partial_\mu \xi_{n,p_l}(x) \sim \lambda^2 \xi_{n,p_l}(x). \tag{2.52}$$

Finally, the label operator also allows us to relate $\hat{\xi}_n$ and ξ_n without the need of a sum over labels. By defining $\xi_n(x) = \sum_{p_l\neq 0} \xi_{n,p_l}$ we see that

$$\begin{aligned}\hat{\xi}_n(x) &= \sum_{p_l\neq 0} e^{-ip_l\cdot x}\xi_{n,p_l}(x) = e^{-i\mathcal{P}\cdot x}\sum_{p_l\neq 0}\xi_{n,p_l}(x)\\ &= e^{-i\mathcal{P}\cdot x}\xi_n(x)\end{aligned} \tag{2.53}$$

We can at last construct the leading order Lagrangian. Our previously derived result in eq. (2.39) (repeated here for convenience) was

$$\mathcal{L} = \bar{\hat{\xi}}_n\left(in\cdot D + i\not{D}_\perp \frac{1}{i\bar{n}\cdot D} i\not{D}_\perp\right)\frac{\not{\bar{n}}}{2}\hat{\xi}_n. \tag{2.54}$$

We now change $i\partial_\mu \to (\mathcal{P}_\mu + i\partial_\mu)$ and $\hat{\xi}_n \to e^{-i\mathcal{P}\cdot x}\xi_n$, such that the covariant derivative becomes $D^\mu = (\mathcal{P}^\mu + i\partial^\mu) + g(A_n^\mu + A_{us}^\mu)$, with the notation $\mathcal{P}^\mu = (0, \overline{\mathcal{P}}, \mathcal{P}_\perp)$. By expanding our derivative operators we get

$$\begin{aligned} in\cdot D &= i\, n\cdot\partial + g\, n\cdot A_n + g\, n\cdot A_{us}\\ iD_\perp &= (\mathcal{P}_\perp^\mu + gA_{n\perp}^\mu) + \mathcal{O}(\lambda^2)\\ i\bar{n}\cdot D_\perp &= (\overline{\mathcal{P}} + gA_{n\perp}) + \mathcal{O}(\lambda^2)\end{aligned} \tag{2.55}$$

The final result for the leading order Lagrangian $\mathcal{L}^{(0)}_{n\xi}$ is then

$$\mathcal{L}^{(0)}_{n\xi} = e^{-ix\cdot\mathcal{P}}\bar{\xi}_n\left(in\cdot D + i\not{D}_{n\perp}\frac{1}{i\bar{n}\cdot D_n}i\not{D}_{n\perp}\right)\frac{\not{\bar{n}}}{2}\xi_n. \tag{2.56}$$

where we defined the collinear covariant derivatives in which the $\mathcal{O}(\lambda^2)$ are dropped:

$$\begin{aligned} iD^\mu_{n\perp} \equiv& \mathcal{P}^\mu_\perp + gA_{n\perp} \\ i\,\bar{n}\cdot D_n \equiv& \overline{\mathcal{P}} + g\bar{n}\cdot A_{n\perp} \end{aligned} \tag{2.57}$$

The gluon SCET Lagrangian $\mathcal{L}^{(0)}_{ng}$ can be derived using the same procedure. The starting point is the gluon QCD Lagrangian,

$$\mathcal{L}_{\text{gauge}} = -\frac{1}{2}\text{Tr}[G_{\mu\nu}G^{\mu\nu}] + \tau\text{Tr}[(i\partial_\mu A^\mu)] + 2\text{Tr}[\bar{c}\,i\partial_\mu iD^\mu\,c], \tag{2.58}$$

with $G_{\mu\nu} = \frac{i}{g}[D_\mu, D_\nu]$, where the second and third term correspond to the gauge-fixing and ghost Lagrangian respectively, as we saw in chapter 1. We then expand the covariant derivative and keep only the leading order terms - just like we did for $\mathcal{L}^{(0)}_{n\xi}$. This corresponds to making the following replacements in (2.58):

$$\begin{aligned} iD^\mu \to i\mathcal{D}^\mu \equiv& \frac{n^\mu}{2}(\overline{\mathcal{P}} + g\,\bar{n}\cdot A_n) + (\mathcal{P}^\mu_\perp + g\,A^\mu_{n\perp}) + \frac{\bar{n}^\mu}{2}(i\bar{n}\cdot\partial + g\,n\cdot A_n + g\,n\cdot A_{us}), \\ i\partial^\mu \to i\mathcal{D}^\mu_{us} \equiv& \frac{n^\mu}{2}\overline{\mathcal{P}} + \mathcal{P}^\mu_\perp + \frac{\bar{n}^\mu}{2}i\,n\cdot\partial + \frac{\bar{n}^\mu}{2}g\,n\cdot A_{us}, \end{aligned} \tag{2.59}$$

resulting in the SCET gluon Lagrangian $\mathcal{L}^{(0)}_{ng}$,

$$\mathcal{L}^{(0)}_{ng} = \frac{1}{2g^2}\text{Tr}\{([i\mathcal{D}^\mu, i\mathcal{D}_\mu])^2\} + \tau\text{Tr}\{([i\mathcal{D}^\mu_{us}, A_{n\mu}])^2\} + 2\text{Tr}\{\bar{c}_n[i\mathcal{D}^\mu_{us}, [i\mathcal{D}_\mu, c_n]]\}. \tag{2.60}$$

Finally, the ultrasoft quark and gluon Lagrangian is simply the QCD action with ultrasoft fields, yielding

$$\mathcal{L}^{(0)}_{us} = \bar{\psi}_{us}i\not{D}_{us}\psi_{us} - \frac{1}{2}\text{Tr}\{(G^{\mu\nu}_{us})^2\} + \tau_{us}\text{Tr}\{(i\partial_\mu A^\mu_{us})^2\} + 2\text{Tr}\{\bar{c}_{us}i\partial_\mu iD^\mu_{us}c_{us}\}, \tag{2.61}$$

with $iD^\mu_{us} = i\partial^\mu + A^\mu_{us}$.

2.2.3 Symmetries of SCET

In this section we focus on two of the symmetries of SCET: reparametrization invariance and gauge symmetry.

The choice of n^μ and $\bar{n}^\mu$ vectors for the light-cone coordinates selected a specific frame, and by performing an expansion in the power counting using these coordinates we have broken Lorentz invariance. However, the freedom we possess to choose n^μ and $\bar{n}^\mu$ reflects this symmetry. This is known as *reparametrization invariance* (RPI), implying that the SCET Lagrangian remains invariant under transformations of the basis vectors n^μ and $\bar{n}^\mu$ that do not spoil the power counting of fields.

Recall that the only requirement for n^μ and $\bar{n}^\mu$ to be a valid set of light-cone coordinates is that they satisfy $n^2 = \bar{n}^2 = 0$ and $n \cdot \bar{n} = 2$. There are three types of RPI transformations on n^μ and $\bar{n}^\mu$ that take us to another equally valid set of light-cone coordinates,

$$\text{(I)} \begin{cases} n^\mu \to n^\mu + \Delta_\perp^\mu \\ \bar{n}^\mu \to \bar{n}^\mu \end{cases}, \quad \text{(II)} \begin{cases} n^\mu \to n^\mu \\ \bar{n}^\mu \to \bar{n}^\mu + \epsilon_\perp^\mu \end{cases}, \quad \text{(III)} \begin{cases} n^\mu \to e^\alpha\, n^\mu \\ \bar{n}^\mu \to e^{-\alpha}\, \bar{n}^\mu \end{cases} \tag{2.62}$$

with $\Delta_\perp \cdot n = \Delta_\perp \cdot \bar{n} = \epsilon_\perp \cdot n = \epsilon_\perp \cdot \bar{n} = 0$. RPI tranformations (I) and (II) are infinitesimal, while (III) is finite. We can derive the scaling of $\Delta_\perp, \epsilon_\perp$ and α by imposing that these transformations must not change the direction of collinear momenta. Therefore,

$$\begin{aligned} n \cdot p \to n \cdot p + \Delta_\perp \cdot p_\perp \sim \lambda^2 &\implies \Delta_\perp^\mu \sim \lambda \\ \bar{n} \cdot p \to \bar{n} \cdot p + \epsilon_\perp \cdot p_\perp \sim 1 &\implies \epsilon_\perp^\mu \sim 1, \end{aligned} \tag{2.63}$$

and $\alpha \sim 1$ as well. This means only $\Delta_\perp^\mu$ is constrained by the power counting.

RPI is automatically preserved when working from the top-down but serves as a useful consistency condition on SCET operators when working from the bottom-up. For example, the implications of RPI-III are that n^μ and $\bar{n}^\mu$ can only appear in operators in three combinations

$$(A \cdot n)(B \cdot \bar{n}), \qquad \frac{A \cdot n}{B \cdot n}, \qquad \frac{A \cdot \bar{n}}{B \cdot \bar{n}}, \tag{2.64}$$

for arbitrary A^μ and B^μ.

We turn now to the gauge symmetry of SCET. The same way we expanded the Lagrangian, we must also expand the gauge transformations. This results in two types of gauge transformations: collinear and ultrasoft

$$U_n(x) = \exp\{i\alpha_n^a t_a\}, \qquad U_{us}(x) = \exp\{i\alpha_{us}^a t_a\} \tag{2.65}$$

Under a ultrasoft gauge transformation the ultrasoft fields ψ_{us} and A^μ_{us}, and the collinear fields ξ_n and A^μ_n transform as

$$\text{Ultrasoft:} \quad \begin{cases} \psi_{us}(x) & \to U_{us}(x)\psi_{us}(x) \\ A^\mu_{us}(x) & \to U_{us}(x)A^\mu_{us}(x)U^\dagger_{us}(x) + \frac{i}{g}U_{us}(x)\partial^\mu U^\dagger_{us}(x), \\ \xi_n(x) & \to U_{us}(x)\xi_n(x) \\ A^\mu_n(x) & \to U_{us}(x)A^\mu_n(x)U^\dagger_{us}(x) \end{cases}$$

On the other hand ultrasoft fields cannot transform under collinear gauge transformations, as this would lead to the field having a large momentum and therefore no longer be ultrasoft. This tells us that collinear gauge transformation cannot turn ultrasoft fields into collinear fields. Under collinear gauge transformations the fields transform as:

$$\text{Collinear:} \quad \begin{cases} \psi_{us}(x) & \to \psi_{us}(x) \\ A^\mu_{us}(x) & \to A^\mu_{us}(x), \\ \xi_n(x) & \to U_n(x)\xi_n(x) \\ A^\mu_n(x) & \to U_n(x)A^\mu_n(x)U^\dagger_n(x) + \frac{i}{g}U_n(x)\mathcal{D}_{us}U^\dagger_n(x) \end{cases}$$

It's now worth examining a key concept in the discussion of gauge symmetry in SCET: the *Wilson line*. In gauge theory a Wilson line tracks the gauge dependence along a spacetime trajectory. Consider the difference of a fermion field ψ at two spacetime points under a $SU(N)$ transformation,

$$\psi(y) - \psi(x) \to U(y)\psi(y) - U(x)\psi(x). \tag{2.66}$$

We see this difference is not gauge covariant, but it can be made so by introducing a Wilson line $W(x, y)$,

$$W(x, y) = \mathbf{P} \exp\left\{ig \int_y^x \mathrm{d}s^\mu A_\mu(s)\right\}, \tag{2.67}$$

where $\mathbf{P}$ is the path-ordering symbol. A key property of the Wilson line is that it transforms as

$$W(x, y) \to U(x)W(x, y)U^\dagger(y), \tag{2.68}$$

thereby allowing us to write the gauge covariant difference

$$W(x, y)\psi(y) - \psi(x) \to U(x)[W(x, y)\psi(y) - \psi(x)]. \tag{2.69}$$

Returning to SCET, we work with two types of Wilson lines: the collinear Wilson line W_n and the soft Wilson line Y_n

$$W_n \equiv \mathbf{P}\exp\left\{ig_s\int_{-\infty}^{0}\mathrm{d}s\,\bar{n}\cdot A_n(x+s\bar{n})\right\}$$
$$Y_n \equiv \mathbf{P}\exp\left\{ig_s\int_{-\infty}^{0}\mathrm{d}s\,n\cdot A_{us}(x+sn)\right\}. \tag{2.70}$$

A more specific notation for Y_n would also denote whether the ultrasoft Wilson line is attached to quarks or antiquarks, and whether these are incoming or outgoing, but for the purposes of this section the one shown above is sufficient. Let us focus for now on the collinear Wilson line W_n. The collinear Wilson line accounts for an infinite number of collinear gluon emissions, which becomes more apparent when written in momentum space,

$$W_n = \sum_k \sum_{\text{perms}} \frac{(-g_s)^k}{k!}\left(\frac{\bar{n}\cdot A_n(q_1)\times ...\times \bar{n}\cdot A_n(q_k)}{[\bar{n}\cdot q_1][\bar{n}\cdot(q_1+q_2)]\times ...\times[\bar{n}\cdot(q_1+....+q_k)]}\right). \tag{2.71}$$

The collinear Wilson line is also defined through

$$i\bar{n}\cdot D_n W_n \equiv \bar{n}_\mu(\mathcal{P}^\mu + gA_n^\mu)W_n = 0. \tag{2.72}$$

From this equation one can derive the following operator relation

$$\frac{1}{i\bar{n}\cdot D_n} = W_n\frac{1}{\overline{\mathcal{P}}}W_n^\dagger, \tag{2.73}$$

enabling us to trade collinear covariant derivatives for Wilson lines, which will prove useful later. A crucial feature of W_n is how it transforms under collinear and ultrasoft gauge transformations:

$$\begin{aligned}&\text{Collinear:} \quad W_n(x)\to U_n(x)W_n(x)\\ &\text{Ultrasoft:} \quad W_n(x)\to U_{us}(x)W_n(x)U_{us}^\dagger(x).\end{aligned} \tag{2.74}$$

These transformation properties allow us to write down the so-called *gauge-invariant building blocks*,

$$\chi_n = W_n^\dagger\xi_n, \qquad \mathcal{B}_{n\perp}^\mu = \frac{1}{g_s}\Big[\frac{1}{\overline{\mathcal{P}}}W_n^\dagger[iD_{n\perp},\bar{n}\cdot D_n]W_n\Big], \tag{2.75}$$

also known as the *quark jet field* χ_n and the *gluon jet field* $\mathcal{B}_{n\perp}^\mu$. Here the $\overline{\mathcal{P}}$ and derivatives only act on the fields inside the outer square brackets. It can be proven to all orders in the power counting that the collinear quark and gluon fields χ_n and A_n can only appear in operators of the SCET Lagrangian through χ_n and $\mathcal{B}_{n\perp}^\mu$.

2.2.4 Factorization in SCET

In this section we will demonstrate one of the most powerful features of SCET: the ability to arrive at factorization theorems through a field-redefinition. In particular, we will go through an example of ultrasoft-collinear factorization whereby we decompose our SCET Lagrangian into decoupled ultrasoft and collinear sectors.

Recall we introduced the ultrasoft Wilson line Y_n in (2.70). In similar fashion to the collinear Wilson line W_n, Y_n encodes an infinite amount ultrasoft emissions, satisfying the relations $Y_n^\dagger Y_n = Y_n Y_n^\dagger = 1$ and

$$in \cdot D_{us} Y_n(x) = 0, \tag{2.76}$$

which can be shown to imply the following operator relation,

$$Y_n^\dagger in \cdot D_{us} Y_n = in \cdot \partial. \tag{2.77}$$

One can now carry out the central step in this derivation: the Bauer-Pirjol-Stewart (BPS) field redefinitions [15],

$$\xi_n(x) = Y_n(x)\xi_n^{(0)}(x), \qquad A_n^\mu(x) = Y_n(x) A_n^{(0)\mu}(x) Y_n^\dagger(x). \tag{2.78}$$

The $\xi_n^{(0)}$ and $A_n^{(0)}$ are the new collinear quark and collinear gluon fields respectively, now invariant under ultrasoft transformations. Note also that since $\overline{\mathcal{P}}$ and $Y_n(x)$ commute, the gluon field redefinition implies the following modification to the collinear Wilson line W_n

$$W_n(x) = Y_n(x) W_n^{(0)}(x) Y_n^\dagger(x). \tag{2.79}$$

Plugging in the BPS field redefinitions into the $\mathcal{L}_{n\xi}^{(0)}$ Lagrangian we derived, we obtain

$$\begin{aligned}
\mathcal{L}_{n\xi}^{(0)} &= e^{-ix\cdot\mathcal{P}} \bar{\xi}_n \left(in\cdot D + i\not{D}_{n\perp} W_n \frac{1}{i\bar{n}\cdot D_n} W_n^\dagger i\not{D}_{n\perp} \right) \frac{\not{\bar{n}}}{2} \xi_n \\
&= e^{-ix\cdot\mathcal{P}} \bar{\xi}_n \left(in\cdot D_{us} + g_s n\cdot A_n + (\not{\mathcal{P}}_\perp + g_s \not{A}_{n\perp}) W_n \frac{1}{\overline{\mathcal{P}}} W_n^\dagger (\not{\mathcal{P}}_\perp + g_s \not{A}_{n\perp}) \right) \frac{\not{\bar{n}}}{2} \xi_n \\
&= e^{-ix\cdot\mathcal{P}} \bar{\xi}_n^{(0)} \left(in\cdot\partial + g_s n\cdot A_n^{(0)} + (\not{\mathcal{P}}_\perp + g_s \not{A}_{n\perp}^{(0)}) W_n^{(0)} \frac{1}{\overline{\mathcal{P}}} W_n^{(0)\dagger} (\not{\mathcal{P}}_\perp + g_s \not{A}_{n\perp}^{(0)}) \right) \\
&\quad \times \frac{\not{\bar{n}}}{2} \xi_n^{(0)},
\end{aligned} \tag{2.80}$$

where the last line is independent from the ultrasoft gluon field A_{us}^μ. The takeaway from this quick derivation is that in the original Lagrangian the ultrasoft

fields only appeared in the $in \cdot D$ term, and through the BPS field redefinition and the use of (2.77) we were able to remove A^μ_{us} from the collinear Lagrangian. After the same procedure is employed to the collinear gluon Lagrangian, we have succesfully decoupled the collinear and ultrasoft sectors,

$$\mathcal{L}^{(0)}_n[\xi_n, A^\mu_n, n\cdot A_{us}] = \mathcal{L}^{(0)}_n[\xi^{(0)}_n, A^{(0)\mu}_n, 0], \tag{2.81}$$

where $\mathcal{L}^{(0)}_n = \mathcal{L}^{(0)}_{n\xi} + \mathcal{L}^{(0)}_{ng}$. It is worth pointing out that the ultrasoft interactions with the collinear fields have not completely disappeared from our theory. What the BPS field redefinition achieves is to have them removed from the Lagrangian and introduced into currents. Consider J_{dijets}, the current producing two jets through $e^+e^- \to$ dijets (i.e. producing quark jet fields $\bar{\chi}_n$ and χ_n)

$$J_{\text{dijets}} \equiv \bar{\chi}_{\bar{n}}\Gamma\chi_n = (\bar{\xi}_{\bar{n}}W^\dagger_{\bar{n}})\Gamma(W_n\xi_n) = \underbrace{(\bar{\xi}^{(0)}_{\bar{n}}W^{(0)\dagger}_{\bar{n}})}_{\text{anti-collinear}} \times \underbrace{(Y^\dagger_{\bar{n}}Y_n)}_{\text{ultrasoft}} \times\Gamma\times \underbrace{(W^{(0)\dagger}_n\xi^{(0)}_n)}_{\text{collinear}}. \tag{2.82}$$

This constitutes an example of *factorization*, the operator producing two quark jets is decomposed into to the product of collinear, ultrasoft and anti-collinear sectors. This factorization theorem directly translates to the level of the cross-section. Consider the cross-section σ for $e^+e^- \to \gamma^* \to$ dijets

$$\sigma = \sum_X^{\text{restric.}} (2\pi)^4\delta^4(q - p_X)L_{\mu\nu}\langle 0|J^{\dagger\nu}(0)|X\rangle\langle X|J^\mu(0)|0\rangle, \tag{2.83}$$

where the sum over X is restricted to dijet configurations and $L_{\mu\nu}$ is the leptonic tensor. The fact that we were able to write the Lagrangian as a sum of decoupled sectors implies the factorization of Hilbert space

$$\mathcal{L}^{(0)}_{\text{SCET}} = \mathcal{L}^{(0)}_n + \mathcal{L}^{(0)}_{\bar{n}} + \mathcal{L}^{(0)}_{\text{us}} \implies |X\rangle = |X_n\rangle\otimes|X_{\bar{n}}\rangle\otimes|X_{us}\rangle. \tag{2.84}$$

In order to factorize the cross-section we still need to perform measurements on the final state that put us in a dijet configuration. Here we use the hemisphere jet invariant masses m_J and $m_{\bar{J}}$, which ensure we are in the dijet case when $m_J, m_{\bar{J}} \ll Q$, where Q denotes the hard scale of the process. Using the factorized version of the current (2.82) and Hilbert space, it can be shown that the cross section factorizes

$$\frac{\mathrm{d}\sigma}{\mathrm{d}m^2_J\mathrm{d}m^2_{\bar{J}}} = \sigma_0 H(Q)\int \mathrm{d}l^+\mathrm{d}l^- J(m^2_J - Ql^+)J(m^2_{\bar{J}} - Ql^-)S(l^+, l^-), \tag{2.85}$$

where we introduced the *hard* function H, the *soft* function S, and the *jet* functions J. The hard function is defined as the square of the Wilson coefficients $C(Q)$,

$$H(Q) = |C(Q)|^2. \tag{2.86}$$

Likewise, the soft function and the jet functions have definitions in terms of squared matrix elements of SCET operators, which we omit here for simplicity but which can be found in ref. [21]. Unsurprisingly, the jet function will play a central role in the rest of this thesis. In section 2.2.6 we have a closer look at a specific jet function: the *semi-inclusive jet function*, which will serve as the basis for all the jet functions subsequently computed.

Having introduced factorization in SCET we are now familiar with all the necessary ingredients in order to resum Sudakov logarithms, which will be the topic of the next section.

2.2.5 Resumming Sudakov double logarithms

In the previous sections we introduced SCET and demonstrated its ability to arrive at factorization theorems that isolate physics occurring at different scales. The next step is to see how we can use this effective theory to resum IR logarithms - the Sudakov double logs - using renormalization group techniques. Consider a function F^{bare} (e.g. a hard, soft, jet or beam function) with multiplicative renormalization

$$F^{\text{bare}} = Z_F(\mu)F(\mu). \tag{2.87}$$

The function $F(\mu)$ also depends on its so-called natural scale ω_F, which we have omitted it as argument for simplicity but appears through $\ln \mu/\omega_F$ terms. The above equation leads to a multplicative RGE since the μ-independence of the bare function gives

$$\mu\frac{\mathrm{d}}{\mathrm{d}\mu}F(\mu) = \gamma_F(\mu)F(\mu), \qquad \gamma_F(\mu) \equiv -\frac{1}{Z_F(\mu)}\mu\frac{\mathrm{d}}{\mathrm{d}\mu}Z_F(\mu). \tag{2.88}$$

In SCET the anomalous dimension $\gamma_F(\mu)$ takes the general form

$$\gamma_F(\mu) = \rho_F\,\Gamma_{\text{cusp}}[\alpha_s]\ln\frac{\mu^2}{\omega_F^2} + \gamma_F[\alpha_s], \tag{2.89}$$

where ρ_F is a constant and ω_F is again the natural scale of $F(\mu)$. This form holds to all orders in perturbation theory. At this point we highlight $\gamma_F(\mu)$ contains an explicit dependence on the scale μ through the single logarithm $\ln\mu$, whose presence is a signature of Sudakov double logarithms. Furthermore, it can be shown by consistency of top-down evolution versus bottom-up evolution that no more than a single logarithm of μ can appear in the anomalous dimension.

The coefficient of $\ln\mu$ is related to the so-called *cusp anomalous dimension* $\Gamma_{\text{cusp}}[\alpha_s]$, governing the renormalization of Wilson lines that meet at a "cusp"

angle β_{12} between lines along the four-vectors n_1^μ and n_2^μ, with $\cosh\beta_{12} = (n_1 \cdot n_2)/\sqrt{n_1^2 n_2^2}$. Therefore $\Gamma_{\rm cusp}[\alpha_s]$ is a universal ingredient, which is currently known up to four-loop order [49]. The expansion of $\Gamma_{\rm cusp}[\alpha_s]$ up to three-loops can be found in Appendix B. Finally, the remaining term $\gamma_F[\alpha_s]$ is known as the *non-cusp anomalous dimension* and is specific to its function F.

The solution to the RGE (2.88) is then

$$F(\mu) = U_F(\mu,\mu_0)F(\mu_0), \tag{2.90}$$

with $U_F(\mu,\mu_0)$ known as the *evolution kernel*,

$$U_F(\mu,\mu_0) = e^{2\rho_F K_\Gamma(\mu,\mu_0)+K_\gamma(\mu,\mu_0)}\left(\frac{\mu_0}{\omega}\right)^{2\rho_F\,\eta_\Gamma(\mu,\mu_0)}, \tag{2.91}$$

which allows us to run the function F from a scale μ to another scale μ_0. The functions K_Γ, η_Γ and K_γ are defined as

$$\begin{aligned}
K_\Gamma^i(\mu,\mu_0) &= \int_{\alpha_s(\mu_0)}^{\alpha_s(\mu)} \frac{{\rm d}\alpha_s}{\beta[\alpha_s]}\Gamma^i_{\rm cusp}[\alpha_s]\int_{\alpha_s(\mu_0)}^{\alpha_s}\frac{{\rm d}\alpha_s'}{\beta[\alpha_s']}\\
\eta_\Gamma^i(\mu,\mu_0) &= \int_{\alpha_s(\mu_0)}^{\alpha_s(\mu)} \frac{{\rm d}\alpha_s}{\beta[\alpha_s]}\Gamma^i_{\rm cusp}[\alpha_s]\\
K_\gamma^i(\mu,\mu_0) &= \int_{\alpha_s(\mu_0)}^{\alpha_s(\mu)} \frac{{\rm d}\alpha_s}{\beta[\alpha_s]}\gamma^i[\alpha_s].
\end{aligned} \tag{2.92}$$

It is these functions that resum $\ln(\mu/\mu_0)$ terms *in the exponent*, which is why we claimed in section 1.2 that this was the natural counting for renormalization group methods like SCET. The order up to which individual ingredients are needed to achieve a given logarithmic accuracy is displayed in table 2.1. The K_Γ, η_Γ and K_γ functions are given to NNLL accuracy in appendix B.

Another type of RGE arises when the renormalization of the bare function $F^{\rm bare}$ occurs through a convolution:

$$F^{\rm bare}(\tau) = \int {\rm d}\tau' Z_F(\tau-\tau';\mu)F(\tau';\mu). \tag{2.93}$$

In such case the RGE is

$$\mu\frac{\rm d}{{\rm d}\mu}F(\tau;\mu) = \int {\rm d}\tau'\gamma_F(\tau-\tau';\mu)F(\tau';\mu), \tag{2.94}$$

with the anomalous dimension γ_F defined as

$$\gamma_F(\tau;\mu) \equiv -\int {\rm d}\tau' Z_F^{-1}(\tau-\tau';\mu)\mu\frac{\rm d}{{\rm d}\mu}Z_F(\tau';\mu), \tag{2.95}$$

Accuracy	Γ_{cusp}	γ	β	$C(\alpha_s)$
LL	1-loop	-	1-loop	-
NLL	2-loop	1-loop	2-loop	-
NLL$'$	2-loop	1-loop	2-loop	1-loop
NNLL	3-loop	2-loop	3-loop	1-loop
NNLL$'$	3-loop	2-loop	3-loop	2-loop

Table 2.1 Order to which different perturbative ingredients are needed in order to achieve a given logarithmic accuracy. Here Γ_{cusp} denotes the cusp anomalous dimension, γ the non-cusp anomalous dimension and β the QCD β-function. $C(\alpha_s)$ refers to the perturbative coefficients of equation (1.41)

and takes the general form

$$\gamma_F(\tau;\mu) = \Gamma_{\text{cusp}}[\alpha_s]\left(\rho_F\,\delta(\tau)\ln\frac{\mu^2}{\omega^2} - 2\left[\frac{\Theta(\tau)}{\tau}\right]_+\right) + \gamma_F[\alpha_s]\delta(\tau). \tag{2.96}$$

The solution to the RGE (2.94) is

$$F(\tau,\mu) = \int \mathrm{d}\tau' U(\tau-\tau';\mu,\mu_0)F(\tau';\mu_0), \tag{2.97}$$

where the expression for the evolution kernel U_F is given by

$$U_F(\tau;\mu,\mu_0) = \frac{e^{2\rho_F K_\Gamma(\mu,\mu_0)+K_\gamma(\mu,\mu_0)+2\rho_F\gamma_E\eta_\Gamma(\mu,\mu_0)}}{\Gamma[-2\rho_F\,\eta_\Gamma(\mu,\mu_0)]}\left[\frac{\Theta(\tau)}{\tau^{1+2\rho_F\eta_\Gamma(\mu,\mu_0)}}\right]_+ \tag{2.98}$$

2.2.6 The semi-inclusive jet function

All jet functions computed in this thesis are related to the SCET semi-inclusive jet function, originally introduced in ref. [50] and first used for jet substructure studies in ref. [51]. The semi-inclusive jet function $J_i(z,\omega_J,\mu)$ characterizes how an initiating parton i transforms into a jet of radius R and energy fraction $z=\omega_J/\omega$, with ω and ω_J being the large light-cone momentum component of i and the resulting jet, respectively.

The motivation for using the semi-inclusive jet functions is that it allows us to compute jet substructure observables for *inclusive* jet measurements $pp\to$ jet $+X$, where X represents the sum over all particles in the final state other than the observed jet (in case of an n-jet event, the one event contributes to the

inclusive jet cross section n times). This is in contrast to exclusive processes $pp \to n$-jets, where a certain number of signal jets is identified but one vetoes additional jets. Before the introduction of the semi-inclusive jet functions many jet substructure observables in SCET were computed for exclusive jets.

While for certain processes considering exclusive jet production is key (e.g. Higgs or vector boson production associated with n-jets), most jet substructure measurements are performed for inclusive jet production. It would therefore be appropriate to use a factorization formalism specifically formulated for inclusive jet production, as opposed to exclusive. Furthermore, this also allows us to avoid potentially large power corrections $\mathcal{O}(p_T^{\text{veto}}/Q)$, where p_T^{veto} is the jet veto (the transverse momentum above which no jet can be observed) and Q is the hard scale of the process.

The semi-inclusive is defined in terms of the gauge-invariant building blocks introduced in section 2.2.3 as

$$\begin{aligned} J_q(z,\omega,\mu) &= \frac{z}{2N_c}\mathrm{Tr}\left[\frac{\bar{n}\!\!\!/}{2}\langle 0|\delta(\omega-\bar{n}\cdot\mathcal{P})\chi_n(0)|JX\rangle\langle JX|\bar{\chi}_n(0)|0\rangle\right] \\ J_g(z,\omega,\mu) &= -\frac{z\omega}{2(N_c^2-1)}\langle 0|\delta(\omega-\bar{n}\cdot\mathcal{P})\mathcal{B}_{n\perp}^{\mu}(0)|JX\rangle\langle JX|\mathcal{B}_{n\perp}^{\mu}(0)|0\rangle \end{aligned} \quad (2.99)$$

Here $|JX\rangle$ represents the observed jet J and the unobserved final-state particles X, where the sum over X is implied. This definition demonstrates why the semi-inclusive jet function is consistent with inclusive jet production. In concrete terms, the $J_i(z,\omega,\mu)$ denote the probability of the parton i with energy ω to transform into a jet with energy $\omega_J = z\,\omega$.

The SCET diagrams contributing to the quark and gluon semi-inclusive jet functions can be seen in figures 2.4 and 2.5 respectively. The forward matrix element can be computed as the sum over all cuts, however only cuts through the loops (resulting in two final-state partons) contribute. All virtual contributions contain scaleless integrals and thus vanish in dimensional regularization.

Let us take a closer look at the quark case at NLO. When cutting through the loop, there are three contributions we need to take into account: 1) both quark and gluon are inside the jet, 2) only quark is inside the jet and 3) only gluon is inside the jet. For a specific jet algorithm these configurations induce different angular and energy restrictions on the collinear phase space. Summing over all three contributions yields the quark semi-inclusive jet function (the procedure is similar for the gluon). At NLO, the quark and gluon semi-inclusive jet functions for anti-k_t jets are given by

$$\begin{aligned} J_q(z,\omega_J,\mu) &= \delta(1-z) + \frac{\alpha_s}{2\pi}\left[\frac{1}{\epsilon}+\ln\left(\frac{\mu^2}{p_T^2R^2}\right)\right]\left[P_{qq}(z)+P_{gq}(z)\right] \\ &\quad - \frac{\alpha_s}{2\pi}\left\{C_F\left[2(1+z^2)\mathcal{L}_1(1-z)+(1-z)\right] - \delta(1-z)C_F\left(\frac{13}{2}-\frac{2\pi^2}{3}\right)\right. \end{aligned}$$

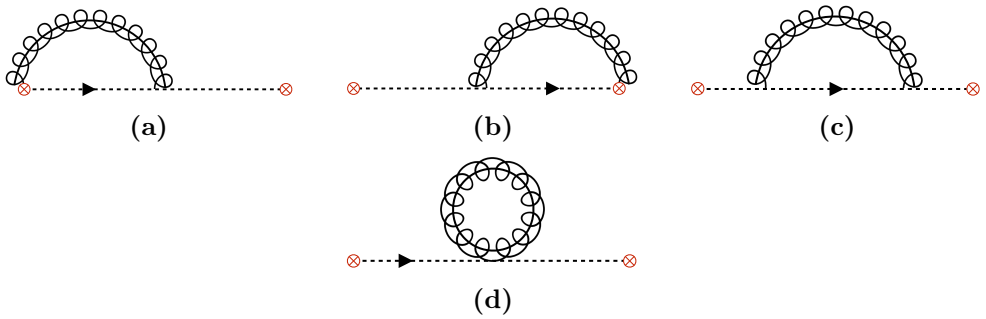

Figure 2.4 Diagrams contributing to the quark semi-inclusive jet function. The $\otimes$ symbols denote insertions of the quark jet field χ_n.

$$
\begin{aligned}
&\quad + 2P_{gq}(z)\ln(1-z) + C_F z\Big\} \\
J_g(z,\omega_J,\mu) &= \delta(1-z) + \frac{\alpha_s}{2\pi}\left[\frac{1}{\epsilon} + \ln\left(\frac{\mu^2}{p_T^2 R^2}\right)\right]\left[P_{gg}(z) + 2n_f P_{qg}(z)\right] \\
&\quad - \frac{\alpha_s}{2\pi}\Bigg\{\frac{4C_A(1-z+z^2)^2}{z}\mathcal{L}_1(1-z) - \delta(1-z)C_A\Bigg[\left(\frac{67}{9} - \frac{2\pi^2}{3}\right) \\
&\quad - \frac{23}{9}T_F n_f\Bigg] + 4n_f\left(P_{qg}(z)\ln(1-z) + T_F z(1-z)\right)\Bigg\}
\end{aligned}
\tag{2.100}
$$

Here the $P_{ij}(z)$ denote the Altarelli-Parisi splitting functions and $\mathcal{L}_n(1-z)$ are plus distributions, both provided in appendix A. Note there are only single poles $1/\epsilon$ and single logarithms in μ, in contrast with exclusive jet functions which have double poles and double logarithms. From these expressions one can obtain the anomalous dimension of the semi-inclusive jet function $\gamma_{ij} = \frac{\alpha_s}{2\pi}P_{ji}(z)$. This leads to an RGE that coincides with the standard DGLAP evolution,

$$
\mu\frac{\mathrm{d}}{\mathrm{d}\mu}J_i(z,\omega_J,\mu) = \frac{\alpha_s}{\pi}\sum_j\int_z^1\frac{\mathrm{d}z'}{z'}P_{ji}\Big(\frac{z}{z'}\Big)J_j(z',\omega_J,\mu). \tag{2.101}
$$

Solving this equation allows us to perform resummation of single $\ln R$ logs for inclusive jet cross sections with small jet radius R.

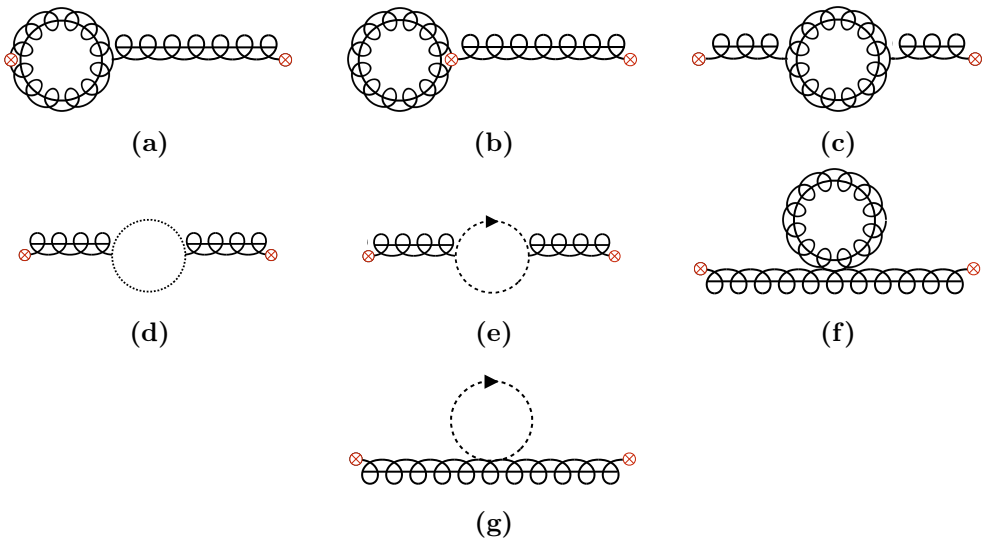

Figure 2.5 Diagrams contributing to the gluon semi-inclusive jet function. The $\otimes$ symbols denote insertions of the gluon jet field $\mathcal{B}^{\mu}_{n\perp}$.

3

The jet shape at NLL′

As we discussed in the introduction of this thesis, the jet shape is a classic jet substructure observable that maps out the transverse energy profile of jets [52]. It is one of the most frequently studied jet substructure observables, which has been measured at a variety of collider experiments over the past decades. The existing data sets include jet shape measurements in pp, $p\bar{p}$, ep, e^+e^- and heavy-ion collisions, and the range of different center-of-mass energies (E_{cm}) makes the jet shape a unique testing ground for precision QCD studies. In order to achieve a meaningful comparison between the experimental data and theoretical calculations, we need to be able to make precise predictions within perturbative QCD, which is the goal of this work.

Jet shapes have been used to constrain parton shower event generators, including their models of hadronization and the underlying event contribution, see e.g. ref. [53]. Furthermore, QCD predicts that the distribution of particles in gluon jets is broader than in quark jets, making the jet shape a useful observable to discriminate between quark and gluon jets (see ref. [54] for a recent review on quark/gluon discrimination).

We consider inclusive jet production, $pp \to \text{jet} + X$, where any observed jet in a given transverse momentum p_T and rapidity η interval is taken into account, and we sum over everything else (X) in the final state. Given such an identified jet with radius R, the integrated jet shape $\psi(r)$ and the differential jet shape $\rho(r)$ are defined as follows

$$\psi(r) = \frac{\sum_{r_i<r} p_{Ti}}{\sum_{r_i<R} p_{Ti}}\,, \qquad \rho(r) = \frac{\mathrm{d}\psi(r)}{\mathrm{d}r}\,, \tag{3.1}$$

see fig. 0.4. Here r_i denotes the distance in the (η, ϕ) plane of particle i in the jet to the jet axis, and p_{Ti} is its transverse momentum with respect to the beam axis. The dependence on the p_T, η and radius R of the observed jet is left implicit. The integrated jet shape is normalized by construction, i.e. $\psi(R) = 1$. Note that it is important for the jet shape which jet axis is chosen. We will

focus on the standard jet axis, which is consistent with the currently existing data sets. For a discussion of the jet shape using the winner-take-all axis [55], see refs. [56, 57].

The first jet shape measurements were already performed by the OPAL collaboration at LEP [58]. It has also been measured at the Tevatron [59–61], and at HERA in both deep inelastic scattering [62–65] and photoproduction [66]. At the LHC, jet shape measurements on an inclusive jet sample were performed by ATLAS [67] and CMS [68] at $E_{\mathrm{cm}} = 7$ TeV. The jet shape has also been measured for heavy-flavor jets [69, 70]. We leave an extensive comparison to all these data sets for future work, focussing only on the LHC data in this chapter. In recent years, jet shapes have also received a growing attention in heavy-ion collisions as a probe of the properties of the quark-gluon plasma. The transverse energy profile of jets that traverse the hot and dense QCD medium gets modified in comparison to jets in pp collisions. See refs. [71, 72] for recent experimental results from the LHC.

In this work we build upon the framework for jet shapes developed by some of us in the context of subjet distributions [56], and extend it to full next-to-leading logarithmic (NLL′) accuracy. We employ Soft Collinear Effective Theory (SCET) [12–16] in order to achieve the resummation of $\ln R$ and $\ln(r/R)$. The starting point is our factorization of the cross section differential in jet transverse momentum p_T, rapidity η, and the energy fraction z_r contained in a subjet of radius r centered along the jet axis,

$$\begin{aligned}\frac{\mathrm{d}\sigma}{\mathrm{d}p_T\,\mathrm{d}\eta\,\mathrm{d}z_r} = &\sum_{a,b,c} f_a(x_a,\mu) \otimes f_b(x_b,\mu) \otimes \mathcal{H}_{ab}^c\left(x_a, x_b, \eta, p_T/z, \mu\right) \\ &\otimes \mathcal{G}_c^{\mathrm{jet}}(z, z_r, p_T R, r/R, \mu)\,. \end{aligned} \tag{3.2}$$

Here $f_{a,b}$ denote the PDFs for the incoming protons, the hard functions $\mathcal{H}_{ab}^c$ describe the hard scattering $ab \to c + X$ and $\otimes$ denote appropriate integrals over the momentum fractions $x_{a,b}$ and z. The production of the jet, including the measurement of the energy fraction z_r, is captured by the jet function $\mathcal{G}_c^{\mathrm{jet}}$. The factorization in eq. (3.2) holds for narrow jets and is analogous to inclusive hadron production, with fragmentation functions replaced by jet functions [50, 73, 74]. The integrated jet shape $\psi(r)$ in eq. (3.1) is then given by the energy average of the z_r differential cross section normalized by the inclusive jet cross section

$$\psi(r) = \int_0^1 dz_r\, z_r \frac{\mathrm{d}\sigma}{\mathrm{d}p_T\,\mathrm{d}\eta\,\mathrm{d}z_r} \Big/ \frac{\mathrm{d}\sigma}{\mathrm{d}p_T\,\mathrm{d}\eta}\,. \tag{3.3}$$

The expression for $\psi(r)$ involves single logarithms in the jet radius parameter $\alpha_s^n \ln^n R$ and double logarithms in the ratio of the two jet radii $\alpha_s^n \ln^{2n}(r/R)$,

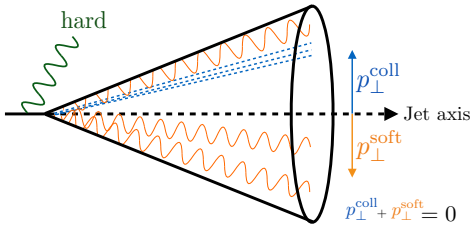

Figure 3.1 Illustration of the refactorized expression of the jet function $\mathcal{G}_c$ in eq. (3.4) in the limit $r \ll R$. Hard radiation at the jet scale $p_T R$ is allowed outside the observed jet. The collinear radiation (blue) is offset from the jet axis, due to the recoil from the soft radiation (orange) inside the jet, since the jet axis is along the jet momentum.

which can be large and will be resummed. The resummation of logarithms in the jet radius parameter R follows from the usual DGLAP evolution equations satisfied by the jet function $\mathcal{G}_c^{\text{jet}}$. This was found to be a characteristic feature of single-inclusive jet substructure observables, see e.g. refs. [51, 74–76].

The resummation of logarithms in r/R requires a treatment within SCET_{II} due to the recoil-effect of soft radiation, as pointed out in ref. [56]. This resummation is thus similar to that encountered for transverse momentum dependent observables [77–82]. It is accomplished by refactorizing the jet function $\mathcal{G}_c^{\text{jet}}$ in eq. (3.2) in the limit $r \ll R$ as

$$\mathcal{G}_c^{\text{jet}}(z, z_r, p_T R, r/R, \mu) \overset{\text{NLL}'}{=} \sum_d H_{cd}(z, p_T R, \mu) \int \mathrm{d}^2 k_\perp \, C_d(z_r, p_T r, k_\perp, \mu, \nu) \times S_d^{\text{G}}(k_\perp, \mu, \nu R) \, S_d^{\text{NG}}\Big(\frac{r}{R}\Big) \Big[1 + \mathcal{O}\Big(\frac{r}{R}\Big)\Big] . \tag{3.4}$$

Here, the hard functions H_{cd} describe how the parton c coming from the hard-scattering produces a jet of size R and of parton flavor d, carrying a fraction z of the initial parton. The collinear function C_d and the soft function S_d^{G} take into account collinear and (global) soft radiation inside the jet. We integrate over the transverse momentum $k_\perp$ generated by the soft radiation, accounting for its recoil on the collinear radiation. By solving the associated renormalization group (RG) equations of the different functions, we achieve the resummation of logarithms in r/R. This involves both the standard renormalization group evolution in the invariant mass scale μ, as well as an evolution in the rapidity scale ν, as discussed in sec. 3.1. We calculate the collinear functions C_d for the first time at one-loop order, accounting for the dependence on the recoil $k_\perp$. We also include the contribution of non-global logarithms (NGLs) [83],

		Fixed-order	β	γ_μ	γ_ν	NGLs
$\ln R$	LL	tree	1-loop	1-loop	-	-
	NLL	1-loop	2-loop	2-loop	-	-
	NNLL	2-loop	3-loop	3-loop	-	-
$\ln(r/R)$	LL	tree	1-loop	1-loop	-	-
	NLL	tree	2-loop	2-loop	1-loop	LL
	NLL′	1-loop	2-loop	2-loop	1-loop	LL
	NNLL	1-loop	3-loop	3-loop	2-loop	NLL

Table 3.1 The perturbative ingredients needed at various orders in the $\ln R$ and $\ln(r/R)$ resummation. The columns correspond to the loop order of the fixed-order ingredients, the QCD beta function, the μ and ν anomalous dimensions, and the non-global logarithms. The non-cusp part of the μ anomalous dimension is only needed at one-loop order lower than indicated above.

which are captured by the function $S_d^{\rm NG}$ in eq. (3.4), but only affect the region where r/R is very small. The simple (multiplicative) treatment of the NGLs in eq. (3.4) is the reason this equation is only valid to NLL′ accuracy. The refactorized cross section in eq. (3.4) which is given in terms of hard, collinear and soft functions in the limit $r \ll R$ is illustrated in fig. 3.1. In particular, we show the effect of the recoil due to the soft radiation inside the jet.

The perturbative order of the various ingredients needed for the $\ln R$ and $\ln(r/R)$ resummation is summarized in table 5.2. We work at NLL′ accuracy in the $\ln(r/R)$ resummation, as this is commensurate with an NLL resummation of $\ln R$. Going beyond this accuracy will be daunting, especially in the treatment of non-global logarithms. We would like to stress that earlier jet shape calculations [84–86] are formally only accurate to leading-logarithmic (LL) order in their treatment of the logarithms of r/R. In particular, the contribution from the rapidity evolution, as well as the non-global logarithms, that both first enter at NLL accuracy, are included here for the first time. In addition, earlier calculations did not account for the inclusive jet sample, where the resummation of logarithms of the jet radius R changes the ratio of quark and gluon jets, thereby affecting the spectrum already at LL accuracy.

Finally, comparisons between our predictions and LHC data suggest a significant effect of nonperturbative physics (underlying event and hadronization) on the jet shape, particularly for small jet p_T. This is consistent with the picture that arises from studying these effects in Pythia [87]. We will include them in our analysis by using a simple one-parameter model, finding good agreement with the data.

The remainder of this chapter is organized as follows: The theoretical frame-

work used to calculate the jet shape is discussed in sec. 3.1, with certain ingredients relegated to the appendices. We present a detailed derivation of the collinear function, relevant for the resummation of logarithms in r/R, in sec. 3.2. The details that enter our numerical evaluation of the cross section are described in sec. 3.3, and first (perturbative) results for quark and gluon jets are presented there. Nonperturbative effects are investigated in sec. 3.4, for which two simple models are explored. In sec. 3.5 we show our final results, which we compare to available pp data from the LHC, and we conclude in sec. 3.6.

3.1 Framework

In this section we present the theoretical framework that we use to obtain our results. In sec. 3.1.1 we describe the factorization formulae and how they enable resummation. We then rearrange these formulae in sec. 3.1.2, to separate them into the inclusive production of jets and the jet shape itself. In sec. 3.1.3 the one-loop hard function is given, and in sec. 3.1.4 we discuss the soft function and non-global logarithms. The calculation of the collinear function at one-loop, accounting for the effect of recoil, is one of the main new results and presented separately in sec. 3.2. The one-loop expressions for the jet function for $r \lesssim R$ are given in app. C.2, and the anomalous dimensions are listed in app. B.3.1.

3.1.1 Factorization and resummation

The cross section describing the measurement of the fraction z_r of jet energy inside the cone of radius r around the jet axis, in an inclusive sample of jets produced in pp collisions, factorizes as shown in equation (3.2).

The parton distribution functions f_a and f_b describe extracting a parton of flavor a and b out of the proton, and the function $\mathcal{H}_{ab}^{c}$ [88] encodes their hard scattering in which the parton with flavor c, rapidity η and transverse momentum p_T/z is produced. The subsequent formation of the jet with transverse momentum $z \times p_T/z = p_T$ moving in the same direction, as well as the jet shape measurement, is encoded in the jet function $\mathcal{G}_c^{\text{jet}}$.[1] This collinear factorization requires that $R \ll 1$ to keep the $\mathcal{O}(R^2)$ power corrections small. In several examples it has been observed that these power corrections are still small for values of R up to 0.7 [89]. Note that this factorization formula is identical to that for the inclusive fragmentation of hadrons, with the fragmentation

[1] In ref. [56] this was called the central subjet function and a hat was included on top of $\mathcal{G}$, to distinguish it from other jet functions in that paper.

function replaced by our jet function.

The jet function $\mathcal{G}_c^{\text{jet}}$ describes the formation of the jet as well as the jet shape measurement through z_r, and has the following matrix-element definition in SCET,

$$\mathcal{G}_q^{\text{jet}}(z, z_r, p_T R, r/R, \mu) = 16\pi^3 \sum_X \frac{1}{2N_c} \operatorname{Tr}\Big[\frac{\bar{n}\!\!\!/}{2}\langle 0|\delta\Big(2 - \frac{z\,\bar{n}\cdot\mathcal{P}}{p_T}\Big)\delta^2(\mathcal{P}_\perp)\chi_n(0)|X\rangle \times \langle X|\bar{\chi}_n(0)|0\rangle\Big] \sum_{J_R\in X} \delta\big(p_T - p_T(J_R)\big)\delta\Big(z_r - \frac{p_T(j_r)}{p_T}\Big), \tag{3.5}$$

for quark jets, and analogously for gluon jets. Here we exploit that the measurement is invariant under boosts along the beam axis, to set the jet rapidity η equal to zero.[2] We will repeatedly make use of the following decomposition of a vector p^μ in light-cone coordinates where $n^\mu = (1,0,0,1)$ and $\bar{n}^\mu = (1,0,0,-1)$ are light-like vectors, and $p_\perp^\mu$ denotes the transverse components. The collinear field $\bar{\chi}_n$ in eq. (3.5) describes the quark that initiates the jet, averaged over its spin and color configurations, leading to the factor $1/(2N_c)$. It contains a Wilson line to ensure (collinear) gauge invariance. The $\delta(2 - z\,\bar{n}\cdot\mathcal{P}/p_T)$ fixes the quark field to have transverse momentum p_T/z with respect to the *beam* axis, and the $\delta^2(\mathcal{P}_\perp)$ fixes our light-cone coordinates to be along the momentum of the initial parton. The last line describes the sum over all jets J_R in the final state $|X\rangle$, with transverse momentum p_T, of which a fraction z_r is inside the central subjet j_r. The functions $\mathcal{G}_q^{\text{jet}}$ and $\mathcal{G}_g^{\text{jet}}$ were calculated at one loop in ref. [56], and their expressions are collected in app. C.2.

The factorization in (3.2) separates the physics at scales

$$\mu_f \sim \Lambda_{\text{QCD}}\,, \qquad \mu_{\mathcal{H}} \sim p_T\,, \qquad \mu_{\mathcal{G}} \sim p_T R\,. \tag{3.6}$$

By evolving $\mathcal{G}$ from its natural scale $\mu_{\mathcal{G}}$ to $\mu_{\mathcal{H}}$, the logarithms of $\mu_{\mathcal{G}}/\mu_{\mathcal{H}} \sim R$ are resummed. This involves the DGLAP evolution,

$$\mu\frac{\mathrm{d}}{\mathrm{d}\mu}\,\mathcal{G}_i^{\text{jet}}(z, z_r, p_T R, r/R, \mu) = \sum_j \int_z^1 \frac{\mathrm{d}z'}{z'}\,\frac{\alpha_s}{\pi} P_{ji}(z/z')\,\mathcal{G}_j^{\text{jet}}(z', z_r, p_T R, r/R, \mu), \tag{3.7}$$

where the one-loop splitting functions are given in appendix A.2.

[2] This avoids spurious factors of $\cosh\eta$ in intermediate expressions. They arise due to the difference between the energy and transverse momentum of the jet, and are compensated for by the angular size of the jet, which also depends on η because the jet is defined in (η, ϕ) coordinates.

Mode:	Scaling $(\bar{n}\cdot p, n\cdot p, p_\perp)$
hard(-collinear)	$p_T(1, R^2, R)$
collinear	$p_T(1, r^2, r)$
(collinear-)soft	$p_T(r/R, rR, r)$

Table 3.2 The parametric scalings of the momenta of the modes that enter in the factorization of the jet function for $r \ll R$.

For $r \ll R$, the jet function contains large logarithms of r/R that also require resummation. This is achieved through a second factorization [56][3]

$$\mathcal{G}_c^{\text{jet}}(z, z_r, p_T R, r/R, \mu) \overset{\text{NLL}'}{=} \sum_d H_{cd}(z, p_T R, \mu) \int \mathrm{d}^2 k_\perp \, C_d(z_r, p_T r, k_\perp, \mu, \nu) \times S_d^{\text{G}}(k_\perp, \mu, \nu R) \, S_d^{\text{NG}}\Big(\frac{r}{R}\Big) \Big[1 + \mathcal{O}\Big(\frac{r}{R}\Big)\Big] . \quad (3.8)$$

The momentum scalings of the modes in SCET, corresponding to the various ingredients in eq. (3.8), are listed in table 3.2. If we boost to a frame where the jet and out-of-jet region are complementary hemispheres, this is the usual power counting for hard, collinear and soft radiation, which is why we use this nomenclature instead of hard-collinear and collinear-soft. The hard function H_{cd} describes how the initial parton c produces a jet of radius R with parton flavor d and a fraction z of the initial transverse momentum with respect to the *beam* axis. Within the jet, the parton d can only undergo energetic splittings of angles of order r, otherwise the collinear radiation would lie outside the cone of radius r.[4] The fraction z_r of this collinear radiation within the cone of size r is described by the collinear function C_d. The collinear function also accounts for the transverse momentum offset $k_\perp$ of the initial collinear parton with respect to the *jet* axis, due to recoil against soft radiation. In sec. 3.2 we will present the first one-loop calculation of the collinear function for $k_\perp \neq 0$. The distribution of this recoil is encoded in the soft function, which we separate into a global contribution S_d^{G} and non-global logarithms S_d^{NG}. Non-global logarithms [83] arise because only soft radiation *inside* the jet affects the position of the axis, and our simple treatment of them is the

[3] This is identical to eq. (3.4) and repeated for convenience. Note that we adopted a slightly different convention for the arguments of the involved functions in comparison to ref. [56].

[4] Of course there could be a splitting inside the jet of angular size R that is balanced in such a way that there is also collinear radiation inside the cone of size r at the center of the jet, but such configurations give a power suppressed contribution. This is very similar to the power suppression of the contribution from two nearly back-to-back jets in Higgs production at small transverse momentum, discussed in e.g. ref. [81].

reason why eq. (3.8) only holds to NLL′ accuracy, see sec. 3.1.4. The $\mathcal{O}(r/R)$ power corrections in eq. (3.8) can be extracted from $\mathcal{G}_c^{\text{jet}}$, and will be included.

Transverse momentum dependent observables generically suffer from rapidity divergences. We will employ the η-regulator [81, 90], for which ν denotes the corresponding rapidity renormalization scale. The factorization in eq. (3.8) separates the jet function into ingredients at the scales

$$\begin{aligned} &\mu_H \sim p_T R\,, && \mu_C \sim p_T\, r\,, && \mu_{S^{\text{G}}} \sim p_T\, r\,, \\ &&& \nu_C \sim p_T\,, && \nu_{S^{\text{G}}} \sim p_T\, \frac{r}{R}\,. \end{aligned} \tag{3.9}$$

By evaluating the ingredients at their natural scales and using the RG evolution to evolve them to a common scale, the global logarithms of $\mu_C/\mu_H \sim \mu_{S^{\text{G}}}/\mu_H \sim \nu_{S^{\text{G}}}/\nu_C \sim r/R$ are resummed. The RG equations are[5]

$$\begin{aligned} \mu\frac{\mathrm{d}}{\mathrm{d}\mu}\, H_{cd}(z, p_T R, \mu) &= \sum_e \int_z^1 \frac{\mathrm{d}z'}{z'}\, \gamma^H_{ce}\Big(\frac{z}{z'}, p_T R, \mu\Big)\, H_{ed}(z', p_T R, \mu)\,. \\ \mu\frac{\mathrm{d}}{\mathrm{d}\mu}\, C_d(z_r, p_T r, k_\perp, \mu, \nu) &= \gamma^C_d(\mu, \nu/p_T)\, C_d(z_r, p_T r, k_\perp, \mu, \nu)\,. \\ \mu\frac{\mathrm{d}}{\mathrm{d}\mu}\, S^{\text{G}}_d(k_\perp, \mu, \nu R) &= \gamma^S_d(\mu, \nu R)\, S^{\text{G}}_d(k_\perp, \mu, \nu R)\,, \\ \nu\frac{\mathrm{d}}{\mathrm{d}\nu}\, C_d(z_r, p_T r, k_\perp, \mu, \nu) &= -\int \frac{\mathrm{d}^2 k'_\perp}{(2\pi)^2}\, \gamma^\nu_d(k_\perp - k'_\perp, \mu)\, C_d(z_r, p_T r, k'_\perp, \mu, \nu)\,. \\ \nu\frac{\mathrm{d}}{\mathrm{d}\nu}\, S^{\text{G}}_d(k_\perp, \mu, \nu R) &= \int \frac{\mathrm{d}^2 k'_\perp}{(2\pi)^2}\, \gamma^\nu_d(k_\perp - k'_\perp, \mu)\, S^{\text{G}}_d(k'_\perp, \mu, \nu R)\,. \end{aligned} \tag{3.10}$$

The anomalous dimensions are collected in B.3.1. As is clear from eq. (3.8), the anomalous dimensions of the hard, collinear and soft function should combine to give the anomalous dimension of the jet function, which we checked. The μ-evolution sums double logarithms, and the ν-evolution sums single logarithms. We also include the leading non-global logarithms to obtain the desired NLL′ accuracy, which will be discussed in sec. 3.1.4.

3.1.2 Separating the jet production and jet shape

We now rearrange our calculation in a way that simplifies the numerical implementation, effectively separating the jet production and the jet shape.[6] We

[5] The expressions in ref. [56] contain a typo, as the convolution in $k_\perp$ for the ν-RG equations was omitted.

[6] A similar rearrangement was carried out for hadron fragmentation inside a jet in ref. [73].

start by writing $\mathcal{G}_c^{\text{jet}}$ as

$$\mathcal{G}_c^{\text{jet}}(z, z_r, p_T R, r/R, \mu) \equiv \sum_d J_{cd}(z, p_T R, \mu) \tilde{\mathcal{G}}_d^{\text{jet}}\big(z_r, p_T R, r/R, \mu\big) + \mathcal{O}(\alpha_s^2), \tag{3.11}$$

where

$$\tilde{\mathcal{G}}_d^{\text{jet}}\big(z_r, p_T R, r/R, \mu\big) = \int \mathrm{d}z' \left[\mathcal{G}_d^{\text{jet}}(z', z_r, p_T R, r/R, \mu) - J_d^{(1)}(z', p_T R, \mu)\, \delta(1 - z_r)\right]. \tag{3.12}$$

Here J_d is the semi-inclusive jet function [50, 74] that enters in inclusive jet production. J_{cd} is directly related, except that it not only keeps track of the flavor c of the initiating parton but also the flavor d of the jet, so

$$\sum_d J_{cd}(z, p_T R, \mu) = J_c(z, p_T R, \mu)\,. \tag{3.13}$$

Its one-loop expressions are given in eq. (3.22). Note that eq. (3.11) is not a factorization of physics at different scales, as the natural scale of $\mathcal{G}^{\text{jet}}$ and J is both $p_T R$. However, this is why it is justified to work to finite order in α_s. We exploited that at one-loop order the nontrivial z-dependence cancels between $\mathcal{G}_d^{\text{jet}}$ and J_d, i.e. their difference is proportional to $\delta(1 - z)$, since the splitting where one parton is outside the jet is treated the same in both calculations. This delta function is removed by the integral over z.

Combining J_{cd} with the rest of (3.2), we identify this as the cross section for the inclusive production of jets of flavor d,

$$\begin{aligned}\frac{\mathrm{d}\sigma_d}{\mathrm{d}\eta\, \mathrm{d}p_T} = \sum_{a,b,c} \int \frac{\mathrm{d}x_a}{x_a}\, f_a(x_a, \mu) \int \frac{\mathrm{d}x_b}{x_b}\, f_b(x_b, \mu) \int \frac{\mathrm{d}z}{z}\, \mathcal{H}_{ab}^c(x_a, x_b, \eta, p_T/z, \mu) \\ \times J_{cd}(z, p_T R, \mu)\big[1 + \mathcal{O}(R^2)\big]\,.\end{aligned} \tag{3.14}$$

By summing over d and using eq. (3.13), this reproduces the inclusive jet cross section in refs. [50, 74]. Eq. (3.3) then implies that the remainder in eq. (3.12) corresponds to the jet shape $\psi_c(r)$ for a jet of flavor c, after taking the second Mellin moment of z_r,

$$\psi_d(r) = \int \mathrm{d}z \left[\int \mathrm{d}z_r\, z_r\, \mathcal{G}_d^{\text{jet}}(z, z_r, p_T R, r/R, \mu) - J_d^{(1)}(z, p_T R, \mu)\right] + \mathcal{O}(\alpha_s^2)\,. \tag{3.15}$$

Using the expressions in app. C.2, the jet shape for $r \lesssim R$ is given by

$$\psi_{q,r\lesssim R}(r) = 1 + \frac{\alpha_s C_F}{2\pi}\bigg[-\frac{1}{2}L_{r/R}^2 + \frac{3}{2}L_{r/R} - \frac{9}{2} + \frac{6r}{R} - \frac{3r^2}{2R^2}\bigg],$$
$$\psi_{g,r\lesssim R}(r) = 1 + \frac{\alpha_s}{2\pi}\bigg[-\frac{C_A}{2}L_{r/R}^2 + \frac{\beta_0}{2}L_{r/R} + C_A\Big(-\frac{203}{36} + \frac{8r}{R} - \frac{3r^2}{R^2} + \frac{8r^3}{9R^3} - \frac{r^4}{4R^4}\Big) + T_F n_f\Big(\frac{41}{18} - \frac{4r}{R} + \frac{3r^2}{R^2} - \frac{16r^3}{9R^3} + \frac{r^4}{2R^4}\Big)\bigg], \tag{3.16}$$

which is properly normalized, $\psi_{d,r\lesssim R}(R) = 1$.

For $r \ll R$, the factorization of $\mathcal{G}$ in eq. (3.8) leads to the following expression for the jet shape

$$\psi_{d,r\ll R}(r) \overset{\text{NLL}'}{=} \tilde{H}_d(p_T R,\mu) \int \mathrm{d}^2 k_\perp \int \mathrm{d}z_r\, z_r\, C_d(z_r, p_T r, k_\perp, \mu, \nu) \times S_d^{\mathrm{G}}(k_\perp,\mu,\nu R)\, S_d^{\mathrm{NG}}\Big(\frac{r}{R}\Big)\Big[1 + \mathcal{O}\Big(\frac{r}{R}\Big)\Big], \tag{3.17}$$

where

$$\tilde{H}_d(p_T R,\mu) = \int \mathrm{d}z \sum_e \Big[H_{de}(z, p_T R, \mu) - J_{de}^{(1)}(z, p_T R, \mu)\Big]. \tag{3.18}$$

The contribution of $H_{de}^{(1)}$ is removed by subtracting $J_{de}^{(1)}$, but there is a constant remainder $\propto \delta_{de}\delta(1-z)$ since $J_{de}^{(1)}$ also receives a contribution when both partons are inside the jet. This constant is contained in $\tilde{H}_d$, where it is multiplied by the Sudakov factor from the evolution kernels, ensuring that it's contribution vanishes for $r \to 0$ (as required). In our implementation of eq. (3.17), we 1) include the evolution kernels from evolving the ingredients between their natural scales, 2) expand the fixed-order ingredients, i.e. dropping cross terms such as $C^{(1)}S^{(1)}$, and 3) include the corrections contained in $\mathcal{O}(r/R)$, which can be read off from eq. (3.16).

3.1.3 Hard function

The hard function H_{cd} in eq. (3.8) is up to one-loop order given by [56, 82]

$$H_{qq}(z, p_T R, \mu) = \delta(1-z) + \frac{\alpha_s}{2\pi}\bigg[C_F\delta(1-z)\Big(-\frac{L_R^2}{2} - \frac{3}{2}L_R + \frac{\pi^2}{12}\Big) + L_R P_{qq}(z) - 2C_F(1+z^2)\Big(\frac{\ln(1-z)}{1-z}\Big)_+ - C_F(1-z)\bigg],$$
$$H_{qg}(z, p_T R, \mu) = \frac{\alpha_s}{2\pi}\bigg[\Big(L_R - 2\ln(1-z)\Big)P_{gq}(z) - C_F z\bigg],$$

$$
\begin{aligned}
H_{gq}(z, p_T R, \mu) &= \frac{\alpha_s}{2\pi}\bigg[\Big(L_R - 2\ln(1-z)\Big)P_{qg}(z) - T_F 2z(1-z)\bigg], \\
H_{gg}(z, p_T R, \mu) &= \delta(1-z) + \frac{\alpha_s}{2\pi}\bigg[\delta(1-z)\Big(-C_A\frac{L_R^2}{2} - \frac{\beta_0}{2}L_R + C_A\frac{\pi^2}{12}\Big) \\
&\quad + L_R P_{gg}(z) - \frac{4C_A(1-z+z^2)^2}{z}\left(\frac{\ln(1-z)}{1-z}\right)_+\bigg].
\end{aligned} \tag{3.19}
$$

where the splitting functions are given in eq. (A.6) and L_R is

$$
L_R = \ln\left(\frac{\mu^2}{p_T^2 R^2}\right). \tag{3.20}
$$

The hard function is formally a matching coefficient. At one-loop order it is simply the contribution to $\mathcal{G}_c$ from the region of phase space where the two partons produced by a splitting of c are not clustered together. The second index d denotes the parton inside the jet.

The hard function $\tilde{H}_d$ in eq. (3.18) is given by

$$
\begin{aligned}
\tilde{H}_q(p_T R, \mu) &= 1 + \frac{\alpha_s C_F}{2\pi}\left(-\frac{1}{2}L_R^2 - \frac{3}{2}L_R - \frac{13}{2} + \frac{3\pi^2}{4}\right) + \mathcal{O}(\alpha_s^2), \\
\tilde{H}_g(p_T R, \mu) &= 1 + \frac{\alpha_s}{2\pi}\bigg[C_A\Big(-\frac{1}{2}L_R^2 - \frac{5}{12} + \frac{3\pi^2}{4}\Big) + \beta_0\Big(-\frac{1}{2}L_R - \frac{23}{12}\Big)\bigg] + \mathcal{O}(\alpha_s^2).
\end{aligned} \tag{3.21}
$$

For completeness we mention that at one-loop order the semi-inclusive jet function with identified jet flavor J_{cd} is

$$
J_{cd}^{(1)}(z, p_T R, \mu) = H_{cd}^{(1)}(z, p_T R, \mu) - \delta_{cd}\delta(1-z)\tilde{H}_c^{(1)}(p_T R, \mu), \tag{3.22}
$$

in terms of the above equations. The J_{cd} are also given explicitly in appendix C.1.

3.1.4 Soft function and non-global logarithms

Up to NLL′ order, the global soft function for quark jets can be calculated from

$$
S_q^{\mathrm{G}}(k_\perp, \mu, \nu R) \overset{\mathrm{NLL'}}{=} \frac{1}{N_c}\sum_{X_s}\langle 0|\bar{\mathrm{T}}[Y_{\bar{n}}^\dagger Y_n]\,|X\rangle\langle X|\mathrm{T}[Y_n^\dagger Y_{\bar{n}}]|0\rangle\,\delta^2\Big(k_\perp - \sum_{i\in\mathrm{jet}} k_{i,\perp}\Big), \tag{3.23}
$$

where the delta function sums the transverse momentum $k_{i,\perp}$ with respect to the *jet axis* of soft radiation in X that is inside the jet. Soft radiation does

not resolve individual collinear splittings, and so soft radiation emitted by the collinear particles in the jet can be encoded by the eikonal Wilson line $Y_n^\dagger$. At NLL′, the one-loop calculation of the soft function comes with the tree-level hard function, so there is a single parton moving in the $\bar{n}$ direction, resulting in $Y_{\bar{n}}$. At higher orders, real emissions in the hard function (outside the jet) will result in additional Wilson lines [91,92], see also ref. [93]. This complicates the non-global logarithms, but is fortunately beyond the accuracy at which we are working.

A one-loop calculation yields [56]

$$S_q^{\mathrm{G}}(k_\perp,\mu,\nu R) = \delta^2(k_\perp) + \frac{\alpha_s C_F}{2\pi^2}\bigg[-\frac{1}{\mu^2}\Big(\frac{\ln(k_\perp^2/\mu^2)}{k_\perp^2/\mu^2}\Big)_+ + \frac{1}{\mu^2}\,\frac{1}{(k_\perp^2/\mu^2)_+}\,\ln\frac{\nu^2R^2}{4\mu^2} - \frac{\pi^2}{12}\delta(\vec{k}_\perp^{\,2})\bigg]. \tag{3.24}$$

For S_g^{G} the Wilson lines are in the adjoint representation, instead of the fundamental representation, and the overall normalization in the definition is modified from $1/N_c$ to $1/(N_c^2-1)$. The one-loop result for S_g^{G} is simply given by replacing $C_F \to C_A$ in eq. (3.24).

The non-global logarithms arise from soft emission patterns that simultaneously probe the jet and out-of-jet region [83]. Since we consider $R \ll 1$, the NGLs are the same as in the hemisphere case [94]. Indeed, a direct calculation of the leading contribution at order α_s^2 gives rise to

$$-\frac{\alpha_s^2 C_F C_i}{24\pi}\,\frac{1}{(p_T R)^2}\Big(\frac{\ln(k_\perp^2/(p_T R)^2)}{k_\perp^2/(p_T R)^2}\Big)_+, \tag{3.25}$$

where the hard scale $p_T R$ arises from the emission outside the jet, and the color factor $C_i = C_F$ for quarks and C_A for gluons. The integral in eq. (3.8) with the tree-level collinear function in eq. (3.29), leads to

$$\begin{aligned}&\int \mathrm{d}^2k_\perp \Theta(k_\perp < p_T r) \times -\frac{\alpha_s^2 C_F C_i}{24\pi}\,\frac{1}{(p_T R)^2}\Big(\frac{\ln(k_\perp^2/(p_T R)^2)}{k_\perp^2/(p_T R)^2}\Big)_+ \\ &= -\frac{\alpha_s^2 C_F C_i}{12}\,\ln^2\Big(\frac{R}{r}\Big).\end{aligned} \tag{3.26}$$

We obtain the same result if we had directly taken the NGL at order α_s^2 of the hemisphere case [83], with R/r as the argument of the logarithm.

Beyond order α_s^2, we should write the NGLs in terms of plus distributions of $k_\perp/(p_T R)$, and convolve these with the global soft function and the collinear function. However, at NLL′ only the leading NGLs are required, and we may

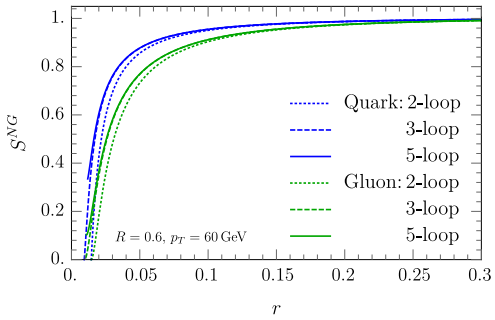

Figure 3.2 The non-global contribution to the soft function in eq. (4.28) for quark jets (blue) and gluon jets (green) with $R = 0.6$ at $p_T = 60$ GeV. Shown are the results up to two-loop (dotted), three-loop (dashed) and five-loop order (solid).

directly take the NGLs of the hemisphere case with the ratio R/r as the argument of the logarithm, which is significantly simpler. This is justified because both the NGLs and the rapidity resummation are single logarithmic series of plus distributions in transverse momentum. All subtleties from convolutions of plus distributions in transverse momentum are subleading, i.e. whether we first convolve these single logarithmic series with each other, and then integrate them against the tree-level collinear function that sets the upperbound $k_\perp = p_T r$, or directly integrate each of them up to $k_\perp = p_T r$, is the same at the accuracy that we are working.

The leading NGLs in the hemisphere case are described by a universal function, where in our case the argument of the logarithm is R/r. We will work in the large N_c approximation (the leading NGLs without this approximation have been studied in ref. [95]). Rather than using the fit of ref. [83], we employ the solution to the BMS equation [96] up to five-loop order [97],

$$S_q^{\rm NG}(\widehat{L}) = 1 - \frac{\pi^2}{24}\widehat{L}^2 + \frac{\zeta_3}{12}\widehat{L}^3 + \frac{\pi^4}{34560}\widehat{L}^4 + \Big(-\frac{\pi^2\zeta_3}{360} + \frac{17\zeta_5}{480}\Big)\widehat{L}^5 + \mathcal{O}(L^6)\,, \tag{3.27}$$

where

$$\widehat{L} = \frac{\alpha_s N_c}{\pi} \ln\frac{R}{r}\,. \tag{3.28}$$

The advantage of using this result is that it allows us to test the perturbative convergence, which is excellent for the range of r/R we are interested in. Specifically, there is a small difference from including the cubic term in (3.27), but the effect of subsequent terms is not visible, as is clear from fig. 3.2.

This figure also shows that the effect of the non-global contribution to the soft function is limited to rather small values of r. For the gluon case we have $S_g^{\rm NG} = (S_q^{\rm NG})^2$, which follows from rewriting the adjoint Wilson line in terms of a fundamental and anti-fundamental Wilson line.[7]

3.2 Collinear function including recoil

The definition of the collinear function is similar to eq. (3.5), and is given by the following expression for the quark case,

$$C_q(z_r, p_T r, k_\perp, \mu, \nu) = 16\pi^3 \sum_X \frac{1}{2N_c} \mathrm{Tr}\Big[\frac{\bar{\eta}\!\!\!/}{2}\langle 0|\delta(2p_T - \bar{n}\cdot\mathcal{P})\delta^2(\mathcal{P}_\perp - k_\perp)\chi_n(0)|X\rangle \times \langle X|\bar{\chi}_n(0)|0\rangle\Big] \times \delta\Big(z_r - \frac{p_T(j_r)}{p_T}\Big)\,.$$

As before, we take the jet rapidity η equal to zero, since the measurement is invariant under boosts along the beam axis. In contrast to eq. (3.5), all this collinear radiation is inside the jet, so there is no sum over jets in X or measurement of z. The recoil due to soft radiation is accounted for through the $\delta^2(\mathcal{P}_\perp - k_\perp)$. At tree level, the collinear function is given by

$$C_d(z_r, p_T r, k_\perp, \mu, \nu) = \delta(1 - z_r)\,\Theta(k_\perp < p_T r)\,, \tag{3.29}$$

for both quarks ($d = q$) and gluons ($d = g$). This simply states that as long as the recoil is not too large ($k_\perp < p_T r$), the parton is inside the cone of radius r around the jet axis, and $z_r = 1$.

In this section we calculate the collinear function at order α_s, which involves the collinear splitting of an initial quark or gluon into two partons. We give the collinear phase-space and matrix elements in 3.2.1, and the geometry of the setup is described in 3.2.2. The resulting integrals are performed in detail for the quark case in 3.2.3, and results for the gluon case are presented in 3.2.4.

3.2.1 Collinear phase-space and matrix elements

Due to the recoil of the soft radiation, the jet axis is not aligned with the initial parton, requiring us to take the azimuthal dependence into account in

[7] Alternatively, one can use non-abelian exponentation, and note that the webs only differ by a factor C_F vs. C_A, implying $\ln S_g^{\rm NG} = (C_A/C_F)\ln S_q^{\rm NG} = \ln(S_q^{\rm NG})^2$, in the large N_C approximation. We thank D. Neill for discussions on this.

the phase-space integration of the collinear-matrix elements,

$$\int \mathrm{d}\Phi_2 \sigma^c_{2,q} = \frac{\alpha_s}{2\pi^2}\frac{(e^{\gamma_E}\mu^2)^\epsilon}{\Gamma(1-\epsilon)}\int_0^{2\pi}\mathrm{d}\phi\int_0^1 \mathrm{d}x\,\hat{P}_{qq}(x)\int\frac{\mathrm{d}q_\perp}{q_\perp^{1+2\epsilon}},$$
$$\int \mathrm{d}\Phi_2 \sigma^c_{2,g} = \frac{\alpha_s}{2\pi^2}\frac{(e^{\gamma_E}\mu^2)^\epsilon}{\Gamma(1-\epsilon)}\int_0^{2\pi}\mathrm{d}\phi\int_0^1 \mathrm{d}x\,\left[n_f\hat{P}_{qg}(x)+\frac{1}{2}\hat{P}_{gg}(x)\right]\int\frac{\mathrm{d}q_\perp}{q_\perp^{1+2\epsilon}}\,. \tag{3.30}$$

Here $\mathrm{d}\Phi_2$ denotes the two-body collinear phase-space integration and $\sigma^c_{2,q}$ is the collinear matrix element squared. The two partons have transverse momentum $q_\perp$ with respect to the initial parton and carry a fraction z and $1-z$ of its longitudinal momentum, whose distribution is described by the splitting functions[8]

$$\begin{aligned}
\hat{P}_{qq}(x) &= C_F\Big[\frac{1+x^2}{1-x}-\epsilon(1-x)\Big],\\
\hat{P}_{qg}(x) &= T_F\Big[1-2x(1-x)-2\epsilon\,x(1-x)\Big],\\
\hat{P}_{gg}(x) &= 2C_A\Big[\frac{x}{1-x}+\frac{1-x}{x}+x(1-x)\Big].
\end{aligned} \tag{3.31}$$

We will make frequent use of the angles of the partons with respect to the initial parton,

$$\beta_1 = \frac{q_\perp}{xp_T}\,,\qquad \beta_2 = \frac{q_\perp}{(1-x)p_T} \tag{3.32}$$

where p_T is the transverse momentum of the jet.

3.2.2 Geometry of the measurement

We now describe the geometry of the setup, starting with the case where the initial parton is inside the central subjet. Projecting the jet onto a plane perpendicular to the jet axis, as shown in the left panel of fig. 3.3, we can treat the polar angles as distances since $r \ll 1$. The central subjet corresponds to a circle of radius r, and the recoil due to the total transverse momentum $k_\perp$ of soft radiation in the jet corresponds to a displacement of the initial collinear parton by a distance $\theta = k_\perp/p_T$. The angles β_i also correspond to distances, though the azimuthal angle ϕ remains a true angle.

The condition for each of the partons produced by the splitting to be inside the central subjet is $\beta_i \le \beta_1^{\max}$, displayed in the right panel of fig. 3.3. Some

[8] We introduce a hat to avoid potential confusion with the splitting functions given in eq. (A.6).

Figure 3.3 Projection of the central subjet of radius r onto a plane perpendicular to the jet axis. θ is the displacement due to recoil and is here assumed to be less than r. In the left panel a splitting is shown. In the right panel $\beta_i^{\max}$ is shown, which is the upper bound on β_i such that the corresponding parton lies inside the central subjet.

trigonometry yields

$$\beta_{1,2}^{\max} = r\sqrt{1+\frac{\theta^2}{r^2}-2\frac{\theta}{r}\left(\pm\cos\phi\sqrt{1-\frac{\theta^2}{r^2}\sin^2\phi}+\frac{\theta}{r}\sin^2\phi\right)}, \tag{3.33}$$

The case $\theta > r$, where the initial parton is outside of the jet, requires the setup depicted in fig. 3.4. Here only one parton produced in the splitting can be inside the central subjet, and there is a minimum and maximum value for β_i. For parton 2,

$$\beta_2^{\min,\max} = \theta\left[\cos\phi \mp \sqrt{\frac{r^2}{\theta^2}-\sin^2\phi}\right], \tag{3.34}$$

and the expressions for $\beta_1^{\min,\max}$ can be obtained by substituting $\phi \to \phi + \pi$. These expressions are not valid for all ϕ, breaking down when the square root becomes imaginary. The maximum ϕ is shown in the right panel of fig. 3.4, and leads to the following boundaries

$$\begin{aligned} &\text{parton 1:} && \pi - \phi_{\max} < \phi < \pi + \phi_{\max}\,, && \phi_{\max} = \arcsin\left(\frac{r}{\theta}\right) \\ &\text{parton 2:} && -\phi_{\max} < \phi < \phi_{\max}\,. \end{aligned} \tag{3.35}$$

3.2.3 Integrals for the quark collinear function

We now present the calculation of the collinear function for an initiating quark, separating the two cases:

$$C_q^{(1)}(z_r, p_T r, k_\perp, \mu, \nu) = \Theta(k_\perp < p_T r)\, C_q^{(\theta<r)} + \Theta(k_\perp > p_T r)\, C_q^{(\theta>r)}. \tag{3.36}$$

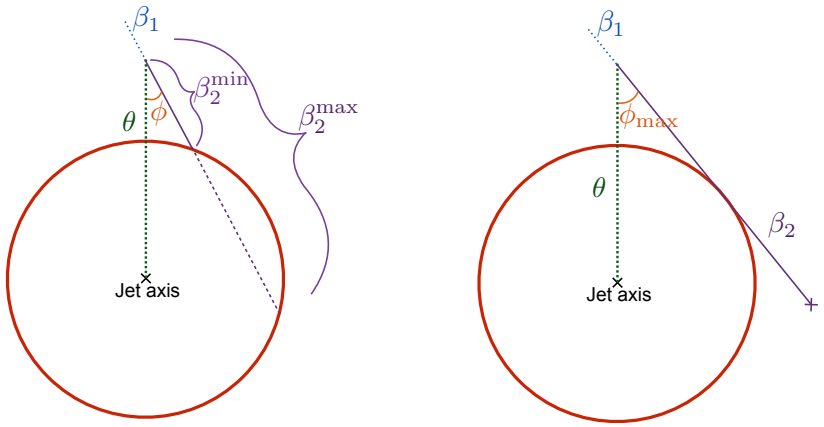

Figure 3.4 Geometry of the central subjet when the recoil θ is larger than the radius r. In the left panel the minimum and maximum values of β_2 are shown such that this parton is inside the central subjet. The right panel depicts the maximum value of ϕ.

In the first case

$$
\begin{aligned}
C_q^{(\theta<r)} &= (\mathrm{A})_{\theta<r} + (\mathrm{B})_{\theta<r} + (\mathrm{C})_{\theta<r}\,, \\
(\mathrm{A})_{\theta<r} &= \delta(1-z_r) \int \mathrm{d}\Phi_2\, \sigma^c_{2,q}\, \Theta(\beta_1 < \beta_1^{\max})\Theta(\beta_2 < \beta_2^{\max})\,, \\
(\mathrm{B})_{\theta<r} &= \int \mathrm{d}\Phi_2\, \sigma^c_{2,q}\, \delta(x-z_r)\, \Theta(\beta_1 < \beta_1^{\max})\Theta(\beta_2 > \beta_2^{\max})\,, \\
(\mathrm{C})_{\theta<r} &= \int \mathrm{d}\Phi_2\, \sigma^c_{2,q}\, \delta(1-x-z_r)\, \Theta(\beta_1 > \beta_1^{max})\Theta(\beta_2 < \beta_2^{max}),
\end{aligned}
\tag{3.37}
$$

where (A) refers to the case when both partons end up inside the subjet, (B) when only parton 1 (quark) ends up inside and (C) when only parton 2 (gluon) does (using the same labels as in ref. [56]). In the second case only one parton can be inside the subjet, and

$$
\begin{aligned}
C_q^{(\theta>r)} &= (\mathrm{B})_{\theta>r} + (\mathrm{C})_{\theta>r}\,, \\
(\mathrm{B})_{\theta>r} &= \int \mathrm{d}\Phi_2\, \sigma^c_{2,q}\, \delta(x-z_r)\, \Theta(\pi - \phi_{\max} < \phi < \pi + \phi_{\max})\, \Theta(\beta_1^{\min} < \beta_1 < \beta_1^{\max})\,, \\
(\mathrm{C})_{\theta>r} &= \int \mathrm{d}\Phi_2\, \sigma^c_{2,q}\, \delta(1-x-z_r)\, \Theta(-\phi_{\max} < \phi < \phi_{\max})\, \Theta(\beta_2^{\min} < \beta_2 < \beta_2^{\max})\,.
\end{aligned}
\tag{3.38}
$$

The contribution where neither parton is inside is irrelevant, since then $z_r = 0$.

We now set out to calculate these integrals. For $(\mathrm{A})_{\theta<r}$ we use eq. (3.32) to rewrite the x integral and Θ functions

$$\begin{aligned}\int_0^1 \mathrm{d}x\,\Theta(\beta_1<\beta_1^{\max})\Theta(\beta_2<\beta_2^{\max}) &= \int_0^1 \mathrm{d}x\,\Theta(q_\perp<xp_T\beta_1^{\max})\,\Theta(q_\perp<(1-x)p_T\beta_2^{\max})\\ &= \int_0^{\widetilde{\beta}} \mathrm{d}x\,\Theta(q_\perp<xp_T\beta_1^{\max})\\ &\quad+\int_{\widetilde{\beta}}^1 \mathrm{d}x\,\Theta(q_\perp<(1-x)p_T\beta_2^{\max}),\end{aligned}\tag{3.39}$$

where $\widetilde{\beta}$ with $0<\widetilde{\beta}<1$ is given by

$$\widetilde{\beta}=\frac{\beta_2^{\max}}{\beta_1^{\max}+\beta_2^{\max}}\,.\tag{3.40}$$

Inserting this in eq. (3.37), and performing the x and $q_\perp$ integrals, we obtain

$$\begin{aligned}(\mathrm{A})_{\theta<r} = \frac{\alpha_s C_F}{2\pi^2}\,\delta(1-z_r)\int_0^{2\pi}\mathrm{d}\phi\Big\{&\frac{1}{2\epsilon^2}+\frac{1}{\epsilon}\Big(\frac{L_2}{2}+\frac{3}{4}\Big)+\frac{L_2^2}{4}+\frac{3L_2}{4}-\ln^2(1-\widetilde{\beta})\\ &+2\ln\widetilde{\beta}\ln(1-\widetilde{\beta})-\frac{3}{2}\ln(1-\widetilde{\beta})+2\mathrm{Li}_2\big(1-\widetilde{\beta}\big)-\frac{\widetilde{\beta}}{2}+2-\frac{3\pi^2}{8}\Big\},\end{aligned}\tag{3.41}$$

in terms of L_i defined as

$$L_i=\ln\left(\frac{\mu^2}{p_T^2(\beta_i^{\max})^2}\right).\tag{3.42}$$

We cannot perform the integral over ϕ analytically, as it involves the rather complicated expression in eq. (3.33). However, this is not a problem as we have already isolated the divergences.

The calculation of $(\mathrm{B})_{\theta<r}$ involves rapidity divergences, which we regulate using the η regulator, resulting in

$$\begin{aligned}(\mathrm{B})_{\theta<r} &= \frac{\alpha_s C_F}{2\pi^2}\,\frac{e^{\epsilon\gamma_E}}{\Gamma(1-\epsilon)}\,\mu^{2\epsilon}\int_0^{2\pi}\mathrm{d}\phi\int_{\widetilde{\beta}}^1\mathrm{d}x\,\delta(x-z_r)\Big[\frac{1+x^2}{1-x}-\epsilon(1-x)\Big]\\ &\quad\times\Big[\frac{\nu}{2(1-x)p_T}\Big]^\eta\int_{(1-x)p_T\beta_2^{\max}}^{xp_T\beta_1^{\max}}\frac{\mathrm{d}q_\perp}{q_\perp^{1+2\epsilon}}\\ &= \frac{\alpha_s C_F}{2\pi^2}\int_0^{2\pi}\mathrm{d}\phi\,\Big\{\delta(1-z_r)\Big[\frac{1}{\eta}\Big(\frac{1}{\epsilon}+L_1\Big)-\frac{1}{2\epsilon^2}+\frac{1}{\epsilon}\Big(L_\nu-\frac{L_2}{2}\Big)+L_\nu L_1\\ &\quad-\frac{L_2^2}{4}+\frac{\pi^2}{24}\Big]+\Theta\big(z_r>\widetilde{\beta}\big)\Big[-(1+z_r^2)\Big(\frac{\ln(1-z_r)}{1-z_r}\Big)_+\end{aligned}$$

$$- \ln\left(\frac{\widetilde{\beta}}{1-\widetilde{\beta}}\right)\frac{1+z_r^2}{(1-z_r)_+} + \frac{(1+z_r^2)\ln z_r}{1-z_r}\Bigg]\Bigg\}. \tag{3.43}$$

where L_ν is defined as

$$L_\nu = \ln\frac{\nu}{2p_T}\,. \tag{3.44}$$

Performing a similar calculation for $(\mathrm{C})_{\theta<r}$ we obtain

$$(\mathrm{C})_{\theta<r} = \frac{\alpha_s}{2\pi^2}\int_0^{2\pi}\mathrm{d}\phi\,\Theta\big(z_r > 1-\widetilde{\beta}\big)\Bigg\{P_{gq}(z_r)\Bigg[\ln\bigg(\frac{z_r}{1-z_r}\bigg) + \ln\bigg(\frac{\widetilde{\beta}}{1-\widetilde{\beta}}\bigg)\Bigg]\Bigg\}. \tag{3.45}$$

Note that the factor C_F is inside the P_{gq} splitting function, which was defined in eq. (A.6).

Moving on to the case $\theta > r$, we also have to regulate rapidity divegences for $(B)_{\theta>r}$,

$$\begin{aligned}(\mathrm{B})_{\theta>r} &= \frac{\alpha_s C_F}{2\pi^2}\,\frac{e^{\epsilon\gamma_E}}{\Gamma(1-\epsilon)}\,\mu^{2\epsilon}\int_{\pi-\phi_{\max}}^{\pi+\phi_{\max}}\mathrm{d}\phi\int_0^1\mathrm{d}x\,\delta(x-z_r)\Big[\frac{1+x^2}{1-x} - \epsilon(1-x)\Big] \\ &\quad\times\bigg(\frac{\nu}{2(1-x)p_T}\bigg)^{\eta}\int_{xp_T\beta_1^{\min}}^{xp_T\beta_1^{\max}}\frac{\mathrm{d}q_\perp}{q_\perp^{1+2\epsilon}} \\ &= \frac{\alpha_s C_F}{2\pi^2}\left[\delta(1-z_r)\Big(\frac{2}{\eta}+2L_\nu\Big) - \frac{1+z_r^2}{(1-z_r)_+}\right]\int_{-\phi_{\max}}^{\phi_{\max}}\mathrm{d}\phi\ln\bigg(\frac{\beta_2^{\min}}{\beta_2^{\max}}\bigg)\end{aligned} \tag{3.46}$$

Note that we changed the ϕ integration region, which is why the final expression involves $\beta_2^{\min,\ \max}$ rather than $\beta_1^{\min,\ \max}$. An analogous computation for $(\mathrm{C})_{\theta>r}$ yields

$$(\mathrm{C})_{\theta>r} = -\frac{\alpha_s}{2\pi^2}\,P_{gq}(z_r)\int_{-\phi_{\max}}^{\phi_{\max}}\mathrm{d}\phi\ln\bigg(\frac{\beta_2^{\min}}{\beta_2^{\max}}\bigg). \tag{3.47}$$

Adding up all the contributions,

$$\begin{aligned}C_q^{(\theta<r)} = \frac{\alpha_s C_F}{2\pi^2}\int_0^{2\pi}\mathrm{d}\phi\Bigg\{&\delta(1-z_r)\Bigg[\frac{1}{\eta}\Big(\frac{1}{\epsilon}+L_1\Big) + \frac{1}{\epsilon}\Big(L_\nu+\frac{3}{4}\Big) + L_\nu L_1 + \frac{3L_1}{4} \\ &- \ln^2(1-\widetilde{\beta}) + 2\ln\widetilde{\beta}\ln(1-\widetilde{\beta}) - \frac{3}{2}\ln\widetilde{\beta} + 2\mathrm{Li}_2(1-\widetilde{\beta}) - \frac{\widetilde{\beta}}{2} - \frac{\pi^2}{3} + 2\Bigg] \\ &+ \Theta(z_r>\widetilde{\beta})\Bigg[-(1+z_r^2)\bigg(\frac{\ln(1-z_r)}{1-z_r}\bigg)_+ + \ln\bigg(\frac{z_r(1-\widetilde{\beta})}{\widetilde{\beta}}\bigg)\frac{1+z_r^2}{(1-z_r)_+}\Bigg]\end{aligned}$$

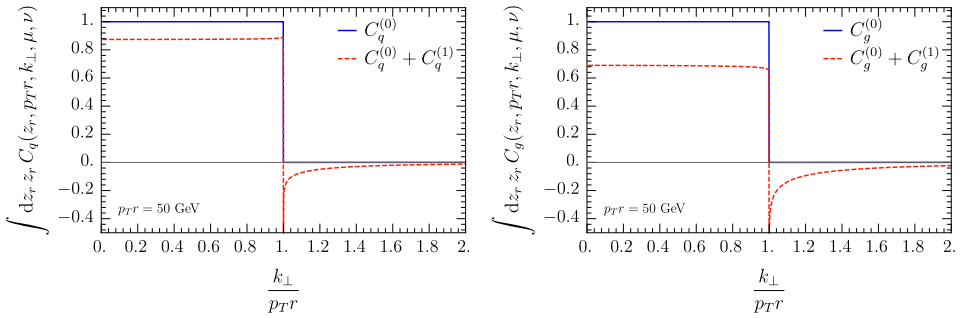

Figure 3.5 The linear z_r moment of the collinear function for quark jets (left) and gluon jets (right) at tree level (blue) and including one-loop corrections (red dashed), evaluated at the scales $\mu = p_T r$ and $\nu = p_T$.

$$+ \Theta(z_r > 1 - \widetilde{\beta}) \left[\frac{1 + (1 - z_r)^2}{z_r} \ln\left(\frac{z_r \widetilde{\beta}}{(1 - z_r)(1 - \widetilde{\beta})} \right) \right] \Bigg\},$$

$$C_q^{(\theta > r)} = \frac{\alpha_s C_F}{2\pi^2} \left[\delta(1 - z_r) \left(\frac{2}{\eta} + 2L_\nu \right) - \frac{1 + z_r^2}{(1 - z_r)_+} - \frac{1 + (1 - z_r)^2}{z_r} \right] \int_{-\phi_{\max}}^{\phi_{\max}} \mathrm{d}\phi \ln\left(\frac{\beta_2^{\min}}{\beta_2^{\max}} \right), \tag{3.48}$$

For the jet shape we only need the second Mellin moment of z_r ($\int \mathrm{d}z_r\, z_r$) of the collinear function, which we plot for quark jets in the left panel of fig. 3.5. The result depends on $k_\perp/(p_T r)$, shown on the horizontal axis, and on $p_T r$, through the scale in α_s. First we note that the one-loop corrections are of order 10%, as is typical. At tree level there is a single collinear particle that is simply inside the jet if the recoil due to soft radiation is not too large, $k_\perp < p_T r$. One-loop corrections allow for nonzero values of the collinear function for larger values of $k_\perp$. That the collinear function attains a negative value is not a concern, since it does not correspond to a physical quantity (indeed, this depends on our choice of μ and ν-scales). We also note that the divergence at $k_\perp = p_T r$ from one-loop corrections is integrable.

3.2.4 Gluon collinear function

The calculation of the collinear function for gluons follows very similar steps. Splitting the calculation into the $\theta < r$ and $\theta > r$ contribution, we obtain

$$C_g^{(\theta < r)} = \frac{\alpha_s}{2\pi^2} \int_0^{2\pi} \mathrm{d}\phi \Bigg(\delta(1 - z_r) \Bigg\{ C_A \left[\frac{1}{\eta} \left(\frac{1}{\epsilon} + \frac{L_1}{4} + \frac{L_2}{4} \right) + \frac{1}{\epsilon} \left(L_\nu + \frac{11}{12} \right) \right.$$

$$
\begin{aligned}
&+\Big(\frac{L_\nu}{2}+\frac{11}{24}\Big)(L_1+L_2)-\frac{1}{2}\ln^2\frac{1-\widetilde{\beta}}{\widetilde{\beta}}-\frac{11}{12}\ln\big(\widetilde{\beta}(1-\widetilde{\beta})\big)+\frac{1}{6}\widetilde{\beta}(1-\widetilde{\beta})\\
&-\frac{\pi^2}{6}+\frac{67}{36}\Big]+n_f T_F\Big[-\frac{1}{3\epsilon}-\frac{1}{6}(L_1+L_2)+\frac{1}{3}\ln\big(\widetilde{\beta}(1-\widetilde{\beta})\big)\\
&-\frac{1}{3}\widetilde{\beta}(1-\widetilde{\beta})-\frac{5}{9}\Big]\Big\}+\Theta(z_r>\widetilde{\beta})\Big\{-C_A\frac{(1-z_r+z_r^2)^2}{z_r}\bigg(\frac{\ln(1-z_r)}{1-z_r}\bigg)_+\\
&+C_A\frac{(1-z_r+z_r^2)^2}{z_r(1-z_r)_+}\ln\bigg(\frac{z_r(1-\widetilde{\beta})}{\widetilde{\beta}}\bigg)+n_f T_F(z_r^2+(1-z_r)^2)\\
&\times\ln\bigg(\frac{z_r(1-\widetilde{\beta})}{(1-z_r)\widetilde{\beta}}\bigg)\Big\}\Big)\,,\\
C_g^{(\theta>r)}=&\frac{\alpha_s}{2\pi^2}\Big\{2C_A\Big[\delta(1-z_r)\Big(\frac{1}{\eta}+L_\nu\Big)-\frac{(1-z_r+z_r^2)^2}{z_r(1-z_r)_+}\Big]\\
&-2n_f T_F(z_r^2+(1-z_r)^2)\Big\}\int_{-\phi_{\max}}^{\phi_{\max}}\mathrm{d}\phi\ln\bigg(\frac{\beta_2^{\min}}{\beta_2^{\max}}\bigg)\,.
\end{aligned}
\tag{3.49}
$$

The second Mellin moment of the gluon collinear function is shown in the right panel of fig. 3.5. Its features are similar to that for quark jets (left panel), except that the one-loop corrections are larger due to the larger color factor (C_A vs. C_F).

3.3 Implementation and first results

This section describes how we implement our formulae to obtain numerical predictions. In sec. 3.3.1 our central scale choice is discussed. We then describe how we match our formulae for $r \ll R$ and $r \lesssim R$ in sec. 3.3.2. The scale variations used to assess the perturbative uncertainty are given in sec. 3.3.3. We conclude in sec. 3.3.4 with some first, purely perturbative, results for the jet shape for quark and gluons jets.

3.3.1 Central scale choice

We start by discussing the scales for the regime $r \lesssim R$, described by the factorization in eq. (3.2). We take

$$
\mu_{\mathcal{H}} = p_T\,, \qquad \mu_{\mathcal{G}} = p_T R\,, \tag{3.50}
$$

as our central scale choice. In the regime $r \ll R$, $\mathcal{G}$ is refactorized in terms of hard, collinear and soft functions, see eq. (3.8). We will take as their central

scales

$$\mu_{\mathcal{H}} = p_T\,, \qquad \mu_H = p_T R\,, \qquad \mu_C = p_T r\,, \qquad \mu_S = p_T r\,,$$
$$\nu_C = p_T\,, \qquad \nu_S = \frac{1}{b_\perp R}\,. \tag{3.51}$$

We deviate from eq. (3.9) by expressing ν_S in terms of $b_\perp$, which is the Fourier conjugate variable of $k_\perp$ (not p_T). Since collinear and soft modes contribute to $k_\perp$, one expects that parametrically $p_T r \sim k_\perp \sim 1/b_\perp$. However, expressing ν_S in terms of $b_\perp$ avoids a well-known problem with choosing scales in momentum space for transverse momentum resummation [98] (see also refs. [99, 100]). Often one also chooses μ_C and μ_S in term of $b_\perp$, but this is not required here. In particular, our choice in eq. (3.51) ensures that the μ-evolution from μ_H down to $\mu_C = \mu_S$ is essentially the same as in the jet shape calculation in ref. [86].

3.3.2 Matching predictions for $r \ll R$ and $r \lesssim R$

A common approach to matching different regimes in SCET is to use profile scales [101, 102], that would smoothly interpolate between eqs. (3.50) and (3.51). Unfortunately, it is challenging to simultaneously obtain good predictions for the integrated and differential jet shape in this way. By choosing scales for $\psi(r)$, i.e. for the cross section integrated up to r in terms of the upper bound of this integration, one automatically ensures that $\psi(R) = 1$, since the scales in eq. (3.50) will be used when $r = R$. However, the corresponding differential jet shape $\rho(r)$ tends to have artifacts, since the scales depend on r and their derivatives enter through the chain rule. Conversely, choosing scales directly for $\rho(r)$, i.e. for the cross section differential in r, avoids these artifacts. However, the resulting jet shape is generically no longer normalized, i.e. integrating $\rho(r)$ no longer gives $\psi(R) = 1$, because the scales in the integrand are not equal to eq. (3.50) but depend on the integration variable r. A solution to this problem has been proposed in ref. [103], but is not easy to implement.

Rather than using profile scales to interpolate between $r \ll R$ and $r \lesssim R$, we will directly interpolate between them:

$$\psi(r) = \Big[1 - g\Big(\frac{r}{R}\Big)\Big]\,\psi_{r\ll R}(r) + g\Big(\frac{r}{R}\Big)\,\psi_{r\lesssim R}(r)\,, \tag{3.52}$$

which was inspired by ref. [104]. Here $\psi_{r\ll R}$ and $\psi_{r\lesssim R}$ correspond to eqs. (3.17) and (3.16), respectively. The function $g(r)$ is zero for $r \ll R$ and one for r close to R, smoothly interpolating between the two cases. We implement this

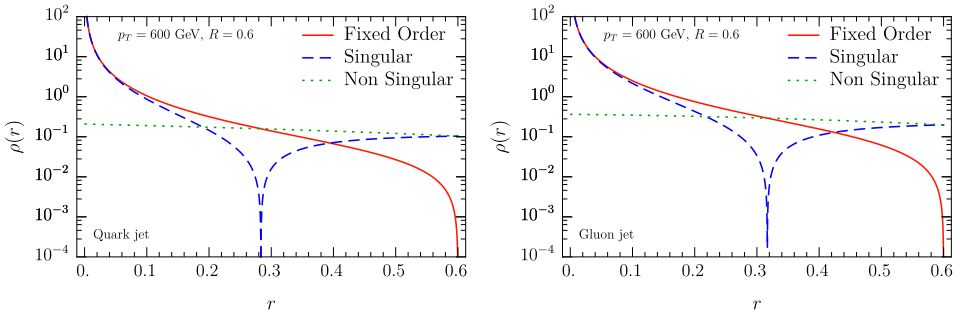

Figure 3.6 The differential jet shape at order α_s for quark jets (left) and gluon jets (right) at $p_T = 600$ GeV and $R = 0.6$. Shown are $\rho_{r \lesssim R}$ (red solid), decomposed in its singular $\rho_{r \ll R}$ (blue dashed) and nonsingular (green dotted) contribution that correspond to the power corrections in eq. (3.17).

using the following double-quadratic function

$$g(x) = \begin{cases} 0 & x \le x_1 \\ \frac{(x-x_1)^2}{(x_2-x_1)(x_3-x_1)} & x_1 \le x \le x_2 \\ 1 - \frac{(x-x_3)^2}{(x_3-x_1)(x_3-x_2)} & x_2 \le x \le x_3 \\ 1 & x_3 \le x \ . \end{cases} \tag{3.53}$$

An advantage of this method over the use of profile scales is that we can determine $\psi_{r \ll R}$ and $\psi_{r \lesssim R}$ once and for all before creating the interpolation. In addition, it makes it possible to match LL resummation of r/R to the NLO result in the region where $r \sim R$. (Normally this breaks down because the single logarithmic term $\alpha_s \ln(r/R)$ in the NLO result is not resummed at LL accuracy.)

To determine the transition points x_i in eq. (3.53), we assess the numerical size of the corrections to the factorization of $\psi_{r \ll R}$ at $\mathcal{O}(\alpha_s)$, shown in fig. 3.6. The solid red curve shows the differential jet shape, the blue dashed curve shows its singular contribution obtained from the factorization in eq. (3.17), and the green dotted curve is the difference (often called the nonsingular), all at $\mathcal{O}(\alpha_s)$. It is essential that the resummation of logarithms of r/R is turned off before we enter the region where the singular is no longer a good approximation to the full jet shape, leading us to choose

$$x_1 = 0.15\,, \qquad x_2 = (x_1 + x_3)/2\,, \qquad x_3 = 0.38. \tag{3.54}$$

Specifically, x_1 corresponds roughly to the point where the nonsingular is 10% of the cross section, and x_3 is chosen close to the point where the singular and nonsingular are equal in size. These points are somewhat arbitrarily chosen, and will be varied as part of the uncertainty estimate.

3.3.3 Scale variations and perturbative uncertainties

For our uncertainty estimate, we take the envelope of the following variations

1. Vary all scales in eq. (3.51) simultaneously up and down by a factor of 2.
2. Vary $\mu_{\mathcal{H}}$ and μ_H simultaneously up and down by a factor of 2.
3. Vary μ_C and μ_S simultaneously up and down by a factor of 2.
4. Vary ν_C up and down by a factor of 2.
5. Vary ν_S up and down by a factor of 2.
6. Vary the transition point x_3 between 0.33 to 0.48.

We can interpret the first as a fixed-order uncertainty, since it only changes the overall scales and not the ratios between them, which are the logarithms that are being resummed. The second and third variation probe the μ resummation, since they vary the hierarchy between μ_H and $\mu_C = \mu_S$, and similarly the fourth and fifth probe the rapidity resummation. While the evolution kernels are very similar for the variations in 2 and 3, the scales of different fixed-order ingredients are probed: The change in the evolution kernel is (partially) cancelled by a corresponding change in H for variation 2 and by $C \otimes S$ for variation 3, so they are not redundant. The same is true for variations 4 and 5. Variation 6 probes the uncertainty from our interpolation between the resummation and fixed-order region. We also explored the dependence on the transition point x_1, but it has a small effect and thus would not impact the total uncertainty.

3.3.4 First results for quark and gluon jets

In fig. 3.7 we show the integrated jet shape for quark and gluon jets with transverse momentum 60 and 500 GeV, comparing LL, NLL and NLL′, all matched to NLO. We start by noting that our resummed calculations converge, i.e. the bands overlap and are smaller at NLL′ than at LL. As these plots show, the uncertainty bands are larger at small p_T and for gluon jets, which is not surprising since the perturbative corrections are simply larger in these cases due to the size of α_s and the color factor (C_A vs. C_F), respectively. At LL the bands are quite large, and they remain sizable at NLL′, even though this exceeds the accuracy of previous jet shape calculations. We believe that this is due to our more conservative uncertainty estimate, described in sec. 3.3.3. Indeed, for gluon jets with $p_T = 60$ GeV, the NLL′ central curve lies only

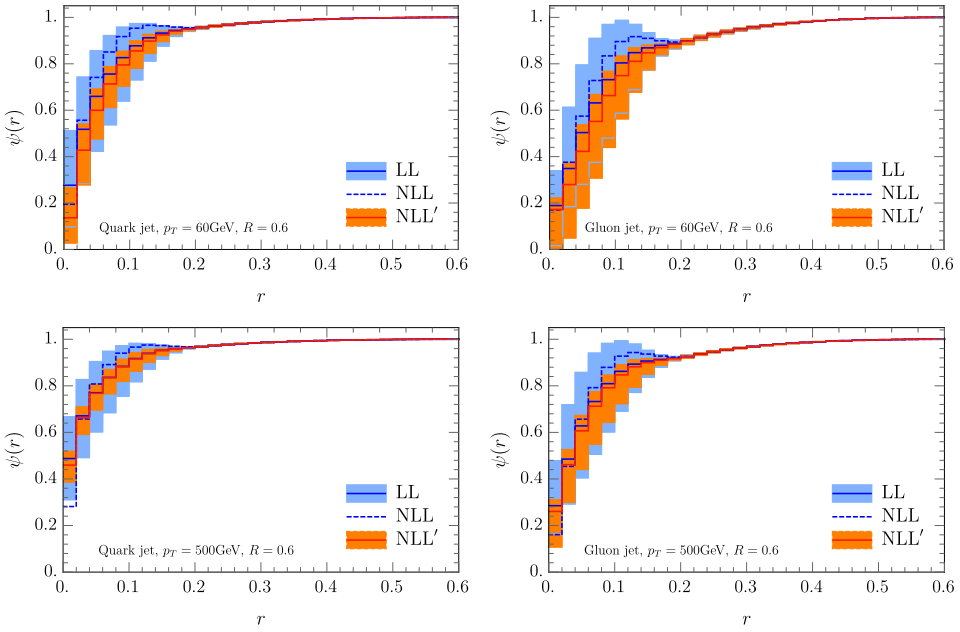

Figure 3.7 The integrated jet shape for quark jets (left) and gluon jets (right) for $p_T = 60$ GeV (top) and 500 GeV (bottom) and $R = 0.6$. Shown are LL (blue solid curve and band), NLL (blue dashed curve) and NLL′ (orange solid curve and band), all matched to NLO. The bands indicate the perturbative uncertainties estimated using the procedure in sec. 3.3.3.

just inside the LL uncertainty, warranting these large bands. For large r all predictions overlap, since in each case we match to NLO. In this region there are no large logarithms of r/R, so it is not surprising that the uncertainties are small. It is hard to gauge whether their size is reasonable, since we only have one perturbative order in this region (at LO $\psi(r)$ is simply 1). Lastly we note that the NLL curve is not monotonic. That this unphysical behavior arises at NLL but not LL is due to the non-cusp anomalous dimension, whose contribution becomes equal and opposite in size to that of the cusp anomalous dimension. At NLL′ this is remedied by the inclusion of one-loop corrections to the ingredients in the factorization formula.

Fig. 3.8 illustrates the effect of the rapidity resummation and non-global logarithms on the jet shape for quark and gluon jets, by showing the integrated and differential jet shape with and without them. Both effects enter for the first time at NLL and were not taken into account in previous calculations. They are clearly important for $r \ll R$, where their size is about half that of the NLL′ uncertainty band in fig. 3.7, but are of course irrelevant in the

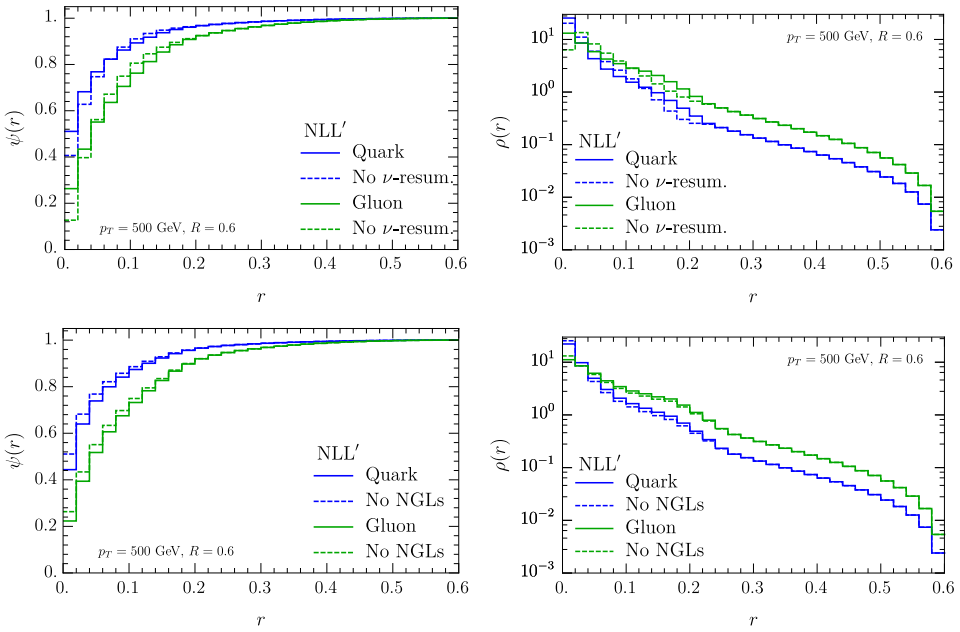

Figure 3.8 The integrated (left) and differential (right) jet shape for quark jets (blue) and gluon jets (green) at NLL′ with $p_T = 500$ GeV and $R = 0.6$. The top row shows the result with (solid) and without (dashed) rapidity resummation. The bottom row shows the result with (solid) and without (dashed) non-global logarithms.

region where the resummation of logarithms of r/R is turned off. The effect of the rapidity resummation is still significant in the transition region and is only turned off by the matching to fixed order, whereas the effect of NGLs is already small before the transition. The NGLs push the energy distribution in the jet out to larger values of r, in agreement with the trend observed in e.g. ref. [105] for the jet mass distribution. This is clear from the integrated jet shape, and in the differential jet shape this arises through a decrease in the first bin (not as visible due to the logarithmic scale) and an increase in subsequent bins.

3.4 Nonperturbative effects

At the LHC, nonperturbative corrections to the jet shape can be large, particularly for smaller values of the jet p_T. These arise from the underlying event and hadronization effects. In this section we will explore simple models to ac-

count for these effects in our predictions. We will use PYTHIA 8.2 [87] to assess how reasonable these models are, by applying them to parton level predictions and comparing the result to hadron level predictions, including multi-parton interactions and initial-state radiation[9]. When we later apply this model to our predictions, we will use LHC data to fit the model parameter.

In the first model, we treat these effects by simply adding a uniform energy density to the jets. Explicitly

$$\text{Model 1:} \quad \rho(r) \to \frac{2f}{1+f}\frac{r}{R^2} + \frac{1}{1+f}\rho(r)\,, \tag{3.55}$$

where $\rho(r)$ is the differential jet shape and the fraction f describes the size of the nonperturbative radiation compared to the perturbative contribution from our calculation. The dependence on r/R is linear because it scales with the circumference of the circle of radius r.

In the second model, the nonperturbative effects are again treated by adding energy. However, rather than considering a uniform distribution, we will assume this additional energy is completely localized, thus displacing the jet axis. The location (r', ϕ') of this extra energy is then (uniformly) integrated over the jet. In terms of the differential jet shape $\rho(r)$ this amounts to

Model 2:

$$\begin{aligned}
\rho(r) \to & \frac{1}{\pi(1+f)^2R^2}\int_0^{(1+f)R} \mathrm{d}r'\, r' \int_0^{2\pi} \mathrm{d}\phi' \Bigg\{ \frac{f}{1+f}\,\delta\Big(r - \frac{r'}{1+f}\Big) \\
& + \frac{1}{1+f}\int_0^R \mathrm{d}r''\,\rho'(r'')\,\delta\Bigg[r - \bigg((r'')^2 + \frac{2r'r''f}{1+f}\cos\phi + \frac{(r')^2f^2}{(1+f)^2}\bigg)^{1/2}\Bigg]\Bigg\} \\
& = \frac{2f}{1+f}\,\frac{r}{R^2} + \frac{4r}{\pi f^2(1+f)R^2}\int_{\max\{0,r-fR\}}^{\min\{R,r+fR\}} \mathrm{d}r''\,\rho(r'') \\
& \quad \int_{|r_*-r_*''|}^{\min\{1,r_*+r_*''\}} \mathrm{d}r_*'\, \frac{r_*'}{\sqrt{2(r_*^2+(r_*')^2)(r_*'')^2 - (r_*^2-(r_*')^2)^2 - (r_*'')^4}}\,,
\end{aligned} \tag{3.56}$$

The first term in the curly brackets (on the first line) corresponds to the contribution to the jet shape from the extra energy. Upon integration this results in the first term on the third line, in agreement with eq. (3.55). However, the jet shape also gets smeared by the displacement of the jet axis. Specifically, the r'' integral in the second term integrates over the jet shape, taking into account the displacement from the extra energy at (r', ϕ') through the delta

[9] This is not a nonperturbative contribution. However, we include it, because in our approach initial-state radiation is formally $\mathcal{O}(R^2)$ suppressed.

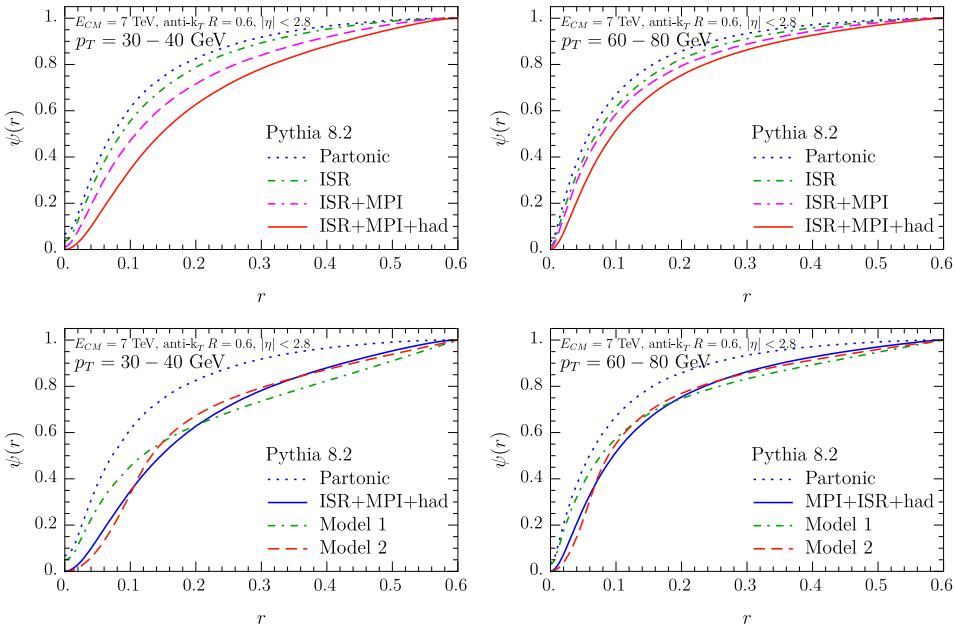

Figure 3.9 Jet shape in PYTHIA at $E_{\rm cm} = 7$ TeV for anti-k_T jets with radius $R = 0.6$, rapidity $|\eta| < 2.8$ and transverse momentum $p_T = 30 - 40$ GeV (left) and $p_T = 60 - 80$ GeV (right). The top row shows results at parton level (blue dotted), including initial-state radiation (green dot-dashed), also multi-parton interactions (magenta dashed), and also hadronization (blue solid). The bottom row repeats the blue dotted and solid curves, where the effect of ISR, MPI and hadronization are either modeled using eq. (3.55) (green dot-dashed) or eq. (3.56) (orange dashed), and the parameter f is fitted.

function. In the final expression we eliminated the ϕ' integral using the delta function, and introduced

$$r_* = \frac{r}{fR}\,, \qquad r'_* = \frac{r'}{(1+f)R}\,, \qquad r''_* = \frac{r''}{fR} \tag{3.57}$$

to remove any explicit dependence on f and R in the r' integral. Thus we can determine this integral numerically once and for all, to obtain the kernel against which we integrate the jet shape in the remaining r'' integral.

In fig. 3.9 we show the partonic and hadronic jet shape obtained from PYTHIA, and investigate to what extent multiparton interactions, initial-state radiation and hadronization effects can be described by one of the models above. The top row shows the contribution of each of these effects, the bottom row shows a fit (of the coefficient f) to these effects using one of the models

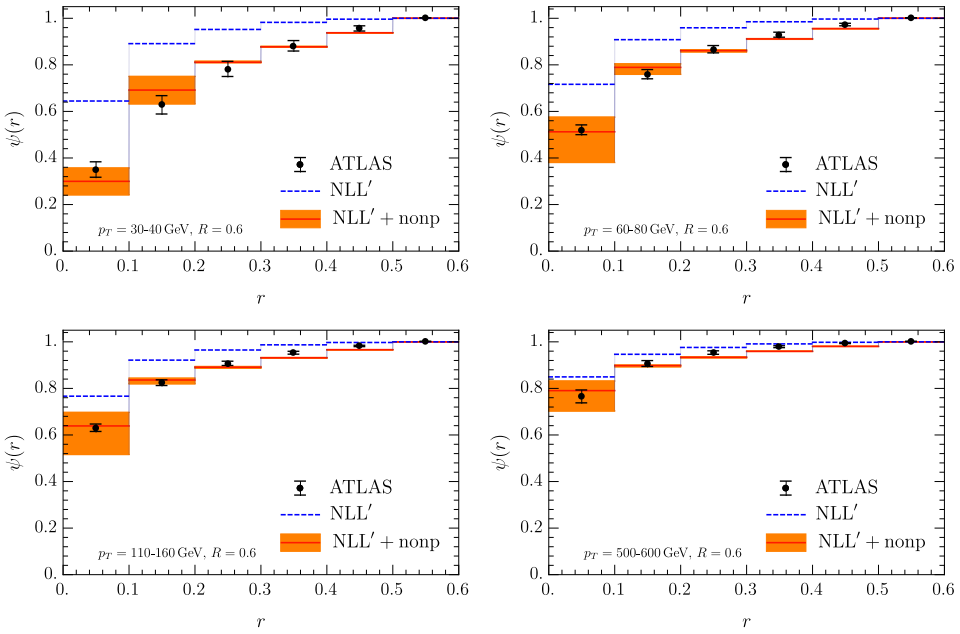

Figure 3.10 Comparison of our theoretical calculation at NLL′ accuracy for the inclusive jet shape $\psi(r)$ to the data from ATLAS [67]. The inclusive anti-k$_T$ jet sample is reconstructed for a jet radius of $R = 0.6$ and $|\eta| < 2.8$ measured at $E_{\text{cm}} = 7$ TeV. Four representative jet p_T intervals in the range $30 - 600$ GeV are shown, as indicated in the panels. Our purely perturbative calculation is shown (dashed blue), along with the results that include the nonperturbative effects through a model (orange) and perturbative uncertainty band.

proposed here. We find better agreement using model 2, suggesting that these nonperturbative effects are at least fairly localized in the jet. We therefore use model 2 when we compare our results to LHC data in the next section.

3.5 Results for the LHC

In this section, we present comparisons of our theoretical results to data from ATLAS and CMS. We start with the ATLAS data for the integrated and differential jet shape of ref. [67]. Although the central values of the differential and integrated jet shape are directly related, their uncertainties are not because of correlations, which is why we show results for both. The inclusive jet sample $pp \to \text{jet} + X$ was obtained using the anti-k$_T$ algorithm with $R = 0.6$. The jet rapidity was restricted to $|\eta| < 2.8$, and different intervals for its transverse

momentum p_T in the range of $30 - 600$ GeV were considered. In fig. 3.10, we show a comparison of our numerical results to the ATLAS data for the integrated jet shape $\psi(r)$ for four representative p_T intervals, as indicated in the different panels. For all phenomenological results presented in this section, we use the CT14 NLO PDF set of ref. [106]. We show both the purely perturbative calculation (dashed blue curve) as well as the results after including the nonperturbative "model 2" (orange curve and band), described in section 4.5.2. The QCD scale uncertainty is shown only for the final result including the nonperturbative contribution, following the procedure discussed in section 3.3.3. The parameter f of the nonperturbative model is determined from fitting our central curve to the central value of the data. Its value is tabulated in table 3.3 for each p_T interval. At smaller values of the jet transverse momentum, the purely perturbative result and the data disagree significantly, where the perturbative calculation predicts that there is more radiation close to the center of the jet and less near the jet boundary. Nevertheless, we find that the data is well described after including a nonperturbative correction. As is clear from the plots and the table, at higher values of p_T the nonperturbative correction becomes smaller. Indeed, for the highest transverse momentum interval $500 - 600$ GeV we already find a good agreement between the data and our purely perturbative calculation obtained from the QCD factorization theorem. Because the nonperturbative model parametrizes the effect of nonperturbative physics relative to the perturbative prediction for the jet, rather than through some absolute energy scale, it is not surprising that approximately $f \sim 1/p_T$.

In fig. 3.11, we show our numerical results for the differential jet shape $\rho(r)$ in comparison to the corresponding ATLAS data for the same jet kinematics. We use the same f values for the nonperturbative model as for the integrated jet shape. Again we observe that a large nonperturbative correction is needed

ATLAS [67]	p_T [GeV]	30-40	60-80	110-160	500-600
$E_{\text{cm}} = 7$ TeV	f	0.23	0.16	0.11	0.062
CMS [68]	p_T [GeV]	30-40	500-600	600-1000	
$E_{\text{cm}} = 7$ TeV	f	0.28	0.068	0.054	
CMS [71]	p_T [GeV]	> 100			
$E_{\text{cm}} = 2.76$ TeV	f	0.050			

Table 3.3 Fitted values for the parameter f of the nonperturbative "model 2", for the jet transverse momentum intervals of the ATLAS [67] and CMS [68, 71] data that we show here. Note that the jet radius R and the rapidity intervals η differ between the different data sets.

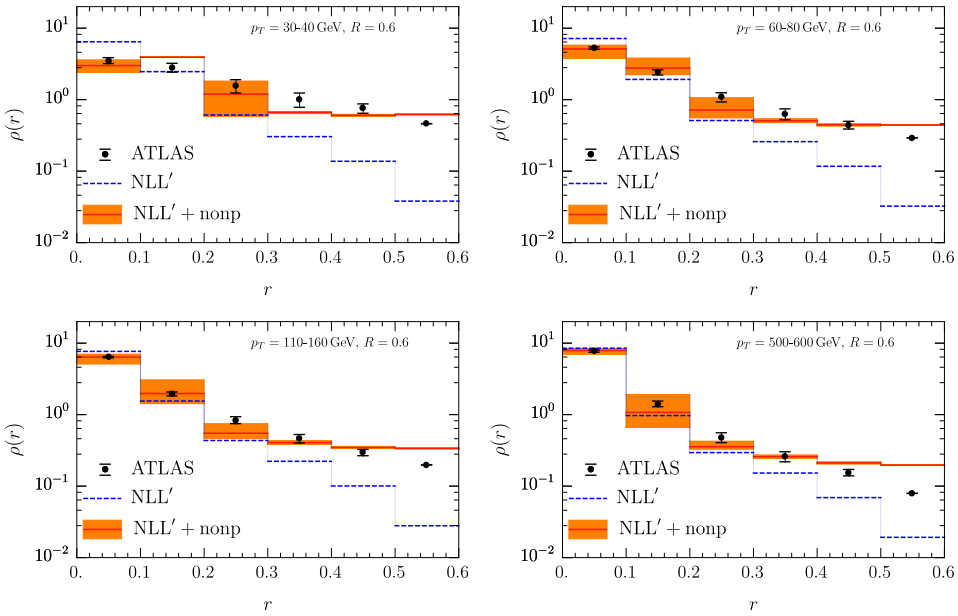

Figure 3.11 Comparison of our numerical results for the differential jet shape $\rho(r)$ and the ATLAS data of [67], for the same kinematics as in fig. 3.10.

to describe the differential jet shape data for jets with low transverse momentum. This is particularly pronounced close to the jet boundary, where no resummation of r/R is required, and the fixed-order expressions in eq. (3.16) clearly undershoot the data. (This was not so visible for the integrated jet shape, since everything is close to one.) For the higher transverse momentum bins, the agreement between the data and the purely perturbative results is improved and only a smaller nonperturbative correction is needed. However, close to the jet boundary, the effect of the nonperturbative correction remains substantial, even for the highest p_T interval. We note that for $p_T = 30 - 40$ GeV, the nonperturbative model causes the second bin to be higher than the first. This feature is already visible in fig. 3.9, both for our model 2 and the curve for Pythia at hadron level, since the integrated jet shape is not the steepest at $r = 0$.

Next, we consider the CMS data set of ref. [68] for the differential jet shape $\rho(r)$, which was also measured at a center-of-mass energy of $E_{\text{cm}} = 7$ TeV. The kinematics of the reconstructed inclusive jet sample is similar to the setup from ATLAS, but now using anti-k$_T$ with $R = 0.7$, $|\eta| < 0.5$ and dividing the jet transverse momentum p_T into several intervals in the range of $30 - 1000$ GeV. In fig. 3.12 we show the comparison of our numerical results with and

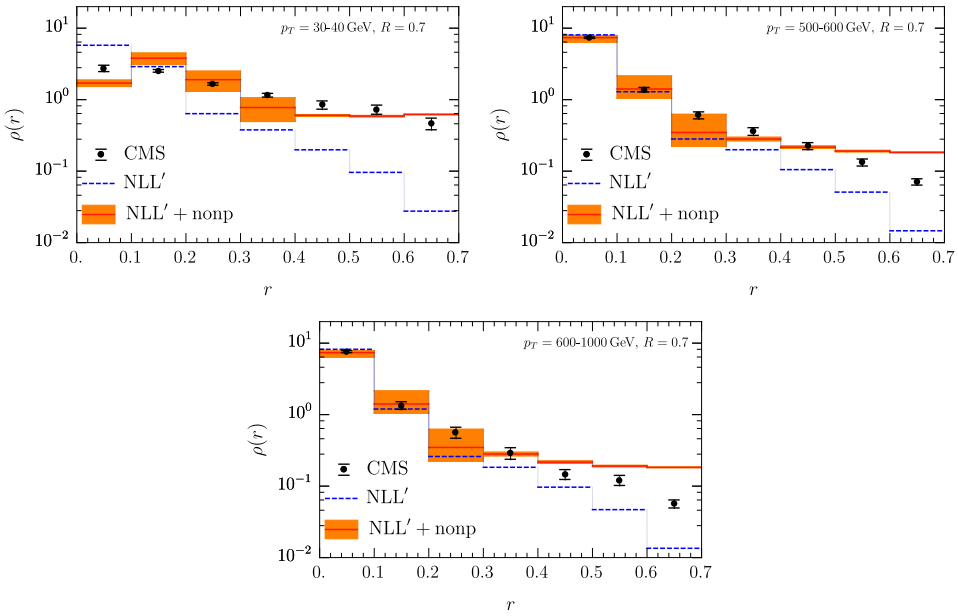

Figure 3.12 Comparison of our numerical results for the differential jet shape $\rho(r)$ to the CMS data of ref. [68]. The jets are obtained using anti-k$_T$ with $R = 0.7$ and, $|\eta| < 0.5$ at $E_{\rm cm} = 7$ TeV. We show the result for three intervals of the jet transverse momentum in the range of $p_T = 30 - 1000$ GeV, as labeled in the different panels.

without the nonperturbative contribution. We again fit the nonperturbative parameter f of "model 2", listing their values in table 3.3. These values are consistent with those obtained for ATLAS, in the cases for which we have a corresponding p_T interval. (They do not need to be exactly the same, given the difference in jet radius and rapidity interval.) We note again that even for the highest jet transverse momentum interval $p_T = 600 - 1000$ GeV a significant nonperturbative correction is needed in order to describe the energy distribution close to the edge of the jet, $r \lesssim R$, as we also observed for the ATLAS data.

Finally, we compare to the differential jet shape measurement of CMS in ref. [71]. This data set was taken at $\sqrt{s} = 2.76$ TeV as a baseline measurement for a heavy-ion analysis. The jets were reconstructed with $p_T > 100$ GeV and $0.3 < |\eta| < 2$ using the anti-k$_T$ algorithm with $R = 0.3$. Analogous to the two data sets discussed above, the jet shape data is separated into six bins with a distance in r of 0.05. An additional cut of $p_{Ti} > 1$ GeV was imposed on the transverse momentum of each particle in the jet, and only charged particles

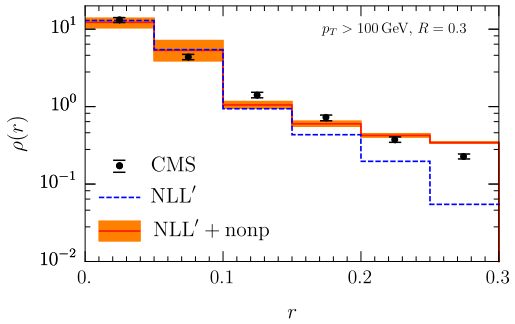

Figure 3.13 Comparison of the differential jet shape $\rho(r)$ and the CMS data of ref. [71]. The jets are obtained using anti-k$_T$ with $R = 0.3$, $p_T > 100$ GeV, $0.3 < |\eta| < 2$ at $E_{\mathrm{cm}} = 2.76$ TeV.

are used to determine the jet shape even though full jets are reconstructed. Furthermore, the jet p_T was smeared to account for the difference of the jet energy resolution between proton-proton and heavy-ion collisions. This should be kept in mind when comparing to our calculation, since we do not include these effects. Nevertheless, we find good agreement as shown in fig. 3.13. The edge of the jet is still dominated by nonperturbative physics for $R = 0.3$. However, the data is closer to the purely perturbative result compared to the jet shape for a similar p_T interval in fig. 3.11 for $R = 0.6$ jets. Indeed, the fitted value of the nonperturbative parameter f, see table 3.3, is about half of that for the p_T interval 110-160 GeV in the ATLAS data. This is not surprising, given the lower center-of-mass energy and the smaller jet radius. In general, we conclude that our numerical results agree well with the data, once the nonperturbative correction is taken into account.

3.6 Conclusions

In this chapter we calculated the jet shape at next-to-leading logarithmic accuracy (NLL′). Specifically, we accounted for the single logarithms of the jet radius R and the double logarithms of r/R at next-to-leading logarithmic order, and match to next-to-leading order. To achieve this accuracy, the recoil of soft radiation on the jet axis must be included when $r \ll R$. This involves the one-loop calculation of a recoil-sensitive collinear function and rapidity logarithms, that we resum using the rapidity renormalization group, as well as non-global logarithms from in vs. out-of-jet soft radiation. Our calculation constitutes the first extension of this classic jet substructure observable beyond leading logarithmic accuracy.

The inclusion of higher-order corrections significantly reduces the uncertainty of the perturbative predictions. However, we also find that the effect of nonperturbative contributions are substantial at the LHC, in particular for low jet transverse momenta and close to the edge of the jet. To enable a comparison to the available data from ATLAS and CMS, we explored two one-parameter models, choosing the model that best captures these effects in Pythia. Including this, we find good agreement between our predictions and LHC data. One interesting future direction is to obtain predictions that can be compared to LEP and HERA data, where these nonperturbative effects should be substantially smaller. On the other hand, for the LHC it is natural to consider grooming, to reduce the contamination from these effects, which we hope to investigate in the future.

4

Calculating the angle between jet axes

In this chapter we study three different jet axes, with varying degrees of sensitivity to soft radiation, which we now introduce: We start from an inclusive sample of jets, obtained by using the anti-k$_T$ algorithm [10] with jet radius parameter $R = 0.8$, and refer to the resulting jet axis as the standard (ST) jet axis. Only jets with rapidity $|\eta| < 2$ are considered, and results for several bins in the jet transverse momentum p_T will be reported. Applying soft drop [23] with $z_{\rm cut} = 0.1$ and several values for β to remove soft radiation, the axis of the resulting groomed jet will be called the groomed (GR) jet axis. Finally, we recluster the original jet using the winner-take-all (WTA) recombination scheme [55, 107], for which the effect of soft radiation is power suppressed, yielding the WTA axis. To ensure that all radiation is inside the jet (i.e. that the jet algorithm returns a single jet) the jet radius is increased. These various axes are pictured in fig. 4.1, where the offset between the ST (black) and GR (green) axis is due to groomed away radiation (gray). The WTA axis (blue) clearly tracks the energetic collinear (blue) radiation.

We will consider the distance $\theta = \sqrt{\Delta\eta^2 + \Delta\phi^2}$ in pseudorapidity η and azimuthal angle ϕ between these axes, denoted with $\theta_{\rm ST,GR}$, $\theta_{\rm ST,WTA}$ and $\theta_{\rm GR,WTA}$, respectively. This distance is boost invariant and for a jet at zero rapidity, i.e. perpendicular to the beam axis, θ is equal to the angle between these axes (in the small angle limit, which we focus on). We therefore refer to this as an angle. These angles characterize the different sensitivity to soft radiation of these axes. In our calculations it will be convenient to express θ as a vector $\vec{k}_\perp$ transverse to the *jet* axis, with $\theta = |\vec{k}_\perp|/p_T$, since vectors can easily be added. To simplify the notation, we will omit the vector symbol when referring to the norm of a vector, i.e. $k_\perp \equiv |\vec{k}_\perp|$.

Given this identification between angles and transverse momenta, it should

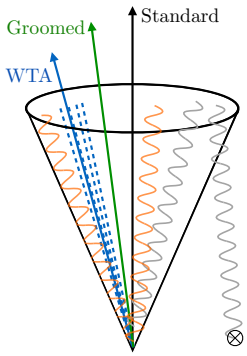

Figure 4.1 The various jet axes: The standard jet axis (black) is along the total momentum of the collinear (blue) and soft (orange) radiation. For the groomed jet axis (green) groomed away soft radiation (gray) is not included. The winner-take-all axis (blue) is insensitive to soft radiation.

come as no surprise that all three angles between the jet axes considered here involve some form of transverse momentum resummation [77–81,108]. As such, it provides another window into the physics of transverse momentum dependent fragmentation functions and parton distribution functions, focusing on the bulk distribution of transverse momentum within jets relative to energetic collections of particles within the jet, not the energy spectrum of the underlying individual particles, similar to refs. [1, 109–115].

We derive the factorization in the small-θ limit within Soft Collinear Effective Theory (SCET) [12–16] and carry out the resummation at next-to-leading logarithmic (NLL or NLL′[1]) accuracy, including the contribution of non-global logarithms [83] in the leading-color approximation. In order to derive the factorization structure for the angle between the standard and groomed jet axis $\theta_{\mathrm{ST,GR}}$, we need to simultaneously consider the soft drop groomed jet radius R_g [23, 122]. We perform the joint resummation of logarithms of the transverse momentum and the soft drop groomed jet radius R_g, and afterwards integrate over R_g. While for the other observables we achieve NLL′ with the resummation of the non-global logs, the factorization for the angle $\theta_{\mathrm{ST,GR}}$ is considerably more complicated, limiting our accuracy to NLL in the global

[1]For NLL′, we simply mean the inclusion of the full matrix element of each function truncated at $O(\alpha_s)$ convolved with resummation kernel, including NGLs in the kernel when their exact structure is known. In ref. [116], a distinct definition of NLL′ was adopted, where one includes all matrix elements at the order where the logarithms generating the resummation first appear. For NGLs, this requires an $O(\alpha_s^2)$ contribution (see ref. [117]), which is beyond our definition of NLL′. For further developments in the theory for NGLs, see refs. [91, 93, 96, 118–121]

logarithms.

There are several potential applications of the observables introduced in this work: First of all, by comparing parton shower event generators to our perturbative calculations and to data from the LHC, models of nonperturbative physics can be constrained, similar to e.g. refs. [53, 123] where jet substructure results were used to constrain the hadronization and underlying event contribution. This is particularly true for the angle between the standard and groomed jet axis, which is very sensitive to nonperturbative physics as it measures the soft radiation which *fails* the soft drop criterion. Interestingly, for the observables considered here the (leading) nonperturbative component is relatively well understood as it is related to the nonperturbative part of the rapidity anomalous dimension in transverse momentum resummation. Indeed, various extractions are available in the literature [124–127], and it was recently proposed that this evolution kernel can also be extracted from lattice QCD [128]. Explicitly, our analysis predicts how the grooming parameters affect the nonperturbative part of the rapidity anomalous dimension on our observables, which can be compared to hadronization models in Monte Carlo parton showers. Moreover, we expect that the observables considered here will have important applications in heavy-ion collisions where jets are used as probes of the created hot and dense QCD medium [129]. For example, the measurement of the angle between the groomed and WTA axis provides a handle on the soft radiation contained in identified jets in the large background produced in heavy-ion collisions. Since the different jet axes considered in this work exhibit a very different sensitivity to soft physics, these observables are ideally suited to quantitatively explore the effects of parton energy loss and jet broadening.

The remainder of this chapter is organized as follows. In sec. 4.1, we introduce the different factorization and resummation formulae in physical terms, which are necessary for the calculation of the angles between the three jet axes. We present all relevant expressions and technical details for the three cases in sec. 4.2 to sec. 4.4. In sec. 4.5, we discuss different aspects of the implementation in impact parameter space and describe our nonperturbative model (which we take from transverse momentum resummation). Numerical results for LHC kinematics are presented in sec. 4.6, and in sec. 4.7 we draw conclusions and present an outlook.

4.1 Factorization and resummation of angles between axes

In this section we describe in physical terms the structure of the cross sections that encode the angles between the different jet axes described in the Introduction. The necessary factorization and resummation techniques are introduced but technical details and expressions of the various functions that appear in these factorization formulae are relegated to subsequent sections.

4.1.1 Jet production

Just like for the jet shape, the first step - common to the calculation of all these angles - is to factorize the hard scattering from the jet production by working in the narrow jet approximation, $R \ll 1$. In several examples it has been observed that the $\mathcal{O}(R^2)$ power corrections to this limit are still small for values of R up to 0.7 [75, 89]. The cross section differential in jet transverse momentum p_T, (pseudo)rapidity η, and $\vec{k}_\perp$ (describing the angle between axes) is given by

$$\frac{\mathrm{d}\sigma}{\mathrm{d}\eta\,\mathrm{d}p_T\,\mathrm{d}^2\vec{k}_\perp} = \sum_{i,j,k} \int \frac{\mathrm{d}x_i}{x_i} f_i(x_i,\mu) \int \frac{\mathrm{d}x_j}{x_j} f_j(x_j,\mu) \int \frac{\mathrm{d}z}{z} \mathcal{H}_{ij}^k(x_i,x_j,\eta,p_T/z,\mu) \times \mathcal{G}_k(z,k_\perp,p_T R,\mu)\big[1+\mathcal{O}(R^2)\big]\,. \tag{4.1}$$

These factorization is the same as (3.2), except we have a different jet function which is sensitive to the angle between axes. In the rest of this chapter we focus on the jet, and therefore denote the parton that initiates it with i, rather than k. We note that eq. (4.1) is simply a more differential version of the factorization for inclusive jet production [50, 73, 74], since integrating our jet function over $\vec{k}_\perp$ yields the semi-inclusive jet function J_i of ref. [50]

$$\int \mathrm{d}^2\vec{k}_\perp\, \mathcal{G}_i(z,k_\perp,p_T R,\mu) = J_i(z,p_T R,\mu)\,. \tag{4.2}$$

We will exploit this sum rule to factor out the jet production from the jet measurement [1, 73], writing:

$$\mathcal{G}_i(z,k_\perp,p_T R,\mu) \equiv \sum_j J_{ij}(z,p_T R,\mu)\tilde{\mathcal{G}}_j\big(k_\perp,p_T R,\alpha_s(\mu)\big). \tag{4.3}$$

Just like in our discussion in the previous chapter, the coefficient J_{ij} is akin to a jet flavor-tagged fragmentation function: it describes how a parton of flavor i fragments into a jet of radius R of flavor j. Note that this is not a

factorization of physics at different scales, and requires keeping track of the jet flavor j. As indicated, the new jet function $\tilde{\mathcal{G}}$ only depends on μ through the strong coupling. These functions satisfy

$$\int \mathrm{d}^2\vec{k}_\perp \, \tilde{\mathcal{G}}_j\big(k_\perp, p_T R, \alpha_s(\mu)\big) = 1, \qquad \sum_j J_{ij}(z, p_T R, \mu) = J_i(z, p_T R, \mu)\,, \tag{4.4}$$

which are sufficient to determine J_{ij} and $\tilde{\mathcal{G}}_j$ from the full expressions for $\mathcal{G}_i$ and J_i. To the order we calculate, we further introduce

$$\tilde{\mathcal{G}}_i\big(k_\perp, p_T R, \alpha_s(\mu)\big) = \frac{1}{\pi}\,\delta(k_\perp^2) + \delta(1-z)\Delta\mathcal{G}_i(k_\perp, p_T R, \mu)\,, \tag{4.5}$$

reporting only on the (simpler) $\Delta\mathcal{G}_i$. This equation defines the function $\Delta\mathcal{G}_i$. Note that we do not need any flavor indicies on the $\delta(k_\perp^2)$ term.

The natural scales of the ingredients in (4.1) are the same as for inclusive jet production

$$\mu_f \sim \Lambda_{\mathrm{QCD}}\,, \qquad \mu_{\mathcal{H}} \sim p_T\,, \qquad \mu_{\mathcal{G}} \sim p_T R\,, \tag{4.6}$$

and the resummation of logarithms of $R = \mu_{\mathcal{G}}/\mu_{\mathcal{H}}$ is achieved by using the DGLAP [130–132] equation to evolve the jet function $\mathcal{G}$ from the jet scale $\mu_{\mathcal{G}}$ to the hard scale $\mu_{\mathcal{H}}$, as we saw in the previous chapter. The splitting functions P_{ji} are at one-loop order given in eq. (A.6).

If $k_\perp \sim p_T R$, there are no additional logarithms to resum as $\mathcal{G}$ involves a single scale. In this case one simply has to calculate $\Delta\mathcal{G}$ for the angle between each pair of axes. However, these distributions are in fact dominated by $k_\perp \ll p_T R$, in which case $\mathcal{G}$ contains two hierarchical scales and needs to be factorized. We will outline this below for each of the angles, relegating much of the details to subsequent sections. To keep the discussion concise, we have focused on the mode structure contributing to each factorization formula we present, which dictates its form. For an introduction to factorization within the SCET formalism, we refer the reader to refs. [22, 47]. For specific examples in the literature on the technical derivation of the factorized cross section for jet observables from the underlying modes of the effective theory, see e.g. refs. [81, 133–137].

4.1.2 Angle between the standard and WTA axis

We start with a leading logarithmic (LL) analysis of the angle between the standard and WTA axes using the Lund diagram [138] shown in the left panel of fig. 4.2. The horizontal axis corresponds to the angle θ and the vertical axis to the momentum fraction z of emissions in the jet. By using the indicated

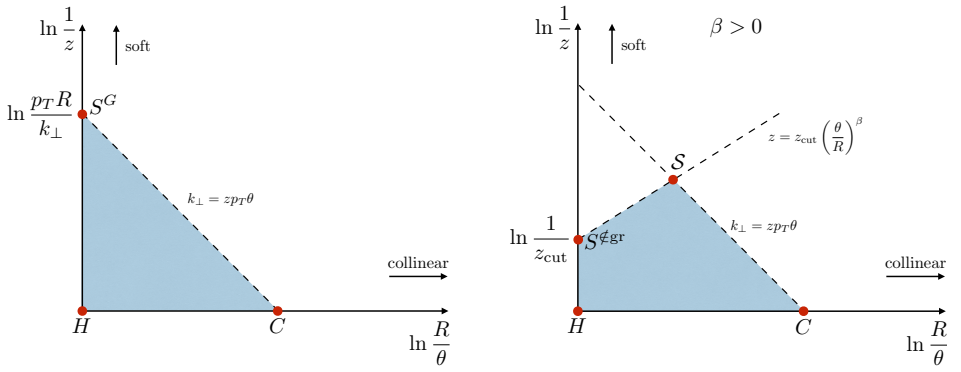

Figure 4.2 Lund diagrams for the angle between the standard and the WTA axis (left) and the groomed and the WTA axis (right). The modes that appear in the factorization for these two observables are indicated with red dots, whose parametric scaling can be read off from this diagram.

logarithmic coordinates, emissions have a uniform emission probability at LL accuracy, allowing one to directly determine the Sudakov factor from the area of the region where emissions are not allowed. In this LL picture the WTA axis is along the single hard parton in the jet, and the offset of the ST axis is due to the transverse momentum $k_\perp$ of the dominant emission. Thus cutting on the transverse momentum $k_\perp < k_\perp^c$ prohibits emissions in the red region. This leads to the following expression for the jet function $\tilde{\mathcal{G}}$ that describes the angle between the standard and WTA axes,

$$\tilde{\mathcal{G}}_i^{\text{ST, WTA}}\big(k_\perp, p_T R, \alpha_s(\mu)\big) \overset{\text{LL}}{=} \frac{1}{2\pi\, k_\perp} \frac{\mathrm{d}}{\mathrm{d}k_\perp} \exp\left[-\frac{\alpha_s C_i}{\pi} \ln^2\left(\frac{p_T R}{k_\perp}\right)\right]. \quad (4.7)$$

This is differential in $\vec{k}_\perp$, and the color factor $C_i = C_F$ (C_A) for $i = q$ ($i = g$).

Extending this analysis beyond LL using SCET, the corners of this region correspond to the degrees of freedom (or modes) in SCET, as encoded in the factorization of $\tilde{\mathcal{G}}$ in the limit $k_\perp \ll p_T R$:

$$\tilde{\mathcal{G}}_i^{\text{ST, WTA}}\big(k_\perp, p_T R, \alpha_s(\mu)\big) \overset{\text{NLL}'}{=} \tilde{H}_i(p_T R, \mu) \int \mathrm{d}^2\vec{k}'_\perp\, C_i(k'_\perp, \mu, \nu) \times \int \mathrm{d}^2\vec{k}''_\perp\, S_i^{\text{G}}(\vec{k}_\perp - \vec{k}'_\perp - \vec{k}''_\perp, \mu, \nu R) S_i^{\text{NG}}\Big(\frac{k''_\perp}{p_T R}\Big)\left[1 + \mathcal{O}\Big(\frac{k_\perp^2}{p_T^2 R^2}\Big)\right]. \quad (4.8)$$

The WTA axis is only sensitive to collinear radiation inside the jet, and the argument $k'_\perp$ of the collinear function C_i simply encodes the angle of the WTA

Mode:	Scaling $(\bar{n}\cdot p, n\cdot p, p_\perp)$
hard	$p_T(1, R^2, R)$
collinear	$(p_T, k_\perp^2/p_T, k_\perp)$
soft	$k_\perp/R(1, R^2, R)$

Table 4.1 For the angle between the ST and WTA axis, the modes that enter in the factorization of the jet function $\mathcal{G}$ are listed above.

axis with respect to the initial collinear parton. The ST axis is along the total jet momentum, so the collinear and soft radiation inside the jet must balance each other, $\vec{k}_{\perp,c} + \vec{k}_{\perp,s} = 0$ (see e.g. fig. 2 of ref. [1]). Consequently, the offset of the initial collinear parton with respect to the standard axis is given by $k_{\perp,s}$, which is the argument of the soft function, and $\vec{k}_\perp = \vec{k}'_\perp + \vec{k}_{\perp,s}$. Because only soft radiation inside the jet contributes to $k_{\perp,s}$, and radiation outside the jet is completely unconstrained, non-global logarithms [83] appear. The function S_i^{NG} encodes the leading non-global logarithms, which in the small R limit are the same as for the hemisphere soft function in e^+e^- [94]. This is the reason why eq. (4.8) is limited to NLL′ accuracy. The hard function $\tilde{H}_i$ in eq. (4.8) describes collinear radiation with energies p_T at angles of order R. Such emissions are not allowed inside the jet, since they would displace the WTA axis but not the ST axis, leading to $k_\perp \sim p_T R$. Following eq. (4.3), we have removed the contribution from jet production, i.e. this is the factorization for $\tilde{\mathcal{G}}$ not $\mathcal{G}$.

The power counting of the modes that underpin the factorization in eq. (4.8) are summarized in table 4.1, in terms of light-cone coordinates

$$p^\mu = \bar{n}\cdot p\,\frac{n^\mu}{2} + n\cdot p\,\frac{\bar{n}^\mu}{2} + p_\perp^\mu\,, \tag{4.9}$$

where $n^\mu = (1,0,0,1)$ is along the jet axis, $\bar{n}^\mu = (1,0,0,-1)$, and $p_\perp^\mu$ denotes the transverse components. The corresponding scales are[2]

$$\begin{aligned} &\mu_H = p_T R\,, && \mu_C = k_\perp\,, && \mu_S = k_\perp\,, \\ & && \nu_C = 2p_T\,, && \nu_S = 2k_\perp/R\,, \end{aligned} \tag{4.10}$$

where μ corresponds to invariant mass scales and ν to rapidity scales. By evaluating each of the ingredients at their natural scale and evolving them to

[2]In our numerical implementation we choose scales in terms of the impact parameter $b_\perp$, instead of its Fourier conjugate to $k_\perp$, to avoid a well-known problem in transverse momentum resummation [98]. See sec. 4.5 for details.

Mode:	Scaling $(\bar{n}\cdot p, n\cdot p, p_\perp)$
hard	$p_T(1, R^2, R)$
soft	$z_{\rm cut} p_T(1, R^2, R)$
collinear	$(p_T, k_\perp^2/p_T, k_\perp)$
collinear-soft	$(a = z_{\rm cut} k_\perp^\beta p_T^{1-\beta} R^{-\beta}, k_\perp^2/a, k_\perp)$

Table 4.2 For the angle between the GR and WTA axis, the modes that enter in the factorization of the jet function $\mathcal{G}$ when $k_\perp \ll z_{\rm cut} p_T R$ are listed above.

a common one using the RG equations

$$\begin{aligned}
\mu\frac{\mathrm{d}}{\mathrm{d}\mu}\,\tilde{H}_i(p_T R,\mu) &= \gamma_i^{\tilde{H}}(p_T R,\mu)\,\tilde{H}_i(p_T R,\mu)\,,\\
\mu\frac{\mathrm{d}}{\mathrm{d}\mu}\,C_i(k_\perp,\mu,\nu/p_T) &= \gamma_i^{C}(\mu,\nu/p_T)\,C_i(k_\perp,\mu,\nu/p_T)\,,\\
\mu\frac{\mathrm{d}}{\mathrm{d}\mu}\,S_i{}^{\rm G}(k_\perp,\mu,\nu R) &= \gamma_i^{S}(\mu,\nu R)\,S_i{}^{\rm G}(k_\perp,\mu,\nu R)\,,\\
\nu\frac{\mathrm{d}}{\mathrm{d}\nu}\,C_i(k_\perp,\mu,\nu/p_T) &= -\int\frac{\mathrm{d}^2\vec{k}'_\perp}{(2\pi)^2}\,\gamma_i^{\nu}(\vec{k}_\perp-\vec{k}'_\perp,\mu)\,C_i(k'_\perp,\mu,\nu/p_T)\,,\\
\nu\frac{\mathrm{d}}{\mathrm{d}\nu}\,S_i{}^{\rm G}(k_\perp,\mu,\nu R) &= \int\frac{\mathrm{d}^2\vec{k}'_\perp}{(2\pi)^2}\,\gamma_i^{\nu}(\vec{k}_\perp-\vec{k}'_\perp,\mu)\,S_i{}^{\rm G}(k'_\perp,\mu,\nu R)\,,
\end{aligned}\tag{4.11}$$

we resum the global logarithms of $k_\perp/(p_T R)$. The anomalous dimensions are collected in B.3.2.

4.1.3 Angle between the groomed and WTA axis

For the angle between the Soft Drop groomed and WTA axis, we will again start with a LL analysis, using the Lund planes shown in fig. 4.2. Soft drop removes wide-angle soft radiation in a jet, so the dominant emission that sets $k_\perp$ must now pass the soft-drop grooming condition, $z > z_{\rm cut}(\theta/R)^\beta$, shown in the right panel. This leads to

$$\begin{aligned}
\tilde{\mathcal{G}}_i^{\rm GR,\,WTA}\big(k_\perp, p_T R, z_{\rm cut}, \beta, \alpha_s(\mu)\big) \overset{\rm LL}{=} \frac{1}{2\pi\, k_\perp}\,\frac{\mathrm{d}}{\mathrm{d}k_\perp}\Bigg\{\exp\Bigg\{-\frac{\alpha_s C_i}{\pi}\Bigg[\ln^2\Big(\frac{p_T R}{k_\perp}\Big)\\
-\Theta(z_{\rm cut} p_T R - k_\perp)\frac{1}{1+\beta}\ln^2\Big(\frac{z_{\rm cut} p_T R}{k_\perp}\Big)\Bigg]\Bigg\}\Bigg\}\,.
\end{aligned}\tag{4.12}$$

Note that if $k_\perp > z_{\rm cut} p_T R$ the soft-drop grooming condition is always satisfied and the Lund diagram is in fact the same as for the ungroomed case, shown in the left panel of fig. 4.2.

Extending our analysis beyond LL accuracy, if $k_\perp \gg z_{\rm cut} p_T R$, the transverse momentum of the radiation that is removed by grooming is negligible compared to the measured $k_\perp$, and the formula for the cross section is the same as in eq. (4.8). We will therefore focus on the case $k_\perp \ll z_{\rm cut} p_T R$, and interpolate between these regimes in our numerical results[3]. The modes in SCET correspond to the red dots at the corners of the blue region in the Lund plane and are summarized in table 4.2. The factorization formula for $\tilde{\mathcal{G}}$ is given by

$$\begin{aligned}\tilde{\mathcal{G}}_i^{\text{ GR, WTA}}\big(k_\perp, p_T R, z_{\rm cut}, \beta, \alpha_s(\mu)\big) &\overset{\text{NLL}'}{=} \tilde{H}_i(p_T R, \mu)\, S_i^{\notin \text{ gr}}(z_{\rm cut} p_T R, \beta, \mu) \\ &\times \int \mathrm{d}^2 \vec{k}'_\perp C_i(k'_\perp, \mu, \nu/p_T) \mathcal{S}_i(\vec{k}_\perp - \vec{k}'_\perp, p_T R, z_{\rm cut}, \beta, \mu, \nu/p_T) \\ &\times S_i^{\rm NG}(z_{\rm cut}) \left[1 + \mathcal{O}\left(\frac{k_\perp^2}{z_{\rm cut}^2 p_T^2 R^2}, z_{\rm cut}, \left(\frac{z_{\rm cut} k_\perp^\beta}{(p_T R)^\beta}\right)^{1/(1+\beta)}\right)\right]. \end{aligned} \tag{4.13}$$

The hard and collinear radiation are unaffected by the grooming and the corresponding functions are thus the same as in eq. (4.8). The collinear-soft function $\mathcal{S}_i$ describes the contribution from collinear-soft radiation that *passes* the grooming condition to the angle between the jet axes. The soft function $S_i^{\notin \text{ gr}}$ encodes the wide-angle soft radiation, which is always groomed away, and therefore does not affect the shape of the $k_\perp$ distribution but only the total rate. In this case non-global logarithms arise because the hard mode and soft mode have the same angular scale, but the soft radiation inside the jet must be much less energetic in order to fail the grooming condition. Fortunately, the leading NGLs are again described by the same function as in eq. (4.8), but now with $z_{\rm cut}$ as argument.

By evaluating each function in eq. (4.13) at its natural scale

$$\begin{aligned} &\mu_H = p_T R\,, \quad \mu_{S^{\notin \text{ gr}}} = z_{\rm cut} p_T R\,, \quad \mu_C = k_\perp\,, \quad \mu_{\mathcal{S}} = k_\perp\,, \\ &\qquad\qquad\qquad\qquad\qquad\qquad \nu_C = 2p_T\,, \quad \nu_{\mathcal{S}} = 2p_T z_{\rm cut}^{\frac{1}{1+\beta}} \left(\frac{k_\perp}{p_T R}\right)^{\frac{\beta}{1+\beta}}\,, \end{aligned} \tag{4.14}$$

and evolving them to a common μ and ν scale, the global logarithms of $k_\perp/(p_T R)$ and $z_{\rm cut}$ are resummed. The renormalization group equations are

[3] One could also separately consider the regime $k_\perp \sim z_{\rm cut} p_T R$, constraining this interpolation.

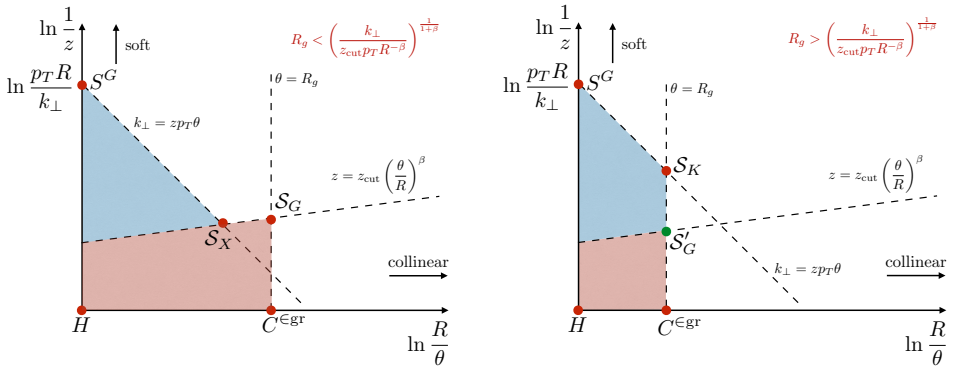

Figure 4.3 Lund diagrams for the angle between the standard and the groomed jet axis when $k_\perp \ll z_{\text{cut}} p_T R$, for regime A (left) and B (right). The relevant SCET modes are indicated by red and green dots, and their power counting can be read off, see table 4.3.

partially the same as in eq. (5.22), except for:

$$\begin{aligned}
\mu \frac{\mathrm{d}}{\mathrm{d}\mu} S_i^{\notin \text{ gr}}(z_{\text{cut}} p_T R, \beta, \mu) &= \gamma_i^{S^{\notin \text{ gr}}}(z_{\text{cut}} p_T R, \beta, \mu)\, S_i^{\notin \text{ gr}}(z_{\text{cut}} p_T R, \beta, \mu)\,, \\
\mu \frac{\mathrm{d}}{\mathrm{d}\mu} \mathcal{S}_i(k_\perp, p_T R, z_{\text{cut}}, \beta, \mu, \nu) &= \gamma_i^{\mathcal{S}}\Big(p_T R, z_{\text{cut}}, \beta, \mu, \nu)\, \mathcal{S}_i(k_\perp, p_T R, z_{\text{cut}}, \beta, \mu, \nu)\,, \\
\nu \frac{\mathrm{d}}{\mathrm{d}\nu} \mathcal{S}_i(k_\perp, p_T R, z_{\text{cut}}, \beta, \mu, \nu) &= \int \frac{\mathrm{d}^2 \vec{k}'_\perp}{(2\pi)^2}\, \gamma_i^\nu(\vec{k}_\perp - \vec{k}'_\perp, \mu)\, \mathcal{S}_i(k'_\perp, p_T R, z_{\text{cut}}, \beta, \mu, \nu)\,.
\end{aligned} \tag{4.15}$$

4.1.4 Angle between the standard and groomed axis

The factorization structure for the angle between the standard and groomed jet axis is rather different. Since collinear radiation is never groomed away, this observable is highly sensitive to soft radiation, similar to collinear drop [139]. The effect of grooming is power suppressed when $k_\perp \gg z_{\text{cut}} p_T R$, so the cross section is power suppressed in this region. We therefore focus on the opposite limit $k_\perp \ll z_{\text{cut}} p_T R$, smoothly matching the cross section to 0 when crossing $k_\perp \sim z_{\text{cut}} p_T R$. It turns out that we must consider the cross section differential in $k_\perp$ and the groomed jet radius R_g, since there are two different cases that need to be considered, and then integrate the combined resummed result over R_g. It is convenient to work in terms of $\theta_g \equiv R_g/R$.

The Lund planes for the LL analysis are shown in fig. 4.3 and will now

Mode:	Regime A	Regime B
hard	$p_T(1, R^2, R)$	
soft	$k_\perp/R(1, R^2, R)$	
collinear	$p_T(1, R_g^2, R_g)$	
collinear-soft$_G$	$z_{\rm cut}\theta_g^\beta p_T(1, R_g^2, R_g)$	
collinear-soft$_X$	$(b, k_\perp^2/b, k_\perp)$	
collinear-soft$_K$		$k_\perp/R_g(1, R_g^2, R_g)$

Table 4.3 The modes that enter in the factorization of $\mathcal{G}$ for the angle between the standard and groomed jet axis, when $k_\perp \ll z_{\rm cut} p_T R$. Regime A (B) correspond to R_g smaller (larger) than $[k_\perp R^\beta/(z_{\rm cut} p_T)]^{1/(1+\beta)}$. We use the shorthand notation $b = (z_{\rm cut} p_T)^{1/(1+\beta)} (k_\perp/R)^{\beta/(1+\beta)}$.

be discussed. We start by considering the measurement of the groomed jet radius. The cross section with a cut $\theta_g < \theta_g^c$ prohibits emissions in the red region with $z > z_{\rm cut}(\theta/R)^\beta$ and $\theta/R > \theta_g^c$ [23]. Ref. [122] extends this analysis to NLL using SCET, exploiting that for the cumulative distribution in θ_g^c one can separately impose $\theta/R < \theta_g^c$ on the collinear and collinear-soft radiation (analogous to the factorization of the measurement in jet veto resummation). If in addition one requires $k_\perp < k_\perp^c$, emissions with $z < z_{\rm cut}(\theta/R)^\beta$ and $\theta/R > \theta_g$ (*not* θ_g^c) are groomed away by soft drop and thus forbidden for $k_\perp = z\theta p_T > k_\perp^c$, corresponding to the blue regions in fig. 4.3. There are now two cases depending on whether θ_g is smaller or larger than $[k_\perp^c/(z_{\rm cut} p_T R)]^{1/(1+\beta)}$, which we will refer to as regime A and B.[4] The Lund diagrams for these regimes are displayed in the left and right panel of fig. 4.3, and the power counting of the momenta corresponding to the modes is summarized in table 4.3.

The situation is the simplest for regime A, since the blue region is insensitive to the precise value of θ_g, i.e. the resummation of θ_g and $k_\perp$ are independent of each other. At LL accuracy, we simply calculate the sum of the area of the red and blue regions to obtain

$$\tilde{\mathcal{G}}_{i,A}^{\rm ST,\,GR}\big(k_\perp, p_T R, z_{\rm cut}, \beta, \theta_g, \alpha_s(\mu)\big) \overset{\rm LL}{=} \frac{1}{2\pi\, k_\perp} \frac{\mathrm{d}}{\mathrm{d}k_\perp} \frac{\mathrm{d}}{\mathrm{d}\theta_g} \exp\left\{ -\frac{\alpha_s C_i}{\pi} \left[\beta \ln^2 \theta_g + 2 \ln\theta_g \ln z_{\rm cut} + \frac{1}{1+\beta} \ln^2\left(\frac{k_\perp}{z_{\rm cut} p_T R}\right)\right]\right\} \tag{4.16}$$

This can be extended beyond LL, using the factorization formula for the jet

[4] In principle one can also consider $\theta_g \sim [k_\perp^c/(z_{\rm cut} p_T R)]^{1/(1+\beta)}$, but this only enters beyond NLL.

function $\tilde{\mathcal{G}}$ differential in θ_g,

$$\tilde{\mathcal{G}}_{i,A}^{\text{ST, GR}}\big(k_\perp, p_T R, z_{\text{cut}}, \beta, \theta_g, \alpha_s(\mu)\big) \overset{\text{NLL}}{=} \frac{\mathrm{d}}{\mathrm{d}\theta_g}\bigg[\tilde{H}_i(p_T R,\mu)\, C_i^{\in\text{gr}}(\theta_g p_T R,\mu)$$
$$\mathcal{S}_{G,i}\big(z_{\text{cut}}\theta_g^{1+\beta} p_T R,\beta,\mu\big)\int \mathrm{d}^2\vec{k}'_\perp\, \mathcal{S}_{X,i}(k'_\perp, p_T R, z_{\text{cut}},\beta,\mu,\nu/p_T)$$
$$\int \mathrm{d}^2\vec{k}''_\perp\, S_i^{\text{G}}(\vec{k}_\perp - \vec{k}'_\perp - \vec{k}''_\perp,\mu,\nu R) S_i^{\text{NG}}\Big(\frac{k''_\perp}{p_T R}\Big)\, \mathcal{S}_i^{\text{NG+AC}}(z_{\text{cut}}\theta_g^\beta)\bigg]. \qquad (4.17)$$

For this angle we restrict ourselves to NLL accuracy, which is why the power corrections to the factorization formula have been omitted. The collinear function $C_i^{\in\text{gr}}$ describes collinear radiation, which is never groomed away. It can provide the emission that sets θ_g, and any other collinear emissions must be at smaller angles. Similarly, for the collinear-soft$_G$ mode, emissions must satisfy $\theta/R < \theta_g^c$ if they pass the soft drop condition, as described by the collinear-soft function $\mathcal{S}_{G,i}$. Wide-angle soft radiation is always groomed away, and its total transverse momentum is described by the same soft function S_i^{G} that we encountered before. Finally, $\mathcal{S}_{X,i}$ describes collinear-soft$_X$ emissions, which only contribute to the transverse momentum if they fail the soft drop condition. There are also non-global logarithms and clustering logarithms associated with the collinear function C_i and collinear-soft function $\mathcal{S}_{G,i}$. The non-global logarithms from correlated hard and soft emissions are the same as for the standard vs. WTA axis and described by S_i^{G}. These are the same as in the resummation of θ_g and described by $\mathcal{S}_i^{\text{NG+AC}}$ [122]. The renormalization group equations for the new ingredients in eq. (4.17) are given by

$$\mu\frac{\mathrm{d}}{\mathrm{d}\mu}\, C_i^{\in\text{gr}}(\theta_g^c p_T R,\mu) = \gamma_i^{C^{\in\text{gr}}}(\theta_g^c p_T R,\mu)\, C_i^{\in\text{gr}}(\theta_g^c p_T R,\mu)\,, \qquad (4.18)$$
$$\mu\frac{\mathrm{d}}{\mathrm{d}\mu}\, \mathcal{S}_{G,i}\big(\mu_{\mathcal{S}_G},\beta,\mu\big) = \gamma_i^{\mathcal{S}_G}\big(\mu_{\mathcal{S}_G},\beta,\mu\big)\, \mathcal{S}_{G,i}\big(\mu_{\mathcal{S}_G},\beta,\mu\big)\,,$$
$$\mu\frac{\mathrm{d}}{\mathrm{d}\mu}\, \mathcal{S}_{X,i}(k_\perp, z_{\text{cut}} p_T R,\beta,\mu,\nu) = \gamma_i^{\mathcal{S}_X}(z_{\text{cut}} p_T R,\beta,\mu,\nu)\, \mathcal{S}_{X,i}(k_\perp, z_{\text{cut}} p_T R,\beta,\mu,\nu)\,,$$
$$\nu\frac{\mathrm{d}}{\mathrm{d}\nu}\, \mathcal{S}_{X,i}(k_\perp, z_{\text{cut}} p_T R,\beta,\mu,\nu) = -\int\frac{\mathrm{d}^2\vec{k}'_\perp}{(2\pi)^2}\, \gamma_i^\nu(\vec{k}_\perp - \vec{k}'_\perp,\mu)\, \mathcal{S}_{X,i}(k'_\perp, z_{\text{cut}} p_T R,\beta,\mu,\nu)\,.$$

We wrote θ_g^c to explicitly indicate that the functions are cumulative distributions, i.e. integrated over θ_g up to θ_g^c. The natural scales of these modes are

$$\mu_H = p_T R,\;\; \mu_{C^{\in\text{gr}}} = p_T R\,\theta_g^c,\;\; \mu_{\mathcal{S}_G} = z_{\text{cut}} p_T R\,(\theta_g^c)^{1+\beta},\;\; \mu_{S^G} = k_\perp,\;\; \mu_{\mathcal{S}_X} = k_\perp,$$
$$\nu_{S^G} = \frac{2k_\perp}{R},\;\; \nu_{\mathcal{S}_X} = \frac{2}{R}\big(z_{\text{cut}} p_T R\, k_\perp^\beta\big)^{\frac{1}{1+\beta}}. \qquad (4.19)$$

For regime B we find it clarifying to work differentially in θ_g. In the LL analysis there must a single emission that sets θ_g, i.e. $\theta/R = \theta_g$ and $z > z_{\text{cut}}\theta_g^\beta$. Any other emissions must be outside the colored area, leading to

$$\tilde{\mathcal{G}}_{i,B}^{\text{ST, GR}}\big(k_\perp, p_T R, z_{\text{cut}}, \beta, \theta_g, \alpha_s(\mu)\big) \overset{\text{LL}}{=} -\frac{\alpha_s C_i}{\pi}\frac{2}{\theta_g}\ln(z_{\text{cut}}\theta_g^\beta) \times \frac{1}{2\pi\, k_\perp}\frac{\mathrm{d}}{\mathrm{d}k_\perp}\exp\left\{-\frac{\alpha_s C_i}{\pi}\left[\ln^2\theta_g + 2\ln\theta_g \ln\Big(\frac{k_\perp}{\theta_g p_T R}\Big)\right]\right\}. \tag{4.20}$$

In the SCET analysis there are the four modes corresponding to the outer corners of the colored region, as one might anticipate. However, the emission that sets θ_g (and only this emission) is sensitive to the soft drop condition, which is why there is also a collinear-soft$_G$ mode contribution in this case. This leads to unusual behavior: the corresponding collinear-soft function only contributes if it has a single emission that sets θ_g. In particular, if it has (independent) emissions that do not set θ_g, these emissions only have the constraint $\theta/R < \theta_g$, resulting in scaleless integrals. The factorization formula in SCET for $\tilde{\mathcal{G}}$ is given by

$$\begin{aligned}\tilde{\mathcal{G}}_{i,B}^{\text{ST, GR}}\big(k_\perp, p_T R, z_{\text{cut}}, \beta, \theta_g, \alpha_s(\mu)\big) &\overset{\text{NLL}}{=} \tilde{H}_i(p_T R, \mu)\left[\frac{\mathrm{d}}{\mathrm{d}\theta_g} C_i^{\in\text{gr}}(\theta_g p_T R, \mu)\right.\\ &\quad\left. + \mathcal{S}'_{G,i}\big(\theta_g, z_{\text{cut}}\theta_g^\beta p_T, \beta, \mu\big) C_i^{\in\text{gr}}(\theta_g p_T R, \mu)\right]\\ &\quad\times \int \mathrm{d}^2\vec{k}'_\perp \mathcal{S}_{K,i}(k'_\perp, \mu, \nu\theta_g R) S_i^{\text{G}}(\vec{k}_\perp - \vec{k}'_\perp, \mu, \nu R) S_i^{\text{NG}}\Big(\frac{k_\perp}{p_T R}\Big).\end{aligned} \tag{4.21}$$

The two terms in the square brackets correspond to the collinear mode setting θ_g (when the derivative acts on $C_i^{\in\text{gr}}$) or the collinear-soft$_G$ mode setting θ_g. While the collinear-soft$_G$ mode has the same power counting as in regime A, the function is very different. This is also reflected in the unusual nature of the renormalization group equation of $\mathcal{S}'_{G,i}$,[5]

$$\mu\frac{\mathrm{d}}{\mathrm{d}\mu}\mathcal{S}'_{G,i}\big(\theta_g, z_{\text{cut}}\theta_g^\beta p_T, \beta, \mu\big) = -\frac{\mathrm{d}}{\mathrm{d}\theta_g}\gamma_i^{C^{\in\text{gr}}}(\theta_g p_T R, \mu), \tag{4.22}$$

which follows from consistency of the factorization theorem and agrees with a direct calculation at order α_s. The terms in the square brackets of eq. (4.21) can be interpreted as a matching coefficient where we integrated out modes at the scales $\theta_g p_T R$ and $z_{\text{cut}}\theta_g^{1+\beta} p_T R$. Its running down to the $k_\perp$ scale will generate

[5] Note that only $R_g > 0$ contributions need to be considered here, since we are differential in R_g and assume regime B. In particular, no (plus) distributions at $R_g = 0$ are required.

non-global logarithms which we conjecture is also described by the function $\mathcal{S}_i^{\mathrm{NG+AC}}$ of ref. [122], but with the different argument $k_\perp/(\theta_g p_T R)$. These NGLs require further study and are not included in our numerical analysis. The function $\mathcal{S}_{K,i}$ describes the contribution to $k_\perp$ from collinear-soft$_K$ emissions that are groomed away, which for this mode simply means $\theta/R > \theta_g$. It's renormalization group equation is given by

$$\begin{aligned}
\mu\frac{\mathrm{d}}{\mathrm{d}\mu}\,\mathcal{S}_{K,i}(k_\perp,\mu,\nu\theta_g R) &= \gamma_i^{\mathcal{S}_K}(\mu,\nu\theta_g R)\,\mathcal{S}_{K,i}(k_\perp,\mu,\nu\theta_g R)\,,\\
\nu\frac{\mathrm{d}}{\mathrm{d}\nu}\,\mathcal{S}_{K,i}(k_\perp,\mu,\nu\theta_g R) &= -\int\frac{\mathrm{d}^2\vec{k}'_\perp}{(2\pi)^2}\,\gamma_i^{\nu}(\vec{k}_\perp-\vec{k}'_\perp,\mu)\,\mathcal{S}_{K,i}(k'_\perp,\mu,\nu\theta_g R).
\end{aligned}\tag{4.23}$$

The natural scales for the modes in this regime are

$$\begin{aligned}
&\mu_H = p_T R\,,\quad \mu_{C^{\in\mathrm{gr}}} = p_T R\,\theta_g\,,\quad \mu_{\mathcal{S}'_G} = z_{\mathrm{cut}} p_T R\,\theta_g^{1+\beta}\,,\quad \mu_{S^G} = k_\perp\,,\qquad \mu_{\mathcal{S}_K} = k_\perp\,,\\
&\qquad\qquad\qquad\qquad\qquad\qquad\qquad\qquad\qquad\qquad \nu_{S^G} = \frac{2k_\perp}{R}\,,\quad \nu_{\mathcal{S}_K} = \frac{2k_\perp}{\theta_g R}.
\end{aligned}\tag{4.24}$$

4.2 Standard vs. winner-take-all axis

In this section we provide further details describing our calculation of the angle between the standard and winner-take-all axis. In sec. 4.2.1 we discuss the calculation of jet function $\tilde{\mathcal{G}}^{\mathrm{ST,WTA}}$ when $k_\perp \sim p_T R$, and the resummation of jet radius logarithms. In sec. 4.2.2 we consider $k_\perp \ll p_T R$, presenting the ingredients that enter the refactorization of $\tilde{\mathcal{G}}$ and checking the singular/nonsingular decomposition. Details on our numerical implementation are give in sec. 4.5, with anomalous dimensions relegated to B.3.2.

4.2.1 Jet function for $k_\perp \sim p_T R$

We are working in the collinear limit $R \ll 1$ and can therefore use the collinear phase-space and squared matrix element [140] given in equation (3.30), to calculate the jet function for the angle between the standard and winner-take-all axis

$$\begin{aligned}
\Delta\mathcal{G}_i^{\mathrm{ST,WTA}}\big(k_\perp, p_T R, \alpha_s(\mu)\big) &= \int \mathrm{d}\Phi_2\,\sigma_{2,i}^c\,\Theta\Big(\frac{q_\perp}{x(1-x)p_T} < R\Big)\\
&\times\left[\Theta\Big(x>\frac{1}{2}\Big)\frac{1}{\pi}\delta\Big(k_\perp^2-\frac{q_\perp^2}{x^2}\Big)+\Theta\Big(x<\frac{1}{2}\Big)\frac{1}{\pi}\delta\Big(k_\perp^2-\frac{q_\perp^2}{(1-x)^2}\Big)-\frac{1}{\pi}\delta(k_\perp^2)\right].
\end{aligned}\tag{4.25}$$

The final term in this expression subtracts off the semi-inclusive jet function, see eq. (5.5). This leads to

$$\begin{aligned}\Delta\mathcal{G}_q^{\text{ST,WTA}}\big(k_\perp, p_T R, \alpha_s(\mu)\big) = \frac{\alpha_s C_F}{\pi^2}\,\Theta\Big(k_\perp < \frac{p_T R}{2}\Big)\Big\{ &-\frac{1}{2\mu^2}\mathcal{L}_1\Big(\frac{k_\perp^2}{\mu^2}\Big) \\ &+ \frac{1}{\mu^2}\mathcal{L}_0\Big(\frac{k_\perp^2}{\mu^2}\Big)\Big[\ln\Big(\frac{p_T R}{\mu}\Big) + \ln\Big(1-\frac{k_\perp}{p_T R}\Big) + \frac{3}{2}\,\frac{k_\perp}{p_T R} - \frac{3}{4}\Big] \\ &+ \delta(k_\perp^2)\Big[-\ln^2\Big(\frac{p_T R}{\mu}\Big) + \frac{3}{2}\ln\Big(\frac{p_T R}{\mu}\Big) - \frac{3}{2}\ln 2 + \frac{\pi^2}{6} - \frac{3}{2}\Big]\Big\},\end{aligned}$$

$$\begin{aligned}\Delta\mathcal{G}_g^{\text{ST, WTA}}\big(k_\perp, p_T R, \alpha_s(\mu)\big) = \frac{\alpha_s}{\pi^2}\,\Theta\Big(k_\perp < \frac{p_T R}{2}\Big)\Big\{ &-\frac{C_A}{2}\frac{1}{\mu^2}\mathcal{L}_1\Big(\frac{k_\perp^2}{\mu^2}\Big) \\ &+ \frac{1}{\mu^2}\mathcal{L}_0\Big(\frac{k_\perp^2}{\mu^2}\Big)\Big[\frac{\beta_0}{2}\Big(\frac{k_\perp^3}{p_T^3 R^3} - \frac{3}{2}\frac{k_\perp^2}{p_T^2 R^2} + \frac{3}{2}\frac{k_\perp}{p_T R} - \frac{1}{2}\Big) \\ &+ C_A\Big(-\frac{3}{2}\frac{k_\perp^3}{p_T^3 R^3} + \frac{9}{4}\frac{k_\perp^2}{p_T^2 R^2} - \frac{3}{4}\frac{k_\perp}{p_T R} + \ln\Big(1-\frac{k_\perp}{p_T R}\Big) + \ln\Big(\frac{p_T R}{\mu}\Big)\Big)\Big] \\ &+ \delta(k_\perp^2)\Big[C_A\Big(-\ln^2\Big(\frac{p_T R}{\mu}\Big) + \frac{\pi^2}{6} + \frac{5}{16}\Big) + \frac{\beta_0}{2}\Big(\ln\Big(\frac{p_T R}{2\mu}\Big) - \frac{29}{24}\Big)\Big]\Big\},\end{aligned} \tag{4.26}$$

where the plus distributions are defined in appendix A.3. Note that the terms where the plus distribution multiplies a power of $k_\perp$ do not require a plus prescription. It is worth emphasizing that in eq. (4.26) the explicit μ dependence cancels between the various terms, so the only μ dependence is in the scale α_s.

4.2.2 Refactorization for $k_\perp \ll p_T R$

We now present expressions for the various ingredients entering in the refactorization of the jet function in eq. (4.8). First of all, we give the coefficients J_{ij} in eq. (4.3) (independent of the angle we consider) in eq. (C.2) and the hard functions in (C.3) .

The global soft function is at one-loop order given by [56, 82]

$$S_i^{\text{G}}(k_\perp, \mu, \nu R) = \frac{1}{\pi}\delta(k_\perp^2) + \frac{\alpha_s C_i}{2\pi^2}\Big[-\frac{1}{\mu^2}\mathcal{L}_1\Big(\frac{k_\perp^2}{\mu^2}\Big) + \frac{1}{\mu^2}\mathcal{L}_0\Big(\frac{k_\perp^2}{\mu^2}\Big)\ln\frac{\nu^2 R^2}{4\mu^2} - \frac{\pi^2}{12}\delta(k_\perp^2)\Big], \tag{4.27}$$

where the color factor $C_i = C_A$ (C_F) for $i = g$ (q). The leading NGLs in the large N_c approximation are taken from the solution to the BMS equation [96]

up to five-loop order [97]

$$S_q^{\rm NG}(\widehat{L}) = 1 - \frac{\pi^2}{24}\widehat{L}^2 + \frac{\zeta_3}{12}\widehat{L}^3 + \frac{\pi^4}{34560}\widehat{L}^4 + \Big(-\frac{\pi^2\zeta_3}{360} + \frac{17\zeta_5}{480}\Big)\widehat{L}^5 + \mathcal{O}(L^6)\,,$$
$$S_g^{\rm NG}(\widehat{L}) = \big[S_q^{\rm NG}(\widehat{L})\big]^2\,. \tag{4.28}$$

The argument of this $S_i^{\rm NG}$ is in impact parameter space given by

$$\widehat{L} = \frac{\alpha_s N_c}{\pi}\ln(b_\perp p_T R)\,. \tag{4.29}$$

While eq. (4.28) technically does not resum the NGLs, we have checked that the effect beyond the cubic term on our numerical results is less than a percent.

The only new ingredient is the collinear function, whose calculation is very similar to eq. (4.25), except that we can drop the restriction that the two particles are inside the jet since this is automatically the case for $k_\perp \ll p_T R$. Explicitly,

$$C_i(k_\perp,\mu,\nu/p_T) = \int \mathrm{d}\Phi_2\,\sigma^c_{2,i}\,\Big(\frac{\nu}{2(1-x)p_T}\Big)^\eta\Big[\Theta\Big(x>\frac{1}{2}\Big)\frac{1}{\pi}\delta\Big(k_\perp^2 - \frac{q_\perp^2}{x^2}\Big) + \Theta\Big(x<\frac{1}{2}\Big)\frac{1}{\pi}\delta\Big(k_\perp^2 - \frac{q_\perp^2}{(1-x)^2}\Big)\Big]\,, \tag{4.30}$$

where we use a rapidity regulator η with associated scale ν [81,90]. This leads to

$$\begin{aligned} C_q(k_\perp,\mu,\nu/p_T) &= \frac{1}{\pi}\delta(k_\perp^2) + \frac{\alpha_s C_F}{\pi^2}\Big[\frac{1}{\mu^2}\mathcal{L}_0\Big(\frac{k_\perp^2}{\mu^2}\Big)\Big(-\frac{3}{4} - \ln\Big(\frac{\nu}{2p_T}\Big)\Big) \\ &\quad + \delta(k_\perp^2)\Big(-\frac{3}{2}\ln 2 - \frac{\pi^2}{6} + \frac{7}{4}\Big)\Big]\,, \\ C_g(k_\perp,\mu,\nu/p_T) &= \frac{1}{\pi}\delta(k_\perp^2) + \frac{\alpha_s}{\pi^2}\Big\{\frac{1}{\mu^2}\mathcal{L}_0\Big(\frac{k_\perp^2}{\mu^2}\Big)\Big(-\frac{\beta_0}{4} - C_A\ln\Big(\frac{\nu}{2p_T}\Big)\Big) \\ &\quad + \delta(k_\perp^2)\Big[C_A\Big(\frac{25}{48} - \frac{\pi^2}{6}\Big) + \frac{\beta_0}{2}\Big(\frac{17}{24} - \ln 2\Big)\Big]\Big\}\,. \end{aligned} \tag{4.31}$$

Alternatively, since at this order there are at most two partons and the WTA is along the most energetic one, we can extract this collinear function from the TMD fragmentation function. In impact parameter $b_\perp$ space, using the conventions of ref. [82], this relationship is given by

$$C_i(b_\perp,\mu,\nu) = \sum_j \int \mathrm{d}z\,\Theta\Big(z-\frac{1}{2}\Big)\,\tilde{C}_{j/i}(z,b_\perp,\mu,\nu)\,. \tag{4.32}$$

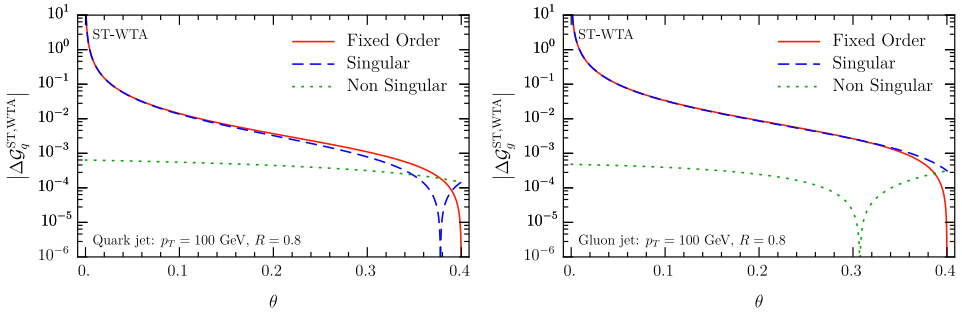

Figure 4.4 Testing the refactorization (blue dashed) of the jet function $\Delta\mathcal{G}^{\mathrm{ST,WTA}}$ (red solid), for the angle between the standard and WTA axis in eq. (4.8) at $\mathcal{O}\alpha_s$. The nonsingular (green dotted) is the difference. The left (right) panel corresponds to quark (gluon) jets.

See also [141]. We conclude this section by verifying the validity of the refactorization in eq. (4.8) in fig. 4.4, by plotting the jet function $\Delta\mathcal{G}$, the singular expression obtained from the right-hand side and their nonsingular difference. We have converted the transverse momentum to an angle, including the appropriate Jacobian $\mathrm{d}^2k_\perp = 2\pi\theta p_T^2\,\mathrm{d}\theta$, and taken $\mu = p_T R$, which only affects the scale in α_s. The nonsingular indeed vanishes for small angles. In fact, the refactorization seems to hold over most of the range, i.e. $\theta = k_\perp/p_T \lesssim 0.4R$.

4.3 Groomed vs. winner-take-all axis

In sec. 4.3.1 we calculate the jet function $\mathcal{G}^{\mathrm{GR,WTA}}$ when $k_\perp \sim z_{\mathrm{cut}} p_T R \sim p_T R$. In sec. 4.2.2 the ingredients that enter its refactorization for $k_\perp \ll z_{\mathrm{cut}} p_T R \ll p_T R$ are given, and the singular/nonsingular decomposition is checked.

4.3.1 Jet function for $k_\perp \sim p_T R$

The calculation is similar to the one in sec. 4.2.1. In terms of the collinear phase-space and matrix element squared in (3.30),

$$\Delta\mathcal{G}_i^{\mathrm{ST,GR}}\big(k_\perp, p_T R, z_{\mathrm{cut}}, \beta, \theta_g, \alpha_s(\mu)\big) = \int \mathrm{d}\Phi_2\, \sigma_{2,i}^c \Theta(\theta < R) \tag{4.33}$$
$$\times \left\{ \Theta\left(\frac{1}{2} > x > z_{\mathrm{cut}}\left(\frac{\theta}{R}\right)^\beta\right) \frac{1}{\pi}\left[\delta\left(k_\perp^2 - \frac{q_\perp^2}{(1-x)^2}\right) - \delta(k_\perp^2)\right] \right.$$
$$\left. + \Theta\left(1 - z_{\mathrm{cut}}\left(\frac{\theta}{R}\right)^\beta > x > \frac{1}{2}\right) \frac{1}{\pi}\left[\delta\left(k_\perp^2 - \frac{q_\perp^2}{x^2}\right) - \delta(k_\perp^2)\right] \right\},$$

using the shorthand $\theta = q_\perp/[x(1-x)p_T]$. The additional condition compared to eq. (4.25) is that the partons must pass soft drop. This leads to

$$
\begin{aligned}
\Delta\mathcal{G}_q^{\mathrm{GR,WTA}}\big(k_\perp, p_T R, z_{\mathrm{cut}}, \beta, \theta_g, \alpha_s(\mu)\big) &= \frac{\alpha_s C_F}{\pi^2}\bigg(\Theta\Big(z_{\mathrm{cut}} p_T R < k_\perp < \frac{p_T R}{2}\Big) \\
&\quad \times \bigg[-\frac{1}{2\mu^2}\mathcal{L}_1\Big(\frac{k_\perp^2}{\mu^2}\Big) + \frac{1}{\mu^2}\mathcal{L}_0\Big(\frac{k_\perp^2}{\mu^2}\Big)\bigg(\ln\Big(\frac{p_T R}{\mu}\Big) + \ln\Big(1 - \frac{k_\perp}{p_T R}\Big) + \frac{3}{2}\frac{k_\perp}{p_T R} - \frac{3}{4}\bigg)\bigg] \\
&\quad + \Theta(k_\perp < z_{\mathrm{cut}} p_T R)\bigg\{ -\frac{\beta}{2(1+\beta)}\frac{1}{\mu^2}\mathcal{L}_1\Big(\frac{k_\perp^2}{\mu^2}\Big) + \frac{1}{\mu^2}\mathcal{L}_0\Big(\frac{k_\perp^2}{\mu^2}\Big)\bigg[\frac{\beta}{1+\beta}\ln\Big(\frac{p_T R}{\mu}\Big) \\
&\quad + \frac{3}{2} z_{\mathrm{cut}}^{\frac{1}{1+\beta}}\Big(\frac{k_\perp}{p_T R}\Big)^{\frac{\beta}{1+\beta}} + \ln\bigg(1 - z_{\mathrm{cut}}^{\frac{1}{1+\beta}}\Big(\frac{k_\perp}{p_T R}\Big)^{\frac{\beta}{1+\beta}}\bigg) - \frac{1}{1+\beta}\ln z_{\mathrm{cut}} - \frac{3}{4}\bigg]\bigg\} \\
&\quad + \delta(k_\perp^2)\bigg[-\frac{\beta}{1+\beta}\ln^2\Big(\frac{p_T R}{\mu}\Big) + \frac{1}{1+\beta}\ln^2 z_{\mathrm{cut}} + \frac{2}{1+\beta}\ln z_{\mathrm{cut}}\ln\Big(\frac{p_T R}{\mu}\Big) \\
&\quad + \frac{3}{2}\ln\Big(\frac{p_T R}{2\mu}\Big) + \frac{2}{\beta}\,\mathrm{Li}_2(z_{\mathrm{cut}}) - \frac{3 z_{\mathrm{cut}}}{\beta} + \frac{\pi^2}{6} - \frac{3}{2}\bigg]\bigg),
\end{aligned}
$$

$$
\begin{aligned}
\Delta\mathcal{G}_g^{\mathrm{GR,WTA}}\big(k_\perp, p_T R, z_{\mathrm{cut}}, \beta, \theta_g, \alpha_s(\mu)\big) &= \frac{\alpha_s}{\pi^2}\bigg(\Theta\Big(z_{\mathrm{cut}} p_T R < k_\perp < \frac{p_T R}{2}\Big) \\
&\quad \bigg\{ -\frac{C_A}{2}\frac{1}{\mu^2}\mathcal{L}_1\Big(\frac{k_\perp^2}{\mu^2}\Big) + \frac{1}{\mu^2}\mathcal{L}_0\Big(\frac{k_\perp^2}{\mu^2}\Big)\bigg[\frac{\beta_0}{2}\bigg(\frac{k_\perp^3}{p_T^3 R^3} - \frac{3}{2}\frac{k_\perp^2}{p_T^2 R^2} + \frac{3}{2}\frac{k_\perp}{p_T R} - \frac{1}{2}\bigg) \\
&\quad + C_A\bigg(-\frac{3}{2}\frac{k_\perp^3}{p_T^3 R^3} + \frac{9}{4}\frac{k_\perp^2}{p_T^2 R^2} - \frac{3}{4}\frac{k_\perp}{p_T R} + \ln\Big(1 - \frac{k_\perp}{p_T R}\Big) + \ln\Big(\frac{p_T R}{\mu}\Big)\bigg)\bigg]\bigg\} \\
&\quad + \Theta(k_\perp < z_{\mathrm{cut}} p_T R)\bigg\{ -C_A\frac{\beta}{2(1+\beta)}\frac{1}{\mu^2}\mathcal{L}_1\Big(\frac{k_\perp^2}{\mu^2}\Big) + \frac{1}{\mu^2}\mathcal{L}_0\Big(\frac{k_\perp^2}{\mu^2}\Big) \\
&\quad \times \bigg[\frac{\beta_0}{2}\bigg(z_{\mathrm{cut}}^{\frac{3}{1+\beta}}\Big(\frac{k_\perp}{p_T R}\Big)^{\frac{3\beta}{1+\beta}} - \frac{3}{2} z_{\mathrm{cut}}^{\frac{2}{1+\beta}}\Big(\frac{k_\perp}{p_T R}\Big)^{\frac{2\beta}{1+\beta}} + \frac{3}{2} z_{\mathrm{cut}}^{\frac{1}{1+\beta}}\Big(\frac{k_\perp}{p_T R}\Big)^{\frac{\beta}{1+\beta}} - \frac{1}{2}\bigg) \\
&\quad + C_A\bigg(\frac{\beta}{1+\beta}\ln\Big(\frac{p_T R}{\mu}\Big) - \frac{3}{2} z_{\mathrm{cut}}^{\frac{3}{1+\beta}}\Big(\frac{k_\perp}{p_T R}\Big)^{\frac{3\beta}{1+\beta}} + \frac{9}{4} z_{\mathrm{cut}}^{\frac{2}{1+\beta}}\Big(\frac{k_\perp}{p_T R}\Big)^{\frac{2\beta}{1+\beta}} \\
&\quad - \frac{3}{4} z_{\mathrm{cut}}^{\frac{1}{1+\beta}}\Big(\frac{k_\perp}{p_T R}\Big)^{\frac{\beta}{1+\beta}} + \ln\Big(1 - z_{\mathrm{cut}}^{\frac{1}{1+\beta}}\Big(\frac{k_\perp}{p_T R}\Big)^{\frac{\beta}{1+\beta}}\Big) - \frac{1}{1+\beta}\ln z_{\mathrm{cut}}\bigg)\bigg]\bigg\} \\
&\quad + \delta(k_\perp^2)\bigg\{ C_A\bigg[-\frac{\beta}{1+\beta}\ln^2\Big(\frac{p_T R}{\mu}\Big) + \frac{1}{1+\beta}\ln^2 z_{\mathrm{cut}} + \frac{2}{1+\beta}\ln z_{\mathrm{cut}}\ln\Big(\frac{p_T R}{\mu}\Big) \\
&\quad + \frac{2}{\beta}\mathrm{Li}_2(z_{\mathrm{cut}}) + \frac{\pi^2}{6} + \frac{5}{16} + \frac{1}{\beta}\Big(z_{\mathrm{cut}}^3 - \frac{9}{4} z_{\mathrm{cut}}^2 + \frac{3}{2} z_{\mathrm{cut}}\Big)\bigg] \\
&\quad + \frac{\beta_0}{2}\bigg[\ln\Big(\frac{p_T R}{2\mu}\Big) - \frac{29}{24} + \frac{1}{\beta}\Big(-\frac{2}{3} z_{\mathrm{cut}}^3 + \frac{3}{2} z_{\mathrm{cut}}^2 - 3 z_{\mathrm{cut}}\Big)\bigg]\bigg\}\bigg). \qquad (4.34)
\end{aligned}
$$

Taking $\beta \to \infty$ we recover $\Delta\mathcal{G}^{\text{ST,WTA}}$. We can obtain the result for $\beta = 0$ by taking the limit of the above expressions. Two particular types of terms that require care are

$$\begin{aligned}
\frac{1}{k_\perp^2}\, z_{\text{cut}}^{\frac{n}{1+\beta}} \Big(\frac{k_\perp}{p_T R}\Big)^{\frac{n\,\beta}{1+\beta}} &= \delta(k_\perp)\Big[\frac{2(1+\beta)}{n\,\beta} z_{\text{cut}}^n - 2 z_{\text{cut}}^n \ln z_{\text{cut}} \\
&\quad - 2 z_{\text{cut}}^n \ln\Big(\frac{p_T R}{\mu}\Big)\Big] + \frac{1}{\mu^2}\mathcal{L}_0\Big(\frac{k_\perp^2}{\mu^2}\Big)\, z_{\text{cut}}^n + \mathcal{O}(\beta)\,, \\
\frac{1}{k_\perp^2}\, \ln\left(1 - z_{\text{cut}}^{\frac{1}{1+\beta}} \Big(\frac{k_\perp}{p_T R}\Big)^{\frac{\beta}{1+\beta}}\right) &= \delta(k_\perp^2)\Big[-\frac{2}{\beta}\, \text{Li}_2(z_{\text{cut}}) - 2\, \text{Li}_2(z_{\text{cut}}) \\
&\quad - 2\ln\Big(\frac{p_T R}{\mu}\Big)\ln(1 - z_{\text{cut}}) - 2\ln(1 - z_{\text{cut}})\ln z_{\text{cut}}\Big] \\
&\quad + \frac{1}{\mu^2}\mathcal{L}_0\Big(\frac{k_\perp^2}{\mu^2}\Big)\ln(1 - z_{\text{cut}}) + \mathcal{O}(\beta)\,. \qquad (4.35)
\end{aligned}$$

The $1/\beta$ poles that appear in these expressions exactly cancel those already present in eq. (4.34). This leads to the following expression for $\beta = 0$

$$\begin{aligned}
&\Delta\mathcal{G}_q^{\text{GR,WTA}}\big(k_\perp, p_T R, z_{\text{cut}}, \beta = 0, \alpha_s(\mu)\big) = \frac{\alpha_s}{\pi^2} C_F \Bigg(\Theta\Big(z_{\text{cut}} p_T R < k_\perp < \frac{p_T R}{2}\Big) \\
&\times \Bigg\{ -\frac{1}{2\mu^2}\mathcal{L}_1\Big(\frac{k_\perp^2}{\mu^2}\Big) + \frac{1}{\mu^2}\mathcal{L}_0\Big(\frac{k_\perp^2}{\mu^2}\Big)\Big[\ln\Big(\frac{p_T R}{\mu}\Big) + \ln\Big(1 - \frac{k_\perp}{p_T R}\Big) + \frac{3}{2}\frac{k_\perp}{p_T R} - \frac{3}{4}\Big]\Bigg\} \\
&+ \Theta\Big(k_\perp < z_{\text{cut}} p_T R\Big)\frac{1}{\mu^2}\mathcal{L}_0\Big(\frac{k_\perp^2}{\mu^2}\Big)\Big[\ln(1 - z_{\text{cut}}) - \ln z_{\text{cut}} + \frac{3}{2} z_{\text{cut}} - \frac{3}{4}\Big] \\
&+ \delta(k_\perp^2)\Big[\ln^2 z_{\text{cut}} + \ln z_{\text{cut}}\Big(2\ln\Big(\frac{p_T R}{\mu}\Big) - 2\ln(1 - z_{\text{cut}}) - 3 z_{\text{cut}}\Big) + \ln\Big(\frac{p_T R}{\mu}\Big) \\
&\times \Big(-2\ln(1 - z_{\text{cut}}) - 3 z_{\text{cut}} + \frac{3}{2}\Big) - 2\, \text{Li}_2(z_{\text{cut}}) + 3 z_{\text{cut}} + \frac{\pi^2}{6} - \frac{3}{2} - \frac{3}{2}\ln 2\Big]\Big)\,, \\
&\Delta\mathcal{G}_g^{\text{GR,WTA}}\big(k_\perp, p_T R, z_{\text{cut}}, \beta = 0, \alpha_s(\mu)\big) = \frac{\alpha_s}{\pi^2}\Bigg(\Theta\Big(z_{\text{cut}} p_T R < k_\perp < \frac{p_T R}{2}\Big)\Bigg\{ \\
&- \frac{C_A}{2}\frac{1}{\mu^2}\mathcal{L}_1\Big(\frac{k_\perp^2}{\mu^2}\Big) + \frac{1}{\mu^2}\mathcal{L}_0\Big(\frac{k_\perp^2}{\mu^2}\Big)\Big[\frac{\beta_0}{2}\Big(\frac{k_\perp^3}{p_T^3 R^3} - \frac{3}{2}\frac{k_\perp^2}{p_T^2 R^2} + \frac{3}{2}\frac{k_\perp}{p_T R} - \frac{1}{2}\Big) \\
&+ C_A\Big(-\frac{3}{2}\frac{k_\perp^3}{p_T^3 R^3} + \frac{9}{4}\frac{k_\perp^2}{p_T^2 R^2} - \frac{3}{4}\frac{k_\perp}{p_T R} + \ln\Big(1 - \frac{k_\perp}{p_T R}\Big) + \ln\Big(\frac{p_T R}{\mu}\Big)\Big)\Big]\Bigg\} \\
&+ \Theta(k_\perp < z_{\text{cut}} p_T R)\,\frac{1}{\mu^2}\mathcal{L}_0\Big(\frac{k_\perp^2}{\mu^2}\Big)\Big[\frac{\beta_0}{2}\Big(z_{\text{cut}}^3 - \frac{3}{2} z_{\text{cut}}^2 + \frac{3}{2} z_{\text{cut}} - \frac{1}{2}\Big) \\
&+ C_A\Big(-\frac{3}{2} z_{\text{cut}}^3 + \frac{9}{4} z_{\text{cut}}^2 - \frac{3}{4} z_{\text{cut}} + \ln(1 - z_{\text{cut}}) - \ln z_{\text{cut}}\Big)\Big]
\end{aligned}$$

$$+\delta(k_\perp^2)\Bigg\{C_A\Bigg[\ln^2 z_{\rm cut}+2\ln z_{\rm cut}\ln\Big(\frac{p_T R}{\mu}\Big)+\Big(\ln z_{\rm cut}+\ln\Big(\frac{p_T R}{\mu}\Big)\Big)\Big(3z_{\rm cut}^3-\frac{9}{2}z_{\rm cut}^2$$
$$+\frac{3}{2}z_{\rm cut}-2\ln(1-z_{\rm cut})\Big)-z_{\rm cut}^3+\frac{9}{4}z_{\rm cut}^2-\frac{3}{2}z_{\rm cut}-2\,{\rm Li}_2(z_{\rm cut})+\frac{\pi^2}{6}+\frac{5}{16}\Bigg]$$
$$+\beta_0\Bigg[\Big(\ln z_{\rm cut}+\ln\Big(\frac{p_T R}{\mu}\Big)\Big)\left(-z_{\rm cut}^3+\frac{3}{2}z_{\rm cut}^2-\frac{3}{2}z_{\rm cut}\right)$$
$$+\frac{1}{3}z_{\rm cut}^3-\frac{3}{4}z_{\rm cut}^2+\frac{3}{2}z_{\rm cut}+\frac{1}{2}\ln\left(\frac{p_T R}{2\mu}\right)-\frac{29}{48}\Bigg]\Bigg\}\Bigg)\,, \tag{4.36}$$

which we checked by also calculating it directly.

4.3.2 Refactorization for $k_\perp \ll p_T R$

The two new ingredients compared to eq. (4.8) are the soft function [142]

$$S_i^{\not\in\ {\rm gr}}(z_{\rm cut}p_T R,\beta,\mu)=1+\frac{\alpha_s C_i}{\pi}\frac{1}{1+\beta}\left[\ln^2\Big(\frac{z_{\rm\ cut}p_T R}{\mu}\Big)-\frac{\pi^2}{24}\right], \tag{4.37}$$

with color factor $C_i=C_A$ (C_F) for $i=g$ (q), and the collinear-soft function[6]

$$\mathcal{S}_i{}^{\rm G}(k_\perp,p_T R,z_{\rm cut},\beta,\mu,\nu/p_T)=\frac{1}{\pi}\delta(k_\perp^2)+\frac{\alpha_s C_i}{\pi^2}\Bigg[-\frac{\beta}{2(1+\beta)}\frac{1}{\mu^2}\mathcal{L}_1\Big(\frac{k_\perp^2}{\mu^2}\Big)$$
$$+\frac{1}{\mu^2}\mathcal{L}_0\Big(\frac{k_\perp^2}{\mu^2}\Big)\ln\left(\frac{\nu}{2p_T}\,z_{\rm\ cut}^{-1/(1+\beta)}\Big(\frac{p_T R}{\mu}\Big)^{\frac{\beta}{1+\beta}}\right)-\frac{\beta}{1+\beta}\delta(k_\perp^2)\frac{\pi^2}{24}\Bigg]. \tag{4.38}$$

Taking the $\beta\to\infty$ limit, $S_i^{\not\in\ {\rm gr}}\to 1$ and $\mathcal{S}_i{}^{\rm G}(k_\perp,p_T R,z_{\rm cut},\beta,\mu,\nu/p_T)\to S_i{}^{\rm G}(k_\perp,\mu,\nu R)$ in eq. (4.27), recovering the result without grooming. The NGLs are encoded by the same expression in eq. (4.28), but now involve the following logarithm

$$\widehat{L}=-\frac{\alpha_s N_c}{\pi}\ln z_{\rm cut}\,. \tag{4.39}$$

We numerically test the size of the power corrections to the refactorization in eq. (4.13), by plotting the jet function $\Delta\mathcal{G}$, the singular expression obtained from the right-hand side and their nonsingular difference. As in fig. 4.4, we show the distribution differential in θ and take $\mu=p_T R$. The nonsingular encodes the size of power corrections and is very small at small angles. There is a transition at $\theta=z_{\rm cut}R$, since for larger angles there is no effect of grooming, and the plot coincides with that in fig. 4.4. Since this transition is still in the resummation region, this does not imply that there is no effect of grooming for larger angles in the *resummed* cross section.

[6] We thank Z. B. Kang and K. Lee for corroborating this result.

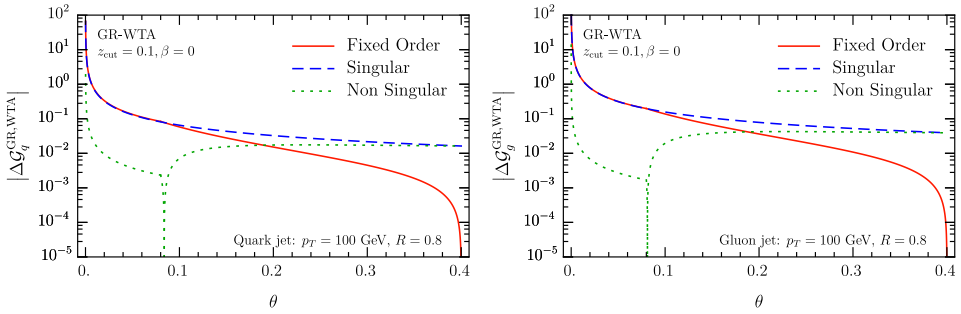

Figure 4.5 Testing the refactorization (blue dashed) of the jet function $\Delta\mathcal{G}^{\rm GR,WTA}$ (red solid), for the angle between the groomed axis (with $z_{\rm cut} = 0.1$, $\beta = 0$) and WTA axis in eq. (4.8) at $\mathcal{O}\alpha_s$. The nonsingular (green dotted) is the difference. The left (right) panel corresponds to quark (gluon) jets.

4.4 Standard vs. groomed jet axis

We present results for the jet function $\mathcal{G}^{\rm ST,\,GR}$ at fixed order, in the kinematic regime where $k_\perp \sim z_{\rm cut} p_T R \sim p_T R$, in sec. 4.4.1. The ingredients entering its refactorization are given in sec. 4.4.2.

4.4.1 Jet function for $k_\perp \sim p_T R$

The measurement for the jet function differential in the groomed radius θ_g and the angle between the standard and groomed jet axis, encoded in $k_\perp$, is given by

$$\begin{aligned}\Delta\mathcal{G}_i^{\rm ST,GR}\big(k_\perp, p_T R, z_{\rm cut}, \beta, \theta_g, \alpha_s(\mu)\big) = \int \mathrm{d}\Phi_2\, \sigma_{2,i}^c \Theta(\theta < R) \qquad (4.40)\\ \Big[\Theta\big(x > z_{\rm cut}(\theta/R)^\beta\big)\,\Theta\big(1-x > z_{\rm cut}(\theta/R)^\beta\big)\,\frac{1}{\pi}\delta(k_\perp^2)\,\delta(\theta_g - \theta/R)\\ + \Theta\big(1-x < z_{\rm cut}(\theta/R)^\beta\big)\,\frac{1}{\pi}\delta\Big(k_\perp^2 - \frac{q_\perp^2}{x^2}\Big)\,\delta(\theta_g)\\ + \Theta\big(x < z_{\rm cut}(\theta/R)^\beta\big)\,\frac{1}{\pi}\delta\Big(k_\perp^2 - \frac{q_\perp^2}{(1-x)^2}\Big)\delta(\theta_g) - \frac{1}{\pi}\delta(k_\perp^2)\delta(\theta_g)\Big],\end{aligned}$$

using the shorthand $\theta = q_\perp/[x(1-x)p_T]$. When the softest particle is groomed away, the groomed axis lies on top of the remaining parton, whereas the axes

coincide when the parton passes grooming. We find

$$
\begin{aligned}
&\Delta\mathcal{G}_q^{\mathrm{ST,GR}}\big(k_\perp, p_T R, z_{\mathrm{cut}}, \beta, \theta_g, \alpha_s(\mu)\big) = \frac{\alpha_s C_F}{\pi^2}\bigg(\delta(k_\perp^2)\Theta(\theta_g<1)\Big[(3z_{\mathrm{cut}}-2)\beta\mathcal{L}_1(\theta_g)\\
&+\Big(3z_{\mathrm{cut}}-\frac{3}{2}-2\ln z_{\mathrm{cut}}\Big)\mathcal{L}_0(\theta_g)+\frac{2}{\theta_g}\ln(1-z_{\mathrm{cut}}\theta_g^\beta)\Big]+\delta(\theta_g)\Theta(k_\perp<z_{\mathrm{cut}}p_T R)\\
&\times\bigg\{-\frac{1}{2(1+\beta)}\,\frac{1}{\mu^2}\mathcal{L}_1\Big(\frac{k_\perp^2}{\mu^2}\Big)+\frac{1}{\mu^2}\mathcal{L}_0\Big(\frac{k_\perp^2}{\mu^2}\Big)\bigg[\frac{3}{2}\frac{k_\perp}{p_T R}-\frac{3}{2}\Big(\frac{k_\perp}{p_T R}\Big)^{\frac{\beta}{1+\beta}} z_{\mathrm{cut}}^{\frac{1}{1+\beta}}\\
&+\ln\Big(1-\frac{k_\perp}{p_T R}\Big)-\ln\bigg(1-\Big(\frac{k_\perp}{p_T R}\Big)^{\frac{\beta}{1+\beta}} z_{\mathrm{cut}}^{\frac{1}{1+\beta}}\bigg)+\frac{1}{1+\beta}\ln\Big(\frac{z_{\mathrm{cut}}p_T R}{\mu}\Big)\bigg]\bigg\}\\
&+\delta(\theta_g)\delta(k_\perp^2)\bigg[-\frac{1}{1+\beta}\ln^2\Big(\frac{z_{\mathrm{cut}}p_T R}{\mu}\Big)+\frac{3}{\beta}z_{\mathrm{cut}}\bigg]\bigg),\\
&\Delta\mathcal{G}_g^{\mathrm{ST,GR}}\big(k_\perp, p_T R, z_{\mathrm{cut}}, \beta, \theta_g, \alpha_s(\mu)\big) = \frac{\alpha_s}{\pi^2}\bigg(\delta(k_\perp^2)\Theta(\theta_g<1)\bigg\{\frac{\beta_0}{2}\big[(2z_{\mathrm{cut}}^3-3z_{\mathrm{cut}}^2\\
&+3z_{\mathrm{cut}}-1)\mathcal{L}_0(\theta_g)+(6z_{\mathrm{cut}}^3-6z_{\mathrm{cut}}^2+3z_{\mathrm{cut}})\beta\mathcal{L}_1(\theta_g)\big]+C_A\Big[\Big(-3z_{\mathrm{cut}}^3+\frac{9}{2}z_{\mathrm{cut}}^2\\
&-\frac{3}{2}z_{\mathrm{cut}}-2\ln z_{\mathrm{cut}}\Big)\mathcal{L}_0(\theta_g)+\Big(-9z_{\mathrm{cut}}^3+9z_{\mathrm{cut}}^2-\frac{3}{2}z_{\mathrm{cut}}-2\Big)\beta\mathcal{L}_1(\theta_g)\\
&+\frac{2}{\theta_g}\ln\Big(1-z_{\mathrm{cut}}\theta_g^\beta\Big)\Big]\bigg\}+\delta(\theta_g)\Theta\big(k_\perp<z_{\mathrm{cut}}p_T R\big)\bigg\{-\frac{C_A}{2(1+\beta)}\,\frac{1}{\mu^2}\mathcal{L}_1\Big(\frac{k_\perp^2}{\mu^2}\Big)\\
&+\frac{1}{\mu^2}\mathcal{L}_0\Big(\frac{k_\perp^2}{\mu^2}\Big)\bigg[\frac{\beta_0}{2}\bigg(\frac{k_\perp^3}{p_T^3R^3}-\Big(\frac{k_\perp}{p_T R}\Big)^{\frac{3\beta}{1+\beta}} z_{\mathrm{cut}}^{\frac{3}{1+\beta}}+\frac{3}{2}\frac{k_\perp^2}{p_T^2R^2}-\frac{3}{2}\Big(\frac{k_\perp}{p_T R}\Big)^{\frac{2\beta}{1+\beta}} z_{\mathrm{cut}}^{\frac{2}{1+\beta}}\\
&-\frac{3}{2}\frac{k_\perp}{p_T R}+\frac{3}{2}\Big(\frac{k_\perp}{p_T R}\Big)^{\frac{\beta}{1+\beta}} z_{\mathrm{cut}}^{\frac{1}{1+\beta}}\bigg)+C_A\bigg(-\frac{3}{2}\frac{k_\perp^3}{p_T^3R^3}+\frac{3}{2}\Big(\frac{k_\perp}{p_T R}\Big)^{\frac{3\beta}{1+\beta}} z_{\mathrm{cut}}^{\frac{3}{1+\beta}}\\
&+\frac{9}{4}\frac{k_\perp^2}{p_T^2R^2}-\frac{9}{4}\Big(\frac{k_\perp}{p_T R}\Big)^{\frac{2\beta}{1+\beta}} z_{\mathrm{cut}}^{\frac{2}{1+\beta}}-\frac{3}{4}\frac{k_\perp}{p_T R}+\frac{3}{4}\Big(\frac{k_\perp}{p_T R}\Big)^{\frac{\beta}{1+\beta}} z_{\mathrm{cut}}^{\frac{1}{1+\beta}}\\
&+\frac{1}{1+\beta}\ln\Big(\frac{z_{\mathrm{cut}}p_T R}{\mu}\Big)+\ln\Big(1-\frac{k_\perp}{p_T R}\Big)-\ln\bigg(1-\Big(\frac{k_\perp}{p_T R}\Big)^{\frac{\beta}{1+\beta}} z_{\mathrm{cut}}^{\frac{1}{1+\beta}}\bigg)\bigg)\bigg]\bigg\}\\
&+\delta(\theta_g)\delta(k_\perp^2)\bigg\{C_A\bigg[\frac{1}{\beta}\Big(-z_{\mathrm{cut}}^3+\frac{9}{4}z_{\mathrm{cut}}^2-\frac{3}{2}z_{\mathrm{cut}}\Big)-\frac{1}{1+\beta}\ln^2\Big(\frac{z_{\mathrm{cut}}p_T R}{\mu}\Big)\bigg]\\
&+\frac{\beta_0}{\beta}\Big(\frac{1}{3}z_{\mathrm{cut}}^3-\frac{3}{4}z_{\mathrm{cut}}^2+\frac{3}{2}z_{\mathrm{cut}}\Big)\bigg\}\bigg).
\end{aligned}
\tag{4.41}
$$

When taking the limit $\beta \to 0$, similar care needs to be taken as for the angle between the groomed and the WTA axis, see eq. (4.35). The corresponding results for quarks and gluons with $\beta = 0$ are given by

$$
\Delta\mathcal{G}_q^{\mathrm{ST,GR}}\big(k_\perp, p_T R, z_{\,\mathrm{cut}}, \beta=0, \theta_g, \alpha_s(\mu)\big) = \tag{4.42}
$$

$$
\begin{aligned}
&\frac{\alpha_s C_F}{\pi^2}\Big\{\delta(k_\perp^2)\Theta(\theta_g<1)\Big(3z_{\rm cut}-\frac{3}{2}-2\ln z_{\rm cut}+2\ln(1-z_{\rm cut})\Big)\mathcal{L}_0(\theta_g)\\
&+\delta(\theta_g)\Theta(k_\perp<z_{\rm cut}p_TR)\Big[-\frac{1}{2\mu^2}\mathcal{L}_1\Big(\frac{k_\perp^2}{\mu^2}\Big)+\frac{1}{\mu^2}\mathcal{L}_0\Big(\frac{k_\perp^2}{\mu^2}\Big)\Big(\ln\Big(1-\frac{k_\perp}{p_TR}\Big)\\
&+\ln\Big(\frac{z_{\rm cut}p_TR}{\mu}\Big)+\frac{3}{2}\frac{k_\perp}{p_TR}-\ln(1-z_{\rm cut})-\frac{3}{2}z_{\rm cut}\Big)\Big]\\
&+\delta(\theta_g)\delta(k_\perp^2)\Big[-\ln^2\Big(\frac{z_{\rm cut}p_TR}{\mu}\Big)+(3z_{\rm cut}+2\ln(1-z_{\rm cut}))\ln\Big(\frac{z_{\rm cut}p_TR}{\mu}\Big)\\
&-3z_{\rm cut}+2{\rm Li}_2(z_{\rm cut})\Big]\Big\},\\
\Delta\mathcal{G}_g^{\rm ST,GR}&\big(k_\perp,p_TR,z_{\rm cut},\beta=0,\theta_g,\alpha_s(\mu)\big)=\\
&\frac{\alpha_s}{\pi^2}\Big(\delta(k_\perp^2)\Theta(\theta_g<1)\Big[\frac{\beta_0}{2}(2z_{\rm cut}^3-3z_{\rm cut}^2+3z_{\rm cut}-1)\mathcal{L}_0(\theta_g)\\
&+C_A\Big(-3z_{\rm cut}^3+\frac{9}{2}z_{\rm cut}^2-\frac{3}{2}z_{\rm cut}-2\ln z_{\rm cut}+2\ln(1-z_{\rm cut})\Big)\mathcal{L}_0(\theta_g)\Big]\\
&+\delta(\theta_g)\Theta(k_\perp<z_{\rm cut}p_TR)\Big\{-\frac{C_A}{2\mu^2}\mathcal{L}_1\Big(\frac{k_\perp^2}{\mu^2}\Big)+\frac{1}{\mu^2}\mathcal{L}_0\Big(\frac{k_\perp^2}{\mu^2}\Big)\\
&\times\Big[\frac{\beta_0}{2}\Big(\frac{k_\perp^3}{p_T^3R^3}+\frac{3}{2}\frac{k_\perp^2}{p_T^2R^2}-\frac{3}{2}\frac{k_\perp}{p_TR}-z_{\rm cut}^3-\frac{3}{2}z_{\rm cut}^2+\frac{3}{2}z_{\rm cut}\Big)\\
&+C_A\Big(-\frac{3}{2}\frac{k_\perp^3}{p_T^3R^3}+\frac{9}{4}\frac{k_\perp^2}{p_T^2R^2}-\frac{3}{4}\frac{k_\perp}{p_TR}+\ln\Big(1-\frac{k_\perp}{p_TR}\Big)+\ln\Big(\frac{z_{\rm cut}p_TR}{\mu}\Big)\\
&-\ln(1-z_{\rm cut})+\frac{3}{2}z_{\rm cut}^3-\frac{9}{4}z_{\rm cut}^2+\frac{3}{4}z_{\rm cut}\Big)\Big]\Big\}\\
&+\delta(\theta_g)\delta(k_\perp^2)\Big\{C_A\Big[-\ln^2\Big(\frac{z_{\rm cut}p_TR}{\mu}\Big)+\Big(-3z_{\rm cut}^3+\frac{9}{2}z_{\rm cut}^2-\frac{3}{2}z_{\rm cut}\\
&+2\ln(1-z_{\rm cut})\Big)\ln\Big(\frac{z_{\rm cut}p_TR}{\mu}\Big)+z_{\rm cut}^3-\frac{9}{4}z_{\rm cut}^2+\frac{3}{2}z_{\rm cut}+{\rm Li}_2(z_{\rm cut})\Big]\\
&+\beta_0\Big[(z_{\rm cut}^3-\frac{3}{2}z_{\rm cut}^2+\frac{3}{2}z_{\rm cut})\ln\Big(\frac{z_{\rm cut}p_TR}{\mu}\Big)-\frac{1}{3}z_{\rm cut}^3+\frac{3}{4}z_{\rm cut}^2-\frac{3}{2}z_{\rm cut}\Big]\Big\}\Big).
\end{aligned}
$$

4.4.2 Refactorization for $k_\perp \ll p_TR$

We start with the new functions that enter in the factorization for regime *A*. The same collinear function appeared in the factorization of the soft drop groomed jet radius, and is up to one-loop order given by [122]

$$
C_q^{\in\,\rm gr}(\theta_g^c p_TR,\mu)=1+\frac{\alpha_s C_F}{\pi}\Big[\ln^2\Big(\frac{\mu}{\theta_g^c p_TR}\Big)+\frac{3}{2}\ln\Big(\frac{\mu}{\theta_g^c p_TR}\Big)+\frac{13}{4}-\frac{3\pi^2}{8}\Big],
$$

$$C_g^{\in\ \mathrm{gr}}(\theta_g^c p_T R,\mu) = 1+\frac{\alpha_s}{\pi}\bigg[C_A\ln^2\Big(\frac{\mu}{\theta_g^c p_T R}\Big)+\frac{\beta_0}{2}\ln\Big(\frac{\mu}{\theta_g^c p_T R}\Big)+C_A\Big(\frac{5}{24}-\frac{3\pi^2}{8}\Big) - \beta_0\frac{23}{24}\bigg]. \tag{4.43}$$

It is related to the unmeasured jet function of ref. [136]. Next, we consider the collinear-soft functions. $\mathcal{S}_{G,i}$ also appeared in the factorization of the soft drop groomed jet radius, and is given by [122]

$$\mathcal{S}_{G,i}\big(z_{\mathrm{cut}}\theta_g^{1+\beta}p_T R,\beta,\mu\big) = 1+\frac{\alpha_s C_i}{\pi(1+\beta)}\bigg[-\ln^2\Big(\frac{\mu}{z_{\mathrm{cut}}\theta_g^{1+\beta}p_T R}\Big)+\frac{\pi^2}{24}\bigg] \tag{4.44}$$

The collinear-soft function $\mathcal{S}_{X,i}$ is sensitive to $k_\perp$ and the soft drop grooming condition, and is up to one-loop order given by

$$\mathcal{S}_{X,i}(k_\perp,p_T R,z_{\mathrm{cut}},\beta,\mu,\nu/p_T) = \frac{1}{\pi}\delta(k_\perp^2)+\frac{\alpha_s C_i}{\pi^2}\bigg[\frac{\beta}{2(1+\beta)}\frac{1}{\mu^2}\mathcal{L}_1\Big(\frac{k_\perp^2}{\mu^2}\Big) - \frac{1}{\mu^2}\mathcal{L}_0\Big(\frac{k_\perp^2}{\mu^2}\Big)\ln\bigg(\frac{\nu}{2p_T}\,z_{\mathrm{cut}}^{-1/(1+\beta)}\Big(\frac{p_T R}{\mu}\Big)^{\frac{\beta}{1+\beta}}\bigg)+\frac{\beta}{1+\beta}\delta(k_\perp^2)\frac{\pi^2}{24}\bigg]. \tag{4.45}$$

Note that the $\mathcal{O}(\alpha_s)$ term here is the same as the collinear-soft function $\mathcal{S}_i^{\mathrm{G}}$ in eq. (4.38), but with opposite sign.

In regime B, the $\mathcal{S}'_{G,i}$ is in fact simply the derivative of $\mathcal{S}_{G,i}$ with respect to θ_g. The only additional result needed is the collinear-soft $\mathcal{S}_{K,i}$, which is differential both in $k_\perp$ and θ_g. A one-loop calculation yields,[7]

$$\mathcal{S}_{K,i}(k_\perp,\mu,\nu\theta_g R) = \frac{1}{\pi}\delta(k_\perp^2)+\frac{\alpha_s C_i}{\pi^2}\bigg[\frac{1}{2\mu^2}\mathcal{L}_1\Big(\frac{k_\perp^2}{\mu^2}\Big)-\frac{1}{\mu^2}\mathcal{L}_0\Big(\frac{k_\perp^2}{\mu^2}\Big)\ln\Big(\frac{\theta_g R\nu}{2\mu}\Big) + \frac{\pi^2}{24}\delta(k_\perp^2)\bigg]. \tag{4.46}$$

Similar to the other angles considered above, we finish this section by comparing the singular and nonsingular terms at order α_s, as shown in fig. 4.6. Specifically, we compare the singular terms to the full fixed order expression for both quark (left) and gluon jets (right). Here we merged the contributions from regime A and B and integrate out the R_g dependence. We observe that the singular terms dominate over the entire range of θ.

[7] Note that the one-loop contribution to $\mathcal{S}_{K,i}$ is equal to that of the global soft function S_i^G in eq. (4.27) with $R\to\theta_g R$ and a different overall sign.

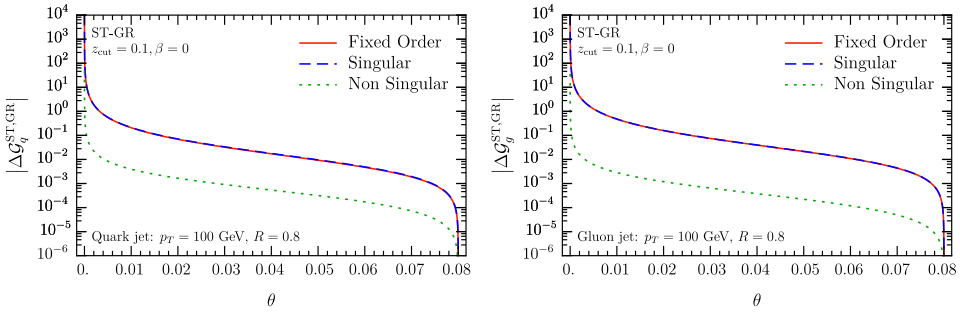

Figure 4.6 Testing the refactorization of the jet function $\Delta\mathcal{G}^{\rm ST,GR}$ where we include both regions A and B, see eqs. 4.17 and eq. (4.21) at $\mathcal{O}\alpha_s$. We show the full fixed order result (solid red), the singular distributions (dashed blue) and the difference between the two which corresponds to the nonsingular pieces (dotted green) is the difference. The left (right) panel corresponds to quark (gluon) jets.

4.5 Numerical implementation

In this section we present details of the numerical implementation relevant for the results presented below. We start by describing how the resummation of $k_\perp/(p_T R)$ is carried out and matched to fixed order in sec. 4.5.1. In addition, we discuss scale choices and how we obtain perturbative QCD scale uncertainties for each angle. A discussion of nonperturbative effects can be found in sec. 4.5.2.

4.5.1 Resummation, matching and uncertainties

The refactorization formulas in secs. 4.1.2, 4.1.3 and 4.1.4 are written in terms of convolutions in $\vec{k}_\perp$ since the individual contributions to the transverse momentum from each mode are added up vectorially. By going to impact parameter $b_\perp$ space, these equations become multiplicative which thus avoids the convolution structure and makes the implementation more straightforward. The same reasoning applies to the RG evolution equations, for which the convolution integrals also become multiplicative in $b_\perp$ space. We then implement the $b_\perp$ space version of the formulas in sec. 4.1 and carry out the resummation, after which we perform a numerical inverse Fourier transform to obtain or predictions for the angle in $k_\perp$ space in the resummation region. We note that the natural scales of the different functions in $b_\perp$ space can be obtained from eqs. (4.10), (4.14), (4.19) and (4.24) with the replacement $k_\perp \to \mu_b = 2e^{-\gamma_E}/b_\perp$.

Instead of using profile scales to merge the resummation of $k_\perp/(p_T R)$ with the fixed order (FO) calculations for $\tilde{\mathcal{G}}$, we perform the matching by directly interpolating between the two results

$$\tilde{\mathcal{G}}_{\text{match}} = g(\theta)\,\tilde{\mathcal{G}}_{\text{FO}} + [1 - g(\theta)]\,\tilde{\mathcal{G}}_{\text{resum}}. \tag{4.47}$$

The function g is 0 in the resumation region, 1 in the fixed order region and it smoothly interpolates between both regimes. For our numerical implementation we choose the same double quadratic function (3.53), the same as for the jet shape.

The choice of the transition points x_1 and x_3 depends on the angle we consider. For each angle, we determine the transition point between the resummation and fixed order region by comparing the singular and nonsingular terms at fixed order as shown in figs. 4.4, 4.5 and 4.6.

For the angle between the standard and WTA jet axes, we conclude from the the left panel of fig. 4.4 that the refactorization of the cross section is valid until $\theta \sim 0.35$, where the singular and the nonsingular (power corrections) become of comparable size. This indicates we have reached the region where one should use the fixed-order expression. Likewise, for the gluon (right panel) we see the resummation is necessary for almost the entire range that is shown in the figure, and we can transition to fixed-order result at slightly higher values, here $\theta \sim 0.38$.

For the angle between the WTA and groomed jet axes we need to perform two transitions. The refactorization formula (4.13) is expected to accurately describe the full fixed-order expression in the limit $k_\perp \ll z_{\text{cut}} p_T R$, implying that it will only reproduce the terms proportional to $\Theta(k_\perp < z_{\text{cut}} p_T R)$ in $\Delta\mathcal{G}$. Once we go to values of $k_\perp$ that are larger than $z_{\text{cut}} p_T R$, the fixed-order expression becomes equal to the ungroomed case, where the singular terms still dominate. This explains why in fig. 4.5 there is a sudden change in the behavior of the power corrections at $\theta = z_{\text{cut}} R$, which corresponds to the transition between the theta functions of the fixed order expression. Therefore, we need to switch from the groomed resummed case to the ungroomed resummed result at $\theta = z_{\text{cut}} R$. We then proceed to transition from the ungroomed resummed to the fixed order result just as in the case of the angle between the standard and WTA jet axes.

By examining fig. 4.6, we notice that the refactorization for the angle between the standard and groomed jet axes is particularly good throughout the whole range of θ. Thus we transition to the fixed-order expression only at the very end, requiring that the cross section vanishes at $\theta = z_{\text{cut}} R$.

The predictions for the angle between the standard and WTA axes and the groomed and WTA axes are computed at NLL$'$ accuracy. The perturbative

QCD scale uncertainties are obtained by varying all scales simultaneously up and down by a factor of 2, by individually varying them by a factor of 2, and then taking the envelope. The angle between the standard and groomed axes is calculated at NLL accuracy. At this accuracy the scale variations give rather large uncertainties which may be up to 50% in some kinematic regions, because there is no (partial) cancellation between the evolution kernels and fixed-order ingredients as the scales are varied. We therefore only show the central curve for this angle. However, the general features of the prediction, such as the angle at which the distribution peaks, do not change much. In order to integrate out the dependence on the soft drop groomed radius R_g, we freeze the running of the coupling constant at the scale 0.5 GeV. We explored the dependence of our results on this cutoff scale by varying it by factors of 2 and found that the impact on the final numerical results is very small, especially compared to the QCD scale uncertainty at NLL accuracy.

4.5.2 Nonperturbative effects

For all observables considered in this work, we work in impact parameter $b_\perp$ space and perform a numerical Fourier inverse transformation. For large $b_\perp$, we enter the nonperturbative regime and therefore we adopt the so-called b_*-prescription [77], modifying the scale $\mu_b = 2e^{-\gamma_E}/b_*$ with

$$b_* = b_\perp / \sqrt{1 + (b_\perp / b_\perp^{\max})^2}. \tag{4.48}$$

Here $b_\perp^{\max}$ is chosen such that b_* avoids the Landau pole for all values of $b_\perp$ and approaches $b_\perp$ at low values of $b_\perp$. We follow ref. [143] in making the approximation that the dominant nonperturbative hadronization effects are due to the nonperturbative component of the rapidity anomalous dimension, as it is multiplied by a large logarithm of the ratio of the respective rapidity scales of the $b_\perp$-dependent collinear(-soft) and soft functions. The all-orders result of the rapidity anomalous dimension is given by

$$\gamma_{\nu,i}^S(\mu) = -2 \int_{\mu_b}^{\mu} \mathrm{d}\ln\mu' \, \Gamma_{\mathrm{cusp}}^i \left[\alpha_s\left(\mu'\right)\right] + \gamma_f^i(\mu) - g_K\left(b_\perp, b_\perp^{\max}\right) , \tag{4.49}$$

where the non-cusp part γ_f^i vanishes to the accuracy at which we are working. The choice of μ_b as the lower bound of the integral in eq. (4.49) is compensated for by introducing the nonperturbative model function g_K, which needs to be determined by a fit to experimental data. For the two variables g_2, $b_\perp^{\max}$ which parametrize our nonperturbative model, we use the fitted results of ref. [144] where

$$g_K(b_\perp, b_\perp^{\max}) = g_2(b_\perp^{\max}) b_\perp^2 , \tag{4.50}$$

with $b_\perp^{\max} = 1.5\ \text{GeV}^{-1}$ and $g_2(b_\perp^{\max}) = 0.18\ \text{GeV}^2$. For the gluon case, we include an additional factor of C_A/C_F in g_2. Note that this parametrization of g_K vanishes in the limit $b_\perp \to 0$. Other extractions of these or related nonperturbative parameters can be found for example in refs. [124–127]. For example, for the angle between the standard and the groomed jet axis, we include in regime A the following nonperturbative exponent in $b_\perp$ space

$$\exp\Big[- g_K(b_\perp, b_*) \frac{1}{1+\beta} \ln \frac{z_{\text{cut}} p_T R}{\mu_b} \Big] . \tag{4.51}$$

We note that the nonperturbative component in this case vanishes in the limit $\beta \to \infty$, which is consistent with the expectation that the the two axes are aligned in the limit that the grooming condition is removed. Similarly in regime B, the nonperturbative component vanishes when $\theta_g = 1$ which corresponds to the case where the standard and groomed jet axis are aligned.

4.6 Results for the LHC

In this section, we present numerical results for the angles between the different jet axes as introduced in the previous sections. We start with the angle between the standard and the WTA axes, see sec. 4.2. Throughout this section, we use the CT14 NLO PDF set [106]. In fig. 4.7, we show the perturbative results at NLL′ accuracy including a QCD scale uncertainty band, which is obtained by varying all scales and taking the envelope, as discussed in sec. 4.5.1 above. We consider inclusive jets in proton-proton collisions at $\sqrt{s} = 13$ TeV at central rapidities $|\eta| < 2$ where jets are reconstructed using the anti-k$_T$ algorithm with $R = 0.8$. We choose four exemplary jet transverse momentum intervals between $p_T = 30 - 1200$ GeV as indicated in each panel of the figure. As expected, we observe the typical Sudakov suppression for small angles. As the jet p_T is increased, the distribution becomes narrower and peaks at small values of θ. For comparison, we also show Pythia 8.2 [87] results at parton level and including Initial State Radiation (ISR), Multi Parton Interactions (MPI) and hadronization effects. Note that the spike seen in the lowest θ bin of the Pythia results at parton level is due to the shower cutoff. Overall, we find very good agreement between our perturbative results and the Pythia 8.2 simulations. Only for the lowest jet transverse momentum bin $p_T = 30 - 50$ GeV, we observe that the Pythia results are not within the displayed uncertainty band. This is the case with the largest contribution from ISR and MPI, which are not (or only partially) contained in our calculation. Note that in this (and subsequent) figures we show results for fairly small angles. To access these experimentally it would be natural to consider track-based

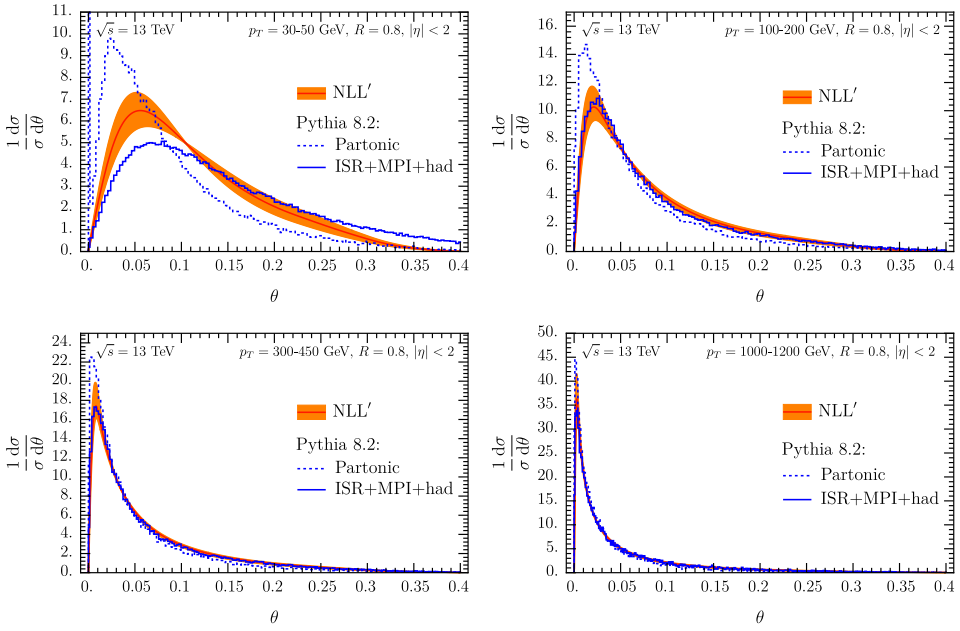

Figure 4.7 Numerical results for the angle between the WTA and the standard jet axis at NLL′ accuracy (orange curve and band) for four jet transverse momentum intervals as indicated in the figure. We choose proton-proton collisions at $\sqrt{s} = 13$ TeV where jets are identified with the anti-k$_T$ algorithm with $R = 0.8$ at central rapidity with $|\eta| < 2$. For comparison, we show Pythia 8.2 results at parton level (dotted blue) and when ISR, MPI and hadronization are included (solid blue).

measurements, since these have vastly superior angular resolution. On the theory side this could be included in the calculation by using ref. [145].

We explore ISR, MPI and hadronization in more detail within Pythia 8.2 in fig. 4.8, for the two jet transverse momentum intervals $p_T = 30 - 50$ GeV (left) and $p_T = 100 - 200$ GeV (right) (corresponding to the upper row in fig. 4.7). All three contributions are sources of additional soft radiation in the jet. The standard jet axis is sensitive to this additional soft radiation whereas the WTA axis is insensitive, leading to the broadening of the distribution seen in the figure. We observe that in the lower p_T interval in fig. 4.8 ISR and MPI are the dominant effects, which are relevant over the entire displayed range of θ. For the higher p_T interval, ISR is the most important effect. The correction due to hadronization is only relevant for small values of θ for both p_T intervals considered here, in agreement with the model in sec. 4.5.2.

Next, we investigate differences between quark and gluon jets. We separately

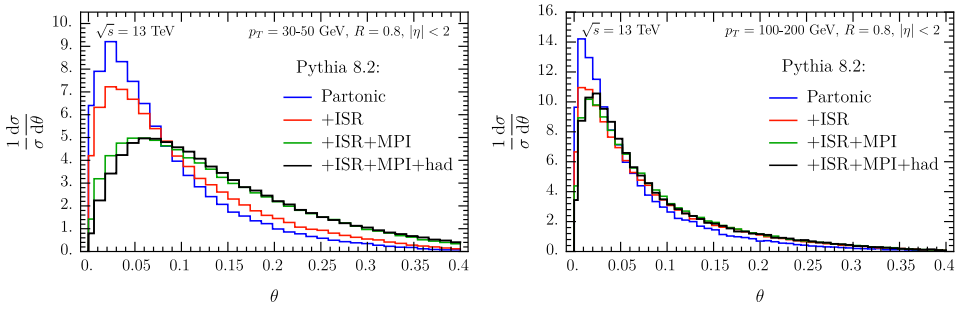

Figure 4.8 PYTHIA results for the angle between the standard and WTA jet axis, for the kinematics corresponding to the upper row in fig. 4.7. Shown are the partonic result (blue), including ISR (red), MPI (green) and also hadronization (black).

show the quark (blue) and gluon (red) distributions in fig. 4.9 for $p_T = 100$ GeV (dashed) and 200 GeV (dotted). The p_T integrated result, where we include appropriate quark/gluon fractions, is shown by the solid red curve. Gluons radiate more, and therefore the standard and WTA axes are further separated, leading to a broader distribution for gluon jets compared to quark jets.

We now consider the angle between the WTA and the soft drop groomed jet axes. First, we study the impact of soft drop grooming in fig. 4.10, choosing the same kinematical setup as in fig. 4.7 with the jet transverse momentum interval of $p_T = 100 - 200$ GeV as a representative example. The ungroomed result is shown for reference. For the soft drop grooming parameters we choose $z_{\mathrm{cut}} = 0.1$ and $\beta = 0$, 1, 2 (left panel) and $z_{\mathrm{cut}} = 0.05$, 0.1, 0.2, 0.3 and $\beta = 1$ (right panel), and the corresponding curves are shown at NLL$'$ accuracy. From the left panel, we observe that the ungroomed result is approached for large values of β, which is expected as the ungroomed result is recovered in the limit $\beta \to \infty$. Similarly, the right panel shows that for smaller values of z_{cut} the ungroomed result is approximated. We also note that the transition point between the groomed and the ungroomed distribution depends on z_{cut} but it is independent of β. This is consistent with the perturbative results presented in sec. 4.3 above. In general, we observe that the grooming leads to a distribution that peaks at smaller values of the angle θ. This can be understood in the sense that soft drop grooming removes soft radiation from the jet and therefore the groomed axis and the WTA axis, which is insensitive to soft radiation by construction, are closer in angle than the WTA and the standard jet axis. The size of the peak at small values of θ is enhanced when more aggressive grooming parameters are chosen, i.e. small values of β or large

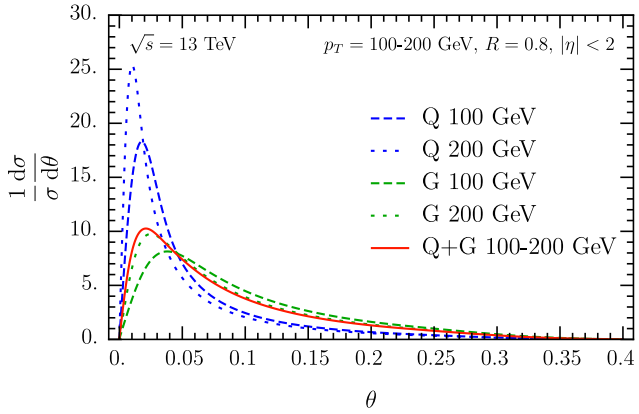

Figure 4.9 Quark (blue) and gluon (red) distributions for the angle between the standard and the WTA axis for $p_T = 100$ GeV (dashed) and 200 GeV (dotted). The solid line shows the p_T integrated result summed over quarks and gluons which corresponds to the central curve in the upper right panel of fig. 4.7.

values of $z_{\,\mathrm{cut}}$.

Next, we show the comparison of our perturbative results to Pythia 8.2 simulations. In fig. 4.11, we show the comparison of our perturbative results for $z_{\mathrm{cut}} = 0.1$ and $\beta = 0$, including the nonperturbative model as described in sec. 4.5.2, and the Pythia results at parton level and including ISR, MPI and hadronization. We choose the same kinematics as in fig. 4.7. In the highest jet p_T bins, the difference between the two calculations is very small and the cross section for the angle between the WTA and the groomed jet axes has a narrow peak at very small values $\theta \lesssim 0.01$ which implies that the two jet axes almost agree. In the lowest p_T bin there is still a small discrepancy between the perturbative results and Pythia due to ISR, MPI and hadronization. We observe that soft drop grooming does not significantly reduce the size of these effects at low p_T, compared to the ungroomed case shown in fig. 4.7.

Further, we present numerical results for the angle between the standard and the soft drop groomed jet axes. Our numerical results at NLL accuracy are shown in fig. 4.12 along with Pythia results, for the same LHC kinematics as in fig. 4.7. We integrated out the dependence on the soft drop groomed radius R_g, but note that in principle it is possible to directly obtain double differential results from our numerical setup. This may be advantageous if it is experimentally necessary to impose an additional cut on the soft drop groomed radius R_g

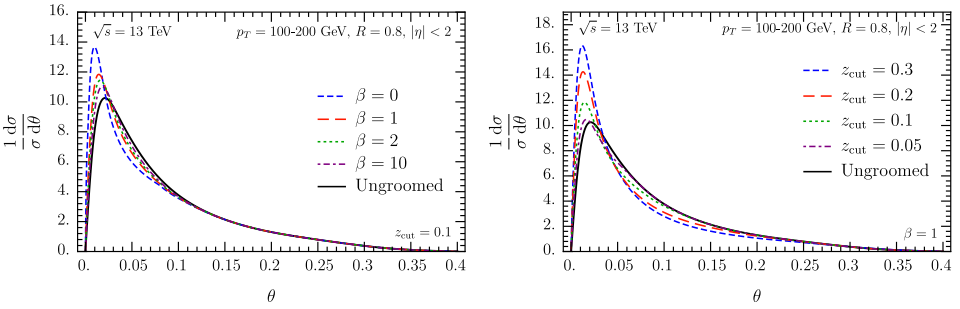

Figure 4.10 Left: Numerical results for the angle between the WTA and the soft drop groomed jet axis with $z_{\,\rm cut} = 0.1$ and different values of $\beta = 0, 1, 2, 10$. Right: Results for a fixed value of $\beta = 1$ but different values of $z_{\,\rm cut} = 0.05, 0.1, 0.2, 0.3$. In both panels we show the ungroomed result (solid black) for comparison.

as is sometimes the case for groomed jet substructure observables [146–148]. Even though this observable is more sensitive to soft physics, the agreement between Pythia and our perturbative results is nevertheless good. We observe that the perturbative results vanish for $\theta \to 0$, whereas the Pythia results show a spike in the leftmost bin. In Pythia the spike corresponds to jets where no branch gets groomed away and, hence, the standard and soft drop groomed jet axis are exactly aligned. We note that in general the difference between the two Pythia curves shown in fig. 4.12 is larger than for the other two angles considered above. This is expected as the angle between the standard and groomed jet axes is very soft sensitive making this observable a promising candidate to tune parton shower event generators.

In fig. 4.13, we show the dependence of the angle between the standard and groomed axes on the grooming parameter β for $p_T = 100 - 200$ GeV which corresponds to the upper right panel of fig. 4.12. We choose four exemplary β values 0, 1, 2, 3 (different dashing and colors) but the same $z_{\,\rm cut} = 0.1$. In the limit $\beta \to \infty$, the grooming is removed and the ungroomed jet is recovered, which implies that the two jet axes considered here are aligned. This manifests itself in our numerical results by the fact that the curves shown in fig. 4.13 eventually approach a delta function at $\theta = 0$ for large values of β. Note that we obtain the correct limit numerically because the nonperturbative exponent in $b_\perp$ space approximates unity for $\beta \to \infty$ (regime A), see the discussion in sec. 4.5.2. Similarly, we consider four different values of $z_{\rm cut}$, suggesting that in the limit $z_{\rm cut} \to 0$ the distribution also approaches a delta function, even though our formalism is strictly speaking not valid in this limit.

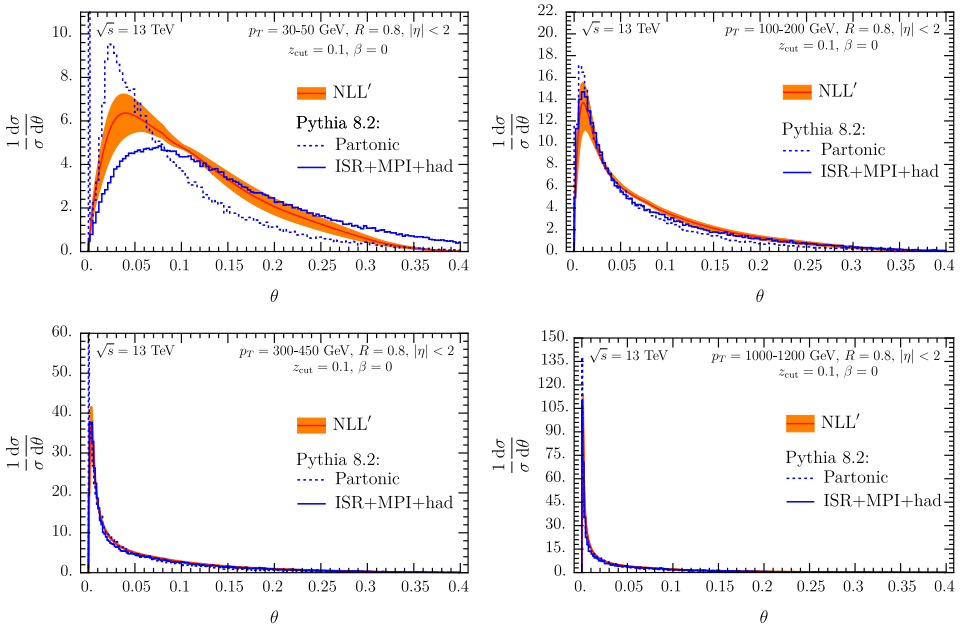

Figure 4.11 Numerical results for the angle between the WTA and the soft drop groomed jet axis with $z_{\rm cut} = 0.1$ and $\beta = 0$ at NLL′ accuracy. We consider the same kinematics as in fig. 4.7 and compare to the corresponding Pythia 8.2 results.

We next examine the sensitivity of each observable to nonperturbative physics. In fig. 4.14 we focus on the lowest p_T-bin, $30-50$ GeV, where the effect of nonperturbative physics is largest. At larger jet transverse momentum, the nonperturbative effects arise at smaller angles and are therefore strongly Sudakov suppressed by the resummation. To gauge the nonperturbative sensitivity, we vary the model parameter $g_2(b_\perp^{\max})$ defined in eq. (4.50) between our canonical choice of $g_2(b_\perp^{\max}) = 0.18$ GeV^2 to twice and half its value. The angle between the winner-take-all axis and either the standard or the groomed axis has the least sensitivity to our choices of nonperturbative parameters. The effect of the nonperturbative model does not change the spectrum at large angles, so the nonperturbative sensitivity is most apparent in the peak of the distribution. Furthermore, the variation of $g_2(b_\perp^{\max})$ is within the perturbative uncertainty estimated from scale variations. In stark contrast, the angle of the standard to groomed axes displays a large sensitivity, and at no point in the spectrum do we see any turning off of the nonperturbative physics.

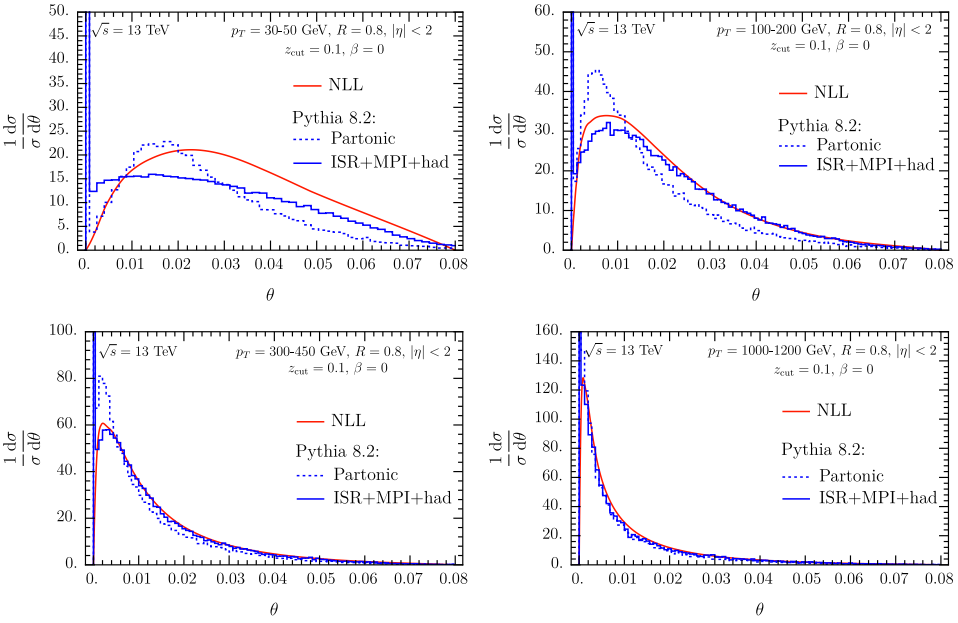

Figure 4.12 Numerical results for the angle θ between the standard and the soft drop groomed jet axis with $z_{\rm cut} = 0.1$ and $\beta = 0$ at NLL accuracy. We consider the same LHC kinematics as in fig. 4.7 and compare to the corresponding Pythia 8.2 results.

4.7 Conclusions

In this chapter we presented a first calculation of the angles between different jet axes. We considered three different jet axes: The standard jet axis, the soft drop groomed jet axis and the jet axis using a winner-take-all recombination scheme. Our studies were motivated by the different soft sensitivity of these different jet axes. The winner-take-all scheme yields a jet axis which is insensitive to soft radiation at leading power and also the soft drop groomed jet axis has a reduced sensitivity to soft physics compared to the standard jet axis. By considering the angles between different axes, the soft radiation pattern inside reconstructed jets can be studied. Within Soft Collinear Effective Theory, we performed calculations at next-to-leading logarithmic (NLL′ or NLL) accuracy, where large logarithms of the angle between the the standard and groomed vs. the winner-take-all axes are resummed to all orders, including the contribution of non-global logarithms in the leading color approximation. We presented numerical results for relevant LHC kinematics at $\sqrt{s} = 13$ TeV and compared our results to Pythia 8.2 simulations. Overall we found very

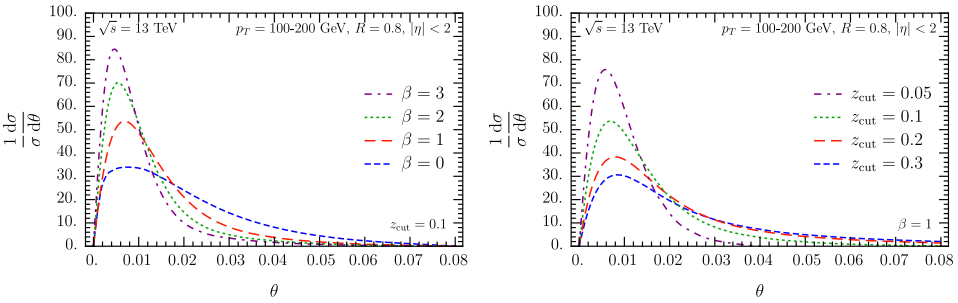

Figure 4.13 The angle between the standard and soft drop groomed jet axis for the same kinematics as in the upper right panel of fig. 4.12 but for different values of $\beta = 0 - 3$ (left), and for different values of $z_{\rm cut}$ (right).

good agreement except for jets with very low jet transverse momentum, where different nonperturbative and power-suppressed effects play an important role.

The angle between the standard and soft drop groomed jet axes is particularly soft sensitive, as shown in fig. 4.14, as it is a measure of the radiation which is groomed away by the soft drop algorithm. The corresponding factorization theorem depends on the soft drop groomed jet radius R_g. We resummed large logarithms of both the angle between the jet axes and the groomed radius R_g, integrating over R_g after the resummation is performed to obtain a distribution for the angle between the axes. The all-order structure of non-global logarithms for this observable is nontrivial, limiting the accuracy of our calculation in this case. The soft sensitivity of the angle between the standard and groomed jet axis makes this observable very well suited to tune parton shower event generators, however, further theoretical work must be done to extend the resummation to NLL$'$ including non-global correlations, before such studies can be conducted.

We included nonperturbative effects in impact parameter space by introducing a model function, which is related to the nonperturbative component of the rapidity anomalous dimension relevant for transverse momentum resummation. This was crucial to obtain a sensible β-dependence for the angle between the standard and groomed jet axis. Therefore, the observables considered here can provide important constraints on this universal nonperturbative quantity.

We expect that the observables considered here will have important applications in proton-proton as well as heavy-ion collisions at the LHC and RHIC. In addition to the aforementioned tuning of parton shower Monte Carlo programs, or studying the nonperturbative contribution to the rapidity anomalous dimension, it could provide valuable insight into the effect of the medium in heavy

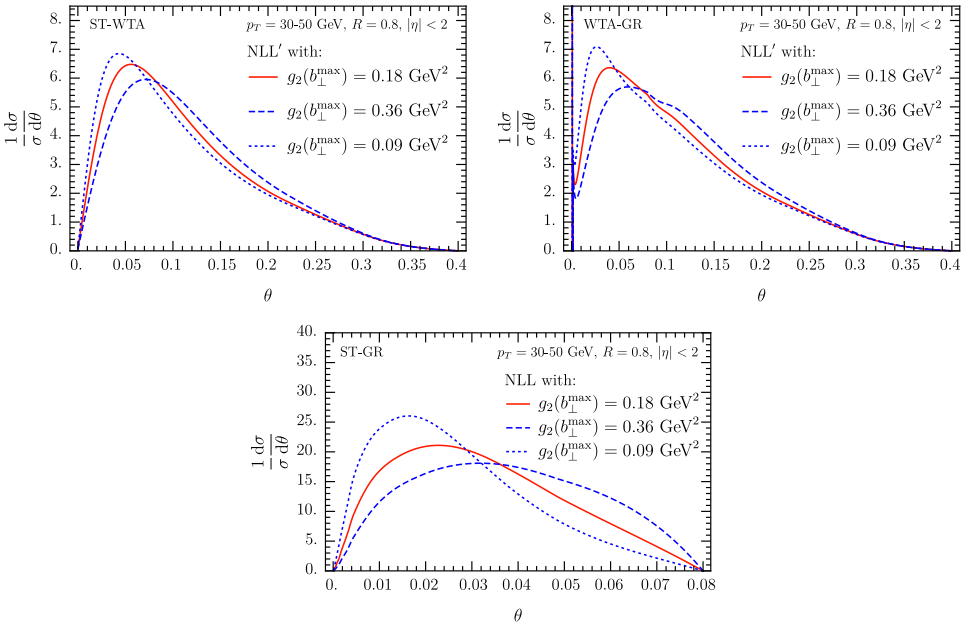

Figure 4.14 The nonperturbative sensitivity of the angle between the WTA and ST axis (upper left), WTA and GR axis (upper right) and ST and GR axis (bottom), for the kinematics corresponding to the upper left panel of fig. 4.7. Shown are our NLL′ (or NLL) result with the default $g_2(b_\perp^{\max}) = 0.18$ GeV^2 (orange), as well as double (blue dashed) and half (blue dotted) this value.

ion collisions. Furthermore, for jets with a large radius parameter, these axes could be sensitive to the color flow of a collision, similar to the pull [115, 149]. As we noted, a measurement using charged particle tracks would be necessary to access the small angles we consider. Thus, another future direction is to directly incorporate the effect of a track-based measurement in our calculations.

5

Jet energy drop

As discussed in chapter 2, a crucial ingredient for making meaningful jet substructure theory-data comparisons is the development of jet grooming techniques that are compatible with theoretical calculations. Grooming techniques address the highly-contaminated environment at hadron colliders, systematically removing soft wide-angle radiation from the observed jets, see fig. 5.1, thereby also reducing hadronization effects. Examples are trimming [24], pruning [150], soft killer [151], soft drop [23], iterated soft drop [25] and recursive soft drop [152]. Initially, grooming (desirable for experiment) and theoretical precision seemed mutually exclusive, but some of these grooming techniques are quite amenable to calculations in perturbative QCD. Specific examples include: the soft-drop groomed jet mass [142, 153, 154], the groomed jet radius [122] and the repositioning of the jet axes due to grooming [2], as we saw last chapter. Experimental results for soft-drop groomed jet observables can be found in refs. [146–148,155–161], and for related recent theoretical calculations of groomed jet substructure observables see refs. [162–179].

In this chapter, we consider the jet energy drop, which is given by the relative transverse momentum (or energy) difference between the groomed and ungroomed (i.e. original) jet,

$$\Delta_E = \frac{p_T - p_T^{\mathrm{gr}}}{p_T} = 1 - \frac{p_T^{\mathrm{gr}}}{p_T}\,. \tag{5.1}$$

We consider the jet energy drop for three grooming procedures that have been used by experimental collaborations: i) trimming, ii) soft drop and iii) iterated soft drop. This observable is of great interest for characterizing the impact of grooming on the measured jets. In particular, the soft sensitivity of these observables makes them ideally suited for tuning parton shower event generators, see e.g. refs. [53, 180]. While we focus in this chapter on the comparison to Pythia in the perturbative regime, studying the nonperturbative regime requires a field theoretic understanding of the effects on grooming, which have

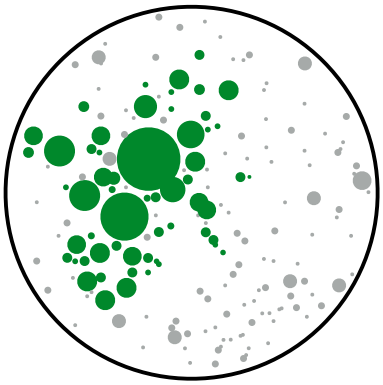

Figure 5.1 Schematic picture of a jet, with circles representing radiation whose size corresponds to its energy. Wide-angle soft radiation (grey) is groomed away, resulting in the groomed jet (green).

been discussed in refs. [2, 172]. For models describing the nonperturbative effect with grooming, see refs. [153, 164, 166, 171, 181–183]. Similarly, collinear drop [139] also probes soft radiation, by "taking the difference" of two soft drop grooming procedures with different parameters. However, this removes the softest radiation, which is kept in our case.

For each grooming procedure, we develop the factorization formula for jet energy drop within Soft Collinear Effective Theory (SCET) [12–16], which allows for the resummation of large logarithmic corrections to all orders at next-to-leading logarithmic (NLL′) order. The logarithms we resum are those of the jet energy drop, as well as the jet radius and grooming parameters. We will treat all logarithms as independent, but in principle, one can refine predictions (e.g. near the endpoint in Δ_E) by considering parametric relations between the jet energy drop and grooming parameters. To obtain our predictions, we included the one-loop expression for the ingredients of the factorization theorem, the one-loop anomalous dimensions, and two-loop cusp anomalous dimension, and the non-global [83] and Abelian logarithms including clustering effects [184]. While there has been significant progress in the study of NGLs [91, 93, 96, 105, 118–121, 185–187], including clustering effects [188–193], we restrict to their contribution at order α_s^2, since the higher order terms are numerically irrelevant for our phenomenological results.

In order to resum the relevant logarithms for soft drop, we perform a joint resummation of logarithms of Δ_E and the soft drop groomed jet radius R_g [23, 122]. For these two variables, we develop a two-dimensional scale-setting technique in order to perform numerical calculations. Depending on the relative

scaling of Δ_E and R_g, a different factorization formula is obtained, which are matched before integrating over a range of R_g or integrating it out completely. For the special case of soft-drop parameter $\beta = 0$, the corresponding cross section is not infrared safe but Sudakov safe [23], and so resummation is essential to obtain a prediction. Other examples of Sudakov-safe observables include the soft-drop momentum sharing fraction z_g [26], ratios of two angularities [194, 195], and the jet-pull angle [113, 115, 149]. In this work, we extend previous results of the jet energy drop for soft drop with $\beta = 0$ beyond (modified) leading logarithmic accuracy.

The remainder of this chapter is organized as follows. In the three subsequent sections 5.1-5.3 we discuss the jet energy drop for the three grooming algorithms: Iterated soft drop, soft drop, and trimming. In each section, we first introduce the grooming procedure (though soft drop is already described in sec. 5.1), and present results at fixed order. We then factorize the cross section to resum large logarithmic corrections to all orders, and give expressions for all necessary perturbative ingredients, as well as non-global and clustering logarithms. In addition, we discuss profile scales and present numerical results for LHC kinematics, which we compare to Pythia. Note that sec. 5.1 contains many of the basic ingredients that are also needed in subsequent sections, such as the collinear factorization for inclusive jet production. In sec. 5.4, we draw conclusions and present an outlook.

5.1 Iterated soft drop

We start in sec. 5.1.1 by reviewing the factorization of the inclusive jet cross section in terms of PDFs, hard functions, and jet functions. This initial step exploits the collimated nature of jets, but is independent of further details of the jet measurement. It is therefore the same for the jet energy drop calculation for all three grooming procedures discussed in this work. The (iterated) soft drop algorithm was introduced in chapter 2. We present results for the corresponding one-loop jet function in sec. 5.1.2. In sec. 5.1.3, we discuss the refactorization of this jet function and resummation of the logarithms of the jet energy drop Δ_E and grooming parameter z_{cut}. In particular, we include results for all relevant functions at one-loop order, needed for our numerical results at NLL$'$. Non-global and clustering logarithms are discussed in sec. 5.1.4, and sec. 5.1.5 describes our central scale choice, as well as the scale variations used to assess the perturbative uncertainty. Finally, in sec. 5.1.6 we present numerical studies for LHC kinematics.

5.1.1 Jet production

Once more, we consider generic jet substructure measurements performed on an inclusive jet sample, as the discussion in this section applies to all jet energy drop observables in this chapter. The factorization follows exactly the same structure as in chapters 3 and 4, except the jet function is replaced by $\mathcal{G}_k(z, \Delta_E, p_T R, \mu)$. The jet function $\mathcal{G}_k$ also accounts for the jet energy drop Δ_E, and thus depends on the grooming parameters of the algorithm under consideration. Since the discussion so far is independent of the specific grooming procedure we have omitted dependence on the grooming parameters here, but will include them when describing specific cases below. As we focus on this jet function and its refactorization in the remainder of this work, we find it convenient to change the parton flavor index $\mathcal{G}_k$ to $\mathcal{G}_i$ from this point on. The characteristic scales of the various ingredients are the same as for inclusive jet production

$$\mu_f \sim \Lambda_{\mathrm{QCD}}\,, \qquad \mu_{\mathcal{H}} \sim p_T\,, \qquad \mu_{\mathcal{G}} \sim p_T R\,. \tag{5.2}$$

The resummation of logarithms of the jet radius $R = \mu_{\mathcal{G}}/\mu_{\mathcal{H}}$ is achieved by evolving the jet function $\mathcal{G}_i$ from the jet scale $\mu_{\mathcal{G}}$ to the hard scale $\mu_{\mathcal{H}}$, using the time-like DGLAP evolution equation [130–132]

$$\mu \frac{\mathrm{d}}{\mathrm{d}\mu}\, \mathcal{G}_i(z, \Delta_E, p_T R, \mu) = \sum_j \int_z^1 \frac{\mathrm{d}z'}{z'}\, \frac{\alpha_s}{\pi} P_{ji}(z/z')\, \mathcal{G}_j(z', \Delta_E, p_T R, \mu)\,. \tag{5.3}$$

The relevant Altarelli-Parisi splitting functions P_{ji} are collected in eq. (A.6).

Integrating the jet function $\mathcal{G}_i$ over the jet energy drop variable Δ_E, the semi-inclusive jet function J_i of ref. [50] is obtained

$$\int_0^1 \mathrm{d}\Delta_E\, \mathcal{G}_i(z, \Delta_E, p_T R, \mu) = J_i(z, p_T R, \mu)\,. \tag{5.4}$$

At next-to-leading order (NLO), it is convenient to rewrite the jet function $\mathcal{G}_i$ as

$$\mathcal{G}_i(z, \Delta_E, p_T R, \mu) = J_i(z, p_T R, \mu)\, \delta(\Delta_E) + \delta(1-z) \Delta\mathcal{G}_i(\Delta_E, p_T R, \alpha_s(\mu))\,. \tag{5.5}$$

At this order, the initial parton splits into at most two other partons. The distribution in Δ_E is encoded in the second term, which only receives a contribution when both partons are inside the jet, so $z = 1$. In the following sections, we only report on $\Delta\mathcal{G}_i$, which encodes the dependence on the grooming procedure and only depends on the scale μ through the strong coupling.

Using eq. (5.5), we write

$$\mathcal{G}_i(z, \Delta_E, p_T R, \mu) = \sum_j J_{ij}(z, p_T R, \mu) \Big[\delta(\Delta_E) + \Delta\mathcal{G}_j\big(\Delta_E, p_T R, \alpha_s(\mu)\big) \Big] + \mathcal{O}(\alpha_s^2)$$
$$\equiv \sum_j J_{ij}(z, p_T R, \mu)\, \tilde{\mathcal{G}}_j\big(\Delta_E, p_T R, \alpha_s(\mu)\big)\,, \tag{5.6}$$

conveniently separating the formation process of inclusive jets (J_{ij}) from the grooming and Δ_E measurement ($\tilde{\mathcal{G}}_i$) [1, 73]. Note that eq. (5.6) is not a separation of physics at different scales. Upon summation over the flavor index j, we recover the semi-inclusive jet function

$$J_i(z, p_T R, \mu) = \sum_j J_{ij}(z, p_T R, \mu)\,. \tag{5.7}$$

The coefficients J_{ij} are given by equation (C.2) [1].

5.1.2 Fixed-order results

When the jet energy drop Δ_E and the grooming parameter z_{cut} are not parametrically small, i.e. Δ_E, z_{cut} are both order one, a fixed-order calculation of the relevant jet function $\Delta\mathcal{G}_i^{\text{ISD}}$ is sufficient, which we present here. In sec. 5.1.3, we will consider the case where they are parametrically small and lead to large logarithms in the jet function, requiring resummation.

To calculate the jet function $\Delta\mathcal{G}_i^{\text{ISD}}$, we can use the squared matrix element and the phase space in the collinear limit [140] (similar to eq. (3.30))

$$\int \mathrm{d}\Phi_2\, \sigma^c_{2,q} = \frac{\alpha_s}{\pi} \frac{e^{\epsilon\gamma_E}}{\Gamma(1-\epsilon)} \left(\frac{\mu}{E}\right)^{2\epsilon} \int_0^1 \frac{\mathrm{d}x}{(x(1-x))^{2\epsilon}}\, C_F \left[\frac{1+x^2}{1-x} - \epsilon\,(1-x)\right] \int \frac{\mathrm{d}\theta}{\theta^{1+2\epsilon}}\,, \tag{5.8}$$

$$\int \mathrm{d}\Phi_2\, \sigma^c_{2,g} = \frac{\alpha_s}{\pi} \frac{e^{\epsilon\gamma_E}}{\Gamma(1-\epsilon)} \left(\frac{\mu}{E}\right)^{2\epsilon} \int_0^1 \frac{\mathrm{d}x}{(x(1-x))^{2\epsilon}} \Big\{ C_A \Big[\frac{x}{1-x} + \frac{1-x}{x} + x(1-x)\Big]$$
$$+ n_f T_F \Big[x^2 + (1-x)^2 - 2\epsilon\, x(1-x)\Big] \Big\} \int \frac{\mathrm{d}\theta}{\theta^{1+2\epsilon}}\,, \tag{5.9}$$

where θ is the angle between the two partons and E is the energy of the parton initiating the jet.[1] The one-loop jet function for soft drop and iterated soft drop are identical. However, differences appear at higher orders, leading to

[1] For a jet at central rapidity $E = p_T$ and the distance in (η, ϕ) corresponds (approximately) to an angle. Boost invariance implies that our calculation is valid for general rapidity.

rather different factorization structures. The measurement function for the jet function for (iterated) soft drop is given by

$$\begin{aligned}
&\Delta\mathcal{G}_i^{\rm ISD}(\Delta_E, p_T R, z_{\rm cut}, \beta, \alpha_s(\mu)) \\
&\quad= \int \mathrm{d}\Phi_2\, \sigma^c_{2,i} \Theta\left(\theta < R\right) \Big[\Theta\big(x > z_{\rm cut}(\theta/R)^\beta\big)\Theta\big(1-x > z_{\rm cut}(\theta/R)^\beta\big)\delta(\Delta_E) \\
&\qquad + \Theta\big(x > z_{\rm cut}(\theta/R)^\beta\big)\Theta\big(1-x < z_{\rm cut}(\theta/R)^\beta\big)\delta(\Delta_E - (1-x)) \\
&\qquad + \Theta\big(x < z_{\rm cut}(\theta/R)^\beta\big)\Theta\big(1-x > z_{\rm cut}(\theta/R)^\beta\big)\delta(\Delta_E - x) - \delta(\Delta_E)\Big].
\end{aligned} \tag{5.10}$$

The last term subtracts the semi-inclusive jet function, as required for $\Delta\mathcal{G}_i^{\rm ISD}$, see eq. (5.5). Performing the integrals and expanding in distributions, we find for quark and gluon jets the following results

$$\begin{aligned}
&\Delta\mathcal{G}_q^{\rm ISD}(\Delta_E, p_T R, z_{\rm cut}, \beta, \alpha_s(\mu)) \\
&\quad= \frac{\alpha_s C_F}{\pi}\frac{1}{\beta}\Bigg\{\Theta(\Delta_E < z_{\rm cut})\Bigg[-2\left[\frac{\ln\Delta_E}{\Delta_E}\right]_+ + 2\ln z_{\rm cut}\frac{1}{[\Delta_E]_+} \\
&\qquad + \left(3 - \frac{2}{1-\Delta_E}\right)\ln\Big(\frac{\Delta_E}{z_{\rm cut}}\Big)\Bigg] + \delta(\Delta_E)\left[-\ln^2 z_{\rm cut} + 3z_{\rm cut} - 2{\rm Li}_2(z_{\rm cut})\right]\Bigg\},
\end{aligned} \tag{5.11}$$

$$\begin{aligned}
&\Delta\mathcal{G}_g^{\rm ISD}(\Delta_E, p_T R, z_{\rm cut}, \beta, \alpha_s(\mu)) \\
&\quad= \frac{\alpha_s}{\pi}\frac{1}{\beta}\Bigg\{\Theta(\Delta_E < z_{\rm cut})\Bigg(-2C_A\left[\frac{\ln\Delta_E}{\Delta_E}\right]_+ + 2C_A\ln z_{\rm cut}\frac{1}{[\Delta_E]_+} \\
&\qquad - \left[2C_A\left(\frac{1}{1-\Delta_E} - 2 + \Delta_E - \Delta_E^2\right) + 2n_f T_F\left(\Delta_E^2 + (1-\Delta_E)^2\right)\right]\ln\Big(\frac{\Delta_E}{z_{\rm cut}}\Big)\Bigg) \\
&\qquad + \delta(\Delta_E)\Bigg[C_A\Bigg(-\ln^2 z_{\rm cut} + 4z_{\rm cut} - \frac{z_{\rm cut}^2}{2} + \frac{2}{9}z_{\rm cut}^3 - 2{\rm Li}_2(z_{\rm cut})\Bigg) \\
&\qquad + n_f T_F\left(-z_{\rm cut} + z_{\rm cut}^2 - \frac{4}{9}z_{\rm cut}^3\right)\Bigg]\Bigg\}.
\end{aligned} \tag{5.12}$$

From eq. (5.11) we read off that the jet energy drop is bounded by $\Delta_E < z_{\rm cut}$ at NLO. Note that by construction (see eq. (5.6)) we have

$$\int_0^1 \mathrm{d}\Delta_E\, \Delta\mathcal{G}_i^{\rm ISD}(\Delta_E, p_T R, z_{\rm cut}, \beta, \alpha_s(\mu)) = 0\,. \tag{5.13}$$

As a consistency check, we investigate several limits of the grooming parameters. First, we consider the limit $\beta \to \infty$. As can be seen from eq. (5.11), the entire jet function $\Delta\mathcal{G}_i^{\rm ISD}$ is proportional to $1/\beta$ and vanishes in this limit.

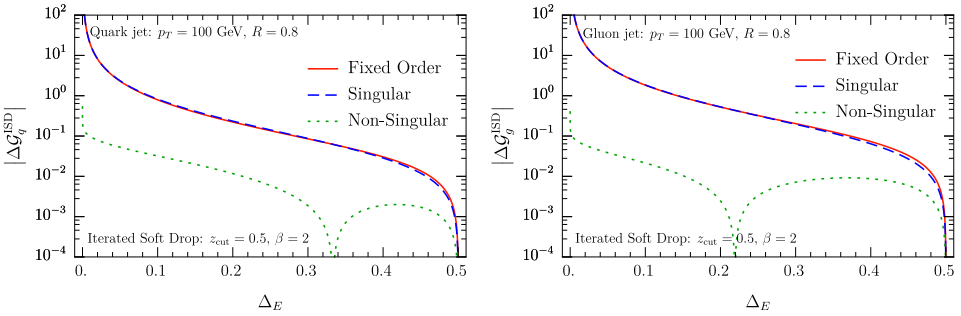

Figure 5.2 Comparison of the full one-loop result for jet function for iterated soft drop $\Delta\mathcal{G}_i^{\rm ISD}$ (solid red), its singular (dashed blue) and non-singular terms (dotted green), for jets initiated by quarks (left) and gluons (right).

Indeed, for $\beta \to \infty$ the soft drop condition in $z > z_{\rm cut}(\theta/R)^\beta$ is always trivially satisfied and no branches are removed from the jet. Second, since $\Delta\mathcal{G}_i^{\rm ISD}$ is proportional to $1/\beta$ we cannot take the limit $\beta \to 0$ at fixed order. Indeed, for iterated soft drop, the jet energy drop with $\beta = 0$ is not IRC safe. For regular soft drop the case $\beta = 0$ is still Sudakov safe, as discussed in section 5.2.4. Third, we consider the limit $z_{\rm cut} \to 0$, which (similar to $\beta \to \infty$) corresponds to the limit of no grooming. To see more clearly that $\Delta\mathcal{G}_i^{\rm ISD}$ also vanishes in this limit, we rewrite it as follows: The plus distributions in eq. (5.11) are defined such that they vanish when integrated over the interval $0 < \Delta_E < 1$. We can rewrite these distributions such that they instead vanish when integrating over the interval $0 < \Delta_E < z_{\rm cut}$ of the theta function that multiplies the distributions, which we indicate by the subscript $\Theta+$. For example, for the quark case this yields

$$\Delta\mathcal{G}_q^{\rm ISD} = \frac{\alpha_s C_F}{\pi}\frac{1}{\beta}\left\{\Theta(\Delta_E < z_{\rm cut})\left[-2\left[\frac{\ln\Delta_E}{\Delta_E}\right]_{\Theta+} + 2\ln z_{\rm cut}\frac{1}{[\Delta_E]_{\Theta+}} + \left(3 - \frac{2}{1-\Delta_E}\right)\ln\left(\frac{\Delta_E}{z_{\rm cut}}\right)\right] + \delta(\Delta_E)\left[3z_{\rm cut} - 2{\rm Li}_2(z_{\rm cut})\right]\right\}, \tag{5.14}$$

and similarly for the gluon, making it clear that $\Delta\mathcal{G}_i^{\rm ISD}$ vanishes in the limit $z_{\rm cut} \to 0$.

We end this section by comparing the singular terms, obtained by expanding $\Delta\mathcal{G}_i^{\rm ISD}$ in the limit $\Delta_E \ll z_{\rm cut} \ll 1$, to the full NLO expression of $|\Delta\mathcal{G}_i^{\rm ISD}|$, shown in fig. 5.2. We chose representative values of the soft-drop parameters and jet kinematics, indicated in the figure. We observe at NLO the non-singular power corrections, which equals the difference between the singular terms and

the fixed-order NLO, are very small compared to singular terms at NLO over the entire range of Δ_E, suggesting the importance of all-order resummation, which is discussed in the next section. Because the non-singular is so small, we do not include it as a matching correction, since its impact on our results is negligible.

5.1.3 Factorization and resummation

In this section we discuss the refactorization of the jet function for iterated soft drop, which will enable the resummation of the logarithms of the jet energy drop Δ_E and grooming parameter z_{cut}. Typically $z_{\text{cut}} = 0.1$ (we will consider larger values as well), so we assume the parametric scaling $\Delta_E \ll z_{\text{cut}} \ll 1$. We start with a leading logarithmic (LL) analysis of the jet energy drop, by analyzing the Lund diagram [138] shown in fig. 5.3. By using the logarithm of the angle θ and momentum fraction z on the horizontal and vertical axis, emissions have a uniform probability distribution in this plane at LL accuracy. The grooming condition and the measurement are indicated by the two dashed lines. For the cross section with jet energy drop below some value Δ_E, emissions inside the shaded triangular area in the Lund plane are not allowed. Such emissions are not groomed away and therefore lead to a value of the jet energy drop that is larger than Δ_E. Here it is important to note that for iterated soft drop all branches along the leading branch are tested against the soft drop condition, whereas the original soft drop terminates once the criterion $z > z_{\text{cut}}(\theta/R)^\beta$ is met. From the area of the vetoed region we can calculate the LL expression for the cross section cumulative in Δ_E, from which we obtain the differential result by taking the derivative:

$$\tilde{\mathcal{G}}_i^{\text{ISD}}\big(\Delta_E, p_T R, z_{\text{cut}}, \beta, \alpha_s(\mu)\big) \overset{\text{LL}}{=} \frac{\mathrm{d}}{\mathrm{d}\Delta_E} \exp\left[-\frac{\alpha_s C_i}{\pi}\frac{1}{\beta}\ln^2\left(\frac{z_{\text{cut}}}{\Delta_E}\right)\right]. \quad (5.15)$$

The color factors are $C_q = C_F$ ($C_g = C_A$) for jets initiated by a quark (gluon).

We will now extend the resummation to NLL′ accuracy using SCET. The power counting of the relevant modes in the effective theory can be read off from the Lund diagram, and correspond to the red dots at the corners of the triangle. There are two soft modes S_Z and S_G located on the vertical axis, which are sensitive to the jet boundary as well as the energy drop and grooming condition, respectively. In addition, there is a collinear-soft [196, 197] mode $\mathcal{S}_X$, located at the intersection (hence the subscript X) of the two dashed lines representing the measurement and the grooming condition, which it is therefore sensitive to. We note that for iterated soft drop there is no hard mode, which would correspond to the origin of the Lund diagram, in contrast to most jet substructure observables. Physically, this arises because energy drop

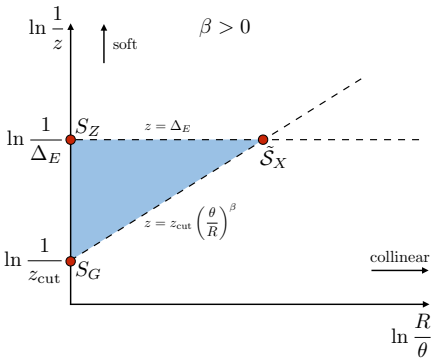

Figure 5.3 Lund diagram for the jet energy drop Δ_E for iterative soft drop grooming, with $\Delta_E \ll z_{\rm cut} \ll 1$. At LL accuracy, emissions in the shaded triangle are vetoed. The relevant modes in SCET correspond to the red dots at the corners of the triangle, with their power counting summarized in table 5.1.

with $z_{\rm cut} \ll 1$ only probes (collinear-)soft radiation. The relevant scaling of the three modes is summarized in table 5.1, in terms of the light-cone components of their momenta,

$$p^\mu = \bar{n}\cdot p \, \frac{n^\mu}{2} + n\cdot p \, \frac{\bar{n}^\mu}{2} + p_\perp^\mu \,, \tag{5.16}$$

where $n^\mu = (1,0,0,1)$ is along the jet axis, $\bar{n}^\mu = (1,0,0,-1)$, and $p_\perp^\mu$ denotes the transverse components. This leads to the following factorization formula for $\tilde{\mathcal{G}}_i^{\rm ISD}$,

$$\begin{aligned}\tilde{\mathcal{G}}_i^{\rm ISD}\big(\Delta_E, p_T R, z_{\rm cut}, \beta, \alpha_s(\mu)\big) &\overset{\rm NLL'}{=} S_{i,G}(z_{\rm cut} p_T R, \beta, \mu) \int \mathrm{d}\Delta'_E \, S_{i,Z}(\Delta'_E, p_T R, \mu) \\ &\quad \times \mathcal{S}_{i,X}(\Delta_E - \Delta'_E, z_{\rm cut}^{-1/\beta} p_T R, \beta, \mu) \, S_i^{\rm NG}\left(\frac{\Delta_E}{z_{\rm cut}}\right).\end{aligned} \tag{5.17}$$

To achieve NLL′ accuracy, we also include the contribution from non-global logarithms, which are accounted for by the non-global function $S_i^{\rm NG}$, discussed in sec. 5.1.4. Strictly speaking, the NGLs should also be included through a convolution in Δ_E, but the difference with the multiplicative treatment above is beyond the accuracy we are working at, see sec. 2.4 of ref. [1].

Mode:	Function:	Scaling $(n\cdot p, \bar{n}\cdot p, p_\perp)$
soft	S_G	$z_{\rm cut}\, p_T\, (R^2, 1, R)$
soft	S_Z	$\Delta_E\, p_T\, (R^2, 1, R)$
collinear-soft	$\mathcal{S}_X$	$\Delta_E\, p_T \Big(\big(\frac{\Delta_E}{z_{\rm cut}}\big)^{2/\beta} R^2, 1, \big(\frac{\Delta_E}{z_{\rm cut}}\big)^{1/\beta} R \Big)$

Table 5.1 The modes in SCET that enter in the refactorization of the jet function $\tilde{\mathcal{G}}_i^{\rm ISD}$ for the jet energy drop with iterated soft drop, with $\Delta_E \ll z_{\rm cut} \ll 1$.

The one-loop expressions for other three functions in eq. (5.17) are given by

$$S_{i,G}(z_{\rm cut} p_T R, \beta, \mu) = 1 + \frac{\alpha_s C_i}{\pi(1+\beta)} \left\{ -\ln^2\left(\frac{\mu}{z_{\rm cut} p_T R}\right) + \frac{\pi^2}{24} \right\}, \tag{5.18}$$

$$\begin{aligned} S_{i,Z}(\Delta_E, p_T R, \mu) = \delta(\Delta_E) + \frac{\alpha_s C_i}{\pi} \Bigg\{ & 2 \left[\frac{\ln \Delta_E}{\Delta_E} \right]_+ - \frac{2}{[\Delta_E]_+} \ln\left(\frac{\mu}{p_T R}\right) \\ & + \delta(\Delta_E) \left[\ln^2\left(\frac{\mu}{p_T R}\right) - \frac{\pi^2}{24} \right] \Bigg\}, \end{aligned} \tag{5.19}$$

$$\begin{aligned} \mathcal{S}_{i,X}(\Delta_E, z_{\rm cut}^{-1/\beta} p_T R, \beta, \mu) = \delta(\Delta_E) + \frac{\alpha_s C_i}{\pi} \Bigg\{ & -2 \frac{1+\beta}{\beta} \left[\frac{\ln \Delta_E}{\Delta_E} \right]_+ \\ & + \frac{2}{[\Delta_E]_+} \ln\left(\frac{\mu}{z_{\rm cut}^{-1/\beta} p_T R}\right) + \delta(\Delta_E) \frac{\beta}{1+\beta} \left[-\ln^2\left(\frac{\mu}{z_{\rm cut}^{-1/\beta} p_T R}\right) + \frac{\pi^2}{24} \right] \Bigg\}. \end{aligned} \tag{5.20}$$

We limited ourselves to reporting only the finite terms of the different functions, as the $1/\epsilon$ poles can be reconstructed from the $\ln \mu$ terms. We have verified that all $\ln \mu$ terms cancel in eq. (5.17), and that the remainder agrees with the NLO result in eq. (5.11) in the limit $\Delta_E \ll z_{\rm cut} \ll 1$, providing a check on the refactorization.

The natural scale of each mode is given by its virtuality. Reading off from table 5.1,

$$\mu_{S_G} \sim z_{\rm cut} p_T R\,, \quad \mu_{S_Z} \sim \Delta_E\, p_T R\,, \quad \mu_{\mathcal{S}_X} \sim \Delta_E^{(1+\beta)/\beta} z_{\rm cut}^{-1/\beta} p_T R\,. \tag{5.21}$$

By evaluating each function in eq. (5.17) at its natural scale, and evolving them to a common scale μ through renormalization group (RG) equations, we achieve the joint resummation of logarithms of Δ_E and $z_{\rm cut}$. The RG equations

are given by

$$\mu\frac{\mathrm{d}}{\mathrm{d}\mu}\,S_{i,G}(z_{\mathrm{cut}}p_TR,\beta,\mu)=\gamma_i^{S_G}(z_{\mathrm{cut}}p_TR,\beta,\mu)\,S_{i,G}(z_{\mathrm{cut}}p_TR,\beta,\mu)\,, \tag{5.22}$$

$$\mu\frac{\mathrm{d}}{\mathrm{d}\mu}\,S_{i,Z}(\Delta_E,p_TR,\mu)=\int\mathrm{d}\Delta'_E\,\gamma_i^{S_Z}(\Delta_E-\Delta'_E,p_TR,\mu)\,S_{i,Z}(\Delta'_E,p_TR,\mu)\,, \tag{5.23}$$

$$\begin{aligned}\mu\frac{\mathrm{d}}{\mathrm{d}\mu}\,\mathcal{S}_{i,X}(\Delta_E,z_{\mathrm{cut}}^{-1/\beta}p_TR,\beta,\mu)=&\int\mathrm{d}\Delta'_E\,\gamma_i^{\mathcal{S}_X}(\Delta_E-\Delta'_E,z_{\mathrm{cut}}^{-1/\beta}p_TR,\beta,\mu)\\&\times\mathcal{S}_{i,X}(\Delta'_E,z_{\mathrm{cut}}^{-1/\beta}p_TR,\beta,\mu)\,,\end{aligned} \tag{5.24}$$

where the corresponding anomalous dimensions can be found in the appendix B.3.3.

Next we discuss in some detail how we solve the different evolution equations, as similar techniques will be employed for the other grooming techniques discussed in subsequent section. Evolving the function $S_{i,G}$ from initial scale μ_0 to the scale μ, using the multiplicative RG equation in eq. (5.18),

$$\begin{aligned}S_{i,G}(z_{\mathrm{cut}}p_TR,\beta,\mu)&=U_{i,S_G}(z_{\mathrm{cut}}p_TR,\beta,\mu,\mu_0)\,S_{i,G}(z_{\mathrm{cut}}p_TR,\beta,\mu_0)\,,\\U_{i,S_G}(z_{\mathrm{cut}}p_TR,\beta,\mu,\mu_0)&=e^{-\frac{2}{1+\beta}K_i(\mu,\mu_0)}\left(\frac{\mu_0}{z_{\mathrm{cut}}p_TR}\right)^{-\frac{2}{1+\beta}\eta_i(\mu,\mu_0)}.\end{aligned} \tag{5.25}$$

The two functions K and η are given in appendix B.2. Similarly, for the evolution equations of the functions $S_{i,Z}$ and $S_{i,X}$, we find

$$S_{i,Z}(\Delta_E,p_TR,\mu)=\int\mathrm{d}\Delta'_E\,U_{i,Z}(\Delta_E-\Delta'_E,p_TR,\mu,\mu_0)\,S_{i,Z}(\Delta'_E,p_TR,\mu_0)\,, \tag{5.26}$$

$$\begin{aligned}\mathcal{S}_{i,X}(\Delta_E,z_{\mathrm{cut}}^{-1/\beta}p_TR,\beta,\mu)=&\int\mathrm{d}\Delta'_E\,U_{i,\mathcal{S}_X}(\Delta_E-\Delta'_E,z_{\mathrm{cut}}^{-1/\beta}p_TR,\beta,\mu,\mu_0)\\&\times\mathcal{S}_{i,X}(\Delta'_E,z_{\mathrm{cut}}^{-1/\beta}p_TR,\beta,\mu_0)\,,\end{aligned} \tag{5.27}$$

where the corresponding evolution factors can be written as

$$U_{i,S_Z}(\Delta_E,p_TR,\mu,\mu_0)=\frac{e^{2K_i(\mu,\mu_0)}}{\Gamma\left[-2\eta_i(\mu,\mu_0)\right]}\left(\frac{\mu_0e^{\gamma_E}}{p_TR}\right)^{2\eta_i(\mu,\mu_0)}\left[\frac{\Theta(\Delta_E)}{\Delta_E^{1+2\eta(\mu,\mu_0)}}\right]_+, \tag{5.28}$$

$$\begin{aligned}U_{i,\mathcal{S}_X}(\Delta_E,z_{\mathrm{cut}}^{-1/\beta}p_TR,\beta,\mu,\mu_0)=&\frac{e^{-\frac{2\beta}{1+\beta}K_i(\mu,\mu_0)}}{\Gamma\left[2\eta_i(\mu,\mu_0)\right]}\left[e^{\gamma_E}\left(\frac{\mu_0}{z_{\mathrm{cut}}^{-1/\beta}p_TR}\right)^{\frac{\beta}{1+\beta}}\right]^{-2\eta_i(\mu,\mu_0)}\\&\times\left[\frac{\Theta(\Delta_E)}{\Delta_E^{1-2\eta(\mu,\mu_0)}}\right]_+.\end{aligned} \tag{5.29}$$

		Fixed-order	β	γ	NGLs
$\ln R$	LL	tree	1-loop	1-loop	-
	NLL	1-loop	2-loop	2-loop	-
	NNLL	2-loop	3-loop	3-loop	-
$\ln \Delta_E, \ln z_{\text{cut}}$	LL	tree	1-loop	1-loop	-
	NLL	tree	2-loop	2-loop	LL
	NLL$'$	1-loop	2-loop	2-loop	LL
	NNLL	1-loop	3-loop	3-loop	NLL

Table 5.2 The required perturbative ingredients needed at different orders (rows) for the resummation of logarithms of the jet radius R, jet energy drop Δ_E and grooming parameter z_{cut} for iterated soft drop. The columns indicate the order of fixed-order ingredients in the factorization, the QCD beta function β, the anomalous dimension γ and NGLs.

The convolutions of the above evolution factors and the soft functions at the initial scale μ_0 in eq. (5.26) can be carried out following e.g. refs. [101, 133]. For completeness, we summarize the required perturbative ingredients in table 5.2. An analogous counting of the perturbative accuracy applies to the other grooming techniques discussed in subsequent sections.

5.1.4 Non-global logarithms

Non-global logarithms (NGLs) start contributing to the jet energy drop at next-to-next-to-leading order (NNLO). For iterated soft drop, we will show that the NGLs are related to the hemisphere case, for which a fit to the leading logarithmic resummation [83] or a perturbative expansion is available [97], in the large-N_c limit. We will show that for our phenomenological results, the effect of NGLs beyond their leading NNLO contribution is negligible, and therefore limit ourselves to this contribution for the other grooming procedures.

The NGLs for iterated soft drop originate from correlations between the two soft modes S_G and S_Z, see fig. 5.3. As jets were identified using the anti-k$_T$ jet algorithm, which provides a hard boundary for soft radiation, we do not have to take into account clustering effects. Starting with the NGL at NNLO, we exploit the small R limit to map the in- and out-of-jet region to two hemispheres [94]. In the strong energy-ordered limit of two soft gluon emissions [83]

$$S_i^{\text{NG}}(\Delta_E, z_{\text{cut}}) = 1 + 8C_iC_A\Big(\frac{\alpha_s}{2\pi}\Big)^2 \int \frac{\mathrm{d}x_1}{x_1}\frac{\mathrm{d}x_2}{x_2} \int \mathrm{d}c_1 \frac{\mathrm{d}\phi_1}{2\pi} \int \mathrm{d}c_2 \frac{\mathrm{d}\phi_2}{2\pi} \Theta(x_1 > x_2)$$

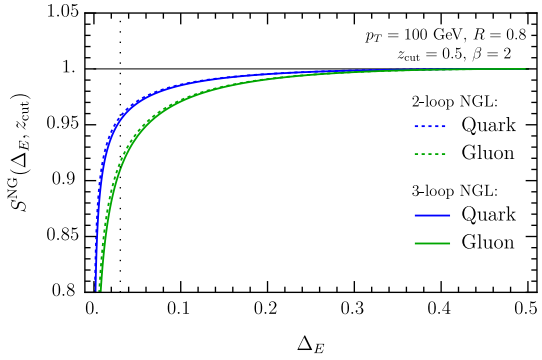

Figure 5.4 Non-global soft contribution $S_i^{\rm NG}$ for the jet energy drop for iterated soft drop, for $i = q$ (blue) and $i = g$ (green), including two-loop (dotted) and three-loop (solid) contributions. The dotted vertical line shows the onset of the nonperturbative region.

$$\times \frac{\cos\phi_2}{(1 - c_1c_2 - s_1s_2\cos\phi_2)\, s_1s_2} \left[\Theta(c_1 < 0) + \Theta(c_1 > 0)\Theta(x_1 > z_{\rm cut}\theta_1^\beta)\right]$$
$$\times \left[\Theta(c_2 < 0) + \Theta(c_2 > 0)\Theta(x_2 < \Delta_E)\right], \tag{5.30}$$

where θ_i are the polar angles of the emissions with $c_i = \cos\theta_i$ and $s_i = \sin\theta_i$, and $x_i = k_{Ti}/p_T$ their energy fractions. The constraints on the soft radiation that are specific to the measurement can be read off from the Lund plane in fig. 5.3 and are encoded in the theta functions on the second and third lines. Specifically, the energy fraction of the most energetic emission has to pass the soft drop criterion if it is inside the jet, whereas the second one has to be less than Δ_E if it is inside. We can replace $x_1 > z_{\rm cut}\theta_1^\beta$ by $x_1 > z_{\rm cut}$, up to subleading NGLs, because $\theta_1 \sim 1$ in the frame where the in and out-jet region are different hemispheres. Outside the jet both emissions are unconstrained. Out of the four resulting contributions, the term $\sim \Theta(c_1 < 0)\Theta(c_2 < 0)$ is scaleless, and the other three terms add up to give[2]

$$S_i^{\rm NG}(\Delta_E, z_{\rm cut}) = 1 - \frac{\pi^2}{3} C_i C_A \left(\frac{\alpha_s}{2\pi}\right)^2 \ln^2\left(\frac{\Delta_E}{z_{\rm cut}}\right). \tag{5.31}$$

This is the usual result for the leading NGL in the hemisphere case, where the argument of the logarithm squared is now given by the ratio of the characteristic scales of the two functions S_G and S_Z in eq. (5.21). We emphasize,

[2]Integrals over x_i that include 0 in the integration domain are divergent. To calculate these, we note that the integral over $0 \le x_i \le 1$ does not yield a large logarithm, allowing us to rewrite the original integral as minus the integral over the complement, which is convergent. The infinities cancel between real and virtual contributions. A similar approach can be used for the angular integral for emissions in the same hemisphere.

however, that this is NGL does not arise in the standard way, as both the high and low energy restrictions are imposed on the *same* hemisphere.

We plot the numerical size of the NNLO non-global contribution to the jet energy drop distribution in fig. 5.4 for quarks and gluons as a function of Δ_E. The region to the left of the dotted vertical line is nonperturbative, as the softest scale in the factorization formula $\mu_{\mathcal{S}_X}$ (see eq. (5.21)) drops below 0.5 GeV. Outside the nonperturbative region, the effect of NGLs is less than 10%. Although this NGL does not arise in the standard way, we still expect that the higher-order corrections are also the same as for the hemisphere case. Thus we explore the effect of higher order corrections using the solution [97] of the BMS equation [96]. We find that the effect of the three-loop contribution is (much) below the percent level, outside the nonperturbative region, as shown in fig. 5.4. The two-loop NGL is thus sufficient for our numerical results in sec. 5.1.6, and we adopt the same practical approach for the grooming algorithms discussed in the subsequent sections.

5.1.5 Profile functions and scale variations

We will now describe our central scale choice, taking particular care to avoid the Landau pole in the nonperturbative region. The scale variations used to estimate the perturbative uncertainty will also be discussed.

We observe from eq. (5.21) that the softest scale $\mu_{\mathcal{S}_X}$ determines the nonperturbative region of the Δ_E distribution,

$$\Delta_E < \left(\frac{\Lambda_{\rm NP} z_{\rm cut}^{1/\beta}}{p_T R}\right)^{\beta/(1+\beta)} . \tag{5.32}$$

Here we take $\Lambda_{\rm NP} = 1.5$ GeV as the value where the scale starts becoming nonperturbative. For instance, we used this value of $\Lambda_{\rm NP}$ in eq. (5.32) to determine the position of the dotted vertical line in fig. 5.4.

To prevent the strong coupling constant α_s from running into the Landau pole for small Δ_E, we use profile functions [101] to freeze the scales at some value $\Lambda_{\rm freeze}$ above the Landau pole. The transition to the fixed-order region (where Δ_E is large) does not require special care, because the non-singular contribution is so small, see fig. 5.2. We make the following choice to smoothly transition

$$f_{\rm pro}(x;x_0) = \begin{cases} x & x > 2x_0 \qquad \text{region I}\,, \\ x_0[1+(x/x_0)^2/4] & x \le 2x_0 \qquad \text{region II}\,. \end{cases} \tag{5.33}$$

Our central scale choice is given by

$$\begin{aligned}
\mu_{\mathcal{S}_X}^{\text{cent}} &= f_{\text{pro}}(\Delta_E^{(1+\beta)/\beta} z_{\text{cut}}^{-1/\beta} p_T R; \Lambda_{\text{freeze}}) \,, \\
\mu_{S_Z}^{\text{cent}} &= \left(\mu_{\mathcal{S}_X}^{\text{cent}} (z_{\text{cut}} p_T R)^{\frac{1}{\beta}}\right)^{\frac{\beta}{1+\beta}} \,, \\
\mu_{S_G}^{\text{cent}} &= z_{\text{cut}} p_T R \,, \\
\mu_{\mathcal{G}}^{\text{cent}} &= p_T R \,, \\
\mu_{\mathcal{H}}^{\text{cent}} &= p_T \,,
\end{aligned} \tag{5.34}$$

where it is important to relate the two scales which depend on Δ_E, such that $\mu_{S_Z}^{\text{cent}}$ also stops running when the softer scale $\mu_{\mathcal{S}_X}^{\text{cent}}$ enters the nonperturbative region. Note that the latter two scales, the hard scale and jet scale, enter our calculation through the jet production described in sec. 5.1.1. We make the choice

$$\Lambda_{\text{freeze}} = 0.2 \text{ GeV} \tag{5.35}$$

throughout this chapter, which ensures that we see the Sudakov peak.

QCD scale uncertainties are obtained by varying the scales of $\mathcal{S}_X$, S_Z individually up and down by a factor of 2 around their central value. We also vary the scales of $S_G, \mathcal{G}, \mathcal{H}$ simultaneously because there is not a large hierarchy between them, since $R = 0.8$ and we generally take $z_{\text{cut}} = 0.5$. Finally, we vary all scales simultaneously up and down, and take the envelope of these variations to obtain the uncertainty band.

5.1.6 Numerical results

In this section we present our numerical results for the jet energy drop for the iterated soft drop algorithm, comparing to Pythia 8.2 simulations [87]. We consider LHC kinematics at $\sqrt{s} = 13$ TeV, reconstructing jets with the anti-k$_T$ algorithm and $R = 0.8$ in the rapidity range of $|\eta| < 2$. Throughout this work, we use the CT14 NLO PDF set [106].

In fig. 5.5, we show our results at NLL and NLL$'$ accuracy for the jet energy drop, and the corresponding results for Pythia at parton level, including initial- and final-state radiation. The different panels correspond to different jet transverse momentum intervals ranging from $p_T = 30$ to 1200 GeV, and we choose the grooming parameters $z_{\text{cut}} = 0.5$ and $\beta = 2$. For the NLL$'$ curves, we include the perturbative uncertainty bands, following the procedure in sec. 5.1.5. We indicate the onset of the nonperturbative region by a dotted vertical line, corresponding to $\mu_{\mathcal{S}_X} \sim 1.5$ GeV (see eq. (5.32)). We use a differential scale setting, which leads to a good prediction for the shape but only ensures the correct normalization up to higher-order corrections. We

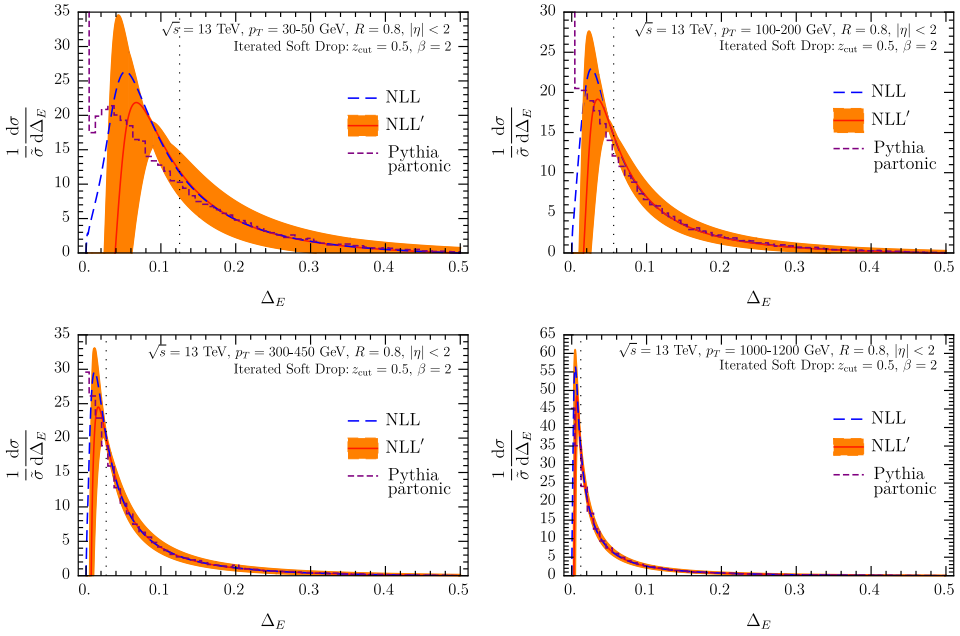

Figure 5.5 Jet energy drop distribution with $z_{\rm cut} = 0.5$ and $\beta = 2$ at NLL (dashed blue) and NLL′ accuracy (orange curve and band), compared to Pythia (dashed purple). The different panels correspond to different jet transverse momenta. The central curves are normalized to unity between the dotted vertical line and the endpoint $\Delta_E = z_{\rm cut}$.

address this by simply normalizing our distribution, though there are more refined proposals (see e.g. ref. [103] for a discussion in the context of the thrust event shape). The NLL′ result becomes unreliable (negative) at small Δ_E, because of large perturbative corrections from $\mathcal{S}_X$, and would anyway need to be supplemented by a nonperturbative model. We therefore use the respective NLL curve (which is always positive) to obtain the normalization factor for the individual quark/gluon predictions and apply this to the NLL′ curves as well. After combining these with the appropriate quark/gluon fractions we normalize the prediction by the cross section $\tilde{\sigma}$ on the interval between the vertical dotted line and the endpoint at $\Delta_E = z_{\rm cut}$, to limit the sensitivity to nonperturbative physics in the perturbative region. We note that the NLL results lie within the uncertainty band of the NLL′, instilling confidence in the convergence of resummed perturbation theory. We also find generally good agreement with Pythia, with the largest differences in the nonperturbative region, as expected. We observe that for lower jet p_T the jet energy drop

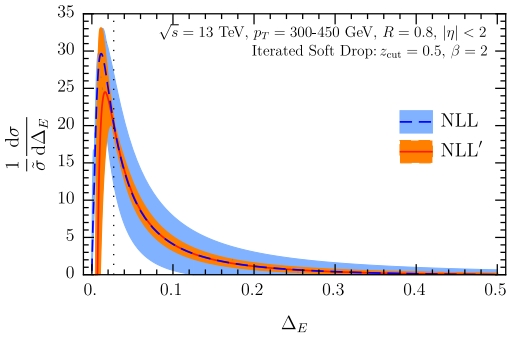

Figure 5.6 Comparison of the QCD scale uncertainties at NLL and NLL′, for the lower left panel of fig. 5.5.

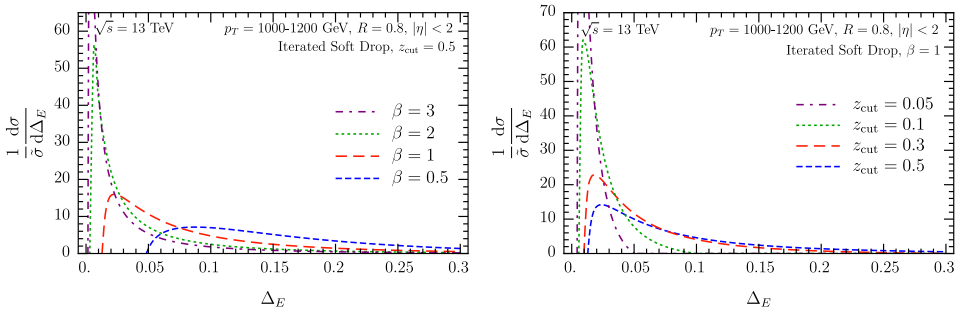

Figure 5.7 The jet energy drop for iterated soft drop at NLL′ for several values of β (left) and $z_{\rm cut}$ (right).

distribution peaks at larger values and is generally broader, which arises from the larger value of α_s.

As an example, we show the QCD scale uncertainty at NLL and NLL′ accuracy in fig. 5.6. We observe a dramatic reduction of the uncertainty band at NLL′. This illustrates the need to perform perturbative calculations at least at NLL′ accuracy, where scale variations in the RG evolution kernels are partially canceled by the NLO results of the different functions, and is the reason we omit the uncertainty band for NLL curves in subsequent plots.

In fig. 5.7, we show the dependence of the jet energy drop on the grooming parameters $z_{\rm cut}$ and β. We consider jets with $p_T = 1000 - 1200$ GeV to limit the effect of the nonperturbative region. In the left panel we fix $z_{\rm cut} = 0.5$ and vary β, while in the right panel we choose $\beta = 1$ and vary $z_{\rm cut}$. As expected from $z > z_{\rm cut}(\theta/R)^\beta$, the energy drop becomes smaller in the limit $\beta \to \infty$ and $z_{\rm cut} \to 0$. Indeed, in these limits, the jet energy drop distributions approach a

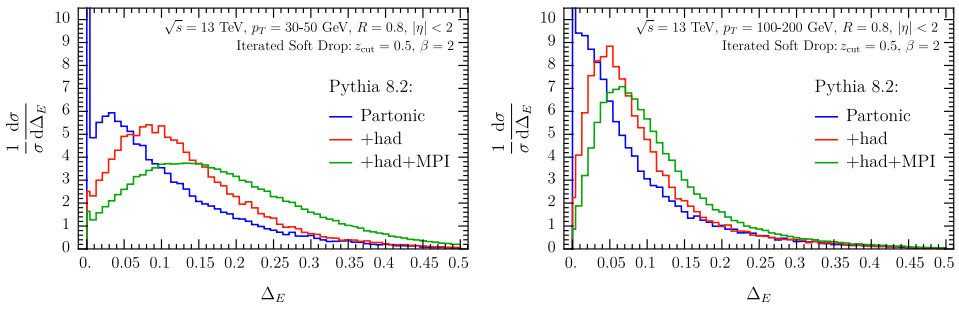

Figure 5.8 PYTHIA results for the jet energy drop with iterated soft drop at parton level (blue), including hadronization (red) and also MPI (green), for $p_T = 30 - 50$ GeV (left) and $100 - 200$ GeV (right). Note that these curves are normalized on the full Δ_E interval.

delta function at $\Delta_E = 0$ (apart from nonperturbative effects).

In fig. 5.8, we study the effect of hadronization and multiple parton interactions (MPI) on the jet energy drop in PYTHIA, for two different bins in the jet transverse momentum. The effect of hadronization is huge: In particular, for jet $p_T = 30 - 50$ GeV about 17% of the jets at parton level are unaffected by grooming (i.e. $\Delta_E = 0$). The effects of MPI are sizable and affect the whole distribution: the radiation due to MPI is uncorrelated to the primary scattering and therefore fairly uniformly distributed over the jet, such that grooming always removes a substantial part of them, independent of the value of Δ_E. This has of course the desired effect of removing them from the groomed jet, but makes our observable particularly sensitive to MPI. Hadronization mostly affects the peak region, shifting its location to the right. The effect of hadronization extends over a larger range of Δ_E than one would expect from the onset of nonperturbative effects estimated in eq. (5.32). The effect of both hadronization and MPI is reduced at higher jet energies.

5.2 Soft drop

In this section we present the calculation of the jet energy drop using regular soft drop grooming. As discussed in chapter 2, the soft drop algorithm terminates once a pair of branches satisfies the criterion in $\min[p_{T,1}, p_{T,2}]/(p_{T,1} + p_{T,2}) > z_{\rm cut}(\theta/R)^\beta$.Therefore, the soft drop condition is not applied to emissions that are at smaller angles than the opening angle between the two branches that satisfy the grooming condition. This leads to a different and more complicated factorization structure than for iterated soft drop, involving

the angle between the two branches that satisfy the soft drop condition.

In our factorization analysis, we consider the cross section differential in both the energy drop Δ_E and the opening angle of the two branches $R_g = \theta_g R$. We identify two separate regimes, depending on the relative size of Δ_E, θ_g, and z_{cut}, as discussed below. After the resummation is performed, we can remove the dependence on θ_g by integrating over it, or, alternatively, calculate the cross section for jet energy drop with a cut on $\theta_g < \theta_g^{\text{cut}}$. A related factorization structure was found in ref. [2], for the angle between the standard and the groomed jet axis. Both observables probe the radiation which is groomed away by soft drop, and are therefore very soft sensitive. Indeed, imposing a cut on θ_g reduces the soft sensitivity of the jet energy drop, as will be demonstrated in sec. 5.2.7. In addition, it can be advantageous for experimental measurements. The (modified) LL jet energy drop cross section was calculated in ref. [23], by means of a conditional probability. We will also explain the connection between this approach and our double differential factorization.

We start by presenting results for the jet function differential in both Δ_E and θ_g at NLO in sec. 5.2.1. In sec. 5.2.2, we discuss in detail the refactorization of the jet function, separated into two factorization regimes, and the resummation of logarithms of Δ_E, θ_g and z_{cut}, including non-global logarithms. We show how the global logarithms can be reproduced by means of a conditional probability in sec. 5.2.3, and discuss the Sudakov-safe case $\beta = 0$ in sec. 5.2.4. In sec. 5.2.5 nonperturbative effects are discussed (in particular for the case where there is a cut on θ_g), and our scale choices are presented in sec. 5.2.6. Finally, in sec. 5.2.7 we present numerical results for LHC kinematics and compare to Pythia results.

5.2.1 Fixed-order results

In our factorization analysis, we need to account for the groomed jet radius θ_g, since its value modifies the structure of the large logarithms in the jet energy drop Δ_E. In particular, we will jointly resum large logarithms involving Δ_E and θ_g, to all orders in α_s. We therefore calculate the double-differential jet function at NLO, which will provide a check on our factorization. However, only the jet function differential in Δ_E enters in the final result (unless a cut on θ_g is imposed).

At NLO, $\Delta\mathcal{G}_i^{\text{SD}}$ is calculated from

$$
\begin{aligned}
&\Delta\mathcal{G}_i^{\text{SD}}(\Delta_E, \theta_g, p_T R, z_{\text{cut}}, \beta, \alpha_s(\mu)) \\
&\quad = \int \mathrm{d}\Phi_2 \, \sigma_{2,i}^c \, \Theta(\theta < R) \Big[\Theta\big(x > z_{\text{cut}}(\theta/R)^\beta\big) \Theta\big(1 - x > z_{\text{cut}}(\theta/R)^\beta\big) \delta(\Delta_E) \delta\big(\theta_g - \theta/R\big) \\
&\qquad + \Theta\big(x > z_{\text{cut}}\big(\theta/R\big)^\beta\big) \Theta\big(1 - x < z_{\text{cut}}(\theta/R)^\beta\big) \delta(\Delta_E - (1-x)) \delta(\theta_g)
\end{aligned}
$$

$$+\,\Theta\big(x<z_{\rm cut}\big(\theta/R\big)^{\beta}\big)\Theta\big(1-x>z_{\rm cut}(\theta/R)^{\beta}\big)\delta(\Delta_E-x)\delta(\theta_g)-\delta(\Delta_E)\delta(\theta_g)\Big]\,. \tag{5.36}$$

At this order terms are either $\propto\delta(\theta_g)$, when one parton fails the soft drop criterion, or $\propto\delta(\Delta_E)$, when both pass. The final term subtracts off the contribution already contained in the semi-inclusive jet function, see eq. (5.5). For quarks and gluons we find to NLO

$$\begin{aligned}
&\Delta\mathcal{G}_q^{\rm SD}(\Delta_E,\theta_g,p_TR,z_{\rm cut},\beta,\alpha_s(\mu))\\
&=\frac{\alpha_sC_F}{\pi}\bigg\{\delta(\Delta_E)\Theta(\theta_g<1)\bigg[(-2+3z_{\rm cut})\beta\bigg[\frac{\ln\theta_g}{\theta_g}\bigg]_+\!+\Big(-2\ln z_{\rm cut}-\frac{3}{2}+3z_{\rm cut}\Big)\frac{1}{[\theta_g]_+}\\
&\quad+\frac{2}{\theta_g}\ln(1-\theta_g^{\beta}z_{\rm cut})\bigg]+\frac{1}{\beta}\Theta(\Delta_E<z_{\rm cut})\delta(\theta_g)\bigg[-2\bigg[\frac{\ln\Delta_E}{\Delta_E}\bigg]_+\!+2\ln z_{\rm cut}\frac{1}{[\Delta_E]_+}\\
&+\Big(3-\frac{2}{1-\Delta_E}\Big)\ln\Big(\frac{\Delta_E}{z_{\rm cut}}\Big)\bigg]+\frac{1}{\beta}\delta(\Delta_E)\delta(\theta_g)[-\ln^2 z_{\rm cut}+3z_{\rm cut}]\bigg\}
\end{aligned}\tag{5.37}$$

$$\begin{aligned}
&\Delta\mathcal{G}_g^{\rm SD}(\Delta_E,\theta_g,p_TR,z_{\rm cut},\beta,\alpha_s(\mu))\\
&=\frac{\alpha_s}{\pi}\bigg(\delta(\Delta_E)\Theta(\theta_g<1)\bigg\{C_A\bigg[\Big(-2-\frac{3}{2}z_{\rm cut}+9z_{\rm cut}^2-9z_{\rm cut}^3\Big)\beta\bigg[\frac{\ln\theta_g}{\theta_g}\bigg]_+\\
&+\Big(-2\ln z_{\rm cut}-\frac{3}{2}z_{\rm cut}+\frac{9}{2}z_{\rm cut}^2-3z_{\rm cut}^3\Big)\frac{1}{[\theta_g]_+}+\frac{2}{\theta_g}\ln\Big(1-z_{\rm cut}\theta_g^{\beta}\Big)\bigg]\\
&+\frac{\beta_0}{2}\bigg[(3z_{\rm cut}-6z_{\rm cut}^2+6z_{\rm cut}^3)\beta\bigg[\frac{\ln\theta_g}{\theta_g}\bigg]_+\!+(-1+3z_{\rm cut}-3z_{\rm cut}^2+2z_{\rm cut}^3)\frac{1}{[\theta_g]_+}\bigg]\\
&+\frac{1}{\beta}\delta(\theta_g)\Theta(\Delta_E<z_{\rm cut})\bigg[C_A\bigg[-2\bigg[\frac{\ln\Delta_E}{\Delta_E}\bigg]_+\!+2\ln z_{\rm cut}\frac{1}{[\Delta_E]_+}\bigg]\\
&-\bigg[C_A\Big(\frac{2}{1-\Delta_E}-4+2\Delta_E-2\Delta_E^2\Big)+2n_fT_F\Big(\Delta_E^2+(1-\Delta_E)^2\Big)\bigg]\ln\Big(\frac{\Delta_E}{z_{\rm cut}}\Big)\bigg]\\
&+\frac{1}{\beta}\delta(\theta_g)\delta(\Delta_E)\bigg[C_A\Big(-\ln^2 z_{\rm cut}+4z_{\rm cut}-\frac{z_{\rm cut}^2}{2}+\frac{2}{9}z_{\rm cut}^3\Big)+n_fT_F\Big(-z_{\rm cut}+z_{\rm cut}^2-\frac{4}{9}z_{\rm cut}^3\Big)\bigg]\bigg\}.
\end{aligned}\tag{5.38}$$

As is clear from the $1/\beta$ poles in the above expressions, the jet energy drop is not IRC safe for soft drop with $\beta=0$. However, unlike for iterated soft drop, $\beta=0$ is Sudakov safe, as will be discussed in sec. 5.2.4. Alternatively, it is also IRC safe if a cut on θ_g is imposed, which removes the singularity at $\theta_g=0$.

Upon integration over the groomed radius θ_g,

$$\int_0^1{\rm d}\theta_g\,\Delta\mathcal{G}_i^{\rm SD}(\Delta_E,\theta_g,p_TR,z_{\rm cut},\beta,\alpha_s(\mu))\overset{\rm NLO}{=}\Delta\mathcal{G}_i^{\rm ISD}(\Delta_E,p_TR,z_{\rm cut},\beta,\alpha_s(\mu))\,. \tag{5.39}$$

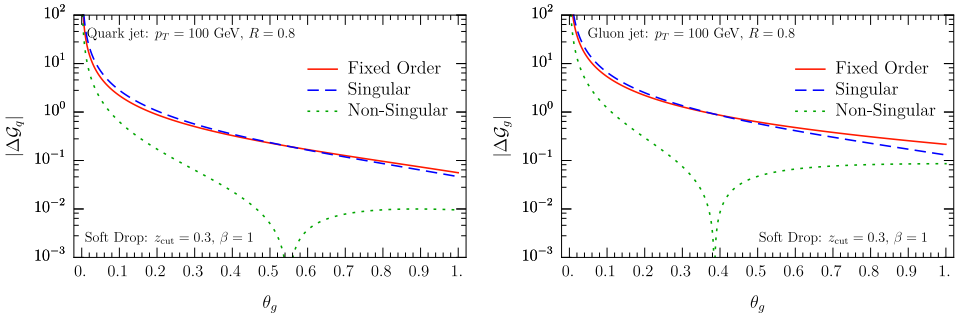

Figure 5.9 Numerical results for the singular, non-singular and fixed-order result of $\Delta\mathcal{G}_i^{\rm SD}$ for soft drop as a function of the groomed jet radius θ_g, for the same jet kinematics as in fig. 5.2 and with grooming parameters $\beta = 1$ and $z_{\rm cut} = 0.3$.

we obtain the jet function for iterated soft drop in eq. (5.11). Consequently, the size of the logarithmically enhanced terms in the jet function is the same as for iterated soft drop, shown in fig. 5.2. For completeness, we also plot the NLO jet function $\Delta\mathcal{G}_i^{\rm SD}$ as a function of θ_g to further assess the numerical size of the power corrections to the singular terms in the limit $\Delta_E \ll z_{\rm cut} \ll 1$. The results in fig. 5.9 show that the power corrections are small as long as θ_g is not too small. We impose a sufficiently large $\theta_g^{\rm cut}$ in our phenomenological studies below, and thus do not need to include a matching correction.

5.2.2 Factorization and resummation

We will consider the kinematic regime where $\Delta_E \ll z_{\rm cut} \ll 1$ and $\theta_g \ll 1$. We obtain two different factorization formulae, depending on whether θ_g is (parametrically) larger or smaller than $(\Delta_E/z_{\rm cut})^{1/\beta}$, discussed below.

Regime A

The Lund diagram for regime A is shown in the left panel of fig. 5.10. The dashed lines show the measurements of Δ_E and θ_g as well as the grooming condition, as indicated in the figure. The cumulative measurement of the groomed radius $\theta_g < \theta_g^c$ vetoes emissions in the red region with momentum fraction $z > z_{\rm cut}(\theta/R)^\beta$ and angles $\theta/R > \theta_g^c$, see also refs. [23, 122]. In addition, we now measure the jet energy drop $\Delta_E < \Delta_E^c$. Emissions with $z < z_{\rm cut}(\theta/R)^\beta$ and $\theta/R > \theta_g$ are groomed away, and contribute to the measured value of Δ_E. Therefore, emissions are vetoed in the blue region. For $\theta_g < (\Delta_E/z_{\rm cut})^{1/\beta}$, we thus obtain the Lund diagram as shown in fig. 5.10. Note

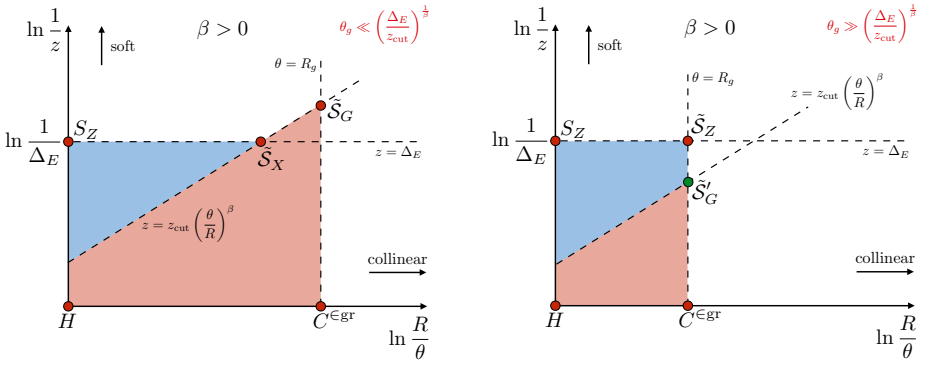

Figure 5.10 Lund diagrams for the energy drop of a soft-drop groomed jet in the region $\Delta_E \ll z_{\text{cut}} \ll 1$ and $\theta_g \ll 1$, for regime A (left) and B (right). The relevant SCET modes are indicated by red and green dots, and their power counting can be read off, see table 5.3.

that to simplify the notation, we omit the superscript c for cumulative variables in fig. 5.10.

We start with the resummed result at LL accuracy, which can be calculated from the vetoed red and blue shaded areas of the Lund diagram. This gives the cumulant from which we obtain the double-differential result by taking derivatives with respect to both Δ_E and θ_g,

$$\begin{aligned}&\tilde{\mathcal{G}}^{\text{SD}}_{i,A}\big(\Delta_E, \theta_g, p_T R, z_{\text{cut}}, \beta, \alpha_s(\mu)\big)\\ &\quad\overset{\text{LL}}{=} \frac{\mathrm{d}}{\mathrm{d}\Delta_E}\frac{\mathrm{d}}{\mathrm{d}\theta_g}\exp\left\{-\frac{\alpha_s C_i}{\pi}\left[\frac{1}{\beta}\ln^2\Big(\frac{z_{\text{cut}}}{\Delta_E}\Big) + 2\ln z_{\text{cut}}\ln\theta_g + \beta\ln^2\theta_g\right]\right\}.\end{aligned} \tag{5.40}$$

We extend this beyond LL using a factorization formula within SCET, for which the modes correspond to red points at the intersections of the dashed lines in the left panel of fig. 5.10. The parametric scaling of the momenta of the hard, collinear, soft, and collinear-soft modes are summarized in table 5.3. (Because this is a refactorization of a collinear function, these modes are strictly speaking hard-collinear, collinear, etc.) The resulting factorization, differential in Δ_E and θ_g, is given by

$$\begin{aligned}&\tilde{\mathcal{G}}^{\text{SD}}_{i,A}\big(\Delta_E, \theta_g, p_T R, z_{\text{cut}}, \beta, \alpha_s(\mu)\big)\\ &\quad\overset{\text{NLL'}}{=} \frac{\mathrm{d}}{\mathrm{d}\theta_g}\bigg[\tilde{H}_i(p_T R,\mu)\, C_i^{\in\text{gr}}(\theta_g p_T R,\mu)\,\mathcal{S}_{i,G}\big(z_{\text{cut}}\theta_g^{1+\beta} p_T R,\beta,\mu\big)\mathcal{S}_i^{\text{NG+AC}}(z_{\text{cut}}\theta_g^{\beta})\\ &\qquad\times\int \mathrm{d}\Delta'_E\,\mathcal{S}_{i,X}(\Delta'_E, p_T R, z_{\text{cut}},\beta,\mu) S_{i,Z}(\Delta_E-\Delta'_E, p_T R,\mu)\, S_i^{\text{NG}}(\Delta_E)\bigg].\end{aligned} \tag{5.41}$$

Mode:	Function:	Regime A	Regime B
hard	H	$p_T(R^2, 1, R)$	
soft	S_Z	$\Delta_E\, p_T(R^2, 1, R)$	
coll	$C^{\in \mathrm{gr}}$	$p_T(R_g^2, 1, R_g)$	
c-soft	$\tilde{\mathcal{S}}_G$	$z_{\mathrm{cut}}\theta_g^\beta p_T(R_g^2, 1, R_g)$	
c-soft	$\tilde{\mathcal{S}}_X$	$\Delta_E\, p_T\Big(\big(\frac{\Delta_E}{z_{\mathrm{cut}}}\big)^{2/\beta} R^2, 1, \big(\frac{\Delta_E}{z_{\mathrm{cut}}}\big)^{1/\beta} R\Big)$	
c-soft	$\tilde{\mathcal{S}}_Z$		$\Delta_E\, p_T(R_g^2, 1, R_g)$

Table 5.3 The scaling of the modes that enter the factorization formulae of the jet energy drop cross section in the kinematic region where $\Delta_E \ll z_{\mathrm{cut}} \ll 1$ and $\theta_g = R_g/R \ll 1$. Regime A (B) correspond to θ_g being smaller (larger) than $(\Delta_E/z_{\mathrm{cut}})^{1/\beta}$.

The hard function $\tilde{H}_i$ is only sensitive to the jet scale and does not depend on Δ_E and θ_g. Note that for iterated soft drop this hard function was absent. The collinear function $C_i^{\in \mathrm{gr}}$ does not depend on Δ_E, since collinear radiation is never groomed away. It can set the measurement of θ_g (when the derivative acts on the collinear function), or account for collinear emissions at smaller angles (when the derivative does not act on it). Next, the collinear-soft function $\mathcal{S}_{i,G}$ is sensitive to the soft drop grooming condition and can also set the groomed radius of the jet θ_g. The three functions discussed so far also appear in the NLL′ factorization of the soft drop groomed radius [122]. The collinear-soft function $\mathcal{S}_{i,X}$ is sensitive to both the Δ_E measurement and the grooming condition, as the corresponding emissions contribute to the jet energy drop if they fail the soft drop criterion. Finally, the soft function $S_{i,Z}$ accounts for soft wide-angle radiation which is always groomed away. The same functions $\mathcal{S}_{i,X}$ and $S_{i,Z}$ enter in the factorization for iterated soft drop in eq. (5.17). Interestingly, in regime A the dependence on Δ_E and θ_g appears in separate parts of the factorization formula.

There are two types of non-global logarithms in eq. (5.41) associated with ungroomed and groomed jet boundary, R and R_g, respectively. These can be treated independently as long as they are sufficiently separated, i.e. $R_g \ll R$. The NGLs at the ungroomed jet boundary arise due to correlations of the out-of-jet region, where the radiation is unconstrained (and thus has energies of order p_T), and the in-jet region, where wide-angle radiation must have energies below $\Delta_E p_T$. This is taken into account by the same non-global soft function as the hemisphere case, $S_i^{\mathrm{NG}}(\Delta_E)$. The $\mathcal{S}_i^{\mathrm{NG+AC}}(z_{\mathrm{cut}}\theta_g^\beta)$ arises at the boundary of the groomed jet. Unlike the hard boundary of the initial ungroomed anti-k$_T$ jet, it is sensitive clustering effects from C/A. This same contribution entered

in the resummation of the groomed jet radius [122], and is given by

$$\mathcal{S}_i^{\mathrm{NG+AC}}(z_{\mathrm{cut}}\theta_g^\beta) = 1 - \frac{4}{9}\frac{\pi^2}{3} C_i C_A \Big(\frac{\alpha_s}{2\pi}\Big)^2 \ln^2\big(z_{\mathrm{cut}}\theta_g^\beta\big)\,. \tag{5.42}$$

The factor 4/9 compared to eq. (5.31) is due to clustering effects.

Here we present the one-loop expressions for the functions in eq. (5.41) that did not appear for iterated soft drop. The hard function $\tilde{H}_i$ [1,56], the collinear function $C_i^{\in \mathrm{gr}}$ and the collinear-soft function $\mathcal{S}_{i,G}$ [122] are given by

$$\begin{aligned}
\tilde{H}_q(p_T R,\mu) &= 1 + \frac{\alpha_s C_F}{\pi}\left[-\ln^2\left(\frac{\mu}{p_T R}\right) - \frac{3}{2}\ln\left(\frac{\mu}{p_T R}\right) - \frac{13}{4} + \frac{3\pi^2}{8}\right],\\
\tilde{H}_g(p_T R,\mu) &= 1 + \frac{\alpha_s}{\pi}\left[C_A\left(-\ln^2\left(\frac{\mu}{p_T R}\right) - \frac{5}{24} + \frac{3\pi^2}{8}\right) + \frac{\beta_0}{2}\left(-\ln\left(\frac{\mu}{p_T R}\right)\right.\right.\\
&\qquad \left.\left. - \frac{23}{12}\right)\right],\\
C_q^{\in \mathrm{gr}}(\theta_g p_T R\,\mu) &= 1 + \frac{\alpha_s C_F}{\pi}\left[\ln^2\left(\frac{\mu}{\theta_g p_T R}\right) + \frac{3}{2}\ln\left(\frac{\mu}{\theta_g p_T R}\right) + \frac{13}{4} - \frac{3\pi^2}{8}\right],\\
C_g^{\in \mathrm{gr}}(\theta_g p_T R,\mu) &= 1 + \frac{\alpha_s}{\pi}\left[C_A \ln^2\left(\frac{\mu}{\theta_g p_T R}\right) + \frac{\beta_0}{2}\ln\left(\frac{\mu}{\theta_g p_T R}\right)\right.\\
&\qquad \left. + C_A\left(\frac{67}{18} - \frac{3\pi^2}{8}\right) - T_F n_f \frac{23}{18}\right],\\
\mathcal{S}_{i,G}(z_{\mathrm{cut}}\theta_g^{1+\beta} p_T R,\beta,\mu) &= 1 + \frac{\alpha_s C_i}{\pi(1+\beta)}\left[-\ln^2\left(\frac{\mu}{z_{\mathrm{cut}}\theta_g^{1+\beta} p_T R}\right) + \frac{\pi^2}{24}\right].
\end{aligned} \tag{5.43}$$

The functions $\mathcal{S}_{i,X}$ and $S_{i,Z}$ are given in eq. (5.18) above. We have verified that combining these ingredients agrees with the fixed-order result for $\Delta\mathcal{G}_i$ in sec. 5.2.1, in the limit where the factorization holds.

To resum the logarithms of Δ_E, θ_g and z_{cut}, we evaluate each of the ingredients in the factorization formula in eq. (5.41) at their natural scale,

$$\begin{aligned}
&\mu_H \sim p_T R\,, \quad \mu_{C^{\in \mathrm{gr}}} \sim \theta_g p_T R\,, \quad \mu_{\mathcal{S}_G} \sim z_{\mathrm{cut}}\theta_g^{1+\beta} p_T R\,, \quad \mu_{S_Z} \sim \Delta_E\, p_T R\,,\\
&\mu_{\mathcal{S}_X} \sim \Delta_E^{(1+\beta)/\beta} z_{\mathrm{cut}}^{-1/\beta} p_T R\,,
\end{aligned} \tag{5.44}$$

and evolve them to a common scale μ. The RG equations for the new ingredi-

ents are

$$\mu \frac{\mathrm{d}}{\mathrm{d}\mu} \tilde{H}_i \left(p_T R, \mu\right) = \gamma_i^{\tilde{H}} \left(p_T R, \mu\right) \tilde{H}_i \left(p_T R, \mu\right) \tag{5.45}$$

$$\mu \frac{\mathrm{d}}{\mathrm{d}\mu} C_i^{\in \mathrm{gr}} \left(\theta_g p_T R, \mu\right) = \gamma_i^{C^{\in \mathrm{gr}}} \left(\theta_g p_T R, \mu\right) C_i^{\in \mathrm{gr}} \left(\theta_g p_T R, \mu\right) , \tag{5.46}$$

$$\mu \frac{\mathrm{d}}{\mathrm{d}\mu} \mathcal{S}_{i,G}(z_{\mathrm{cut}} \theta_g^{1+\beta} p_T R, \beta, \mu) = \gamma_i^{\mathcal{S}_{i,G}}(z_{\mathrm{cut}} \theta_g^{1+\beta} p_T R, \beta, \mu) \, \mathcal{S}_{i,G}(z_{\mathrm{cut}} \theta_g^{1+\beta} p_T R, \beta, \mu) , \tag{5.47}$$

and the one-loop expressions for these anomalous dimensions are given in appendix B.3.3.

Regime B

The Lund diagram for regime B is shown on the right side of fig. 5.10. Since in this case $\theta_g > (\Delta_E / z_{\mathrm{cut}})^{1/\beta}$, there is a white triangle between the dashed lines representing the measurement of Δ_E and the soft drop criterion which is not vetoed. This triangle corresponds to emissions that fail the soft drop criterion and would give a value of Δ_E that is too large, except that the soft drop procedure has already terminated. Different than in regime A, the measurements of Δ_E and θ_g are not independent here. For regime B we work differentially in the groomed radius θ_g. One emission sets the value of θ_g and other emissions must be outside the shaded region with boundary $\theta/R = \theta_g$ and $z = \Delta_E$. At LL accuracy, the resummed result is

$$\tilde{\mathcal{G}}_{i,B}^{\mathrm{SD}}\big(\Delta_E, p_T R, z_{\mathrm{cut}}, \beta, \theta_g, \alpha_s\big) \overset{\mathrm{LL}}{=} -\frac{\alpha_s C_i}{\pi} \frac{2}{\theta_g} \ln(z_{\mathrm{cut}} \theta_g^{\beta}) \frac{\mathrm{d}}{\mathrm{d}\Delta_E} \exp\left\{ -\frac{2\alpha_s C_i}{\pi} \ln \Delta_E \ln \theta_g \right\} . \tag{5.48}$$

The LL result can again be extended to NLL′ using SCET. We identify a total of five modes that contribute. Four of them correspond to the corners of the shaded region in fig. 5.10, indicated by red points. In addition, there is a mode indicated by the green point which is located at the intersection of the grooming condition and $\theta/R = \theta_g$. Since only the emission that sets θ_g is sensitive to the soft drop condition, the collinear-soft $\mathcal{S}'_{i,G}$ mode only contributes if it sets θ_g and has a single emission (see the discussion in ref. [2] and sec. 5.2.3). We find that the extension to NLL′, including non-global

logarithms, can be written as

$$\begin{aligned}
&\tilde{\mathcal{G}}_{i,B}^{\mathrm{SD}}\big(\Delta_E, p_T R, z_{\mathrm{cut}}, \beta, \theta_g, \alpha_s(\mu)\big) \\
&\quad \overset{\text{NLL'}}{=} \tilde{H}_i(p_T R, \mu)\bigg[\frac{\mathrm{d}}{\mathrm{d}\theta_g}\, C_i^{\in \mathrm{gr}}(\theta_g p_T R, \mu) + C_i^{\in \mathrm{gr}}(\theta_g p_T R, \mu)\, \mathcal{S}'_{i,G}\big(\theta_g, z_{\mathrm{cut}}\theta_g^\beta p_T, \beta, \mu\big)\bigg] \\
&\qquad \times \int \mathrm{d}\Delta'_E\, \mathcal{S}_{i,Z}(\Delta'_E, \theta_g p_T R, \mu)\, S_{i,Z}(\Delta_E - \Delta'_E, p_T R, \mu) \mathcal{S}_i^{\mathrm{NG+AC}}(\Delta_E) S_i^{\mathrm{NG}}(\Delta_E)\,.
\end{aligned} \tag{5.49}$$

The function $\mathcal{S}'_{i,G}$ at one-loop order is given by derivative of $\mathcal{S}_{i,G}$ (in regime A) with respect to θ_g. However, emissions in $\mathcal{S}'_{i,G}$ which do not set θ_g are scaleless and hence, the associated RG equation is given by

$$\mu \frac{\mathrm{d}}{\mathrm{d}\mu} \mathcal{S}'_{i,G}(\theta_g, z_{\mathrm{cut}}\theta_g^\beta p_T, \beta, \mu) = -\frac{\mathrm{d}}{\mathrm{d}\theta_g} \gamma_i^{C^{\in \mathrm{gr}}}\left(\theta_g p_T R, \mu\right)\,, \tag{5.50}$$

as required for consistency of the factorization formula in eq. (5.49). The new collinear-soft function $\mathcal{S}_{i,Z}$ in eq. (5.49) is at one-loop order given by

$$\begin{aligned}
\mathcal{S}_{i,Z}(\Delta_E, \theta_g p_T R, \mu) = \delta(\Delta_E) + \frac{\alpha_s C_i}{\pi}\Bigg\{ &-2\left[\frac{\ln \Delta_E}{\Delta_E}\right]_+ + \frac{2}{[\Delta_E]_+} \ln\left(\frac{\mu}{\theta_g p_T R}\right) \\
&+ \delta(\Delta_E)\left[-\ln^2\left(\frac{\mu}{\theta_g p_T R}\right) + \frac{\pi^2}{24}\right]\Bigg\}\,.
\end{aligned} \tag{5.51}$$

It satisfies the RG equation

$$\mu \frac{\mathrm{d}}{\mathrm{d}\mu} \mathcal{S}_{i,Z}\left(\Delta_E, \theta_g p_T R, \mu\right) = \int \mathrm{d}\Delta'_E\, \gamma_i^{\mathcal{S}_Z}\left(\Delta_E - \Delta'_E, \theta_g p_T R, \mu\right) \mathcal{S}_{i,Z}\left(\Delta'_E, \theta_g p_T R, \mu\right)\,, \tag{5.52}$$

with the anomalous dimension again given in appendix B.3.3. The characteristic scales of the ingredients in the factorization formulae for regime B are given by

$$\begin{aligned}
&\mu_H \sim p_T R\,, \quad \mu_{C^{\in \mathrm{gr}}} \sim \theta_g p_T R\,, \quad \mu_{\mathcal{S}'_G} \sim z_{\mathrm{cut}} \theta_g^{1+\beta} p_T R\,, \quad \mu_{S_Z} \sim \Delta_E\, p_T R\,, \\
&\mu_{\mathcal{S}_Z} \sim \Delta_E\, \theta_g\, p_T R\,.
\end{aligned} \tag{5.53}$$

The structure of the non-global logarithms is very similar to regime A, except that the argument of $\mathcal{S}_i^{\mathrm{NG+AC}}$, describing the NGLs at the groomed boundary, is now Δ_E instead of $z_{\mathrm{cut}}\theta_g^\beta$. To understand this change, remember that these NGLs arise from correlated emissions inside and outside the groomed jet radius. Emissions inside are unconstrained (i.e. have energy of order p_T), while the

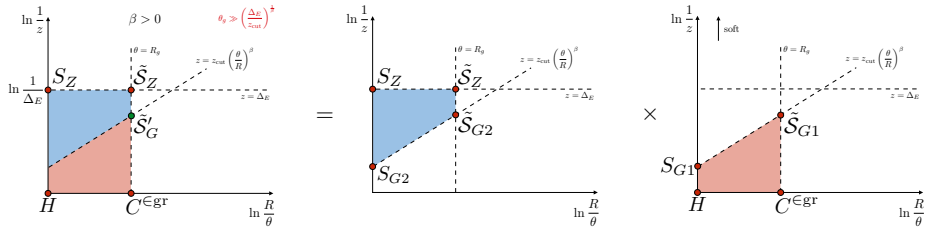

Figure 5.11 Lund diagram analysis in which regime B is written as a conditional probability for Δ_E given a value of θ_g, and the θ_g cross section.

energy of emissions outside is constrained to be below $\Delta_E p_T$, which for regime B is more restrictive than the grooming condition.

In principle one can also consider the intermediate regime $\theta_g \sim (\Delta_E/z_{\rm cut})^{1/\beta}$. The effective theory corresponding to this intermediate case can be obtained from regime A, for which $\tilde{\mathcal{S}}_X$ and $\tilde{\mathcal{S}}_G$ merge, or regime B, for which $\tilde{\mathcal{S}}_Z$ and $\tilde{\mathcal{S}}'_G$ merge into one function. The anomalous dimensions are smooth in this merging, but the function describing these merged modes in the factorization theorem can have different fixed-order expressions (due to terms that become power suppressed in regime A or B). The matching between A and B is thus automatically valid at NLL accuracy, and this intermediate case only needs to be considered if one wants to ensure NLL′ accuracy throughout the intermediate matching regime.

5.2.3 Conditional probability

An alternative way of obtaining the global structure of the factorization for regime B is by means of a conditional probability, which is how the jet energy drop was calculated in ref. [23] at (modified) LL accuracy. We describe how this arises in our SCET framework, providing additional insight on the origin of $\mathcal{S}'_{i,G}$.

The starting point is to write the double differential $\mathcal{G}^{\rm SD}_{i,B}(\Delta_E, \theta_g)$ as

$$\tilde{\mathcal{G}}^{\rm SD}_{i,B}(\Delta_E, \theta_g) = \tilde{\mathcal{G}}^{\rm SD}_i(\Delta_E|\,\theta_g) \times \tilde{\mathcal{G}}^{\rm SD}_i(\theta_g), \tag{5.54}$$

where for brevity we suppress arguments other than Δ_E and θ_g. $\tilde{\mathcal{G}}^{\rm SD}_i(\Delta_E|\,\theta_g)$ denotes the conditional probability to obtain a certain energy drop Δ_E for a given θ_g, i.e. it treats θ_g as a fixed parameter just like the jet radius R. $\tilde{\mathcal{G}}^{\rm SD}_i(\theta_g)$ represents the probability distribution of having a specific value of θ_g, calculated to NLL′ in ref. [122].

This decomposition can also be understood in terms of the Lund plane, as seen in fig. 5.11. Here the conditional probability is depicted by the Lund plane

with a blue vetoed area, while the one with a red vetoed area represents the θ_g distribution. In contrast to the double differential case, for the conditional probability emissions outside the groomed radius that pass the SD condition are now allowed since R_g is treated as a fixed parameter. The relevant modes are again indicated as red dots on the corners, leading to the following factorization for each of these pieces:

$$\begin{aligned}\tilde{\mathcal{G}}_i^{\mathrm{SD}}(\Delta_E|\,\theta_g) &= \mathcal{S}_{i,G2}\big(z_{\mathrm{cut}}\theta_g^{1+\beta}p_T,\beta,\mu\big)S_{i,G2}\big(z_{\mathrm{cut}}p_TR,\beta,\mu\big) \\ &\quad\times\int \mathrm{d}\Delta'_E\,\mathcal{S}_{i,Z}(\Delta'_E,\theta_g p_T R,\mu)\,S_{i,Z}(\Delta_E-\Delta'_E,p_TR,\mu)\,, \\ \tilde{\mathcal{G}}_i^{\mathrm{SD}}(\theta_g) &= \frac{\mathrm{d}}{\mathrm{d}\theta_g}\big[\tilde{H}_i(p_TR,\mu)C_i^{\in\mathrm{gr}}(\theta_g p_TR,\mu) \\ &\quad\times\mathcal{S}_{i,G1}\big(z_{\mathrm{cut}}\theta_g^{1+\beta}p_T,\beta,\mu\big)S_{i,G1}\big(z_{\mathrm{cut}}p_TR,\beta,\mu\big)\big].\end{aligned} \tag{5.55}$$

We now note that the modes S_{G1} and S_{G2} are defined in a similar way: the former vetoes emissions that pass the grooming condition, whereas the latter vetoes emissions that fail said condition. This translates to a minus sign difference in the α_s term of these two functions, i.e. $S_{G1}\times S_{G2}=1+\mathcal{O}(\alpha_s^2)$, removing their contribution. Of course this holds also for multiple independent emissions, exponentiating the one-loop soft function, which is why there is no such mode in the factorization for regime B in eq. (5.49). Similarly, for $\mathcal{S}_{G1}$ and $\mathcal{S}_{G2}$ we have $\mathcal{S}_{G1}\times\mathcal{S}_{G2}=1+\mathcal{O}(\alpha_s^2)$. However, in this case the derivative with respect to θ_g in eq. (5.55) between $\mathcal{S}_{i,G1}$ and $\mathcal{S}_{i,G2}$ prevents them from cancelling, leaving exactly $\mathcal{S}'_{i,G}$ as remainder. Thus we reproduce the factorization theorem for regime B in (5.49), apart from non-global logarithms.

5.2.4 $\beta = 0$ and Sudakov safety

Soft drop with $\beta=0$ corresponds to the modified mass drop tagger of ref. [181]. It is a special case, because the jet energy drop is not IRC safe, as is clear when taking $\beta\to 0$ in the fixed-order result for $\mathcal{G}_i^{\mathrm{SD}}$ in eq. (5.37). (With a cut $\theta_g>\theta_g^c>0$, it is IRC safe.)As was found in ref. [23], the jet energy drop is Sudakov safe, allowing us to safely take the $\beta\to 0$ limit of the cross section in which the logarithms of Δ_E and θ_g are jointly resummed. This works because the Sudakov factor arising from the resummation regularizes the divergence. (See ref. [26] for a discussion of Sudakov safety in the context of the momentum sharing fraction z_g.) In the absence of a cut on θ_g, the jet energy drop is particularly sensitive to nonperturbative effects, as discussed in sec. 5.2.5.

For $\beta=0$, only regime B contributes, which was shown in the right panel of fig. 5.10 for $\beta>0$. In this case, the line corresponding to the soft drop

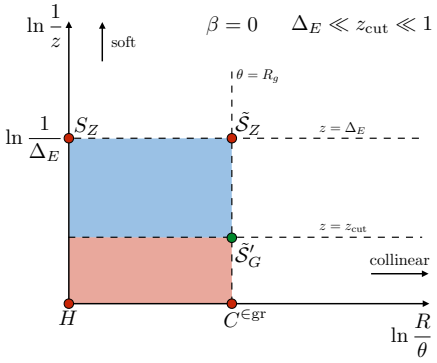

Figure 5.12 The Lund diagram for the jet energy drop with soft drop grooming and $\beta = 0$.

criterion now has slope $\beta = 0$, as shown in fig. 5.12. It is clear from the figure that the θ_g measurement is necessary to regulate the collinear divergence for Δ_E measurements at $\beta = 0$. In fact, we can immediately take $\beta \to 0$ in the ingredients in this regime, and there is no difficulty in obtaining resummed predictions. The IR divergence is in regime A, whose range of applicability is shrunk to the point $\theta_g = 0$ for $\beta \to 0$. In the resummed cross section, it is Sudakov suppressed. With the collinear divergence regulated by the θ_g measurement, we can obtain a Δ_E distribution by integrating over a desired range of θ_g. It is worth noting that LL formulation given in eq. (5.48) yields an α_s independent result when integrated over the entire range of θ_g,

$$\int_0^1 d\theta_g \, \tilde{\mathcal{G}}_{i,B}^{\text{SD}}\big(\Delta_E, p_T R, z_{\text{cut}}, \beta = 0, \theta_g, \alpha_s(\mu)\big) \overset{\text{LL}}{=} \frac{\ln z_{\text{cut}}}{\ln \Delta_E} \,. \tag{5.56}$$

This surprising feature was already pointed out in ref. [23], where they also kept the subleading terms in the splitting functions, compared to the LL expression in eq. (5.48). Our full NLL′ result includes many more contributions but its analytic expression is not particularly tractable.

5.2.5 θ_g and nonperturbative effects

We will now discuss the size of nonperturbative effects, considering the case where we completely integrate over θ_g, as well as imposing a minimum cut on θ_g. As we will see below, introducing a cutoff reduces the sensitivity to nonperturbative effects. It is also advantageous from an experimental point of view, if the tracking efficiency is limited at small θ_g [146].

As usual, we determine the onset of the nonperturbative region by considering the softest scales involved in the factorization formulas in eqs. (5.41) and

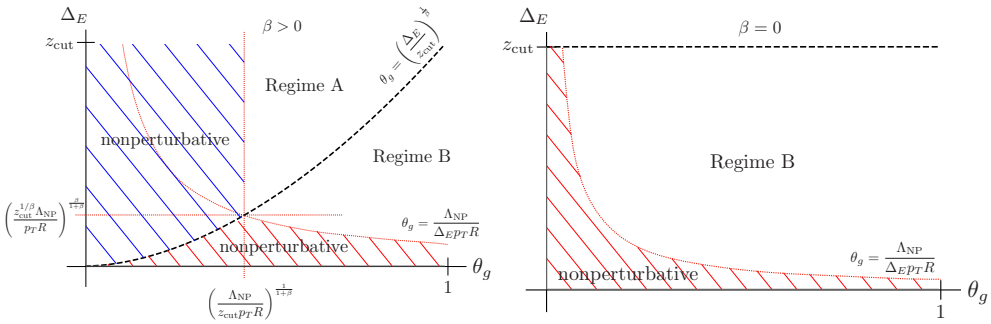

Figure 5.13 The nonperturbative regions for soft drop with $\beta > 0$ (left) and $\beta = 0$ (right). Plots are not to scale to highlight the nonpertubative regions.

(5.49). The softest scales in regime A and regime B are $\mu_{\tilde{\mathcal{S}}_G} \sim z_{\rm cut}\theta_g^{1+\beta} p_T R$ and $\mu_{\tilde{\mathcal{S}}_Z} \sim \Delta_E \theta_g p_T R$, respectively. Therefore, within regime A we use the relation

$$\theta_g < \left(\frac{\Lambda_{\rm NP}}{z_{\rm cut} p_T R}\right)^{\frac{1}{1+\beta}} \quad \text{and} \quad \theta_g < \left(\frac{\Delta_E}{z_{\rm cut}}\right)^{\frac{1}{\beta}} \tag{5.57}$$

to determine the nonperturbative region, while for regime B

$$\left(\frac{\Delta_E}{z_{\rm cut}}\right)^{\frac{1}{\beta}} < \theta_g < \frac{\Lambda_{\rm NP}}{\Delta_E p_T R}\,. \tag{5.58}$$

As discussed in sec. 5.2.4, for $\beta = 0$ we only have regime B, and eq. (5.58) simplifies to

$$\theta_g < \frac{\Lambda_{\rm NP}}{\Delta_E p_T R}\,. \tag{5.59}$$

These nonperturbative regions are illustrated in fig. 5.13.

We now highlight some aspects of nonperturbative contributions to the Δ_E distribution resulting from integrating over (a range of) θ_g.[3] First, we note that the entire Δ_E distribution receives a nonperturbative contribution from the θ_g integration when $\theta_g^{\rm cut} < (\Lambda_{\rm NP}/(z_{\rm cut} p_T R))^{1/(1+\beta)}$, due to region A. If $\theta_g^{\rm cut}$ is above this threshold, the onset of the nonperturbative regions is instead

[3] Usually one does not associate nonperturbative corrections with variables that are integrated over, but in this case Δ_E and θ_g are intertwined by the double-differential factorization. Therefore, the integration of θ_g does not remove the nonperturbative effects coming from factorization scales associated with the θ_g measurement.

determined by region B (corresponding to the red regions in fig. 5.13). In this case the nonperturbative contributions become small for much of the Δ_E distribution, for both $\beta > 0$ and $\beta = 0$, allowing for a purely perturbative calculation. In our numerical studies presented in sec. 5.2.7, we always indicate the corresponding onset of the nonperturbative region by a vertical dotted line. If the cut is chosen such that $\theta_g^{\text{cut}} < (\Lambda_{\text{NP}}/(z_{\text{cut}} p_T R))^{1/(1+\beta)}$, then we have some nonperturbative contributions for Δ_E values even above the indicated vertical line.

5.2.6 Profile functions and scale variations

In this section we describe our choice of central scales, as well as the variations used to assess the perturbative uncertainty. We start with regime A, which is particularly simple because no function in the factorization formula depends on both Δ_E and θ_g, whereas for regime B we need to design two-dimensional profile scales.

In regime A there are no scales that simultaneously depend on both Δ_E and θ_g. Consequently, we can take the same central scales and scale variations for S_Z and $\mathcal{S}_X$ as for iterated soft drop, see sec. 5.1.5. For the additional scales associated with the θ_g measurement (corresponding to the red region in the Lund plane in the left panel of fig. 5.10), we take

$$\begin{aligned} \mu_{\mathcal{S}_G}^{\text{cent}} &= f_{\text{pro}}(z_{\text{cut}} \theta_g^{1+\beta} p_T R; \Lambda_{\text{freeze}}) \,, \\ \mu_{C^{\in \text{gr}}}^{\text{cent}} &= \left[\left(\frac{\mu_{\mathcal{S}_G}^{\text{cent}}}{z_{\text{cut}}} \right)^{1/\beta} p_T R \right]^{\beta/(1+\beta)} \,, \\ \mu_H^{\text{cent}} &= p_T R \,. \end{aligned} \tag{5.60}$$

Here $f_{\text{pro}}(x; x_0)$ ensures that we avoid the Landau pole. Its expression is given in eq. (5.33), and we take the same value $\Lambda_{\text{freeze}} = 0.2$ GeV as for iterated soft drop. By expressing $\mu_{C^{\in \text{gr}}}^{\text{cent}}$ in terms of $\mu_{\mathcal{S}_G}^{\text{cent}}$, we ensure that they stop running simultaneously. QCD scale uncertainties are obtained by varying the scales that also appear for ISD in the same way as described in sec. 5.1.5, while identifying the variation of μ_H^{cent} with the variation of $\mu_{\mathcal{G}}^{\text{cent}}$ as their canonical forms are identical. We also vary the new θ_g dependent scales of $\mu_{\mathcal{S}_G}^{\text{cent}}$ and $\mu_{C^{\in \text{gr}}}^{\text{cent}}$ individually up and down by a factor of 2 around their central value. The perturbative uncertainty band is obtained by taking the envelope of all the variations.

Regime B presents a further complication, since the Δ_E and θ_g measurements can no longer be treated independently. In this case the softest scale is $\mu_{\mathcal{S}_Z} \sim \Delta_E \, \theta_g \, p_T R$, which thus becomes nonperturbative before any other

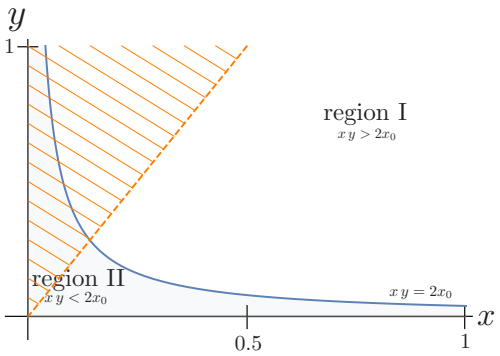

Figure 5.14 The two regions defined in the two-dimensional profile function given in eq. (5.61). All θ_g and Δ_E-dependent scales take on their canonical values in region I and begin to freeze once they enter region II. The involved scales are properly defined only within the factorization of regime B, satisfying the condition $\Delta_E < z_{\text{cut}}\theta_g^\beta$. This condition is indicated by the orange hatched region for $z_{\text{cut}} = 0.5$ and $\beta = 1$, identifying x and y with Δ_E and θ_g, respectively.

scale. As this scale depends on both Δ_E and θ_g, it can run into the nonperturbative region by either Δ_E or θ_g becoming small, corresponding to region II in fig. 5.14. Therefore, we now need a two-dimensional profile to implement the freezing of the scale in the nonperturbative region

$$f_{\text{pro}}^{2d}(x, y; x_0) = \begin{cases} x\,y & x\,y > 2x_0 \quad \text{region I}\,, \\ x_0[1 + (x\,y/x_0)^2/4] & x\,y \leq 2x_0 \quad \text{region II}\,. \end{cases} \tag{5.61}$$

With this new profile function, we define the central scale for $\mu_{\mathcal{S}_Z}$ as

$$\mu_{\mathcal{S}_Z}^{\text{cent}} = f_{\text{pro}}^{2d}\left(\Delta_E, \theta_g; \frac{\Lambda_{\text{freeze}}}{p_T R}\right) p_T R\,, \tag{5.62}$$

to smoothly freeze $\mu_{\mathcal{S}_Z}$ at Λ_{freeze}. The condition $\Delta_E < z_{\text{cut}}\theta_g^\beta$ is necessary to ensure that we stay within regime B, and is indicated in fig. 5.14 by the orange hatched region for $z_{\text{cut}} = 0.5$ and $\beta = 1$, when x and y of eq. (5.61) are identified with Δ_E and θ_g, respectively.

When $\mu_{\mathcal{S}_Z}^{\text{can}}$ starts freezing in region II, we want to ensure that all other scales also stop running. To accomplish this, we define the following profile function

$$g_{\text{pro}}^{2d}(x, y; A, B, c_0, x_0) = \begin{cases} x^{1+B} & x\,y > 2x_0 \quad \text{region I}\,, \\ c_0\left[1 + \left(\frac{x\,y}{2x_0}\right)^{1+A}\left(\frac{1}{c_0}\left(\frac{2x\,x_0}{y}\right)^{\frac{1+B}{2}} - 1\right)\right] & x\,y \leq 2x_0 \quad \text{region II}\,, \end{cases} \tag{5.63}$$

where $A > -1$ controls the rate at which scale freezes to c_0 in region II. The parameter B is chosen according to the canonical behaviors of different scales in region I. The profile function is continuous everywhere and smoothly approaches c_0 as x or y become small. We then take the remaining central scales to be

$$\begin{aligned}
\mu_H^{\text{cent}} &= p_T R\,, \\
\mu_{C^{\in \text{gr}}}^{\text{cent}} &= g_{\text{pro}}^{2d}\Big(\theta_g, \Delta_E; 0, 0, \lambda_{C^{\in \text{gr}}}, \frac{\Lambda_{\text{freeze}}}{p_T R}\Big) p_T R\,, \\
\mu_{\mathcal{S}'_G}^{\text{cent}} &= g_{\text{pro}}^{2d}\Big(\theta_g, \Delta_E; 0, \beta, \lambda_{\mathcal{S}'_G}, \frac{\Lambda_{\text{freeze}}}{p_T R}\Big) z_{\text{cut}} p_T R\,, \\
\mu_{S_Z}^{\text{cent}} &= g_{\text{pro}}^{2d}\Big(\Delta_E, \theta_g; 0, 0, \lambda_{S_Z}, \frac{\Lambda_{\text{freeze}}}{p_T R}\Big) p_T R\,.
\end{aligned} \tag{5.64}$$

This ensures that all θ_g and Δ_E-dependent scales take on their canonical values in region I, given in eq. (5.53), while freezing them in the same region II. Because different scales enter region II with different values, it is natural to freeze them to different λ_i to maintain their relative hierarchy. We take λ_i to be the average value of the scale x^{1+B}, with x and B defined in eq. (5.64), along $\Delta_E\, \theta_g = 2\frac{\Lambda_{\text{freeze}}}{p_T R}$ within regime B, divided by 2. We then vary all scales individually by factors of 2 around their central choices and all simultaneously, taking the envelope to obtain the uncertainty band.

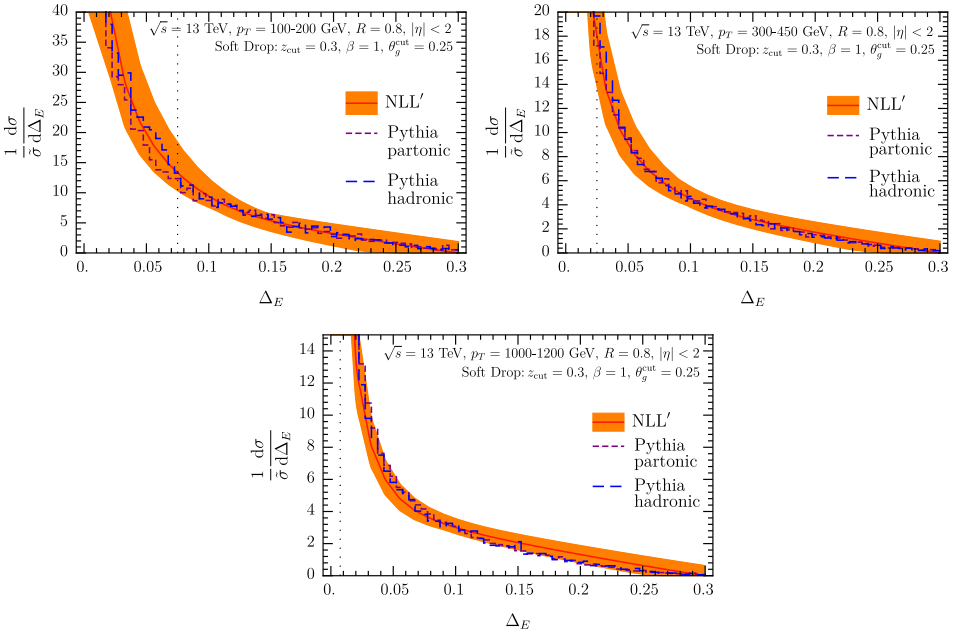

Figure 5.15 Numerical results at NLL′ (orange) for the jet energy drop for soft drop with $z_{\rm cut} = 0.3$, $\beta = 1$ and $\theta_g^{\rm cut} = 0.25$. In addition, we show PYTHIA results at parton (purple dashed) and hadron level (blue dashed) for comparison. The different panels correspond to different jet transverse momenta. The central curves are normalized to unity between the dotted vertical line and the endpoint $\Delta_E = z_{\rm cut}$.

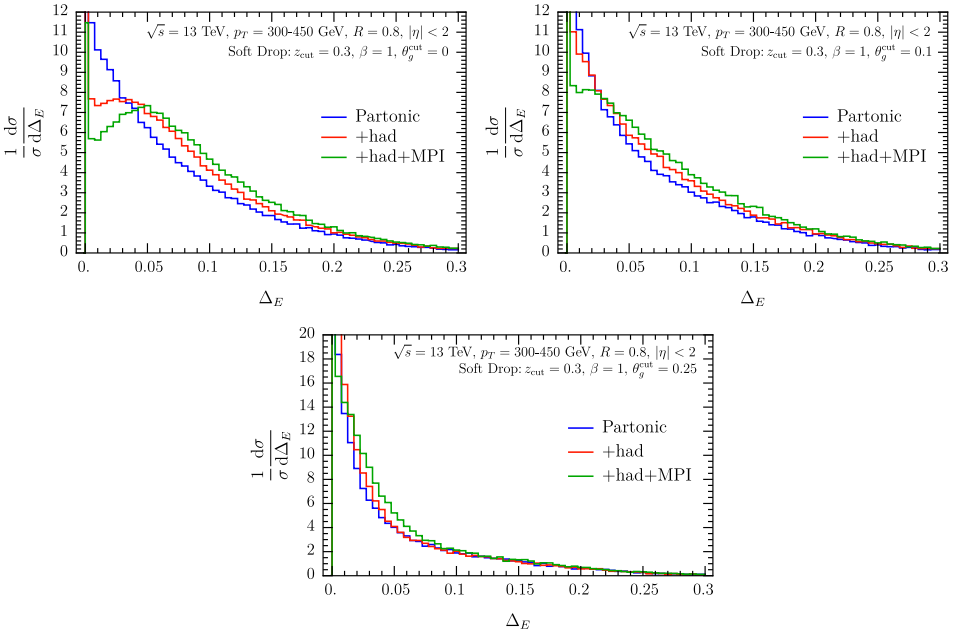

Figure 5.16 PYTHIA results for the jet energy drop with soft drop at parton level (blue) and including hadronization (red) and MPI (green). The three panels correspond to $\theta_g^{\rm cut} = 0$ (top left), 0.1 (top right), 0.25 (bottom). Note that these curves are normalized on the full Δ_E interval.

5.2.7 Numerical results

We start by presenting results for the jet energy drop with soft drop for $z_{\rm cut} = 0.3$, $\beta = 1$, and compare to PYTHIA at parton and hadron level (without MPI). The NLL′ results for $\theta_g^{\rm cut} = 0.25$ and three jet p_T intervals are presented in fig. 5.15. Here we leave out the interval $p_T = 30 - 50$ GeV, which is shown for the other grooming procedures, as the energy drop distribution is nonperturbative over most of the Δ_E range in this case. We indicate the nonperturbative region by the dotted vertical line, and we normalize our results over the perturbative range. We find very good agreement with the PYTHIA results at parton and hadron level, which are also normalized on the same range. For the chosen kinematics, and in particular the $\theta_g^{\rm cut}$ value, the cross section is dominated by perturbative dynamics.

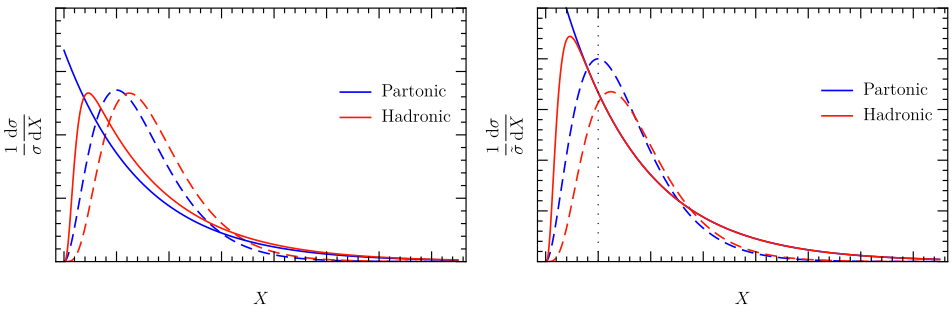

Figure 5.17 We explore the effect of hadronization by taking a falling distribution (solid) or a peaked distribution (dashed), as proxy for the perturbative result (blue) of energy drop (for soft drop) and jet mass, and convolving with a shape function to obtain the red curve. While the effects are similar when normalizing on the full range ($1/\sigma$, left panel), this is no longer the case when normalizing on the region to the right of the vertical dotted line ($1/\tilde{\sigma}$, right panel).

In fig. 5.16, we investigate in more detail the impact of nonperturbative effects using Pythia. We show the parton level results and including corrections due to hadronization and MPI for the jet transverse momentum interval of $p_T = 300 - 450$ GeV. The three panels correspond to three different values of $\theta_g^{\text{cut}} = 0,\ 0.1,\ 0.25$. Here we normalize the result over the entire Δ_E range. We find that nonperturbative effects are small when the relatively large value of $\theta_g^{\text{cut}} = 0.25$ is chosen, which corresponds to the results in fig. 5.15. However, if we lower θ_g^{cut} nonperturbative effects become more important. We observe that hadronization corrections dominate but also MPI leads to a shift of the distribution to larger values of Δ_E. Interestingly, these differences are substantially reduced when normalizing to the perturbative region, indicating that the *shape* in the perturbative region is not much affected by hadronization. This is due to the shape of the perturbative distribution, which we illustrate in fig. 5.17. We consider the case where the perturbative distribution is falling (like here) or peaked (as for jet mass), and convolve with a nonperturbative shape function to model the effect of hadronization. Before normalizing, the effect of this convolution is similar, but this is no longer true after normalizing on a restricted range that does not include the nonperturbative region. When no cut on θ_g is imposed (upper left panel of fig. 5.16), the nonperturbative corrections are very large. We thus conclude that imposing a cut on θ_g allows us to control the soft sensitivity of the jet energy drop.

Next, we consider the jet energy drop for $\beta = 0$, which is a Sudakov safe observable, as discussed in sec. 5.2.4. In fig. 5.18, we show the NLL′ results for

$z_{\text{cut}} = 0.1$ with $\theta_g^{\text{cut}} = 0.25$, choosing the same jet kinematics as in fig. 5.15. In addition, we show PYTHIA results at parton and hadron level, finding again good agreement.

We end this section by comparing in fig. 5.19 our numerical results to the preliminary CMS data of ref. [198]. The grooming parameters chosen by CMS are $z_{\text{cut}} = 0.5$ and $\beta = 1.5$, and a cut on the groomed jet radius of $\theta_g^{\text{cut}} = 0.25$ was imposed. We observe very good agreement in the perturbative region which is indicated by the dotted vertical line. Note that both our theoretical results and the data are normalized in the perturbative region. We note that the data of ref. [146] with $\beta = 0$ and $z_{\text{cut}} = 0.1$ are in the nonperturbative region or $\Delta_E > z_{\text{cut}}$, where our factorization theorem does not apply.

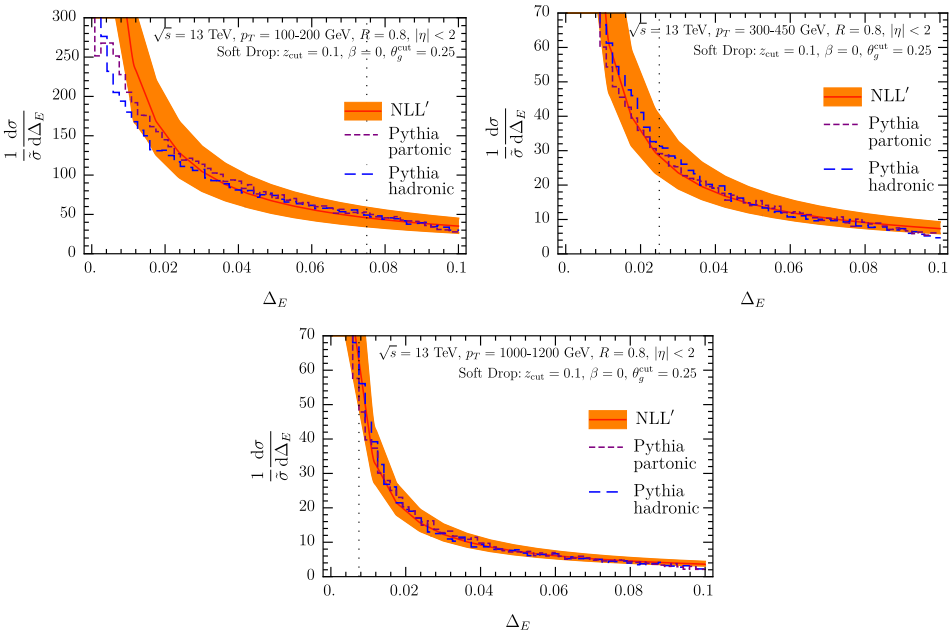

Figure 5.18 Numerical results at NLL′ (orange) for the jet energy drop with soft drop and $z_{\text{cut}} = 0.1$, $\beta = 0$ and $\theta_g^{\text{cut}} = 0.25$. In addition, we show PYTHIA results at parton (purple dashed) and hadron level (blue dashed) for comparison. The different panels correspond to different jet transverse momenta.

5.3 Trimming

In this section we consider the jet energy drop of a trimmed jet. We start by introducing the trimming algorithm in sec. 5.3.1. We then present fixed-order results of the corresponding jet function in sec. 5.3.2, and introduce the

factorization and resummation in sec. 5.3.3, including a discussion of non-global logarithms. In sec. 5.3.4, we present numerical results and compare to Pythia.

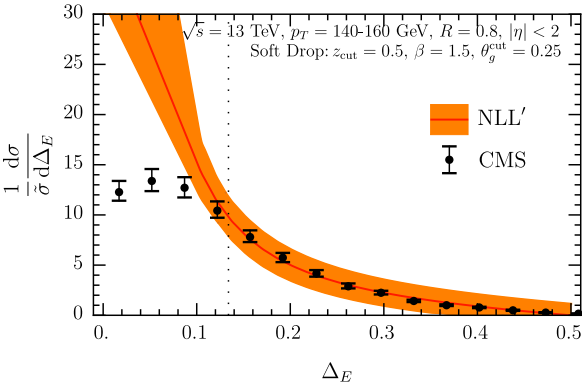

Figure 5.19 Comparison of our theoretical calculation for soft drop and the preliminary CMS data of ref. [198].

5.3.1 The trimming algorithm

Trimming (TR) [24] is one of the first jet-grooming algorithms, which we discussed briefly in chapter 2. It improves the event reconstruction at high luminosity colliders and is frequently used for experimental analyses (particularly ATLAS), see e.g. refs. [199, 200]. Recall from chapter 2 that the grooming proceeds as follows: First jets are reconstructed with the anti-k$_T$ algorithm and jet radius parameter R. The constituents of the identified jets are then reclustered with a smaller jet radius $R_{\rm sub} < R$. Subjets are removed from the jet if their transverse momentum p_{Ti} (or energy) is below a threshold given by $p_{Ti} < f_{\rm cut}\Lambda_{\rm hard}$. Here $f_{\rm cut}$ is a dimensionless quantity and $\Lambda_{\rm hard}$ is a hard scale, which we choose as p_T of the initial ungroomed jet. The trimmed jet is then given by all the particles in the remaining subjets.

In ref. [181] the jet mass of a trimmed jet was calculated, and in refs. [56, 74] the longitudinal momentum fraction $z = p_{Ti}/p_T$ of the reclustered inclusive subjets was considered. Here we consider the jet energy drop induced by the trimming procedure. Similar to soft drop, this observable is particularly sensitive to the soft aspects of jets. In ref. [24] the k$_T$ algorithm was used for reclustering the jets into smaller subjets, as k$_T$ subjets better share the total available jet energy amongst themselves. We use instead the C/A algorithm, such that the clustering effects are the same as for soft drop. (We have checked in Pythia that this has a minimal effect on the jet energy drop distribution.)

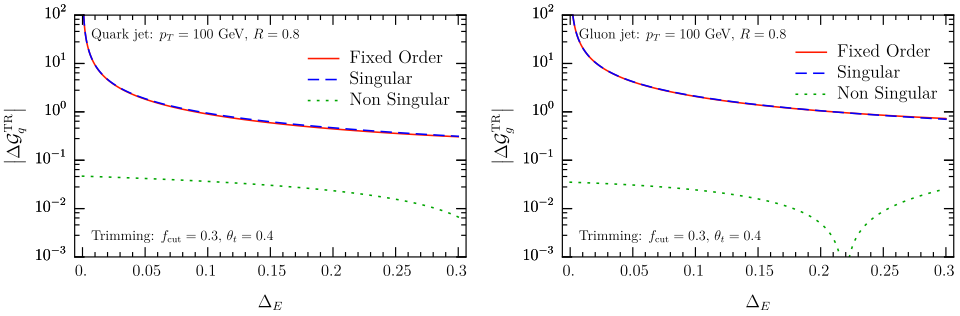

Figure 5.20 Numerical comparison of the size of singular (dashed blue) and non-singular (dotted green) terms of the fixed-order (red) jet function for trimming. We show the quark and gluon result in the left and right panel, respectively.

Typical values of the trimming parameters used in experimental analyses are $R_{\rm sub} = 0.2$ and $f_{\rm cut} = 0.05$, though they depend on the observable under consideration. For our numerical results in sec. 5.3.4, we choose a relatively large value of $f_{\rm cut} = 0.3$ to ensure that a large part of the distribution can be described perturbatively.

5.3.2 Fixed-order results

We denote the jet function that measures the jet energy drop for trimming by $\Delta\mathcal{G}_i^{\rm TR}$. It depends on the grooming parameters $\theta_t \equiv R_{\rm sub}/R$, $f_{\rm cut} < \frac{1}{2}$ and the jet energy drop Δ_E, which is the total energy fraction of the subjets removed by trimming. At NLO, the jet function can be calculated as

$$\begin{aligned}
&\Delta\mathcal{G}_i^{\rm TR}(\Delta_E, p_T R, \theta_t, f_{\rm cut}, \mu) \qquad (5.65)\\
&= \int \mathrm{d}\Phi_2\, \sigma_{2,i}^c\, \Theta(\theta < R) \Big\{ \Theta(\theta > \theta_t R) \Big[\Theta(x > f_{\rm cut})\, \Theta(1 - x > f_{\rm cut})\, \delta(\Delta_E) \\
&\quad + \Theta(x > f_{\rm cut})\, \Theta(1 - x < f_{\rm cut})\, \delta(\Delta_E - x) \\
&\quad + \Theta(x < f_{\rm cut})\, \Theta(1 - x > f_{\rm cut})\, \delta(\Delta_E - (1 - x)) \Big] + \Theta(\theta < \theta_t R)\, \delta(\Delta_E) \\
&\quad - \delta(\Delta_E) \Big\}\,.
\end{aligned}$$

If the two partons are clustered into different subjets $\theta > \theta_t R$, they are individually tested against the trimming condition. As before, the very last term subtracts the contribution already contained in the semi-inclusive jet function.

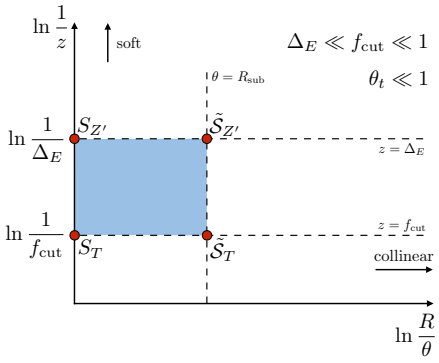

Figure 5.21 Lund diagram for the energy drop of a trimmed jet. The relevant SCET modes are indicated by red dots.

For quark and gluon jets, we find

$$\begin{aligned}
&\Delta\mathcal{G}_q^{\rm TR}(\Delta_E, p_T R, \theta_t, f_{\rm cut}, \alpha_s(\mu)) \\
&\quad = \frac{\alpha_s C_F}{\pi} \ln\theta_t \left\{ \Theta(\Delta_E < f_{\rm cut}) \left[-\frac{2}{1-\Delta_E} - \frac{2}{[\Delta_E]_+} + 3 \right] + \delta(\Delta_E) \big(-2\ln(1-f_{\rm cut}) \right. \\
&\qquad \left. + 2\ln f_{\rm cut} - 3 f_{\rm cut} \big) \right\}, \qquad (5.66)
\end{aligned}$$

$$\begin{aligned}
&\Delta\mathcal{G}_g^{\rm TR}(\Delta_E, p_T R, \theta_t, f_{\rm cut}, \alpha_s(\mu)) \\
&\quad = \frac{\alpha_s}{\pi} \ln\theta_t \left\{ \Theta(\Delta_E < f_{\rm cut}) \left[-2 n_f T_F (\Delta_E^2 + (1-\Delta_E)^2) + C_A \left(4 - \frac{2}{[\Delta_E]_+} \right. \right. \right. \\
&\qquad \left. \left. - \frac{2}{1-\Delta_E} - 2(1-\Delta_E)\Delta_E \right) \right] + \delta(\Delta_E) \left[n_f T_F \left(\frac{4}{3} f_{\rm cut}^3 - 2 f_{\rm cut}^2 + 2 f_{\rm cut} \right) \right. \\
&\qquad \left. \left. + C_A \left(-\frac{2}{3} f_{\rm cut}^3 + f_{\rm cut}^2 - 4 f_{\rm cut} - 2\ln(1-f_{\rm cut}) + 2\ln f_{\rm cut} \right) \right] \right\}. \qquad (5.67)
\end{aligned}$$

We observe that at NLO the jet energy drop Δ_E is always less than $f_{\rm cut}$, similar to (iterated) soft drop where $\Delta_E < z_{\rm cut}$. The plus distribution here is defined on the interval $0 < \Delta_E < 1$. If we rewrite it to be defined on the interval of the theta function $\Theta(\Delta_E < f_{\rm cut})$, the $\ln f_{\rm cut}$ term in the last lines for both the quark and gluon jet function cancels, and we can safely take the limit $f_{\rm cut} \to 0$ (similar to $z_{\rm cut} \to 0$ for iterated soft drop in sec. 5.1.2). In this limit the trimming is removed and the jet function $\Delta\mathcal{G}^{\rm TR}$ thus vanishes. Next we consider the relative size of the singular and non-singular terms for trimming at fixed order in fig. 5.20. We observe that the singular terms dominate over the entire range of Δ_E, suggesting that the resummation is likely important,

and that the matching to NLO does not need to be included in our numerical results. We note that different from iterated soft drop (see fig. 5.2) the NLO distribution does not smoothly go to zero at the endpoint $\Delta_E = f_{\text{cut}}$.

5.3.3 Factorization and resummation

For the trimmed jet energy drop there are three parameters that enter in the large logarithms requiring resummation, namely the energy drop Δ_E and the grooming parameters $f_{\text{cut}}\,, \theta_t$. We will assume $\Delta_E \ll f_{\text{cut}} \ll 1$ and $\theta_t \ll 1$, for which the corresponding Lund diagram is shown in fig. 5.21. The two horizontal dashed lines correspond to the measurement of the jet energy drop $z = \Delta_E$ and the cutoff imposed on the reclustered subjets $z = f_{\text{cut}}$, respectively. The vertical line corresponds to the size of the subjets $R/\theta = R/R_{\text{sub}} = 1/\theta_t$. We note that the Lund diagram here looks quite similar to that for the jet energy drop for soft drop with $\beta = 0$ in fig. 5.12. However, in contrast to the groomed radius θ_g, the subjet radius θ_t has a fixed value. In particular, it is not integrated over after the resummation is performed, as in the case of soft drop. Emissions in the shaded region of the Lund diagram are vetoed and we can read of the resummed LL expression,

$$\tilde{\mathcal{G}}_i^{\text{TR}}\big(\Delta_E, p_T R, f_{\text{cut}}, \theta_t, \alpha_s(\mu)\big) \overset{\text{LL}}{=} \frac{\mathrm{d}}{\mathrm{d}\Delta_E} \exp\left[-\frac{2\alpha_s C_i}{\pi} \ln\left(\frac{\Delta_E}{f_{\text{cut}}}\right) \ln\theta_t\right]. \quad (5.68)$$

The relevant modes in SCET, needed to achieve NLL′ resummation, again correspond to the corners of the shaded region in fig. 5.21. Their power counting is summarized in table 5.4. The refactorization of the jet function for trimming is at NLL′ accuracy given by

$$\begin{aligned} &\tilde{\mathcal{G}}_i^{\text{TR}}\big(\Delta_E, p_T R, f_{\text{cut}}, \theta_t, \alpha_s(\mu)\big) \quad (5.69)\\ &\overset{\text{NLL}'}{=} S_{i,T}(f_{\text{cut}} p_T R, \mu)\, \mathcal{S}_{i,T}(f_{\text{cut}}\, \theta_t\, p_T R, \mu) \int \mathrm{d}\Delta'_E\, S_{i,Z'}(\Delta'_E, p_T R, \mu)\\ &\quad \times \mathcal{S}_{i,Z'}(\Delta_E - \Delta'_E, \theta_t\, p_T R, \mu) S_i^{\text{NG}}(\Delta_E/f_{\text{cut}})\, \mathcal{S}_i^{\text{NG+AC}}(\Delta_E/f_{\text{cut}})\,. \end{aligned}$$

We now provide the NLO expressions for the various ingredients in this factorization. The one-loop soft function $S_{i,\,Z'}$ is the same as $S_{i,\,Z}$, which appeared in the factorization formula of (iterated) soft drop, and is given in eq. (5.17).

Mode:	Function:	Scaling
soft	S_T	$f_{\rm cut}\, p_T(R^2, 1, R)$
soft	$S_{Z'}$	$\Delta_E\, p_T(R^2, 1, R)$
collinear-soft	$\tilde{\mathcal{S}}_T$	$f_{\rm cut}\, p_T(R_{\rm sub}^2, 1, R_{\rm sub})$
collinear-soft	$\tilde{\mathcal{S}}_{Z'}$	$\Delta_E\, p_T(R_{\rm sub}^2, 1, R_{\rm sub})$

Table 5.4 The parametric scaling of the momenta of the various modes in SCET, needed to describe the jet energy drop cross section for trimming with $\Delta_E \ll f_{\rm cut} \ll 1$ and $\theta_t = R_{\rm sub}/R \ll 1$.

The other soft and collinear-soft functions are given by

$$S_{i,T}(f_{\rm cut} p_T R, \mu) = 1 + \frac{\alpha_s C_i}{\pi} \left\{ -\ln^2\left(\frac{\mu}{f_{\rm cut} p_T R}\right) + \frac{\pi^2}{24} \right\}, \tag{5.70}$$

$$\mathcal{S}_{i,T}(f_{\rm cut}\theta_t\, p_T R, \mu) = 1 + \frac{\alpha_s C_i}{\pi} \left\{ \ln^2\left(\frac{\mu}{f_{\rm cut}\theta_t\, p_T R}\right) - \frac{\pi^2}{24} \right\}, \tag{5.71}$$

$$\begin{aligned}\mathcal{S}_{i,Z}(\Delta_E, \theta_t\, p_T R, \mu) = \delta(\Delta_E) + \frac{\alpha_s C_i}{\pi} \Bigg\{ &-2 \left[\frac{\ln \Delta_E}{\Delta_E}\right]_+ + \frac{2}{[\Delta_E]_+} \ln\left(\frac{\mu}{\theta_t\, p_T R}\right) \\ &+ \delta(\Delta_E) \left[-\ln^2\left(\frac{\mu}{\theta_t\, p_T R}\right) + \frac{\pi^2}{24} \right] \Bigg\}. \end{aligned} \tag{5.72}$$

These functions are similar to the ones for soft drop, as they can be obtained by appropriately replacing trimming parameters by soft drop parameters. For example, $\mathcal{S}_{i,Z}$ can be obtained from eq. (5.51) by replacing θ_g by θ_t. Eq. (5.69) contains two contributions from non-global logarithms: First of all, $S_i^{\rm NG}$ arises at the boundary $\theta = R$ of the initial jet, because emissions inside the jet must have $z < \Delta_E$ or $z > f_{\rm cut}$ (for details, see the discussion of the corresponding NGL for iterated soft drop in sec. 5.1.4). Since the jet is obtained by anti-k$_T$ reclustering, it has a hard boundary that is not perturbed by the clustering of soft radiation. The second contribution from NGLs arises at the boundary $\theta = R_g$ of the trimmed subjets. It has a very similar origin: emissions outside of a trimmed subjet must have $z < \Delta_E$ or $z > f_{\rm cut}$. However, because the subjets are obtained with the C/A algorithm, they are sensitive to clustering effects, and there are also Abelian clustering effects. It is described by the same $\mathcal{S}_i^{\rm NG+AC}$ given in eq. (5.42) for soft drop, but with a different argument.

The large logarithms are resummed by evaluating each of the four (global) functions in eq. (5.69) at their characteristic scale

$$\mu_{S_T} \sim f_{\rm cut} p_T R\,, \quad \mu_{\mathcal{S}_T} \sim f_{\rm cut}\theta_t\, p_T R\,, \quad \mu_{S_{Z'}} \sim \Delta_E\, p_T R\,, \quad \mu_{\mathcal{S}_{Z'}} \sim \Delta_E \theta_t\, p_T R\,, \tag{5.73}$$

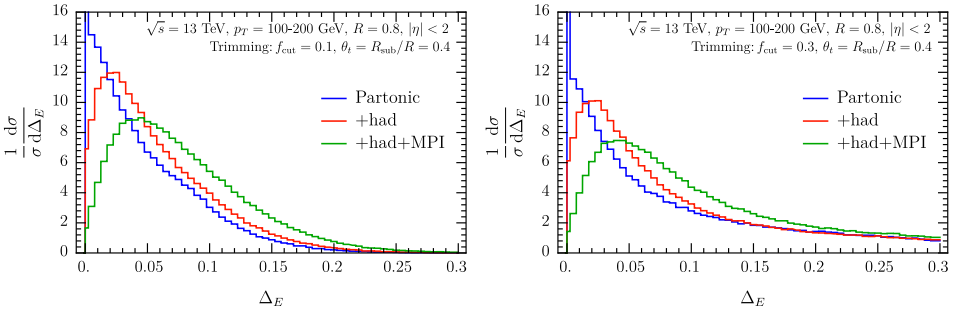

Figure 5.22 PYTHIA results for the jet energy drop with trimming for $f_{\rm cut} = 0.1$ (left panel) and $f_{\rm cut} = 0.3$, at parton level (blue), hadron level (red), and including MPI (green). Note that these curves are normalized on the full Δ_E interval.

and using the RG equations

$$\mu\frac{\mathrm{d}}{\mathrm{d}\mu}\,S_{i,T}(f_{\rm cut}p_T R,\mu) = \gamma_i^{S_T}(f_{\rm cut}p_T R,\mu)\,S_{i,T}(f_{\rm cut}p_T R,\mu)\,, \tag{5.74}$$

$$\mu\frac{\mathrm{d}}{\mathrm{d}\mu}\,\mathcal{S}_{i,T}(f_{\rm cut}\theta_t\,p_T R,\mu) = \gamma_i^{\mathcal{S}_T}(f_{\rm cut}\theta_t\,p_T R,\mu)\,\mathcal{S}_{i,T}(f_{\rm cut}\theta_t\,p_T R,\mu)\,, \tag{5.75}$$

$$\mu\frac{\mathrm{d}}{\mathrm{d}\mu}\,\mathcal{S}_{i,Z'}(\Delta_E,\theta_t\,p_T R,\mu) = \int \mathrm{d}\Delta'_E\gamma_i^{S_{Z'}}(\Delta_E-\Delta'_E,\theta_t\,p_T R,\mu)\,\mathcal{S}_{i,Z'}(\Delta'_E,\theta_t\,p_T R,\mu)\,, \tag{5.76}$$

to evolve them to a common scale. The anomalous dimensions are summarized in the appendix B.3.3.

5.3.4 Numerical results

We start by presenting numerical results for the jet energy drop with trimming. For the four panels in fig. 5.23, we choose the same LHC jet kinematics as in the previous sections. The grooming parameters are taken to be $f_{\rm cut} = 0.3$ and $\theta_t = 0.4$. As mentioned before, the $f_{\rm cut}$ value here is larger than what is typically used in experimental analyses. Our choice is motivated by the fact that for relatively large values of $f_{\rm cut}$ a significant fraction of the jet energy drop cross section is in the perturbative range, where the resummation techniques studied in this work are applicable. This point is illustrated in fig. 5.22, where PYTHIA predictions at parton and hadron level are compared. Explicitly, in the right panel the red and green curves overlap for $\Delta_E \gtrsim 0.15$, while they

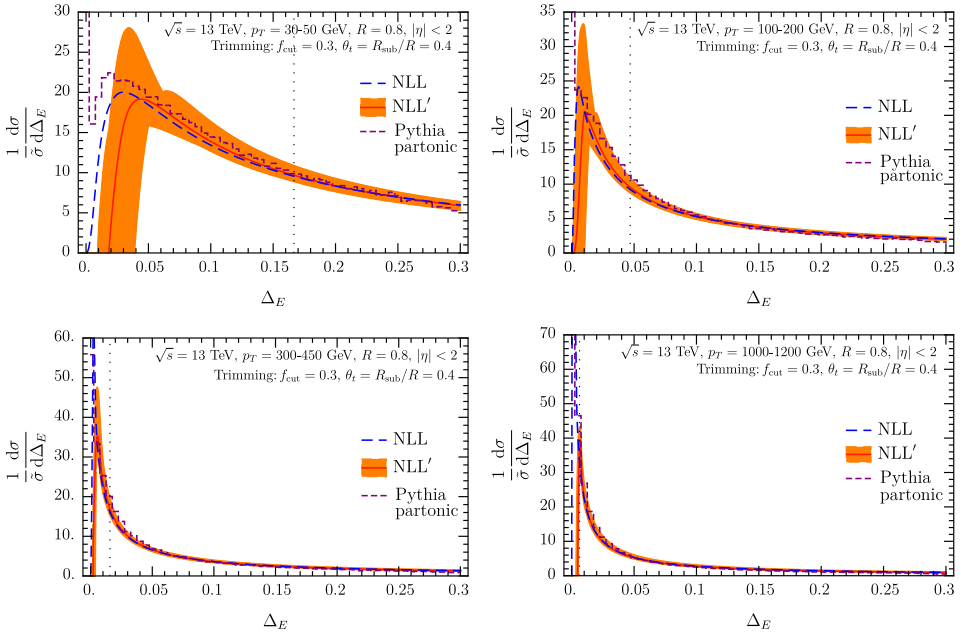

Figure 5.23 Numerical results for the jet energy drop obtained with the trimming algorithm at NLL (blue dashed) and NLL′ (orange) order, compared to Pythia partonic (purple dashed). We choose trimming parameters $f_{\rm cut} = 0.3$ and $\theta_t = 0.4$. The different panels correspond to different jet transverse momenta. The central curves are normalized to unity between the dotted vertical line and $\Delta_E = f_{\rm cut}$.

never completely overlap in the left panel. Similar to soft drop, MPI affects the whole distribution.

In fig. 5.23 we show both the NLL′ and NLL results, finding again that the NLL curve is within the uncertainty band of the NLL′ result in the perturbative region, indicating a good convergence of the resummed cross section. We note that the cross section does not vanish at $\Delta_E = f_{\rm cut}$, consistent with the NLO result shown in fig. 5.20. Indeed, the cross section can extend to Δ_E values well above $f_{\rm cut}$. However, this requires a different factorization formula than eq. (5.69), since we formally assumed $\Delta_E \ll f_{\rm cut}$, and we leave an analysis of the region $\Delta_E \gtrsim f_{\rm cut}$ for future work.

In fig. 5.24 we consider the dependence of the jet energy drop on the grooming parameters θ_t and $f_{\rm cut}$, for a jet $p_T = 1000-1200$ GeV (as in the lower-right panel of fig. 5.23). A larger value of θ_t leads to larger subjet energies, which are more likely to cross the threshold set by $f_{\rm cut}$. This leads to the larger spike

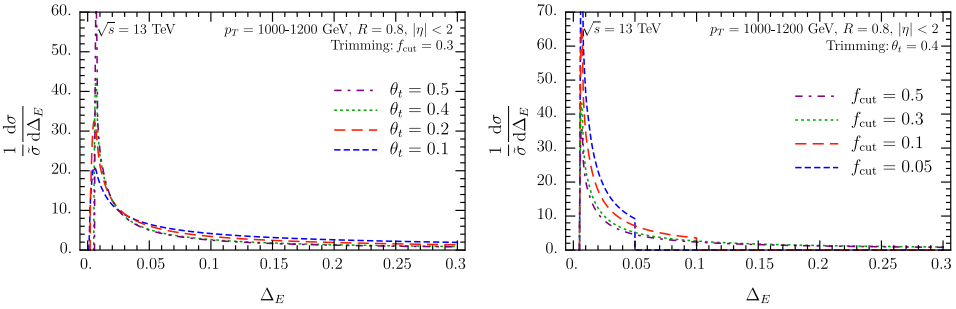

Figure 5.24 Dependence of the jet energy drop for trimming on the grooming parameters θ_t (left) and $f_{\rm cut}$ (right).

near $\Delta_E \approx 0$ in the left panel of fig. 5.24. Similarly, a smaller value of $f_{\rm cut}$ allows more subjets to pass the grooming condition, reducing the jet energy drop. Note that in this case we only plot distributions for $\Delta_E < f_{\rm cut}$, because our factorization formula does not lead to reliable predictions beyond that.

5.4 Conclusions

We have studied the jet energy drop, which is the relative difference in jet energy (or transverse momentum) of a groomed and ungroomed jet, and is a key observable for characterizing the impact of grooming on jets. We considered three different grooming algorithms, frequently used in experimental analyses: i) soft drop, ii) iterated soft drop, and iii) trimming. The jet energy drop is particularly sensitive to soft radiation, making it ideally suited for tuning parton shower event generators to data, particularly to constrain the hadronization model. Since it maps out the soft substructure of jets, it also has significant potential for studying the modification induced by medium effects in proton-nucleus and nucleus-nucleus collisions.

We have developed factorization formulae which allow for an evaluation of the cross sections at next-to-leading logarithmic (NLL′) accuracy, resumming logarithms of the jet radius, jet energy drop, and grooming parameters. We also include the non-global logarithms with C/A clustering effects and Abelian clustering effects at order α_s^2. Formally, one should also resum the NGLs, but from earlier work we note that their effect beyond the leading term is negligible for our phenomenological results. The factorization for soft drop requires a joint resummation of the jet energy drop and groomed jet radius θ_g, and is very sensitive to nonperturbative effects when integrating the resummed cross section over θ_g. This sensitivity can be reduced in a controlled manner by

imposing a minimum cut on θ_g. The energy drop for soft drop with $\beta = 0$ is a Sudakov safe observable, which we calculate also to NLL$'$. We have presented numerical results for all three algorithms and compared to PYTHIA simulations, finding very good agreement in the perturbative region. For soft drop we also compared to CMS data.

6

The soft drop groomed momentum fraction z_g beyond LL

In this chapter, we study the soft drop grooming algorithm [23] and its momentum sharing fraction known as z_g [26]. After reclustering a jet with the Cambridge/Aachen (C/A) [42, 43] algorithm, it iteratively declusters the jet, at each step removing the softer branch if its momentum fraction z fails the soft drop condition

$$z > z_{\text{cut}} \left(\Delta R_{12}/R\right)^{\beta} . \tag{6.1}$$

Here, ΔR_{12} is the distance between the branches in the η-ϕ plane, R is the radius of the initial ungroomed jet, and z_{cut}, β are tuneable grooming parameters. (Soft drop grooming with $\beta = 0$ corresponds to the modified mass drop tagger [181].) Once eq. (6.1) is satisfied, the algorithm terminates and $z_g = z$ and $R_g = \Delta R_{12}$, as illustrated in fig. 6.1. Both z_g and R_g are central to characterizing the two hard branches of the groomed jet.

The momentum sharing fraction z_g has received a lot of attention by both the theoretical and experimental particle and nuclear physics communities in the past years. The main reason is that it allows for the most direct measurement of the QCD (Altarelli-Parisi) splitting functions [131], providing a glimpse into fundamental splittings at parton level. The cross section differential in z_g was measured by the ALICE [148,201], ATLAS [159], CMS [146,202] collaborations at the LHC and by STAR [160] at RHIC, which we compare to in this work. In addition, the z_g distribution was also extracted from CMS open data [203,204].

Our calculation reveals that this measurement not only probes the color charge but also the spin of the parton initiating the jet, and our precision is essential to have sensitivity to this effect in interpreting experimental results. The momentum sharing fraction is also of great interest for heavy-ion colli-

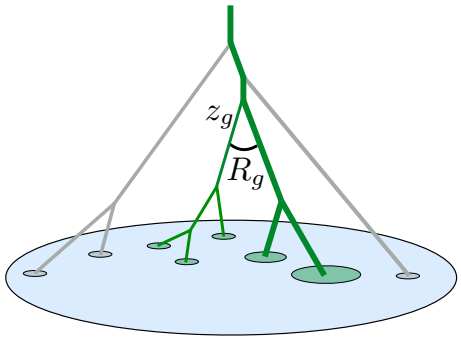

Figure 6.1 Illustration of the clustering tree of a jet: Branches are groomed away (grey) until the soft drop condition in eq. (6.1) is first satisfied. This splitting sets the observables z_g and R_g, and subsequent splittings (green) are kept.

sions, as it probes modifications of hard-collinear splittings in the quark-gluon plasma. For recent theoretical results, see refs. [205–212]. We also expect z_g to be of great phenomenological importance at the future Electron-Ion Collider (EIC) [213].

The observable z_g was first introduced in ref. [26], where a calculation of the corresponding cross section at leading-logarithmic (LL) accuracy was performed. It was found that z_g is Infrared-Collinear (IRC) safe only for $\beta < 0$. For $\beta \geq 0$, z_g is IRC unsafe but calculable: the IRC divergence is tamed by accounting for the Sudakov suppression, making z_g a Sudakov safe observable [40]. The cross section can thus be calculated by performing the joint resummation of the logarithms of z_g and the groomed radius R_g.Alternatively, one can impose a cut on R_g, but this case also requires resummation. Here we extend the work of ref. [26] by setting up a factorization framework within Soft Collinear Effective Theory (SCET) [12,13,15,16,214], which allows for the systematic extension beyond LL. We obtain results at next-to-leading logarithmic (NLL′) accuracy, accounting for non-global logarithms (NGLs) [83]. Our work also provides the first meaningful assessment of perturbative uncertainties, and opens the door to future calculations at higher perturbative accuracy and for a systematic treatment of nonperturbative effects [172, 215].

6.1 Theoretical framework

We now describe how we calculate the cross section differential in the jet's transverse momentum p_T and rapidity η, as well as the groomed jet substruc-

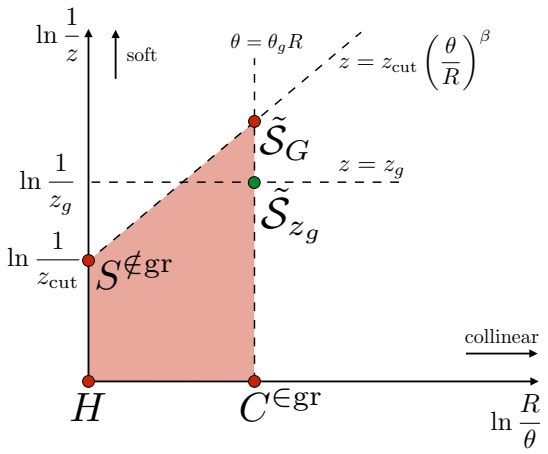

Figure 6.2 Lund diagram for the cross section differential in z_g and θ_g. The green dot corresponds to the emission passing the soft drop condition, and emissions in the red area are vetoed. The modes that appear in the corresponding SCET calculation are indicated by green and red dots.

ture observables z_g and $\theta_g \equiv R_g/R$. For small jet radii, we can separate the production of the inclusive jet sample from the jet substructure measurement using collinear factorization,

$$\frac{\mathrm{d}\sigma}{\mathrm{d}p_T\,\mathrm{d}\eta\,\mathrm{d}z_g\,\mathrm{d}\theta_g} = \sum_i f_i(p_T,\eta,R,\mu) \times \tilde{\mathcal{G}}_i(z_g,\theta_g,p_T R,z_{\mathrm{cut}},\beta,\mu)\,. \tag{6.2}$$

The jet production is summarized by quark/gluon fractions $f_{i=q,g}$, which account for parton distribution functions, the hard-scattering, and semi-inclusive jet functions. The jet functions $\tilde{\mathcal{G}}_i$ (using the notation of ref. [3]) encode the substructure measurement. See earlier chapters for more details on this first step of the factorization.

Next, we calculate the jet function $\tilde{\mathcal{G}}_i$, which we will need to describe the region where z_g is order one. We find at leading order (LO) for $z_g, \theta_g > 0$

$$\tilde{\mathcal{G}}_q^{(1)} = \Theta(1/2 > z_g > z_{\mathrm{cut}}\theta_g^\beta)\,\Theta(\theta_g < 1)\frac{\alpha_s}{\pi}\frac{1}{\theta_g}\big[P_{qq}(z_g) + P_{gq}(z_g)\big]\,, \tag{6.3}$$

and similarly for $\tilde{\mathcal{G}}_g^{(1)}$. Here P_{ij} are the leading-order QCD splitting functions, showing that the measurement of z_g probes these. Since $\tilde{\mathcal{G}}_i^{(1)} \sim 1/\theta_g$, and there is no lower bound on θ_g for $\beta \geq 0$, we cannot integrate out the dependence

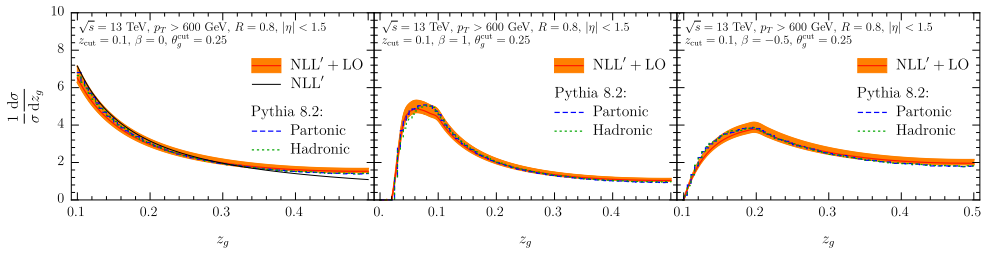

Figure 6.3 Comparison of our numerical results for the momentum sharing fraction z_g at NLL′+LO to Pythia 8 simulations [87] at parton and hadron level, for representative jet kinematics and three choices of soft drop grooming parameters.

on θ_g in this case. The integration over θ_g is only possible after taking into account the Sudakov suppression through resummation.

To achieve this, we perform the resummation of large logarithmic corrections of z_g, θ_g and $z_{\rm cut}$. We start with the result at LL accuracy, which provides physical intuition and helps identify the relevant modes in SCET. It is described by strongly-ordered emission of gluons in the collinear and soft limit. The Lund diagram in fig. 6.2 shows the phase space of such emissions in terms of their energy fraction z and angle θ, with dashed lines indicating the soft drop condition in eq. (6.1) and the measurement of θ_g and z_g. The emission at the green dot sets z_g and θ_g. Emissions in the red region are not allowed, and the corresponding area enters in the Sudakov exponent:

$$\tilde{\mathcal{G}}_i \overset{LL}{=} \Theta(1/2 > z_g > z_{\rm cut}\theta_g^\beta)\frac{2\alpha_s C_i}{\pi}\frac{1}{z_g\,\theta_g} \times \exp\left(-\frac{\alpha_s C_i}{\pi}(\beta \ln^2\theta_g + 2\ln z_{\rm cut}\ln\theta_g)\right), \tag{6.4}$$

Here $C_{i=F,A}$ denotes the appropriate color factor for quarks and gluons, which is the only dependence on the initial parton at LL. As eq. (6.4) indicates, it is now safe to integrate over θ_g due to the Sudakov suppression, and the resulting expression agrees with eq. (14) of ref. [26]. We can extend this result to NLL′ by identifying the relevant modes within SCET, for which the scaling of the momentum components can be read off from the location of the points in the Lund diagram in fig. 6.2. We find

$$\begin{aligned}\tilde{\mathcal{G}}_i = \Theta(1/2 > z_g > z_{\rm cut}\theta_g^\beta)\tilde{H}_i(p_T R,\mu)\, C_i^{\in \rm gr}(\theta_g p_T R,\mu) S_i^{\notin \rm gr}(z_{\rm cut} p_T R,\beta,\mu) \\ \times \tilde{\mathcal{S}}_G(z_{\rm cut}\theta_g^{1+\beta} p_T R,\beta,\mu) \times S_i^{\rm NG}(z_{\rm cut})\left[\frac{\mathrm{d}}{\mathrm{d}z_g}\frac{\mathrm{d}}{\mathrm{d}\theta_g}\tilde{\mathcal{S}}_{z_g}(z_g\theta_g p_T R,\mu)\right. \\ \left. + \tilde{\mathcal{S}}'^{\rm NG}_{i,1}(z_g\theta_g, z_g) + \tilde{\mathcal{S}}'^{\rm NG}_{i,2}\left(z_g\theta_g, \frac{z_g}{z_{\rm cut}\theta_g^\beta}\right)\right].\end{aligned} \tag{6.5}$$

The resummation of logarithms of z_g, θ_g, and $z_{\rm cut}$ is achieved by evaluating each ingredient (except those describing NGLs) at its natural scale, which can be read off from their first argument, and using the renormalization group equations (RGEs) to evolve them to a common scale μ. The modes associated with the red points in fig. 6.2 also appeared in the factorization of the groomed jet radius [122], and the expressions for the corresponding functions can be found there. The mode corresponding to the green point is rather different because it describes the *single* emission that passes the soft drop condition. We set the μ scales for the cross section differential in θ_g and cumulative in z_g, and therefore present the order α_s expression and RGE for the new ingredient $\tilde{\mathcal{S}}_{z_g}$ differential in θ_g:

$$\frac{\mathrm{d}}{\mathrm{d}\theta_g}\tilde{\mathcal{S}}_{z_g}(z_g\theta_g p_T R,\mu) = -\frac{2\alpha_s C_i}{\pi}\frac{1}{\theta_g}\ln\frac{\mu}{z_g\theta_g p_T R}\,,$$
$$\frac{\mathrm{d}}{\mathrm{d}\ln\mu}\frac{\mathrm{d}}{\mathrm{d}\theta_g}\tilde{\mathcal{S}}_{z_g} = -\frac{2\alpha_s C_i}{\pi}\frac{1}{\theta_g}\,. \tag{6.6}$$

A similarly unusual RGE was encountered in chapters 4 and 5, to which we refer the reader for details.

There are three types of non-global logarithms [83] in eq. (6.5): First, the NGLs described by $S_i^{\rm NG}$ are similar to the usual hemisphere case, and arise due to correlations between the unconstrained emissions in the region outside the jet and the radiation inside the jet that fails the grooming condition. Second, the NGLs $\mathcal{S}_{i,1,2}^{\prime\rm NG}$ arise from correlated emissions, where one sets z_g and θ_g (green dot) and the other is either outside the groomed radius and fails the grooming condition or inside the groomed radius and is unconstrained (corresponding to one of the two red dots on the vertical dashed line $\theta = \theta_g R$ in fig. 6.2). These NGLs are sensitive to C/A clustering effects [184,193]. We include their leading contribution at order α_s^2,

$$\tilde{\mathcal{S}}_{i,1}^{\prime\rm NG,(2)}(z_g\theta_g, z_g) = 2.58 C_i C_A \Big(\frac{\alpha_s}{2\pi}\Big)^2 \frac{1}{z_g\theta_g}\ln z_g\,, \tag{6.7}$$

and the form of $\tilde{\mathcal{S}}_{i,2}^{\prime\rm NG,(2)}$ is the same at this order. In our numerical implementation these NGLs are multiplied by the global Sudakov suppression factor, see eq. (6.5), making their numerical size small (percent level).

6.2 Numerical results and comparison to data.

Throughout this section we consider (ungroomed) jets which are reconstructed with the anti-k_T algorithm [10], as in the measurement of the experimental collaborations. We use the parton distribution functions of ref. [106].

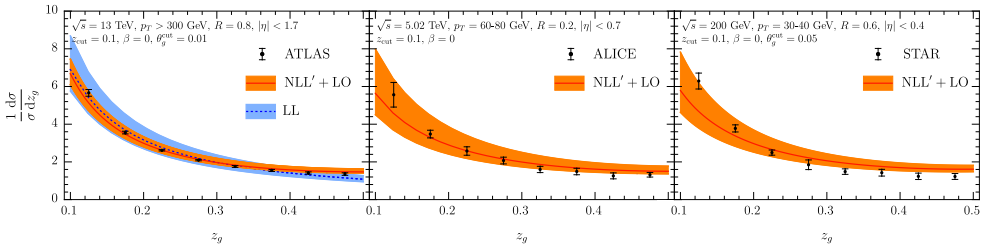

Figure 6.4 Comparison of our results to ATLAS [159], ALICE [201] and STAR [160] data for $\beta = 0$.

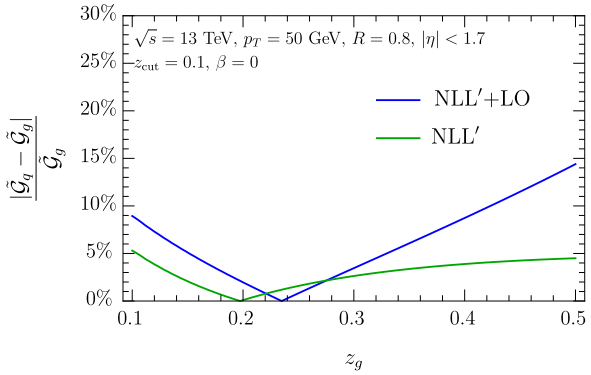

Figure 6.5 Relative difference between the z_g distribution for quark and gluon-initiated jets. The difference between the green and blue curve indicates the size of the nonsingular part of the QCD splitting function, encoding the spin-dependence.

We start by comparing our numerical results at NLL′+LO accuracy to Pythia 8 simulations [87]. The comparison for exemplary jet kinematics is shown in fig. 6.3. We choose three representative values of the grooming parameter β and impose a cutoff on the groomed jet radius of $\theta_g^{\rm cut} > 0.25$ to reduce the sensitivity to nonperturbative physics. The QCD scale uncertainty bands in the figures shown here are obtained by independently varying all relevant scales in eqs. (6.2) and (6.5) by a factor of 2 around the central scale choice. In addition, we smoothly freeze all scales at $\mathcal{O}(1\text{ GeV})$ [101]. The hadronization corrections for the chosen kinematics are very small which can be seen by comparing Pythia results at parton and hadron level.

Overall, we observe very good agreement of our results with Pythia. In addition to the improved precision, there are notable qualitative differences with the earlier results of ref. [26]: The shape of our distribution for $\beta < 0$

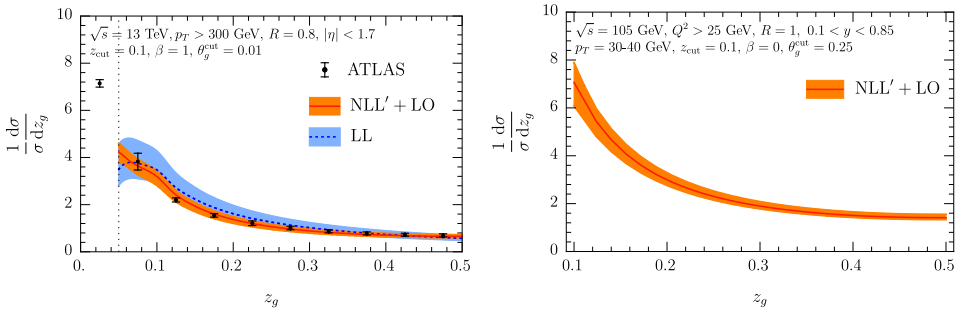

Figure 6.6 Comparison to ATLAS results [159] for $\beta = 1$ (left). Prediction for the Electron-Ion Collider (right).

is rather different, and we find a smooth transition to $\beta = 0$ for $z_g > z_{\rm cut}$, whether we approach from negative or positive β. For large z_g the matching to the LO in eq. (6.3) is essential, which is done multiplicatively because of the common singularity in θ_g. Indeed, the non-singular terms added by the matching are important to achieve good agreement with Pythia, as illustrated in the left panel of fig. 6.3 by the black NLL′ curve (that does not include the matching). This demonstrates the sensitivity of z_g distribution to the full splitting function beyond the leading $1/z_g$ behavior in the singular limit. The size of these corrections, which encode the spin-dependence of the splitting function, are visualized in fig. 6.5. Since their size can be up to order 10%, we expect that this can be probed experimentally by for example comparing inclusive vs. photon-tagged jets or jets with different rapidities.

Next, we compare to the experimental results from ATLAS [159], ALICE [201] and STAR [160] for $\beta = 0$ in fig. 6.4. We normalize our results to the data [1] and impose the same cut on θ_g. The hadronization effects in Pythia for ALICE and STAR kinematics (not shown) are much more sizable than in fig. 6.3, in accord with the larger perturbative uncertainties. Nevertheless, we find very good agreement even for these relatively low jet transverse momenta. We note that the CMS result of ref. [146] is not unfolded, prohibiting a direct comparison. As a representative example, we show the LL QCD scale uncertainty band in the left panel of fig. 6.4 which is significantly larger than at NLL′. This implies that the NLL′ accuracy achieved in this work is needed to match the current experimental precision.

Next, we compare in the left panel of fig. 6.6 our results to ATLAS measurement [159] for $\beta = 1$, as an example. We normalize our results to the data in

[1] The ALICE normalization is not normalized by a few percent, because of their treatment of jets that never pass the soft drop condition.

the region to the right of the dotted line, as our prediction for the left most data point are very sensitive to nonperturbative effects. Note that this was not needed for $\beta = 0$, where z_{cut} provides a lower bound on z_g. We observe excellent agreement! In this case our NLL′+LO prediction is substantially better than the LL result.

Lastly, we present predictions for jet kinematics at the future EIC in the right panel of fig. 6.6. We consider jets reconstructed in the laboratory frame $ep \to e + \text{jet} + X$ for typical EIC kinematics [216, 217] with cuts on the photon virtuality Q^2 and the inelasticity y as indicated in the figure. The clean environment at the EIC will allow studies of hadronization effects, and z_g measurements in single- and di-jet events can help improve our understanding of quark/gluon differences (see also fig. 6.5).

6.3 Conclusions

In this chapter we have presented a calculation of the soft drop groomed momentum sharing fraction z_g at NLL′+LO accuracy. This Sudakov-safe jet substructure observable, which probes the hard branching process inside the jet, constitutes the most direct measurement of the QCD splitting function. Our framework allows for a systematic extension beyond the previously achieved LL accuracy, yielding qualitatively different results for $\beta < 0$ than in an earlier study, and provides the first meaningful assessment of theoretical uncertainties. We also show that z_g probes the QCD splitting function beyond the leading $1/z_g$ dependence, indicating sensitivity to the spin of the particle that initiates the jet. Our calculations indicate that this effect is sufficiently large to be probed experimentally. The momentum sharing fraction z_g is one of the hallmark observables in the field of jet substructure and has been measured by several experimental collaborations at the LHC and RHIC. We compared to the available experimental data and found very good agreement with our purely perturbative calculation. In addition, we provided predictions for the future Electron-Ion Collider. Our precise calculations reduced uncertainties and changed the shape of the prediction, bringing it in excellent agreement with the data.

7

Conclusions

This thesis investigated the use of Soft-Collinear effective theory (SCET) in order to obtain precise QCD predictions for jet substructure observables. We used SCET to obtain factorization theorems that allow us to resum towers of logarithms that become large in certain regions of phase space, improving the convergence of perturbation theory. Pushing for higher orders in logarithmic accuracy is a crucial part of having reliable predictions to be put up against data, and a necessary condition for precision.

In chapter 3, we investigated the classic jet substructure observable known as the *jet shape*. The jet shape maps out the transverse energy profile of jets and is one of the most measured jet substructure observables. We calculated this observable to next-to-leading logarithmic accuracy (NLL′). Specifically, we accounted for the single logarithms of the jet radius R and the double logarithms of r/R at next-to-leading logarithmic order, and match to next-to-leading order. To achieve this accuracy, the recoil of soft radiation on the jet axis must be included when $r \ll R$. This involves the one-loop calculation of a recoil-sensitive collinear function and rapidity logarithms, that we resum using the rapidity renormalization group, as well as non-global logarithms from in vs. out-of-jet soft radiation. Our calculation constitutes the first extension of this classic jet substructure observable beyond leading logarithmic accuracy.

In chapter 4, we presented the first calculation of the angles between different jet axes. We considered three different jet axes: The standard jet axis, the groomed jet axis (in particular, the axis obtained after applying soft drop) and the jet axis obtained using a winner-take-all recombination scheme. Our studies were motivated by the different soft sensitivity of these different jet axes. Within Soft Collinear Effective Theory, we performed calculations at next-to-leading logarithmic (NLL′ or NLL) accuracy, where large logarithms of the angle between the the standard and groomed vs. the winner-take-all axes are resummed to all orders, including the contribution of non-global logarithms in the leading color approximation. The angle between the standard and soft

drop groomed jet axes is particularly soft sensitive, as it is a measure of the radiation which is groomed away by the soft drop algorithm. The corresponding factorization theorem depends on the soft drop groomed jet radius R_g. We resummed large logarithms of both the angle between the jet axes and the groomed radius R_g, integrating over R_g after the resummation is performed to obtain a distribution for the angle between the axes. We included nonperturbative effects in impact parameter space by introducing a model function, which is related to the nonperturbative component of the rapidity anomalous dimension relevant for transverse momentum resummation. This was crucial to obtain a sensible dependence on the grooming parameter β for the angle between the standard and groomed jet axis. Therefore, the observables considered here can provide important constraints on this universal nonperturbative quantity.

In chapter 5, we studied the jet energy drop, which is the relative difference in jet energy (or transverse momentum) of a groomed and ungroomed jet, and is a key observable for characterizing the impact of grooming on jets. Just like the angle between the groomed and the standard jet axes, the jet energy drop is particularly sensitive to soft radiation, making it ideally suited for tuning parton shower event generators to data, particularly to constrain the hadronization model. Since it maps out the soft substructure of jets, it also has significant potential for studying the modification induced by medium effects in proton-nucleus and nucleus-nucleus collisions. We developed factorization formulae that allow for an evaluation of the cross sections at next-to-leading logarithmic (NLL$'$) accuracy, resumming logarithms of the jet radius, jet energy drop, and grooming parameters. We presented numerical results and compared to Pythia simulations, finding very good agreement in the perturbative region.

In chapter 6, we presented a calculation of the soft drop groomed momentum sharing fraction z_g at NLL$'$+LO accuracy. This observable constitutes the most direct measurement of the QCD splitting function. Our framework allowed for a systematic extension beyond the previously achieved LL accuracy, yielding qualitatively different results for $\beta < 0$ than in an earlier study, and provided the first meaningful assessment of theoretical uncertainties. We also showed that z_g probes the QCD splitting function beyond the leading $1/z_g$ dependence, indicating sensitivity to the spin of the particle that initiates the jet. Our calculations indicated that this effect is sufficiently large to be probed experimentally. Moreover, z_g is one of the most important observables in the field of jet substructure and has therefore been measured at a variety of experimental collaborations, both at the LHC and RHIC. We compared our (purely perturbative) calculation to the available experimental data and found very good agreement.

A

Conventions and notation

A.1 Light-cone coordinates

Light-cone coordinates are written with respect to two reference light-like vectors n^μ and $\bar{n}^\mu$ which must satisfy $n^2 = \bar{n}^2 = 0$ and $n \cdot \bar{n} = 2$. One possible choice is

$$n^\mu = (1, 0, 0, 1), \qquad \bar{n}^\mu = (1, 0, 0, -1). \tag{A.1}$$

Any 4-vector w^μ can be represented in the light-cone basis

$$w^\mu = \frac{\bar{n}^\mu}{2} w^+ + \frac{n^\mu}{2} w^- + w_\perp^\mu, \tag{A.2}$$

where

$$p^+ \equiv n \cdot w = w^0 - w^3, \qquad p^- \equiv \bar{n} \cdot w = w^0 + w^3 \qquad \text{and} \qquad w_\perp^\mu \equiv (0, w^1, w^2, 0). \tag{A.3}$$

It is also useful to introduce the notation

$$w^\mu = (w^+, w^-, w_\perp). \tag{A.4}$$

The inner product of two vectors is

$$w \cdot v = \frac{1}{2}(w^+ v^- + w^- v^+) - \vec{w}_\perp \cdot \vec{v}_\perp, \tag{A.5}$$

such that $w^2 = w^+ w^- - \vec{w}_\perp^2$.

A.2 Altarelli-Parisi splitting functions

The one-loop Altarelli-Parisi regularized splitting functions are given by

$$\begin{aligned}
P_{qq}(z) &= C_F \left(\frac{1+z^2}{1-z}\right)_+ , \\
P_{gq}(z) &= C_F \, \frac{1+(1-z)^2}{z} , \\
P_{gg}(z) &= 2C_A \left[\frac{z}{(1-z)_+} + \frac{1-z}{z} + z(1-z)\right] + \frac{\beta_0}{2}\,\delta(1-z) , \\
P_{qg}(z) &= T_F\big[z^2 + (1-z)^2\big],
\end{aligned} \tag{A.6}$$

while the *unregularized* splitting functions in $d = 4 - 2\epsilon$ are

$$\begin{aligned}
\hat{P}_{qq}(x) &= C_F\Big[\frac{1+x^2}{1-x} - \epsilon(1-x)\Big], \\
\hat{P}_{gq}(x) &= C_F\Big[\frac{1+(1-x)^2}{x} - \epsilon x\Big], \\
\hat{P}_{qg}(x) &= T_F\Big[1 - 2x(1-x) - 2\epsilon\, x(1-x)\Big], \\
\hat{P}_{gg}(x) &= 2C_A\Big[\frac{x}{1-x} + \frac{1-x}{x} + x(1-x)\Big].
\end{aligned} \tag{A.7}$$

A.3 Plus distributions

A.3.1 Definition

The plus distribution for a function $f(x)$ divergent at $x = 0$ is defined as

$$[\theta(x) f(x)]_+ \equiv \lim_{\beta\to 0}\left[\theta(x-\beta) f(x) - \delta(x-\beta)\int_\beta^1 \mathrm{d}y\, f(y)\right]. \tag{A.8}$$

From this definition it is clear that $[f(x)]_+ = f(x)$ for $x > \beta$. The plus distribution is well behaved when convolved with a smooth test function $g(x)$

$$\int_0^1 \mathrm{d}x\, g(x)\,[f(x)]_+ = \int_0^1 \mathrm{d}x\,[g(x) - g(0)] f(x), \tag{A.9}$$

implying the boundary condition $\int_0^1 [f(x)]_+ = 0$. We are often dealing with the special cases

$$\begin{aligned}
\mathcal{L}_n(x) &\equiv \left[\frac{\theta(x)\ln^n x}{x}\right]_+ = \lim_{\beta\to 0}\left[\frac{\theta(x-\beta)\ln^n x}{x} + \delta(x-\beta)\frac{\ln^{n+1}\beta}{n+1}\right] \\
\mathcal{L}^\eta(x) &\equiv \left[\frac{\theta(x)}{x^{1-\eta}}\right]_+ = \lim_{\beta\to 0}\left[\frac{\theta(x-\beta)}{x^{1-\eta}} + \delta(x-\beta)\frac{x^\eta - 1}{\eta}\right],
\end{aligned} \tag{A.10}$$

and frequently make use of the identity

$$\frac{\theta(x)}{x^{1+\epsilon}} = -\frac{1}{\epsilon}\delta(x) + \sum_{n=0}^{\infty}(-\epsilon)^n \mathcal{L}_n(x). \tag{A.11}$$

A.3.2 Convolutions of plus distributions

The following convolutions between plus distributions were used throughout the thesis

$$\int \mathrm{d}\tau' \left[\frac{\Theta(\tau_1-\tau')}{(\tau_1-\tau')^{1+\eta_1}}\right]_+ \left[\frac{\Theta(\tau_2-\tau')}{(\tau_2-\tau')^{1+\eta_2}}\right]_+ = \frac{\Gamma(-\eta_1)\Gamma(-\eta_2)}{\Gamma(-\eta_1-\eta_2)} \left[\frac{\Theta(\tau_1-\tau_2)}{(\tau_1-\tau_2)^{1+\eta_1+\eta_2}}\right] \tag{A.12}$$

as well as

$$\begin{aligned}
\int \mathrm{d}\tau' \left[\frac{\Theta(\tau-\tau')}{(\tau-\tau')^{1+\eta}}\right]_+ \delta(\tau') &= \left[\frac{\Theta(\tau)}{\tau^{1+\eta}}\right]_+ \\
\int \mathrm{d}\tau' \left[\frac{\Theta(\tau-\tau')}{(\tau-\tau')^{1+\eta}}\right]_+ \left[\frac{\Theta(\tau')}{\tau'}\right]_+ &= \left[\frac{\Theta(\tau)}{\tau^{1+\eta}}\right]_+ [\ln\tau - H(-1-\eta)] \\
\int \mathrm{d}\tau' \left[\frac{\Theta(\tau-\tau')}{(\tau-\tau')^{1+\eta}}\right]_+ \left[\frac{\Theta(\tau')\ln\tau'}{\tau'}\right]_+ &= \left[\frac{\Theta(\tau)}{\tau^{1+\eta}}\right]_+ \frac{[\ln\tau - H(-1-\eta)]^2 + \frac{\pi^2}{6} - \gamma^{(1)}(-\eta)}{2}.
\end{aligned} \tag{A.13}$$

Here $H(-1-\eta)$ is the harmonic number function and $\psi^{(1)}$ is the first derivative of the digamma function, $\psi^{(1)}(z) = \frac{\mathrm{d}}{\mathrm{d}z}\left[\frac{\Gamma'(z)}{\Gamma(z)}\right]$.

A.4 Fourier transform

The Fourier transform of a function $f(\vec{k}_\perp)$ is defined as

$$f\big(\vec{b}_\perp\big) = \int \mathrm{d}^2k_\perp \, f\big(\vec{k}_\perp\big)\, e^{i\,\vec{b}_\perp\cdot\vec{k}_\perp}, \tag{A.14}$$

and the inverse Fourier transform

$$f\big(\vec{k}_\perp\big) = \int \frac{\mathrm{d}^2k_\perp}{(2\pi)^2} \, f\big(\vec{b}_\perp\big)\, e^{-i\,\vec{b}_\perp\cdot\vec{k}_\perp}. \tag{A.15}$$

If function $f(\vec{k}_\perp)$ has no angular dependence the Fourier transform simplifies to

$$f(b_\perp) = 2\pi \int_0^\infty \mathrm{d}k_\perp k_\perp J_0(k_\perp b_\perp) f(k_\perp), \tag{A.16}$$

where J_0 is the Bessel function and $k_\perp \equiv |\vec{k}_\perp|$, $b_\perp \equiv |\vec{b}_\perp|$. Often we need to Fourier transform plus distributions

$$\frac{1}{\mu^2}\int \mathrm{d}^2 k_\perp \mathcal{L}_n\left(\frac{k_\perp^2}{\mu^2}\right) e^{i\,\vec{b}_\perp\cdot\vec{k}_\perp} = \frac{\pi}{(n+1)!}\ln^{n+1}\left(\frac{\mu_b^2}{\mu^2}\right), \tag{A.17}$$

where $\mu_b \equiv 2e^{-\gamma_E}/b_\perp$.

B

Renormalization Group Evolution

B.1 QCD anomalous dimensions

The expansion of the β-function is given by

$$\beta[\alpha_s, \epsilon] = -2\epsilon\alpha_s + \beta[\alpha_s], \qquad \beta[\alpha_s] = -2\alpha_s \sum_{n=0}^{\infty} \beta_n \Big(\frac{\alpha_s}{4\pi}\Big)^{1+n}, \tag{B.1}$$

where the β_n coefficients up to three-loops are

$$\begin{aligned}
\beta_0 =& \frac{11}{3}C_A - \frac{4}{3}n_f T_F \\
\beta_1 =& \frac{34}{3}C_A^2 - \Big(\frac{20}{3}C_A + 4C_F\Big)n_f T_F \\
\beta_2 =& \frac{2857}{54}C_A^3 + \Big(C_F^2 - \frac{205}{18}C_F C_A - \frac{1415}{54}C_A^2\Big)2n_f T_F + \Big(\frac{11}{9}C_F + \frac{79}{54}C_A\Big)4n_f^2 T_F^2
\end{aligned} \tag{B.2}$$

Likewise, the expansion of the cusp and non-cusp anomalous dimensions are

$$\Gamma^i_{\text{cusp}}[\alpha_s] = \sum_{n=0}^{\infty} \Gamma^i_n \Big(\frac{\alpha_s}{4\pi}\Big)^{1+n}, \qquad \gamma^i[\alpha_s] = \sum_{n=0}^{\infty} \gamma^i_n \Big(\frac{\alpha_s}{4\pi}\Big)^{1+n}, \tag{B.3}$$

The coefficients of the cusp anomalous dimension Γ^i_n have been computed up to three-loops

$$\begin{aligned}
\Gamma^i_0 =& 4C_i \\
\Gamma^i_1 =& 4C_i\Big[\Big(\frac{67}{9} - \frac{\pi^2}{3}\Big)C_A - \frac{20}{9}n_f T_F\Big]
\end{aligned}$$

$$\Gamma_2^i = 4C_i\Big[\Big(\frac{245}{6} - \frac{134\pi^2}{27} + \frac{11\pi^4}{45} + \frac{22\zeta_3}{3}\Big)C_A^2 + \Big(-\frac{418}{27} + \frac{40\pi^2}{27} - \frac{56\zeta_3}{3}\Big)C_A n_f T_F + \Big(-\frac{55}{3} + 16\zeta_3\Big)C_F n_f T_F - \frac{16}{27}n_f^2 T_F^2\Big]. \tag{B.4}$$

Here $C_i = C_F$ for $i = q$ and $C_i = C_A$ for $i = g$.

B.2 Resummation ingredients

The multplicative RGE

$$\mu\frac{\mathrm{d}}{\mathrm{d}\mu}F(\mu) = \gamma_F(\mu)F(\mu), \qquad \gamma_F(\mu) = \rho_F\Gamma_{\mathrm{cusp}}[\alpha_s]\ln\frac{\mu^2}{\omega^2} + \gamma_F[\alpha_s] \tag{B.5}$$

has the solution

$$F(\mu) = U_F(\mu,\mu_0)F(\mu_0), \tag{B.6}$$

with the evolution kernel $U_F(\mu,\mu_0)$ given by

$$U_F(\mu,\mu_0) = e^{2\rho_F K_\Gamma(\mu,\mu_0)+K_\gamma(\mu,\mu_0)}\left(\frac{\mu_0}{\omega}\right)^{2\rho_F\,\eta_\Gamma(\mu,\mu_0)}. \tag{B.7}$$

The functions K_Γ, η_Γ and K_γ are defined as

$$\begin{aligned} K_\Gamma^i(\mu,\mu_0) &= \int_{\alpha_s(\mu_0)}^{\alpha_s(\mu)}\frac{\mathrm{d}\alpha_s}{\beta[\alpha_s]}\Gamma^i_{\mathrm{cusp}}[\alpha_s]\int_{\alpha_s(\mu_0)}^{\alpha_s}\frac{\mathrm{d}\alpha_s'}{\beta[\alpha_s']} \\ \eta_\Gamma^i(\mu,\mu_0) &= \int_{\alpha_s(\mu_0)}^{\alpha_s(\mu)}\frac{\mathrm{d}\alpha_s}{\beta[\alpha_s]}\Gamma^i_{\mathrm{cusp}}[\alpha_s] \\ K_\gamma^i(\mu,\mu_0) &= \int_{\alpha_s(\mu_0)}^{\alpha_s(\mu)}\frac{\mathrm{d}\alpha_s}{\beta[\alpha_s]}\gamma^i[\alpha_s]. \end{aligned} \tag{B.8}$$

Up to NNLL accuracy this functions are given by

$$\begin{aligned} K_\Gamma(\mu,\mu_0) = &-\frac{\Gamma_0}{4\beta_0^2}\left\{\frac{4\pi}{\alpha_s(\mu_0)}\left(1-\frac{1}{r}-\ln r\right) + \left(\frac{\Gamma_1}{\Gamma_0}-\frac{\beta_1}{\beta_0}\right)(1-r+\ln r)\right. \\ &+ \frac{\beta_1}{2\beta_0}\ln^2 r + \frac{\alpha_s(\mu_0)}{4\pi}\left[\left(\frac{\beta_1^2}{\beta_0^2}-\frac{\beta_2}{\beta_0}\right)\left(\frac{1-r^2}{2}+\ln r\right)\right. \\ &\left.\left.+\left(\frac{\beta_1\Gamma_1}{\beta_0\Gamma_0}-\frac{\beta_1^2}{\beta_0^2}\right)(1-r+r\ln r) - \left(\frac{\Gamma_2}{\Gamma_0}-\frac{\beta_1\Gamma_1}{\beta_0\Gamma_0}\right)\frac{(1-r)^2}{2}\right]\right\} \end{aligned}$$

$$\eta_\Gamma(\mu,\mu_0) = -\frac{\Gamma_0}{2\beta_0}\bigg[\ln r + \frac{\alpha_s(\mu_0)}{4\pi}\bigg(\frac{\Gamma_1}{\Gamma_0}-\frac{\beta_1}{\beta_0}\bigg)(r-1) + \frac{\alpha_s^2(\mu_0)}{16\pi^2}\bigg(\frac{\Gamma_2}{\Gamma_0}-\frac{\beta_1\Gamma_0}{\beta_0\Gamma_0}+\frac{\beta_1^2}{\beta_0^2}-\frac{\beta_2}{\beta_0}\bigg)\bigg]$$

$$K_\gamma(\mu,\mu_0) = -\frac{\Gamma_0}{2\beta_0}\bigg[\ln r + \frac{\alpha_s(\mu_0)}{4\pi}\bigg(\frac{\Gamma_1}{\Gamma_0}-\frac{\beta_1}{\beta_0}\bigg)(r-1)\bigg], \tag{B.9}$$

where we defined $r = \alpha_s(\mu)/\alpha_s(\mu_0)$ and we have omitted the superscript $i = q, g$. For RGE containing a convolution

$$\mu\frac{\mathrm{d}}{\mathrm{d}\mu}F(\tau;\mu) = \int \mathrm{d}\tau'\gamma_F(\tau-\tau';\mu)F(\tau';\mu), \tag{B.10}$$

with the anomalous dimension taking the general form

$$\gamma_F(\tau;\mu) = \Gamma_{\mathrm{cusp}}[\alpha_s]\bigg(\rho_F\,\delta(\tau)\ln\frac{\mu^2}{\omega^2} - 2\bigg[\frac{\Theta(\tau)}{\tau}\bigg]_+\bigg) + \gamma_F[\alpha_s]\delta(\tau), \tag{B.11}$$

the solution is

$$F(\tau,\mu) = \int \mathrm{d}\tau' U(\tau-\tau';\mu,\mu_0)F(\tau';\mu_0), \tag{B.12}$$

where the expression for the evolution kernel U_F is given by

$$U_F(\tau;\mu,\mu_0) = \frac{e^{2\rho_F K_\Gamma(\mu,\mu_0)+K_\gamma(\mu,\mu_0)+2\rho_F\gamma_E\eta_\Gamma(\mu,\mu_0)}}{\Gamma[-2\rho_F\,\eta_\Gamma(\mu,\mu_0)]}\bigg[\frac{\Theta(\tau)}{\tau^{1+2\rho_F\eta_\Gamma(\mu,\mu_0)}}\bigg]_+. \tag{B.13}$$

B.3 Anomalous dimensions of SCET modes

B.3.1 Jet shape

$$\begin{aligned}
\gamma^H_{qq}(z,p_TR,\mu) &= \frac{\alpha_s}{\pi}\bigg[C_F\Big(-L_R-\frac{3}{2}\Big)\,\delta(1-z)+P_{qq}(z)\bigg],\\
\gamma^H_{qg}(z,p_TR,\mu) &= \frac{\alpha_s}{\pi}\,P_{gq}(z),\\
\gamma^H_{gg}(z,p_TR,\mu) &= \frac{\alpha_s}{\pi}\bigg[\Big(-C_AL_R-\frac{1}{2}\beta_0\Big)\,\delta(1-z)+P_{gg}(z)\bigg],\\
\gamma^H_{gq}(z,p_TR,\mu) &= \frac{\alpha_s}{\pi}\,P_{qg}(z),\\
\gamma^C_q(\mu,\nu/p_T) &= \frac{\alpha_sC_F}{\pi}\left(2\ln\frac{\nu}{2p_T}+\frac{3}{2}\right),
\end{aligned}$$

$$
\begin{aligned}
\gamma_g^C(\mu,\nu/p_T) &= \frac{\alpha_s}{\pi}\left(2C_A\ln\frac{\nu}{2p_T}+\frac{1}{2}\beta_0\right),\\
\gamma_q^S(\mu,\nu R) &= \frac{\alpha_s C_F}{\pi}\,\ln\frac{4\mu^2}{\nu^2R^2},\\
\gamma_g^S(\mu,\nu R) &= \frac{\alpha_s C_A}{\pi}\,\ln\frac{4\mu^2}{\nu^2R^2},\\
\gamma_q^\nu(k_\perp,\mu) &= 4\alpha_s C_F\,\frac{1}{\mu^2}\,\frac{1}{(k_\perp^2/\mu^2)}_+,\\
\gamma_g^\nu(k_\perp,\mu) &= 4\alpha_s C_A\,\frac{1}{\mu^2}\,\frac{1}{(k_\perp^2/\mu^2)}_+.
\end{aligned}
\tag{B.14}
$$

Here $L_R=\ln\left(\frac{\mu^2}{p_T^2R^2}\right)$. We achieve full NLL′ accuracy by including the two-loop cusp anomalous dimension which amounts to multiplying all $\ln\mu$ and $\ln\nu$ terms by

$$
1+\frac{\alpha_s}{4\pi}\Big[\Big(\frac{67}{9}-\frac{\pi^2}{3}\Big)C_A-\frac{20}{9}\,T_F\,n_f\Big]. \tag{B.15}
$$

B.3.2 Angles between different axes

Here we list all relevant anomalous dimensions in $b_\perp$-space

$$
\begin{aligned}
\gamma_q^{\tilde H}(p_TR,\mu) &= \frac{\alpha_s C_F}{\pi}\Big[2\ln\Big(\frac{p_TR}{\mu}\Big)-\frac{3}{2}\Big],\\
\gamma_g^{\tilde H}(p_TR,\mu) &= \frac{\alpha_s}{\pi}\Big[2C_A\ln\Big(\frac{p_TR}{\mu}\Big)-\frac{1}{2}\beta_0\Big],\\
\gamma_q^C(\mu,\nu/p_T) &= \frac{\alpha_s C_F}{\pi}\left[2\ln\left(\frac{\nu}{2p_T}\right)+\frac{3}{2}\right],\\
\gamma_g^C(\mu,\nu/p_T) &= \frac{\alpha_s}{\pi}\left[2C_A\ln\left(\frac{\nu}{2p_T}\right)+\frac{1}{2}\beta_0\right],\\
\gamma_i^S(\mu,\nu R) &= \frac{2\alpha_s C_i}{\pi}\,\ln\left(\frac{2\mu}{\nu R}\right),\\
\gamma_i^\nu(b_\perp,\mu) &= \frac{2\alpha_s C_i}{\pi}\,\ln\left(\frac{\mu_b}{\mu}\right),\\
\gamma_i^{S^{\notin\,\mathrm{gr}}}(z_{\,\mathrm{cut}}p_TR,\mu) &= \frac{2\alpha_s C_i}{\pi}\,\frac{1}{1+\beta}\,\ln\left(\frac{\mu}{z_{\,\mathrm{cut}}p_TR}\right),\\
\gamma_i^{\mathcal{S}}(p_TR,z_{\mathrm{cut}},\beta,\mu,\nu/p_T) &= \frac{2\alpha_s C_i}{\pi}\,\frac{\beta}{1+\beta}\ln\left[\frac{\mu}{z_{\mathrm{cut}}^{-1/\beta}p_TR}\left(\frac{2p_T}{\nu}\right)^{\frac{1+\beta}{\beta}}\right],\\
\gamma_q^{C^{\in\,\mathrm{gr}}}(\theta_g^cp_TR,\mu) &= \frac{\alpha_s C_F}{\pi}\Big[2\ln\Big(\frac{\mu}{\theta_g^cp_TR}\Big)+\frac{3}{2}\Big],
\end{aligned}
$$

$$\gamma_g^{C^{\in \text{ gr}}}(\theta_g^c p_T R,\mu) = \frac{\alpha_s}{\pi}\Big[2C_A \ln\Big(\frac{\mu}{\theta_g^c p_T R}\Big) + \frac{1}{2}\beta_0\Big]\,,$$

$$\gamma_i^{\mathcal{S}_G}(z_{\text{ cut}}(\theta_g^c)^{1+\beta} p_T R,\mu,\beta) = -\frac{2\alpha_s C_i}{\pi}\frac{1}{1+\beta}\ln\left(\frac{\mu}{z_{\text{cut}}(\theta_g^c)^{1+\beta} p_T R}\right),$$

$$\gamma_i^{\mathcal{S}_X}(z_{\text{ cut}} p_T R,\beta,\mu,\nu R) = -\frac{2\alpha_s C_i}{\pi}\frac{\beta}{1+\beta}\ln\left[\Big(z_{\text{ cut}} p_T R\Big(\frac{2}{\nu R}\Big)^{1+\beta}\Big)^{\frac{1}{\beta}}\mu\right],$$

$$\gamma_i^{\mathcal{S}_K}(\mu,\nu\theta_g R) = -\frac{2\alpha_s C_i}{\pi}\ln\Big(\frac{2\mu}{\nu\theta_g R}\Big)\,, \tag{B.16}$$

where $C_i = C_F$ (C_A) for $i = q$ ($i = g$). We achieve full NLL′ accuracy by including the two-loop cusp anomalous dimension which amounts to multiplying all $\ln\mu$ and $\ln\nu$ terms in eq. (B.16) by

$$1 + \frac{\alpha_s}{4\pi}\Big[\Big(\frac{67}{9} - \frac{\pi^2}{3}\Big)C_A - \frac{20}{9}T_F\, n_f\Big]\,. \tag{B.17}$$

B.3.3 Energy Drop and Soft Drop groomed momentum fraction z_g

Here we list all relevant anomalous dimensions for the energy drop calculation.

$$\gamma_i^{S_G}(z_{\text{cut}} p_T R,\beta,\mu) = -\frac{2\alpha_s C_i}{\pi}\frac{1}{1+\beta}\,\ln\left(\frac{\mu}{z_{\text{cut}} p_T R}\right),$$

$$\gamma_i^{S_Z}(\Delta_E, p_T R,\mu) = -\frac{2\alpha_s C_i}{\pi}\left[\frac{1}{[\Delta_E]_+} - \ln\left(\frac{\mu}{p_T R}\right)\delta(\Delta_E)\right],$$

$$\gamma_i^{\mathcal{S}_X}(\Delta_E, z_{\text{cut}}^{-1/\beta} p_T R,\beta,\mu) = \frac{2\alpha_s C_i}{\pi}\left[\frac{1}{[\Delta_E]_+} - \frac{\beta}{1+\beta}\ln\left(\frac{\mu}{z_{\text{cut}}^{-1/\beta} p_T R}\right)\delta(\Delta_E)\right],$$

$$\gamma_q^{\tilde{H}}(p_T R,\mu) = \frac{\alpha_s C_F}{\pi}\Big[2\ln\Big(\frac{p_T R}{\mu}\Big) - \frac{3}{2}\Big],$$

$$\gamma_g^{\tilde{H}}(p_T R,\mu) = \frac{\alpha_s}{\pi}\Big[2C_A\ln\Big(\frac{p_T R}{\mu}\Big) - \frac{1}{2}\beta_0\Big],$$

$$\gamma_q^{C^{\in \text{ gr}}}(\theta_g^c p_T R,\mu) = \frac{\alpha_s C_F}{\pi}\Big[2\ln\Big(\frac{\mu}{\theta_g^c p_T R}\Big) + \frac{3}{2}\Big]\,,$$

$$\gamma_g^{C^{\in \text{ gr}}}(\theta_g^c p_T R,\mu) = \frac{\alpha_s}{\pi}\Big[2C_A\ln\Big(\frac{\mu}{\theta_g^c p_T R}\Big) + \frac{1}{2}\beta_0\Big]\,,$$

$$\gamma_i^{\mathcal{S}_Z}(\Delta_E,\theta_g\, p_T R,\mu) = \frac{2\alpha_s C_i}{\pi}\left[\frac{1}{[\Delta_E]_+} - \ln\left(\frac{\mu}{\theta_g\, p_T R}\right)\delta(\Delta_E)\right],$$

$$\gamma_i^{\mathcal{S}_{Z'}}(\Delta_E, \theta_t\, p_T R, \mu) = \frac{2\alpha_s C_i}{\pi}\left[\frac{1}{[\Delta_E]_+} - \ln\left(\frac{\mu}{\theta_t\, p_T R}\right)\delta(\Delta_E)\right],$$

$$\gamma_i^{S_T}(f_{\rm cut}\, p_T R, \mu) = -\frac{2\alpha_s C_i}{\pi}\,\ln\left(\frac{\mu}{f_{\rm cut}\, p_T R}\right),$$

$$\gamma_i^{\mathcal{S}_T}(f_{\rm cut}\theta_t\, p_T R, \mu) = \frac{2\alpha_s C_i}{\pi}\ln\left(\frac{\mu}{f_{\rm cut}\theta_t\, p_T R}\right). \tag{B.18}$$

where $C_i = C_F$ (C_A) for $i = q$ ($i = g$). We achieve full NLL$'$ accuracy by including the two-loop cusp anomalous dimension, which multiplies the $\ln\mu$ terms in eq. (B.18).

C

Fixed-order ingredients

C.1 Hard functions

As in 5.1.1, for a jet function $\mathcal{G}$ where we separate the jet production and the measurement of an observable O,

$$\mathcal{G}_i(z, O, p_T R, \mu) \equiv \sum_j J_{ij}(z, p_T R, \mu)\tilde{\mathcal{G}}_j\big(O, p_T R, \alpha_s(\mu)\big), \tag{C.1}$$

the coefficients $J_{ij}(z, p_T R, \mu)$ are given by

$$\begin{aligned}
J_{qq}(z, p_T R, \mu) &= \delta(1-z) + \frac{\alpha_s}{2\pi}\Bigg\{ \ln\Big(\frac{\mu^2}{p_T^2 R^2}\Big) P_{qq}(z) \\
&\qquad + C_F\Bigg[-2(1+z^2)\mathcal{L}_1(1-z) + \Big(\frac{13}{2} - \frac{2\pi^2}{3}\Big)\delta(1-z) - 1 + z\Bigg]\Bigg\}, \\
J_{qg}(z, p_T R, \mu) &= \frac{\alpha_s}{2\pi}\Bigg[\Big(\ln\Big(\frac{\mu^2}{p_T^2 R^2}\Big) - 2\ln(1-z)\Big)P_{gq}(z) - C_F z\Bigg], \\
J_{gq}(z, p_T R, \mu) &= \frac{\alpha_s}{2\pi}\Bigg[\Big(\ln\Big(\frac{\mu^2}{p_T^2 R^2}\Big) - 2\ln(1-z)\Big)P_{qg}(z) - T_F 2z(1-z)\Bigg], \\
J_{gg}(z, p_T R, \mu) &= \delta(1-z) + \frac{\alpha_s}{2\pi}\Bigg\{ \ln\Big(\frac{\mu^2}{p_T^2 R^2}\Big) P_{gg}(z) - \frac{4C_A(1-z+z^2)^2}{z}\mathcal{L}_1(1-z) \\
&\qquad + \Big[C_A\Big(\frac{5}{12} - \frac{2\pi^2}{3}\Big) + \frac{23}{12}\beta_0\Big]\delta(1-z)\Bigg\},
\end{aligned} \tag{C.2}$$

where the splitting functions are given in eq. (A.6). The hard function is up to one-loop order given by

$$\tilde{H}_q(p_T R, \mu) = 1 + \frac{\alpha_s C_F}{2\pi}\left(-\frac{1}{2}\ln^2\left(\frac{\mu^2}{p_T^2 R^2}\right) - \frac{3}{2}\ln\left(\frac{\mu^2}{p_T^2 R^2}\right) - \frac{13}{2} + \frac{3\pi^2}{4}\right) + \mathcal{O}(\alpha_s^2)\,,$$

$$\tilde{H}_g(p_T R,\mu) = 1 + \frac{\alpha_s}{2\pi}\bigg[C_A\bigg(-\frac{1}{2}\ln^2\Big(\frac{\mu^2}{p_T^2R^2}\Big) - \frac{5}{12} + \frac{3\pi^2}{4}\bigg) + \beta_0\bigg(-\frac{1}{2}\ln\Big(\frac{\mu^2}{p_T^2R^2}\Big) - \frac{23}{12}\bigg)\bigg] + \mathcal{O}(\alpha_s^2). \tag{C.3}$$

C.2 Jet shape jet function when $r \lesssim R$

The jet function (or central subjet function) in eq. (3.5) for the anti-k_T algorithm is up to one-loop order given by [56]

$$\begin{aligned}
&\mathcal{G}_q^{\text{jet}}(z, z_r, p_T R, r/R, \mu) \\
&= \delta(1-z)\delta(1-z_r) + \frac{\alpha_s}{2\pi}\bigg\{\delta(1-z_r)L_R\left[P_{qq}(z) + P_{gq}(z)\right] \\
&\quad - \delta(1-z_r)\bigg[2C_F(1+z^2)\Big(\frac{\ln(1-z)}{1-z}\Big)_+ + 2P_{gq}(z)\ln(1-z) + C_F\bigg] \\
&\quad + \delta(1-z)\theta\Big(z_r > \frac{1}{2}\Big)[P_{qq}(z_r) + P_{gq}(z_r)](L_{r/R} + 2\ln z_r) \\
&\quad + \theta(r < R/2)\bigg[\delta(1-z)\delta(1-z_r)C_F\bigg(\frac{7}{2} + 3\ln 2 - \frac{\pi^2}{3}\bigg) \\
&\quad - \delta(1-z)\theta\Big(\frac{1}{2} < z_r < 1 - \frac{r}{R}\Big)[P_{qq}(z_r) + P_{gq}(z_r)]\big(L_{r/R} + 2\ln(1-z_r)\big)\bigg] \\
&\quad + \theta(r > R/2)\bigg[\delta(1-z)\delta(1-z_r)\,C_F\bigg(-\frac{1}{2}L_{r/R}^2 + \frac{3}{2}L_{r/R} - 2L_{r/R}\ln\Big(1-\frac{r}{R}\Big) \\
&\quad + 4\mathrm{Li}_2\Big(1-\frac{r}{R}\Big) + \frac{1}{2} - \frac{2\pi^2}{3} + 6\frac{r}{R}\bigg) - \delta(1-z)\theta\Big(\frac{1}{2} < z_r < \frac{r}{R}\Big) \\
&\quad \times [P_{qq}(z_r) + P_{gq}(z_r)]\big(L_{r/R} + 2\ln z_r\big)\bigg]\bigg\}, \\
&\mathcal{G}_g^{\text{jet}}(z, z_r, p_T R, r/R, \mu) \\
&= \delta(1-z)\delta(1-z_r) + \frac{\alpha_s}{2\pi}\bigg\{\delta(1-z_r)L_R\big[P_{gg}(z) + 2n_f P_{qg}(z)\big] \\
&\quad + \delta(1-z)\theta\Big(z_r > \frac{1}{2}\Big)[P_{gg}(z_r) + 2n_f P_{qg}(z_r)](L_{r/R} + 2\ln z_r) \\
&\quad - \delta(1-z_r)\bigg[4C_A\frac{(1-z+z^2)^2}{z}\Big(\frac{\ln(1-z)}{1-z}\Big)_+ + 4n_f\big(P_{qg}(z)\ln(1-z) + T_F z(1-z)\big)\bigg] \\
&\quad + \theta(r < R/2)\bigg[\delta(1-z)\delta(1-z_r)\bigg(C_A\bigg(\frac{137}{36} + \frac{11}{3}\ln 2 - \frac{\pi^2}{3}\bigg) - T_F n_f\bigg(\frac{23}{18} + \frac{4}{3}\ln 2\bigg)\bigg) \\
&\quad - \delta(1-z)\theta\Big(\frac{1}{2} < z_r < 1 - \frac{r}{R}\Big)[P_{gg}(z) + 2n_f P_{qg}(z)]\big(L_{r/R} + 2\ln(1-z_r)\big)\bigg]
\end{aligned} \tag{C.4}$$

$$
\begin{aligned}
&+\theta(r>R/2)\Bigg[\delta(1-z)\delta(1-z_r)\Bigg[-\frac{C_A}{2}L_{r/R}^2+\frac{\beta_0}{2}L_{r/R}-2C_AL_{r/R}\ln\Big(1-\frac{r}{R}\Big)\\
&+4C_A\mathrm{Li}_2\Big(1-\frac{r}{R}\Big)-C_A\frac{2\pi^2}{3}+C_A\Big(\frac{8r}{R}-\frac{r^2}{R^2}+\frac{4r^3}{9R^3}\Big)\\
&+T_Fn_f\Big(\frac{1}{3}-\frac{4r}{R}+\frac{2r^2}{R^2}-\frac{8r^3}{9R^3}\Big)\Big)\\
&-\delta(1-z)\theta\left(\frac{1}{2}<z_r<\frac{r}{R}\right)\left[P_{gg}(z)+2n_fP_{qg}(z)\right]\left(L_{r/R}+2\ln z_r\right)\Bigg]\Bigg\}.
\end{aligned}
$$

The splitting functions P_{ij} are given in eq. (A.6), and we use the following short-hand notation

$$
L_R=\ln\Big(\frac{\mu^2}{p_T^2R^2}\Big),\qquad L_r=\ln\Big(\frac{\mu^2}{p_T^2r^2}\Big),\qquad L_{r/R}\equiv L_r-L_R=\ln\Big(\frac{R^2}{r^2}\Big). \tag{C.5}
$$

Summary

Humanity has delegated the task of truth-seeking in the natural world to a peculiar group of people known as *scientists*. As emissaries of the public, they band together and venture into the unknown in the hopes of uncovering answers to our most fundamental questions. Even in the absence of definitive explanations, it is still their duty to return home and report their latest findings. In this spirit, the following summary of my thesis is intended for a general audience.

Particle Physics

The quest to understand the fundamental building blocks of matter has been around for millennia. The concept of an atom goes as far back as ancient Greece, when it was introduced by the greek philosopher Democritus to explain the world's complexity in terms of indivisible constituents. Nowadays we know all ordinary matter is made up of atoms, but they are not indivisible. Instead, atoms are composed of a positively charged nucleus surrounded by a cloud of *electrons* carrying negative charge. The nucleus itself is made up of *protons* and *neutrons*, and these are in turn composed of even smaller (point-like as far as we know) particles called *quarks*.

In modern times our mission to understand the fundamental constituents of nature carries on through the field of *particle physics*. The current understanding of particle physics is embodied by the *Standard Model*, which describes all known elementary particles and three of the four fundamental interactions. The strong, weak and electromagnetic interactions are accurately characterized by the Standard Model, but the force of gravity is famously excluded and described instead by Einstein's theory of general relativity. The contents of the Standard Model are compactly summarized in figure 1.

The Standard Model is a remarkably successful theory and hailed as one of the greatest triumphs in the history of science. However, we know our quest for a final theory to be incomplete. In addition to not describing gravity, the Standard Model cannot explain why the universe is composed of only matter and essentially no anti-matter, nor does it account for *dark energy* and *dark*

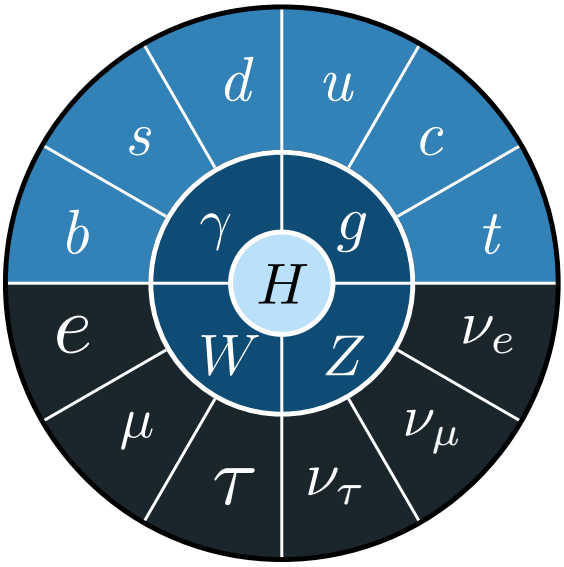

Figure 1 The constituents of the Standard Model of particle physics. The outer ring contains the matter particles known as fermions. The top half of this ring represents the six quark flavors: up (u), down (d), strange (s), charm (c), bottom (b) and top (t). The bottom half are the six leptons: electron (e), muon (μ) and tau (τ) and respective neutrinos (ν_e, ν_μ, ν_τ). The middle ring contains the force carriers of fundamental interactions, known as gauge bosons. The photon (γ) carries the electromagnetic force, the gluon (g) the strong force, while the Z and the W are the carriers of the weak interaction. In the center lies the Higgs boson, responsible for providing mass to elementary particles.

matter, which together are thought to make up 95% of the mass-energy content of the universe. Our search then, continues.

The field of particle physics forms a global community roughly divided into two camps: *theory* and *experiment*. This thesis falls into the theory category but is intimately connected to experiment - indeed many of its results are directly confronted with data. This is often referred to by physicists as *phenomenology*: theory with the purpose of obtaining results that can be compared to experiment. A theorist's main instrument is the mathematical framework known as *Quantum Field Theory* (QFT). QFT incorporates the theories of quantum mechanics (suitable for physics at the subatomic scale) and special relativity (characterizing physics at velocities close to the speed of light) in order to explain subatomic phenomena at high energies. In fact, the success of

quantum field theory is so remarkable that it symbolizes what Eugene Wigner called "*the unreasonable effectiveness of mathematics*". Consider for example the quantity known as the g-factor of the electron dipole magnetic moment, represented by g_e. Despite its intimidating name this quantity simply describes how much an electron behaves like a magnet. The value predicted by theory and the valued measured by experimentalists agree up to twelve significant digits:

$$\begin{aligned} \text{Theoretical prediction:} \quad & g_e^{\text{th}} = 2.002\,319\,304\,363\,287\,(528) \\ \text{Measured quantity:} \quad & g_e^{\text{ex}} = 2.002\,319\,304\,362\,56(35). \end{aligned} \tag{6}$$

This makes g_e the most accurately verified prediction in history.

At the *Messenger Lectures* at Cornell, Richard Feynman summarized the scientific method in one sentence: *If it disagrees with experiment, it's wrong.* In particle physics experiments are usually particle colliders. Just outside of Geneva in Switzerland lies the largest scientific experiment of all time, the Large Hadron Collider (LHC) at CERN. The LHC accelerates protons to speeds near the speed of light and smashes them together at extremely high energies. By closely examining the debris of these collisions, particle physicists try to reconstruct what actually happened, just like a good detective.

Quantum Chromodynamics, jets and effective theories

Out of the three forces contained in the Standard Model this thesis focuses on the strong interaction (sometimes called the nuclear interaction since it's responsible for holding together the nuclei of atoms), which is described by the theory known as *Quantum Chromodynamics* (QCD). Here the prefix *Chromo-* is alluding to the three types of charge of QCD, the *red*, *green* and *blue* charges, collectively known as the *color* charge. One can think of the color charge as the QCD equivalent of the electric charge in electromagnetism, it's simply that there are three of them instead of just one. Therefore, the only particles directly sensitive to the strong interaction are the ones that carry this color charge, of which there are two types: *quarks* and *gluons*. Quarks are the matter particles that make up, for example, protons and neutrons. Gluons on the other hand are the *carriers* of the strong force, meaning that two quarks will either attract or repel by exchanging gluons between them. Naturally, these charges have nothing to do with what is meant by color in day-to-day life, but the naming is incredibly appropriate. One of the most striking characteristics of QCD is that colored particles are never observed on their own, but only in

colorless (or "white") combinations called *hadrons* - a phenomenon known as *color confinement*. Typically these hadrons are either *mesons*: pairs of quark and anti-quark carrying opposite colors, i.e. blue and anti-blue; or *baryons*: groups of three quarks, one red, one blue and one green, resulting in a "white" combination, in analogy with real-life colors.

Another fascinating aspect of QCD is the emergence of *jets*, the central object of study in this thesis. Jets are sprays of collimated particles occurring whenever energetic quarks or gluons are produced in high energy collisions. They are in fact the most frequently detected objects at the LHC and are present in the vast majority of interesting events. Understanding jets is thus absolutely crucial. One can think of jets as QCD lightning strikes hitting the experiment detectors, containing a great deal of information about the dynamics of the theory. In particular studying the radiation pattern inside them - their so-called *substructure* - can help us improve the sensitivity for searches of new particles at the LHC, as well as our understanding of QCD itself.

The other key concept in this thesis is the framework known as an *effective theory*, the physics equivalent of using the right tool for the job. In particular, the work in this thesis relies on *Soft-Collinear effective theory* or SCET. The name is closely related to the types of radiation emitted in jets: *soft* refers to emissions of low-energy particles, while *collinear* to radiation emitted in the same direction as the initial particle is travelling. We use SCET to derive *factorization* theorems, which allow us to break down complicated processes into individual components and analyze them one at a time.

Results

The results of this thesis consist of using SCET to perform precision calculations for jet substructure observables. In chapter 3 we tackled one of the most fundamental questions one can ask regarding the anatomy of a jet: what is the average energy distribution as a function of the distance to the center of the jet? This is a classic jet substructure observable known as the *jet shape*. The jet shape has been measured extensively at a variety of colliders and from the theory side it was not clear how to obtain a precise prediction until now.

The particles that compose a jet at the LHC are more than just those arising from the final state quark or gluon. Radiation emitted from other sources (e.g. proton-proton collisions other than the one we are analyzing) ends up inside the jet as well. This contaminating radiation is unwelcome and procedures have been developed to remove it from jets known as *grooming techniques*. In chapter 5 we performed a detailed study of how much energy is removed

from the jet as it undergoes the grooming procedure for three different types of grooming techniques. These observables stand out because they only probe soft radiation.

A jet axis can roughly be thought of as the jet direction. More concretely, different definitions of axes exist and are suitable for different situations. In chapter 4, we carefully examined the angles between three different axes: the standard, the winner-take-all (WTA) and the groomed jet axis. Each of these angles has a different degree of sensitivity to soft radiation. For example, the WTA axis is insensitive to soft radiation, and the groomed axis is obtained with the particles that remain after the grooming procedure. As such, this angle has a low dependence on soft physics. On the other hand, the angle between the standard and groomed axes is exclusively determined by soft wide-angle radiation.

Finally, in chapter 6 we study an observable called z_g. This observable has received a lot of attention by both the theoretical and experimental particle and nuclear physics communities in the past years because it allows for the most direct measurement of a fundamental QCD object: the splitting functions, which describe the probability of emitting radiation with a given energy. We make the first *precision* calculation for this observable.

Acknowledgements

The work presented in this thesis could not have been accomplished without the strong support of mentors and friends.

First, I want to express my deepest gratitude to my supervisor. Wouter, working with you has truly been an extraordinary experience. You have shaped the way I think about science and research, but more importantly, you have deeply influenced how I face life's problems. Many times I can't help but stand in awe at the way you handle things, and the fact that I get to learn by osmosis by experiencing it first-hand is nothing short of a privilege. Not only that, your kindness and patience were a life-vest during Corona, and particularly so as I was writing this thesis. What else can I say other than that it's been a great pleasure to be your student, and you will forever be someone I look up to.

To my co-promotor, Eric, thank you for the words of wisdom in moments of stress, for always caring about my well-being and for being the one that started my journey through the world of academia.

I want to thank my collaborators Felix Ringer, Kyle Lee, Duff Neill, Darren Scott, Frank Tackmann, Patrick Komiske and Jesse Thaler, both for the exciting work we have done together and for making the experience so much fun. Felix, I consider myself very lucky to have a collaborator like you. Thank you for being a mentor and always being there with desperately needed advice. Your help with navigating the challenges of research is priceless, and many times were it not for you I would be completely clueless. Working with you is an absolute pleasure, and I can only wish for many more years of collaboration together. Darren, thank you for being such a gracious host during my time in Munich and for all the fun times we had together during the years.

For the past four years Nikhef has been my second home. The atmosphere there is something quite special, and I want to thank everyone at the theory group for contributing to such a friendly and stimulating environment. In particular, I want to thank my officemates Franz and Giulio for their crucial guidance in the first year of my PhD. To my friends Lorenzo and Rabah, thank you being my companions (or should I say, comrades) in this journey and for all we have shared together. There were times when your silly jokes were the only thing that uplifted my spirits - doing this without you would have been no fun. I also want to thank my fellow students and postdocs Anders,

Anastasiia, Andrea, Andreas, Antonio, Avanish, Coenraad, Dora, Eleftheria, Elena, Grégoire, Gillian, Giudi, Gilberto, Jake, Jorinde, Jort, Lisa, Marrit, Marko, Melissa, Michi, Nathan, Rhorry, Ruben, Rudi, Sonia and Solange for their company and friendship throughout the years.

A special word of gratitude to my friends and neighbours Isanne and Theodoor, who in the first lockdown were the only people I interacted with for many months, and whose board game nights were the highlight of my week. To my neighbours at OurDomain, thank you for the fun times and being such great people.

To my friends Melo, Jaques, Capinha, Tomás, Manel, there's nothing I can write here that does justice to what we go through together. The whole point to any of this, to life, is to share it with you guys. André, thank you for being the best friend anyone could ever ask for, and truly like a brother to me. It feels like we have known each other for a thousand lives, let us go for another million more.

I also want to thank Adriana for her friendship and kindness throughout the six long years we have lived in the Netherlands.

Por fim, quero agradecer à minha familia, Sissi, P.D., Diogo e Matias: apesar da distância, o vosso carinho chegou sempre aqui. Aos meus sobrinhos, quero que saibam que o vosso riso tem poderes terapêuticos. Um dia, quando forem mais velhos, podemos falar sobre os tempos do tio PP na Holanda. E nesse dia, vou contar-vos também que, fosse onde fosse, vos tinha sempre em mente.

A última palavra desta tese vai, naturalmente, para os meus pais: Paula e Rui. Sabem melhor que ninguém que o vosso apoio foi indispensável para o doutoramento, a vida, e tudo o resto.

Bibliography

[1] P. Cal, F. Ringer and W. J. Waalewijn, *The jet shape at NLL′*, *JHEP* **05** (2019) 143 [1901.06389].

[2] P. Cal, D. Neill, F. Ringer and W. J. Waalewijn, *Calculating the angle between jet axes*, *JHEP* **04** (2020) 211 [1911.06840].

[3] P. Cal, K. Lee, F. Ringer and W. J. Waalewijn, *Jet energy drop*, *JHEP* **11** (2020) 012 [2007.12187].

[4] P. Cal, K. Lee, F. Ringer and W. J. Waalewijn, *The soft drop momentum sharing fraction z_g beyond leading-logarithmic accuracy*, 2106.04589.

[5] ATLAS collaboration, G. Aad et al., *Observation of a new particle in the search for the Standard Model Higgs boson with the ATLAS detector at the LHC*, *Phys. Lett. B* **716** (2012) 1 [1207.7214].

[6] CMS collaboration, S. Chatrchyan et al., *Observation of a New Boson at a Mass of 125 GeV with the CMS Experiment at the LHC*, *Phys. Lett. B* **716** (2012) 30 [1207.7235].

[7] LHCb collaboration, R. Aaij et al., *Test of lepton universality in beauty-quark decays*, 2103.11769.

[8] M. H. Seymour, *Searches for new particles using cone and cluster jet algorithms: A Comparative study*, *Z. Phys. C* **62** (1994) 127.

[9] M. H. Seymour, *The Average number of subjets in a hadron collider jet*, *Nucl. Phys. B* **421** (1994) 545.

[10] M. Cacciari, G. P. Salam and G. Soyez, *The anti-k_T jet clustering algorithm*, *JHEP* **04** (2008) 063 [0802.1189].

[11] A. J. Larkoski, I. Moult and B. Nachman, *Jet Substructure at the Large Hadron Collider: A Review of Recent Advances in Theory and Machine Learning*, *Phys. Rept.* **841** (2020) 1 [1709.04464].

[12] C. W. Bauer, S. Fleming and M. E. Luke, *Summing Sudakov logarithms in $B \to X_s\gamma$ in effective field theory*, *Phys. Rev.* **D63** (2000) 014006 [hep-ph/0005275].

[13] C. W. Bauer, S. Fleming, D. Pirjol and I. W. Stewart, *An Effective field theory for collinear and soft gluons: Heavy to light decays*, *Phys. Rev.* **D63** (2001) 114020 [hep-ph/0011336].

[14] C. W. Bauer and I. W. Stewart, *Invariant operators in collinear effective theory*, *Phys. Lett.* **B516** (2001) 134 [hep-ph/0107001].

[15] C. W. Bauer, D. Pirjol and I. W. Stewart, *Soft collinear factorization in effective field theory*, *Phys. Rev.* **D65** (2002) 054022 [hep-ph/0109045].

[16] M. Beneke, A. P. Chapovsky, M. Diehl and T. Feldmann, *Soft collinear effective theory and heavy to light currents beyond leading power*, *Nucl. Phys.* **B643** (2002) 431 [hep-ph/0206152].

[17] S. Marzani, G. Soyez and M. Spannowsky, *Looking inside jets: an introduction to jet substructure and boosted-object phenomenology*, vol. 958. Springer, 2019, 10.1007/978-3-030-15709-8, [1901.10342].

[18] J. Thaler, *Lectures on jets"*, *, MITP Summer School 2016: "New Physics on Trial at LHC Run II* .

[19] A. V. Manohar, *Introduction to Effective Field Theories*, 1804.05863.

[20] T. Cohen, *As Scales Become Separated: Lectures on Effective Field Theory*, *PoS* **TASI2018** (2019) 011 [1903.03622].

[21] I. Stewart, *Lecture notes in effective field theory*, October, 2013.

[22] I. W. Stewart, *Lectures on the Soft-Collinear Effective Theory*, *MIT Open Course Ware, Effective Field Theory (Spring 2013)* .

[23] A. J. Larkoski, S. Marzani, G. Soyez and J. Thaler, *Soft Drop*, *JHEP* **05** (2014) 146 [1402.2657].

[24] D. Krohn, J. Thaler and L.-T. Wang, *Jet Trimming*, *JHEP* **02** (2010) 084 [0912.1342].

[25] C. Frye, A. J. Larkoski, J. Thaler and K. Zhou, *Casimir Meets Poisson: Improved Quark/Gluon Discrimination with Counting Observables*, *JHEP* **09** (2017) 083 [1704.06266].

[26] A. J. Larkoski, S. Marzani and J. Thaler, *Sudakov Safety in Perturbative QCD*, *Phys. Rev. D* **91** (2015) 111501 [1502.01719].

[27] C. G. Bollini and J. J. Giambiagi, *Dimensional Renormalization: The Number of Dimensions as a Regularizing Parameter*, *Nuovo Cim. B* **12** (1972) 20.

[28] G. 't Hooft and M. J. G. Veltman, *Regularization and Renormalization of Gauge Fields*, *Nucl. Phys. B* **44** (1972) 189.

[29] G. 't Hooft, *Dimensional regularization and the renormalization group*, *Nucl. Phys. B* **61** (1973) 455.

[30] S. Weinberg, *New approach to the renormalization group*, *Phys. Rev. D* **8** (1973) 3497.

[31] Particle Data Group collaboration, P. A. Zyla et al., *Review of Particle Physics*, *PTEP* **2020** (2020) 083C01.

[32] F. Herzog, B. Ruijl, T. Ueda, J. A. M. Vermaseren and A. Vogt, *The five-loop beta function of Yang-Mills theory with fermions*, *JHEP* **02** (2017) 090 [1701.01404].

[33] D. J. Gross and F. Wilczek, *Ultraviolet Behavior of Nonabelian Gauge Theories*, *Phys. Rev. Lett.* **30** (1973) 1343.

[34] H. D. Politzer, *Reliable Perturbative Results for Strong Interactions?*, *Phys. Rev. Lett.* **30** (1973) 1346.

[35] L. G. Almeida, S. D. Ellis, C. Lee, G. Sterman, I. Sung and J. R. Walsh, *Comparing and counting logs in direct and effective methods of QCD resummation*, *JHEP* **04** (2014) 174 [1401.4460].

[36] S. Catani, L. Trentadue, G. Turnock and B. R. Webber, *Resummation of large logarithms in e+ e- event shape distributions*, *Nucl. Phys. B* **407** (1993) 3.

[37] F. Bloch and A. Nordsieck, *Note on the Radiation Field of the electron*, *Phys. Rev.* **52** (1937) 54.

[38] T. Kinoshita, *Mass singularities of Feynman amplitudes*, *J. Math. Phys.* **3** (1962) 650.

[39] T. D. Lee and M. Nauenberg, *Degenerate Systems and Mass Singularities*, *Phys. Rev.* **133** (1964) B1549.

[40] A. J. Larkoski and J. Thaler, *Unsafe but Calculable: Ratios of Angularities in Perturbative QCD*, *JHEP* **09** (2013) 137 [1307.1699].

[41] J. E. Huth et al., *Toward a standardization of jet definitions*, in *1990 DPF Summer Study on High-energy Physics: Research Directions for the Decade (Snowmass 90)*, 12, 1990.

[42] Y. L. Dokshitzer, G. D. Leder, S. Moretti and B. R. Webber, *Better jet clustering algorithms*, *JHEP* **08** (1997) 001 [hep-ph/9707323].

[43] M. Wobisch and T. Wengler, *Hadronization corrections to jet cross-sections in deep inelastic scattering*, in *Monte Carlo generators for HERA physics. Proceedings, Workshop, Hamburg, Germany, 1998-1999*, pp. 270–279, 1998, hep-ph/9907280.

[44] S. Catani, Y. L. Dokshitzer, M. H. Seymour and B. R. Webber, *Longitudinally invariant K_t clustering algorithms for hadron hadron collisions*, *Nucl. Phys.* **B406** (1993) 187.

[45] S. D. Ellis and D. E. Soper, *Successive combination jet algorithm for hadron collisions*, *Phys. Rev.* **D48** (1993) 3160 [hep-ph/9305266].

[46] J. C. Collins, *Renormalization: An Introduction to Renormalization, The Renormalization Group, and the Operator Product Expansion*, vol. 26 of *Cambridge Monographs on Mathematical Physics*. Cambridge University Press, Cambridge, 1986, 10.1017/CBO9780511622656.

[47] T. Becher, A. Broggio and A. Ferroglia, *Introduction to Soft-Collinear Effective Theory*, vol. 896. Springer, 2015, 10.1007/978-3-319-14848-9, [1410.1892].

[48] A. V. Manohar and I. W. Stewart, *The Zero-Bin and Mode Factorization in Quantum Field Theory*, *Phys. Rev.* **D76** (2007) 074002 [hep-ph/0605001].

[49] J. M. Henn, G. P. Korchemsky and B. Mistlberger, *The full four-loop cusp anomalous dimension in $\mathcal{N} = 4$ super Yang-Mills and QCD*, *JHEP* **04** (2020) 018 [1911.10174].

[50] Z.-B. Kang, F. Ringer and I. Vitev, *The semi-inclusive jet function in SCET and small radius resummation for inclusive jet production*, *JHEP* **10** (2016) 125 [1606.06732].

[51] Z.-B. Kang, F. Ringer and I. Vitev, *Jet substructure using semi-inclusive jet functions in SCET*, *JHEP* **11** (2016) 155 [1606.07063].

[52] S. D. Ellis, Z. Kunszt and D. E. Soper, *Jets at hadron colliders at order α_s^3: A Look inside*, *Phys. Rev. Lett.* **69** (1992) 3615 [hep-ph/9208249].

[53] ATLAS collaboration, *New ATLAS event generator tunes to 2010 data*, *ATL-PHYS-PUB-2011-008* (2011) .

[54] P. Gras, S. Höche, D. Kar, A. Larkoski, L. Lönnblad, S. Plätzer et al., *Systematics of quark/gluon tagging*, *JHEP* **07** (2017) 091 [1704.03878].

[55] D. Bertolini, T. Chan and J. Thaler, *Jet Observables Without Jet Algorithms*, *JHEP* **04** (2014) 013 [1310.7584].

[56] Z.-B. Kang, F. Ringer and W. J. Waalewijn, *The Energy Distribution of Subjets and the Jet Shape*, *JHEP* **07** (2017) 064 [1705.05375].

[57] D. Neill, A. Papaefstathiou, W. J. Waalewijn and L. Zoppi, *Phenomenology with a recoil-free jet axis: TMD fragmentation and the jet shape*, 1810.12915.

[58] OPAL collaboration, R. Akers et al., *QCD studies using a cone based jet finding algorithm for e^+e^- collisions at LEP*, *Z. Phys.* **C63** (1994) 197.

[59] CDF collaboration, F. Abe et al., *A Measurement of jet shapes in $p\bar{p}$ collisions at $\sqrt{s} = 1.8$ TeV*, *Phys. Rev. Lett.* **70** (1993) 713.

[60] D0 collaboration, S. Abachi et al., *Transverse energy distributions within jets in $p\bar{p}$ collisions at $\sqrt{s} = 1.8$ TeV*, *Phys. Lett.* **B357** (1995) 500.

[61] CDF collaboration, D. Acosta et al., *Study of jet shapes in inclusive jet production in $p\bar{p}$ collisions at $\sqrt{s} = 1.96$ TeV*, *Phys. Rev.* **D71** (2005) 112002 [hep-ex/0505013].

[62] H1 collaboration, S. Aid et al., *Jets and energy flow in photon - proton collisions at HERA*, *Z. Phys.* **C70** (1996) 17 [hep-ex/9511012].

[63] H1 collaboration, C. Adloff et al., *Measurement of event shape variables in deep inelastic e p scattering*, *Phys. Lett.* **B406** (1997) 256 [hep-ex/9706002].

[64] H1 collaboration, C. Adloff et al., *Measurement of internal jet structure in dijet production in deep inelastic scattering at HERA*, *Nucl. Phys.* **B545** (1999) 3 [hep-ex/9901010].

[65] ZEUS collaboration, J. Breitweg et al., *Measurement of jet shapes in high Q^2 deep inelastic scattering at HERA*, *Eur. Phys. J.* **C8** (1999) 367 [hep-ex/9804001].

[66] ZEUS collaboration, J. Breitweg et al., *Measurement of jet shapes in photoproduction at HERA*, *Eur. Phys. J.* **C2** (1998) 61 [hep-ex/9710002].

[67] ATLAS collaboration, G. Aad et al., *Study of Jet Shapes in Inclusive Jet Production in pp Collisions at $\sqrt{s} = 7$ TeV using the ATLAS Detector*, *Phys. Rev.* **D83** (2011) 052003 [1101.0070].

[68] CMS collaboration, S. Chatrchyan et al., *Shape, Transverse Size, and Charged Hadron Multiplicity of Jets in pp Collisions at 7 TeV*, *JHEP* **06** (2012) 160 [1204.3170].

[69] CDF collaboration, T. Aaltonen et al., *Measurement of b-jet Shapes in Inclusive Jet Production in $p\bar{p}$ Collisions at $\sqrt{s}$ = 1.96-TeV*, *Phys. Rev.* **D78** (2008) 072005 [0806.1699].

[70] ATLAS collaboration, G. Aad et al., *Measurement of jet shapes in top-quark pair events at $\sqrt{s}$ = 7 TeV using the ATLAS detector*, *Eur. Phys. J.* **C73** (2013) 2676 [1307.5749].

[71] CMS collaboration, S. Chatrchyan et al., *Modification of jet shapes in PbPb collisions at $\sqrt{s_{NN}} = 2.76$ TeV*, *Phys. Lett.* **B730** (2014) 243 [1310.0878].

[72] CMS collaboration, C. Collaboration, *Jet shapes for isolated photon-tagged jets in PbPb and pp collisions at $\sqrt{s_{\mathrm{NN}}} = 5.02$ TeV*, .

[73] T. Kaufmann, A. Mukherjee and W. Vogelsang, *Hadron Fragmentation Inside Jets in Hadronic Collisions*, *Phys. Rev.* **D92** (2015) 054015 [1506.01415].

[74] L. Dai, C. Kim and A. K. Leibovich, *Fragmentation of a Jet with Small Radius*, *Phys. Rev.* **D94** (2016) 114023 [1606.07411].

[75] M. Dasgupta, F. Dreyer, G. P. Salam and G. Soyez, *Small-radius jets to all orders in QCD*, *JHEP* **04** (2015) 039 [1411.5182].

[76] D. Neill, I. Scimemi and W. J. Waalewijn, *Jet axes and universal transverse-momentum-dependent fragmentation*, *JHEP* **04** (2017) 020 [1612.04817].

[77] J. C. Collins, D. E. Soper and G. F. Sterman, *Transverse Momentum Distribution in Drell-Yan Pair and W and Z Boson Production*, *Nucl. Phys.* **B250** (1985) 199.

[78] T. Becher and M. Neubert, *Drell-Yan Production at Small q_T, Transverse Parton Distributions and the Collinear Anomaly*, *Eur. Phys. J.* **C71** (2011) 1665 [1007.4005].

[79] J. Collins, *Foundations of perturbative QCD*. Cambridge University Press, 2013.

[80] M. G. Echevarria, A. Idilbi and I. Scimemi, *Factorization Theorem For Drell-Yan At Low q_T And Transverse Momentum Distributions On-The-Light-Cone*, *JHEP* **07** (2012) 002 [1111.4996].

[81] J.-Y. Chiu, A. Jain, D. Neill and I. Z. Rothstein, *A Formalism for the Systematic Treatment of Rapidity Logarithms in Quantum Field Theory*, *JHEP* **05** (2012) 084 [1202.0814].

[82] Z.-B. Kang, X. Liu, F. Ringer and H. Xing, *The transverse momentum distribution of hadrons within jets*, *JHEP* **11** (2017) 068 [1705.08443].

[83] M. Dasgupta and G. P. Salam, *Resummation of nonglobal QCD observables*, *Phys. Lett.* **B512** (2001) 323 [hep-ph/0104277].

[84] M. H. Seymour, *Jet shapes in hadron collisions: Higher orders, resummation and hadronization*, *Nucl. Phys.* **B513** (1998) 269 [hep-ph/9707338].

[85] H.-n. Li, Z. Li and C. P. Yuan, *QCD resummation for jet substructures*, *Phys. Rev. Lett.* **107** (2011) 152001 [1107.4535].

[86] Y.-T. Chien and I. Vitev, *Jet Shape Resummation Using Soft-Collinear Effective Theory*, *JHEP* **12** (2014) 061 [1405.4293].

[87] T. Sjöstrand, S. Ask, J. R. Christiansen, R. Corke, N. Desai, P. Ilten et al., *An Introduction to PYTHIA 8.2*, *Comput. Phys. Commun.* **191** (2015) 159 [1410.3012].

[88] B. Jager, A. Schafer, M. Stratmann and W. Vogelsang, *Next-to-leading order QCD corrections to high p_T pion production in longitudinally polarized pp collisions*, *Phys. Rev.* **D67** (2003) 054005 [hep-ph/0211007].

[89] A. Mukherjee and W. Vogelsang, *Jet production in (un)polarized pp collisions: dependence on jet algorithm*, *Phys. Rev.* **D86** (2012) 094009 [1209.1785].

[90] J.-y. Chiu, A. Jain, D. Neill and I. Z. Rothstein, *The Rapidity Renormalization Group*, *Phys. Rev. Lett.* **108** (2012) 151601 [1104.0881].

[91] A. J. Larkoski, I. Moult and D. Neill, *Non-Global Logarithms, Factorization, and the Soft Substructure of Jets*, *JHEP* **09** (2015) 143 [1501.04596].

[92] T. Becher, M. Neubert, L. Rothen and D. Y. Shao, *Effective Field Theory for Jet Processes*, *Phys. Rev. Lett.* **116** (2016) 192001 [1508.06645].

[93] S. Caron-Huot, *Resummation of non-global logarithms and the BFKL equation*, *JHEP* **03** (2018) 036 [1501.03754].

[94] A. Banfi, M. Dasgupta, K. Khelifa-Kerfa and S. Marzani, *Non-global logarithms and jet algorithms in high-pT jet shapes*, *JHEP* **08** (2010) 064 [1004.3483].

[95] Y. Hatta and T. Ueda, *Resummation of non-global logarithms at finite N_c*, *Nucl. Phys.* **B874** (2013) 808 [1304.6930].

[96] A. Banfi, G. Marchesini and G. Smye, *Away from jet energy flow*, *JHEP* **08** (2002) 006 [hep-ph/0206076].

[97] M. D. Schwartz and H. X. Zhu, *Nonglobal logarithms at three loops, four loops, five loops, and beyond*, *Phys. Rev.* **D90** (2014) 065004 [1403.4949].

[98] S. Frixione, P. Nason and G. Ridolfi, *Problems in the resummation of soft gluon effects in the transverse momentum distributions of massive vector bosons in hadronic collisions*, *Nucl. Phys.* **B542** (1999) 311 [hep-ph/9809367].

[99] P. F. Monni, E. Re and P. Torrielli, *Higgs Transverse-Momentum Resummation in Direct Space*, *Phys. Rev. Lett.* **116** (2016) 242001 [1604.02191].

[100] M. A. Ebert and F. J. Tackmann, *Resummation of Transverse Momentum Distributions in Distribution Space*, *JHEP* **02** (2017) 110 [1611.08610].

[101] Z. Ligeti, I. W. Stewart and F. J. Tackmann, *Treating the b quark distribution function with reliable uncertainties*, *Phys. Rev.* **D78** (2008) 114014 [0807.1926].

[102] R. Abbate, M. Fickinger, A. H. Hoang, V. Mateu and I. W. Stewart, *Thrust at N^3LL with Power Corrections and a Precision Global Fit for $\alpha_s(m_Z)$*, *Phys. Rev.* **D83** (2011) 074021 [1006.3080].

[103] D. Bertolini, M. P. Solon and J. R. Walsh, *Integrated and Differential Accuracy in Resummed Cross Sections*, *Phys. Rev.* **D95** (2017) 054024 [1701.07919].

[104] M. G. Echevarria, T. Kasemets, J.-P. Lansberg, C. Pisano and A. Signori, *Matching factorization theorems with an inverse-error weighting*, *Phys. Lett.* **B781** (2018) 161 [1801.01480].

[105] M. Dasgupta, K. Khelifa-Kerfa, S. Marzani and M. Spannowsky, *On jet mass distributions in Z+jet and dijet processes at the LHC*, *JHEP* **10** (2012) 126 [1207.1640].

[106] S. Dulat, T.-J. Hou, J. Gao, M. Guzzi, J. Huston, P. Nadolsky et al., *New parton distribution functions from a global analysis of quantum chromodynamics*, *Phys. Rev.* **D93** (2016) 033006 [1506.07443].

[107] G. Salam, *E_t^∞ Scheme*, *Unpublished* .

[108] X.-d. Ji, J.-p. Ma and F. Yuan, *QCD factorization for semi-inclusive deep-inelastic scattering at low transverse momentum*, *Phys. Rev.* **D71** (2005) 034005 [hep-ph/0404183].

[109] I. Moult and H. X. Zhu, *Simplicity from Recoil: The Three-Loop Soft Function and Factorization for the Energy-Energy Correlation*, *JHEP* **08** (2018) 160 [1801.02627].

[110] D. Gutierrez-Reyes, I. Scimemi, W. J. Waalewijn and L. Zoppi, *Transverse momentum dependent distributions with jets*, *Phys. Rev. Lett.* **121** (2018) 162001 [1807.07573].

[111] A. Gao, H. T. Li, I. Moult and H. X. Zhu, *Precision QCD Event Shapes at Hadron Colliders: The Transverse Energy-Energy Correlator in the Back-to-Back Limit*, *Phys. Rev. Lett.* **123** (2019) 062001 [1901.04497].

[112] D. Gutierrez-Reyes, I. Scimemi, W. J. Waalewijn and L. Zoppi, *Transverse momentum dependent distributions in e^+e^- and semi-inclusive deep-inelastic scattering using jets*, *JHEP* **10** (2019) 031 [1904.04259].

[113] A. Larkoski, S. Marzani and C. Wu, *Safe Use of Jet Pull*, 1911.05090.

[114] Y. Bao and A. J. Larkoski, *Calculating Pull for Non-Singlet Jets*, 1910.02085.

[115] A. J. Larkoski, S. Marzani and C. Wu, *Theory Predictions for the Pull Angle*, *Phys. Rev.* **D99** (2019) 091502 [1903.02275].

[116] M. Balsiger, T. Becher and D. Y. Shao, *NLL′ resummation of jet mass*, *JHEP* **04** (2019) 020 [1901.09038].

[117] T. Becher, B. D. Pecjak and D. Y. Shao, *Factorization for the light-jet mass and hemisphere soft function*, *JHEP* **12** (2016) 018 [1610.01608].

[118] H. Weigert, *Nonglobal jet evolution at finite N(c)*, *Nucl. Phys.* **B685** (2004) 321 [hep-ph/0312050].

[119] Y. Hagiwara, Y. Hatta and T. Ueda, *Hemisphere jet mass distribution at finite N_c*, *Phys. Lett.* **B756** (2016) 254 [1507.07641].

[120] T. Becher, M. Neubert, L. Rothen and D. Y. Shao, *Factorization and Resummation for Jet Processes*, *JHEP* **11** (2016) 019 [1605.02737].

[121] A. J. Larkoski, I. Moult and D. Neill, *The Analytic Structure of Non-Global Logarithms: Convergence of the Dressed Gluon Expansion*, *JHEP* **11** (2016) 089 [1609.04011].

[122] Z.-B. Kang, K. Lee, X. Liu, D. Neill and F. Ringer, *The soft drop groomed jet radius at NLL*, *JHEP* **02** (2020) 054 [1908.01783].

[123] S. Höche, D. Reichelt and F. Siegert, *Momentum conservation and unitarity in parton showers and NLL resummation*, *JHEP* **01** (2018) 118 [1711.03497].

[124] F. Landry, R. Brock, P. M. Nadolsky and C. P. Yuan, *Tevatron Run-1 Z boson data and Collins-Soper-Sterman resummation formalism*, *Phys. Rev.* **D67** (2003) 073016 [hep-ph/0212159].

[125] P. Sun, J. Isaacson, C. P. Yuan and F. Yuan, *Nonperturbative functions for SIDIS and Drell–Yan processes*, *Int. J. Mod. Phys.* **A33** (2018) 1841006 [1406.3073].

[126] A. Bacchetta, F. Delcarro, C. Pisano, M. Radici and A. Signori, *Extraction of partonic transverse momentum distributions from semi-inclusive deep-inelastic scattering, Drell-Yan and Z-boson production*, *JHEP* **06** (2017) 081 [1703.10157].

[127] V. Bertone, I. Scimemi and A. Vladimirov, *Extraction of unpolarized quark transverse momentum dependent parton distributions from Drell-Yan/Z-boson production*, *JHEP* **06** (2019) 028 [1902.08474].

[128] M. A. Ebert, I. W. Stewart and Y. Zhao, *Determining the Nonperturbative Collins-Soper Kernel From Lattice QCD*, *Phys. Rev.* **D99** (2019) 034505 [1811.00026].

[129] H. A. Andrews et al., *Novel tools and observables for jet physics in heavy-ion collisions*, 1808.03689.

[130] V. N. Gribov and L. N. Lipatov, *Deep inelastic e p scattering in perturbation theory*, *Sov. J. Nucl. Phys.* **15** (1972) 438.

[131] G. Altarelli and G. Parisi, *Asymptotic Freedom in Parton Language*, *Nucl. Phys.* **B126** (1977) 298.

[132] Y. L. Dokshitzer, *Calculation of the Structure Functions for Deep Inelastic Scattering and e^+e^- Annihilation by Perturbation Theory in Quantum Chromodynamics*, *Sov. Phys. JETP* **46** (1977) 641.

[133] S. Fleming, A. H. Hoang, S. Mantry and I. W. Stewart, *Top Jets in the Peak Region: Factorization Analysis with NLL Resummation*, *Phys. Rev. D* **77** (2008) 114003 [0711.2079].

[134] C. W. Bauer, S. P. Fleming, C. Lee and G. F. Sterman, *Factorization of e+e- Event Shape Distributions with Hadronic Final States in Soft Collinear Effective Theory*, *Phys. Rev.* **D78** (2008) 034027 [0801.4569].

[135] I. W. Stewart, F. J. Tackmann and W. J. Waalewijn, *Factorization at the LHC: From PDFs to Initial State Jets*, *Phys. Rev.* **D81** (2010) 094035 [0910.0467].

[136] S. D. Ellis, C. K. Vermilion, J. R. Walsh, A. Hornig and C. Lee, *Jet Shapes and Jet Algorithms in SCET*, *JHEP* **11** (2010) 101 [1001.0014].

[137] T. Becher, G. Bell and M. Neubert, *Factorization and Resummation for Jet Broadening*, *Phys. Lett.* **B704** (2011) 276 [1104.4108].

[138] B. Andersson, G. Gustafson, L. Lonnblad and U. Pettersson, *Coherence Effects in Deep Inelastic Scattering*, *Z. Phys.* **C43** (1989) 625.

[139] Y.-T. Chien and I. W. Stewart, *Collinear Drop*, *JHEP* **06** (2020) 064 [1907.11107].

[140] W. T. Giele and E. W. N. Glover, *Higher order corrections to jet cross-sections in e^+e^- annihilation*, *Phys. Rev.* **D46** (1992) 1980.

[141] R. Bain, Y. Makris and T. Mehen, *Transverse Momentum Dependent Fragmenting Jet Functions with Applications to Quarkonium Production*, *JHEP* **11** (2016) 144 [1610.06508].

[142] Z.-B. Kang, K. Lee, X. Liu and F. Ringer, *The groomed and ungroomed jet mass distribution for inclusive jet production at the LHC*, *JHEP* **10** (2018) 137 [1803.03645].

[143] Y. Makris, D. Neill and V. Vaidya, *Probing Transverse-Momentum Dependent Evolution With Groomed Jets*, *JHEP* **07** (2018) 167 [1712.07653].

[144] A. V. Konychev and P. M. Nadolsky, *Universality of the Collins-Soper-Sterman nonperturbative function in gauge boson production*, *Phys. Lett.* **B633** (2006) 710 [hep-ph/0506225].

[145] H.-M. Chang, M. Procura, J. Thaler and W. J. Waalewijn, *Calculating Track-Based Observables for the LHC*, *Phys. Rev. Lett.* **111** (2013) 102002 [1303.6637].

[146] CMS collaboration, A. M. Sirunyan et al., *Measurement of the Splitting Function in pp and Pb-Pb Collisions at $\sqrt{s_{\mathrm{NN}}} = 5.02$ TeV*, *Phys. Rev. Lett.* **120** (2018) 142302 [1708.09429].

[147] CMS collaboration, A. M. Sirunyan et al., *Measurement of the groomed jet mass in PbPb and pp collisions at $\sqrt{s_{\mathrm{NN}}} = 5.02$ TeV*, *JHEP* **10** (2018) 161 [1805.05145].

[148] ALICE collaboration, S. Acharya et al., *Exploration of jet substructure using iterative declustering in pp and Pb-Pb collisions at LHC energies*, 1905.02512.

[149] J. Gallicchio and M. D. Schwartz, *Seeing in Color: Jet Superstructure*, *Phys. Rev. Lett.* **105** (2010) 022001 [1001.5027].

[150] S. D. Ellis, C. K. Vermilion and J. R. Walsh, *Recombination Algorithms and Jet Substructure: Pruning as a Tool for Heavy Particle Searches*, *Phys. Rev. D* **81** (2010) 094023 [0912.0033].

[151] M. Cacciari, G. P. Salam and G. Soyez, *SoftKiller, a particle-level pileup removal method*, *Eur. Phys. J. C* **75** (2015) 59 [1407.0408].

[152] F. A. Dreyer, L. Necib, G. Soyez and J. Thaler, *Recursive Soft Drop*, *JHEP* **06** (2018) 093 [1804.03657].

[153] C. Frye, A. J. Larkoski, M. D. Schwartz and K. Yan, *Factorization for groomed jet substructure beyond the next-to-leading logarithm*, *JHEP* **07** (2016) 064 [1603.09338].

[154] S. Marzani, L. Schunk and G. Soyez, *A study of jet mass distributions with grooming*, *JHEP* **07** (2017) 132 [1704.02210].

[155] ATLAS collaboration, M. Aaboud et al., *Measurement of the Soft-Drop Jet Mass in pp Collisions at $\sqrt{s} = 13$ TeV with the ATLAS Detector*, *Phys. Rev. Lett.* **121** (2018) 092001 [1711.08341].

[156] STAR collaboration, K. Kauder, *Measurement of the Shared Momentum Fraction z_g using Jet Reconstruction in p+p and Au+Au Collisions with STAR*, *Nucl. Part. Phys. Proc.* **289-290** (2017) 137 [1703.10933].

[157] CMS collaboration, A. M. Sirunyan et al., *Measurements of the differential jet cross section as a function of the jet mass in dijet events from proton-proton collisions at $\sqrt{s} = 13$ TeV*, *JHEP* **11** (2018) 113 [1807.05974].

[158] ATLAS collaboration, T. A. collaboration, *Measurement of the Lund Jet Plane using charged particles with the ATLAS detector from 13 TeV proton–proton collisions*, .

[159] ATLAS collaboration, G. Aad et al., *Measurement of soft-drop jet observables in pp collisions with the ATLAS detector at $\sqrt{s}$ =13 TeV*, *Phys. Rev. D* **101** (2020) 052007 [1912.09837].

[160] STAR collaboration, J. Adam et al., *Measurement of groomed jet substructure observables in p+p collisions at $\sqrt{s}$ =200 GeV with STAR*, *Phys. Lett. B* **811** (2020) 135846 [2003.02114].

[161] ATLAS collaboration, G. Aad et al., *Measurement of the Lund jet plane using charged particles in 13 TeV proton-proton collisions with the ATLAS detector*, 2004.03540.

[162] Y. Makris, *Transverse Momentum Dependent Fragmenting Jet Functions with Applications to Quarkonium Production*, *PoS* **QCDEV2017** (2017) 035.

[163] A. J. Larkoski, I. Moult and D. Neill, *Factorization and Resummation for Groomed Multi-Prong Jet Shapes*, *JHEP* **02** (2018) 144 [1710.00014].

[164] A. J. Larkoski, I. Moult and D. Neill, *Analytic Boosted Boson Discrimination at the Large Hadron Collider*, 1708.06760.

[165] J. Baron, S. Marzani and V. Theeuwes, *Soft-Drop Thrust*, *JHEP* **08** (2018) 105 [1803.04719].

[166] Z.-B. Kang, K. Lee, X. Liu and F. Ringer, *Soft drop groomed jet angularities at the LHC*, *Phys. Lett.* **B793** (2019) 41 [1811.06983].

[167] Y. Makris and V. Vaidya, *Transverse Momentum Spectra at Threshold for Groomed Heavy Quark Jets*, *JHEP* **10** (2018) 019 [1807.09805].

[168] A. Kardos, G. Somogyi and Z. Trócsányi, *Soft-drop event shapes in electron–positron annihilation at next-to-next-to-leading order accuracy*, *Phys. Lett.* **B786** (2018) 313 [1807.11472].

[169] J. Chay and C. Kim, *Factorized groomed jet mass distribution in inclusive jet processes*, *J. Korean Phys. Soc.* **74** (2019) 439 [1806.01712].

[170] D. Napoletano and G. Soyez, *Computing N-subjettiness for boosted jets*, *JHEP* **12** (2018) 031 [1809.04602].

[171] C. Lee, P. Shrivastava and V. Vaidya, *Predictions for energy correlators probing substructure of groomed heavy quark jets*, *JHEP* **09** (2019) 045 [1901.09095].

[172] A. H. Hoang, S. Mantry, A. Pathak and I. W. Stewart, *Nonperturbative Corrections to Soft Drop Jet Mass*, 1906.11843.

[173] D. Gutierrez-Reyes, Y. Makris, V. Vaidya, I. Scimemi and L. Zoppi, *Probing Transverse-Momentum Distributions With Groomed Jets*, *JHEP* **08** (2019) 161 [1907.05896].

[174] A. Kardos, A. Larkoski and Z. Trócsányi, *Soft-Dropped Observables with CoLoRFuLNNLO*, *Acta Phys. Polon. B* **50** (2019) 1891.

[175] S. Marzani, D. Reichelt, S. Schumann, G. Soyez and V. Theeuwes, *Fitting the Strong Coupling Constant with Soft-Drop Thrust*, *JHEP* **11** (2019) 179 [1906.10504].

[176] Y. Mehtar-Tani, A. Soto-Ontoso and K. Tywoniuk, *Dynamical grooming of QCD jets*, 1911.00375.

[177] A. Kardos, A. J. Larkoski and Z. Trócsányi, *Two- and Three-Loop Data for Groomed Jet Mass*, 2002.05730.

[178] A. J. Larkoski, *Improving the understanding of jet grooming in perturbation theory*, *JHEP* **09** (2020) 072 [2006.14680].

[179] A. Lifson, G. P. Salam and G. Soyez, *Calculating the primary Lund Jet Plane density*, 2007.06578.

[180] S. Amoroso et al., *Les Houches 2019: Physics at TeV Colliders: Standard Model Working Group Report*, in *11th Les Houches Workshop on Physics at TeV Colliders: PhysTeV Les Houches*, 3, 2020, 2003.01700.

[181] M. Dasgupta, A. Fregoso, S. Marzani and G. P. Salam, *Towards an understanding of jet substructure*, *JHEP* **09** (2013) 029 [1307.0007].

[182] A. H. Hoang, S. Mantry, A. Pathak and I. W. Stewart, *Extracting a Short Distance Top Mass with Light Grooming*, *Phys. Rev. D* **100** (2019) 074021 [1708.02586].

[183] S. Marzani, L. Schunk and G. Soyez, *The jet mass distribution after Soft Drop*, *Eur. Phys. J. C* **78** (2018) 96 [1712.05105].

[184] R. Appleby and M. Seymour, *Nonglobal logarithms in interjet energy flow with kt clustering requirement*, *JHEP* **12** (2002) 063 [hep-ph/0211426].

[185] A. Hornig, C. Lee, J. R. Walsh and S. Zuberi, *Double Non-Global Logarithms In-N-Out of Jets*, *JHEP* **01** (2012) 149 [1110.0004].

[186] A. Hornig, C. Lee, I. W. Stewart, J. R. Walsh and S. Zuberi, *Non-global Structure of the $O(\alpha_s^2)$ Dijet Soft Function*, *JHEP* **08** (2011) 054 [1105.4628].

[187] M. Balsiger, T. Becher and A. Ferroglia, *Resummation of non-global logarithms in cross sections with massive particles*, 2006.00014.

[188] Y. Delenda, R. Appleby, M. Dasgupta and A. Banfi, *On QCD resummation with k_t clustering*, *JHEP* **12** (2006) 044 [hep-ph/0610242].

[189] K. Khelifa-Kerfa, *Non-global logs and clustering impact on jet mass with a jet veto distribution*, *JHEP* **02** (2012) 072 [1111.2016].

[190] Y. Delenda and K. Khelifa-Kerfa, *On the resummation of clustering logarithms for non-global observables*, *JHEP* **09** (2012) 109 [1207.4528].

[191] R. Kelley, J. R. Walsh and S. Zuberi, *Abelian Non-Global Logarithms from Soft Gluon Clustering*, *JHEP* **09** (2012) 117 [1202.2361].

[192] R. Kelley, J. R. Walsh and S. Zuberi, *Disentangling Clustering Effects in Jet Algorithms*, 1203.2923.

[193] D. Neill, *Non-Global and Clustering Effects for Groomed Multi-Prong Jet Shapes*, *JHEP* **02** (2019) 114 [1808.04897].

[194] A. Larkoski, I. Moult and D. Neill, *Measuring Two Angularities on a Single Jet*, *Int. J. Mod. Phys. Conf. Ser.* **37** (2015) 1560046.

[195] M. Procura, W. J. Waalewijn and L. Zeune, *Joint resummation of two angularities at next-to-next-to-leading logarithmic order*, *JHEP* **10** (2018) 098 [1806.10622].

[196] C. W. Bauer, F. J. Tackmann, J. R. Walsh and S. Zuberi, *Factorization and Resummation for Dijet Invariant Mass Spectra*, *Phys. Rev. D* **85** (2012) 074006 [1106.6047].

[197] M. Procura, W. J. Waalewijn and L. Zeune, *Resummation of Double-Differential Cross Sections and Fully-Unintegrated Parton Distribution Functions*, *JHEP* **02** (2015) 117 [1410.6483].

[198] CMS collaboration, C. Collaboration, *Measurement of groomed jet mass in PbPb and pp collisions at* $\sqrt{s_{NN}} = 5.02$ TeV, .

[199] ATLAS collaboration, G. Aad et al., *Measurement of the jet mass in high transverse momentum* $Z(\to b\bar{b})\gamma$ *production at* $\sqrt{s} = 13$ *TeV using the ATLAS detector*, 1907.07093.

[200] CMS collaboration, A. M. Sirunyan et al., *Search for low mass vector resonances decaying into quark-antiquark pairs in proton-proton collisions at* $\sqrt{s} = 13$ *TeV*, *Phys. Rev. D* **100** (2019) 112007 [1909.04114].

[201] ALICE collaboration, J. Mulligan, *Jet substructure measurements in* pp *and Pb-Pb collisions at* $\sqrt{s_{\rm NN}} = 5.02$ *TeV with ALICE*, 2009.07172.

[202] CMS collaboration, A. M. Sirunyan et al., *Measurement of jet substructure observables in $\mathrm{t\bar{t}}$ events from proton-proton collisions at $\sqrt{s} = 13TeV$*, *Phys. Rev. D* **98** (2018) 092014 [1808.07340].

[203] A. Larkoski, S. Marzani, J. Thaler, A. Tripathee and W. Xue, *Exposing the QCD Splitting Function with CMS Open Data*, *Phys. Rev. Lett.* **119** (2017) 132003 [1704.05066].

[204] A. Tripathee, W. Xue, A. Larkoski, S. Marzani and J. Thaler, *Jet Substructure Studies with CMS Open Data*, *Phys. Rev. D* **96** (2017) 074003 [1704.05842].

[205] Y. Mehtar-Tani and K. Tywoniuk, *Groomed jets in heavy-ion collisions: sensitivity to medium-induced bremsstrahlung*, *JHEP* **04** (2017) 125 [1610.08930].

[206] Y.-T. Chien and I. Vitev, *Probing the Hardest Branching within Jets in Heavy-Ion Collisions*, *Phys. Rev. Lett.* **119** (2017) 112301 [1608.07283].

[207] N.-B. Chang, S. Cao and G.-Y. Qin, *Probing medium-induced jet splitting and energy loss in heavy-ion collisions*, *Phys. Lett. B* **781** (2018) 423 [1707.03767].

[208] H. T. Li and I. Vitev, *Inverting the mass hierarchy of jet quenching effects with prompt b-jet substructure*, *Phys. Lett. B* **793** (2019) 259 [1801.00008].

[209] G. Milhano, U. A. Wiedemann and K. C. Zapp, *Sensitivity of jet substructure to jet-induced medium response*, *Phys. Lett. B* **779** (2018) 409 [1707.04142].

[210] R. Kunnawalkam Elayavalli and K. C. Zapp, *Medium response in JEWEL and its impact on jet shape observables in heavy ion collisions*, *JHEP* **07** (2017) 141 [1707.01539].

[211] J. Casalderrey-Solana, G. Milhano, D. Pablos and K. Rajagopal, *Modification of Jet Substructure in Heavy Ion Collisions as a Probe of the Resolution Length of Quark-Gluon Plasma*, *JHEP* **01** (2020) 044 [1907.11248].

[212] P. Caucal, E. Iancu and G. Soyez, *Deciphering the z_g distribution in ultrarelativistic heavy ion collisions*, *JHEP* **10** (2019) 273 [1907.04866].

[213] R. Abdul Khalek et al., *Science Requirements and Detector Concepts for the Electron-Ion Collider: EIC Yellow Report*, 2103.05419.

[214] C. W. Bauer, S. Fleming, D. Pirjol, I. Z. Rothstein and I. W. Stewart, *Hard scattering factorization from effective field theory*, *Phys. Rev.* **D66** (2002) 014017 [hep-ph/0202088].

[215] A. Pathak, I. W. Stewart, V. Vaidya and L. Zoppi, *EFT for Soft Drop Double Differential Cross Section*, 2012.15568.

[216] M. Arratia, Y. Song, F. Ringer and B. V. Jacak, *Jets as precision probes in electron-nucleus collisions at the future Electron-Ion Collider*, *Phys. Rev. C* **101** (2020) 065204 [1912.05931].

[217] B. S. Page, X. Chu and E. C. Aschenauer, *Experimental Aspects of Jet Physics at a Future EIC*, *Phys. Rev. D* **101** (2020) 072003 [1911.00657].